DOCTOR OF PHILOSOPHY

A theoretical study of coupling and dephasing in semiconductor quantum dots

Dominguez, Javier

Award date:
2004

Awarding institution:
Bangor University

A THEORETICAL STUDY OF COUPLING AND DEPHASING IN SEMICONDUCTOR QUANTUM DOTS

BY JAVIER DOMÍNGUEZ

A thesis submitted in candidature for the degree of

DOCTOR OF PHILOSOPHY

School of Informatics

University of Wales, Bangor

August 2004

In memory of
my father

Acknowledgements

Firstly I would like to thank my supervisor Dr. Paul Rees for his help and advice. Also I would like to thank my group colleagues for providing such a friendly working environment. Marta, thanks for your help, support, patience and encouragement. Eskerrik asko zure laguntzagatik. Dudarik gabe, tesiaren zati garrantzitsuena izan zara.

Generally I would like to thank everyone that helped me juggling physics, equations and quantum dots and especially everyone that juggled with me helping me forget about physics, equations and quantum dots.

Me gustaría agradecer toda la ayuda y el apoyo recibido por mi familia durante todos estos años. A vosotros también va dedicado todo este montón de números símbolos y fórmulas. Marta, gracias de nuevo.

Abstract

In recent years, advances in crystal growth techniques have made it possible to fabricate semiconductor microstructures, which are so small that their electronic and optical properties deviate substantially from those of bulk materials. In these microstructures the electrons and holes energies are confined in one or more directions to a region, which is still considerably larger than the lattice constant but so small that the electron envelope wavefunctions become quantised.

Quantum dots (QD's) are nanometer-scale structures that provide carrier confinement in all three spatial dimensions. In these structures the carrier momentum is also quantised in all three directions and hence a carrier confined within a QD can only occupy certain discrete energy levels, which depend on various factors like the potential barrier depth or the shape of the structure. It is the discrete nature of these energy states that make quantum dots highly attractive for quantum computation and optoelectronic devices.

In this thesis the quantum energy levels of single and coupled quantum dots of different shapes are investigated. Coupled QD systems, which may be considered as 'artificial molecules' have been investigated for their possible application in quantum computing. An understanding of how dots couple in quantum dot molecules is needed. We use the linear combination of quantum dot states approximation in order to obtain the two lowest energy levels of the system and then been able to study the coupling between dots when the potential and the separation between dots are varied.

This coupling can be used as a quantum gate, which is a key to building a quantum processor. This gate is achieve using the coupling between QD's and a mechanism which make it possible to switch this coupling on and off. The time required for the 'switching' needs to be long enough for the operation to be performed coherently.

In the last chapter we study a possible source of decoherence due to the LO-phonon interaction in self-assembled quantum dots (SAD's). We calculate single electron capture-escape rates due to LO-phonon interaction for single SAD and coupled SAD's systems.

Contents

Chapter 1

Introduction

Contents

1.1 Mesoscopic semiconductors structures

It is now possible to fabricate semiconductor microstructures, which are small enough so that quantum effects alter the electronic properties from those of bulk material. In these microstructures, carriers are confined in one or more directions to a region of length L_c, larger than the lattice constant, but so small that the allowed carriers energies become quantised. Structures of this size are called *mesoscopic*. A *Quantum Dot* (QD) is an example of such mesoscopic semiconductor, where the electrons are confined in three space dimensions.

To understand the fundamental concepts of these semiconductors, which cannot be explained using classical mechanics, quantum mechanics must be applied to solid state theory. In this chapter we introduce the concepts of quantum mechanics, which

give the background to calculate the electronic structure of QD's. The electronic state information will be used to investigate the suitability of QD's for semiconductor laser applications and for use in quantum computing. So in the remaining part of this chapter the background theory of quantum dot lasers and quantum computing will be studied.

1.1.1 Schrödinger Equation for electrons

In order to discuss electrons in semiconductors we must understand the equations which determine the state of an electron within a semiconductor.

In the beginning of the twentieth century quantum mechanics emerged in order to describe certain problems Newtonian mechanics or classical electromagnetic theory could not explain. These problems include the photoelectric effect, blackbody spectrum and the rather complex radiation from an excited hydrogen gas[1]. These and other experimental observations lead to the concepts of quantisation of light into photons, the particle-wave duality, the *de Broglie wavelength* and the fundamental equation describing quantum mechanics, namely the *Schrödinger equation.*

1.1.2 The mechanics of waves

In quantum mechanics, the properties and motion of particles are defined in terms of a wave (or state) function, which depends on the momentum. De Broglie stated that a particle of momentum p has an associated wave of wavelength λ given by the following [2]

$$\lambda = \frac{h}{p} \tag{1.1}$$

Therefore, an electron in a vacuum at a position $\mathbf{r}$, away from the influence of any electromagnetic potentials, could be described by a state function which is of the form of a wave, i.e.

$$\psi = \mathrm{e}^{\mathrm{i}(\mathbf{kr}-\omega t)} \tag{1.2}$$

where t is the time, ω the angular frequency and the modulus of the wave vector, k, is given by:

$$k = |\mathbf{k}| = \frac{2\pi}{\lambda} \tag{1.3}$$

The quantum mechanical momentum has been deduced to be a linear operator acting upon the *wavefunction* ψ, with the momentum $\mathbf{p}$ arising as an eigenvalue, i.e.

$$-\mathrm{i}\hbar\nabla\psi = \mathbf{p}\psi \tag{1.4}$$

where

$$\nabla = \frac{\partial}{\partial x}\hat{\mathbf{i}} + \frac{\partial}{\partial y}\hat{\mathbf{j}} + \frac{\partial}{\partial z}\hat{\mathbf{k}} \tag{1.5}$$

which when operating on the electron vacuum wavefunction in Equation 1.2 would give the following:

$$-\mathrm{i}\hbar\nabla\mathrm{e}^{\mathrm{i}(\mathbf{kr}-\omega t)} = \mathbf{p}\mathrm{e}^{\mathrm{i}(\mathbf{kr}-\omega t)} \tag{1.6}$$

and therefore

$$-\mathrm{i}\hbar\left(\frac{\partial}{\partial x}\hat{\mathbf{i}} + \frac{\partial}{\partial y}\hat{\mathbf{j}} + \frac{\partial}{\partial z}\hat{\mathbf{k}}\right)\mathrm{e}^{\mathrm{i}(k_x x+k_y y+k_z z-wt)} \;=\; \mathbf{p}\mathrm{e}^{\mathrm{i}(\mathbf{kr}-wt)} \tag{1.7}$$

$$-\mathrm{i}\hbar\left(\mathrm{i}k_x\hat{\mathbf{i}} + \mathrm{i}k_y\hat{\mathbf{j}} + \mathrm{i}k_z\hat{\mathbf{k}}\right)\mathrm{e}^{\mathrm{i}(k_x x+k_y y+k_z z-wt)} \;=\; \mathbf{p}\mathrm{e}^{\mathrm{i}(\mathbf{kr}-wt)} \tag{1.8}$$

Therefore the eigenvalue:

$$\mathbf{p} = \hbar\left(k_x\hat{\mathbf{i}} + k_y\hat{\mathbf{j}} + k_z\hat{\mathbf{k}}\right) = \hbar\mathbf{k} \tag{1.9}$$

which may be manipulated ($p = \hbar k = (h/2\pi)(2\pi/\lambda)$) to reproduce de Broglie's relationship in Equation 1.1.

Following on from this, classical mechanics gives the kinetic energy of a particle of mass m as[2]

$$T = \frac{1}{2}mv^2 = \frac{(mv)^2}{2m} = \frac{p^2}{2m} \tag{1.10}$$

Therefore it may be expected that the quantum mechanical analogy can also be represented by an eigenvalue equation with an operator:

$$\frac{1}{2m}(-\mathrm{i}\hbar\nabla)^2\psi = T\psi \tag{1.11}$$

where T is the kinetic energy eigenvalue.

When acting upon the electron vacuum wavefunction, i.e.

$$-\frac{\hbar^2}{2m}\nabla^2 \mathrm{e}^{\mathrm{i}(\mathbf{kr}-\omega t)} = T\mathrm{e}^{\mathrm{i}(\mathbf{kr}-\omega t)} \tag{1.12}$$

then

$$-\frac{\hbar^2}{2m}\left({k_x}^2 + {k_y}^2 + {k_z}^2\right)\mathrm{e}^{\mathrm{i}(\mathbf{kr}-\omega t)} = T\mathrm{e}^{\mathrm{i}(\mathbf{Kr}-\omega t)} \tag{1.13}$$

Then the kinetic energy eigenvalue is given by:

$$T = \frac{\hbar^2 k^2}{2m} \tag{1.14}$$

For an electron in a vacuum away from the influence of electromagnetic fields, then the total energy E is just the kinetic energy T. Therefore the dispersion or energy versus momentum (which is proportional to the wave vector k) curves are parabolic, just as for classical free particles, as illustrated in Figure 1.1.

In summary, the equation describing the total energy of a particle in this wave description is called the time-independent Schrödinger Equation and for this case

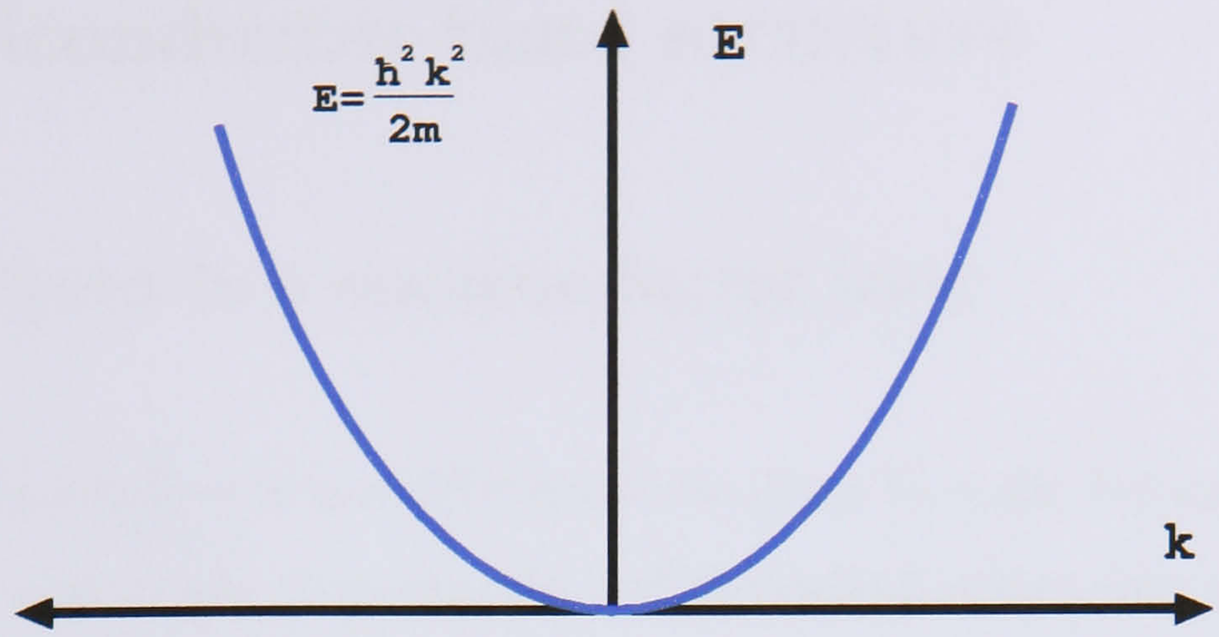

Figure 1.1: The energy versus wavevector curve for an electron in a vacuum.

with only a kinetic energy contribution can be summarised as follows:

$$-\frac{\hbar^2}{2m}\nabla^2\psi = E\psi \tag{1.15}$$

A corresponding equation also exists which includes the time-dependency explicitly; this is obtained by operating on the wave function by the linear operator $i\hbar\partial/\partial t$, i.e.

$$i\hbar\frac{\partial}{\partial t}\psi = i\hbar(-i\omega)e^{i(\mathbf{k}r-\omega t)} \tag{1.16}$$

i.e.

$$i\hbar\frac{\partial}{\partial t}\psi = \hbar\omega\psi \tag{1.17}$$

This eigenvalue $\hbar\omega$ is also the total energy but in a form usually associated with waves, e.g. a photon. These two operations on the wavefunction represent the two complimentary descriptions associated with wave-particle duality. Therefore the time-dependent Schrödinger equation is given by the following

$$i\hbar\frac{\partial}{\partial t}\psi = E\psi \tag{1.18}$$

1.2 Semiconductor band structure

1.2.1 Electrons in a semiconductor laser

Electrons in semiconductors are different from those in a gas because electrons are bounded to the ions in the ground state and in excited states they can move freely. Electrons in semiconductors are organised in allowed energy bands of states, known as *valence* (low energy) and *conduction* bands. An isolated atom has a discrete set of energy levels. In a semiconductor crystal, where atoms interact with each other, the initial atomic energy levels are split into as many sub-levels as atoms in the system. These sub-levels are grouped forming continuous bands of energy, where the highest occupied band is called valence band and the lower unoccupied is called conduction band. These energy bands are separated by a forbidden gap called the *bandgap*, which depends on the material of the semiconductor (see Figure 1.2).

In the absence of thermal or other excitation, the system is in equilibrium and the electron distribution probability is given by the Fermi-Dirac distribution:

$$f(E) = \frac{1}{1 + \mathrm{e}^{\frac{E-E_F}{K_B T}}} \tag{1.19}$$

where E is the energy of the electron and E_F is known as the *Fermi energy level*, and is defined as the energy at which, for zero temperature, all energy states below it are occupied and all above are empty. Moreover, at a finite temperature T, E_F represents the energy at which the occupation probability is $f(E_F) = 1/2$.

When an electron is excited from the valence into the conduction band, an absence of electron within the valence band is created. This empty state is treated as a carrier, known as *hole*. Taking the energy of the electron/hole zero at the bottom/top of the conduction/valence band and the energy sign is positive into the band, as seen in Figure 1.3a), the electron/hole distribution probability in the conduction/valence

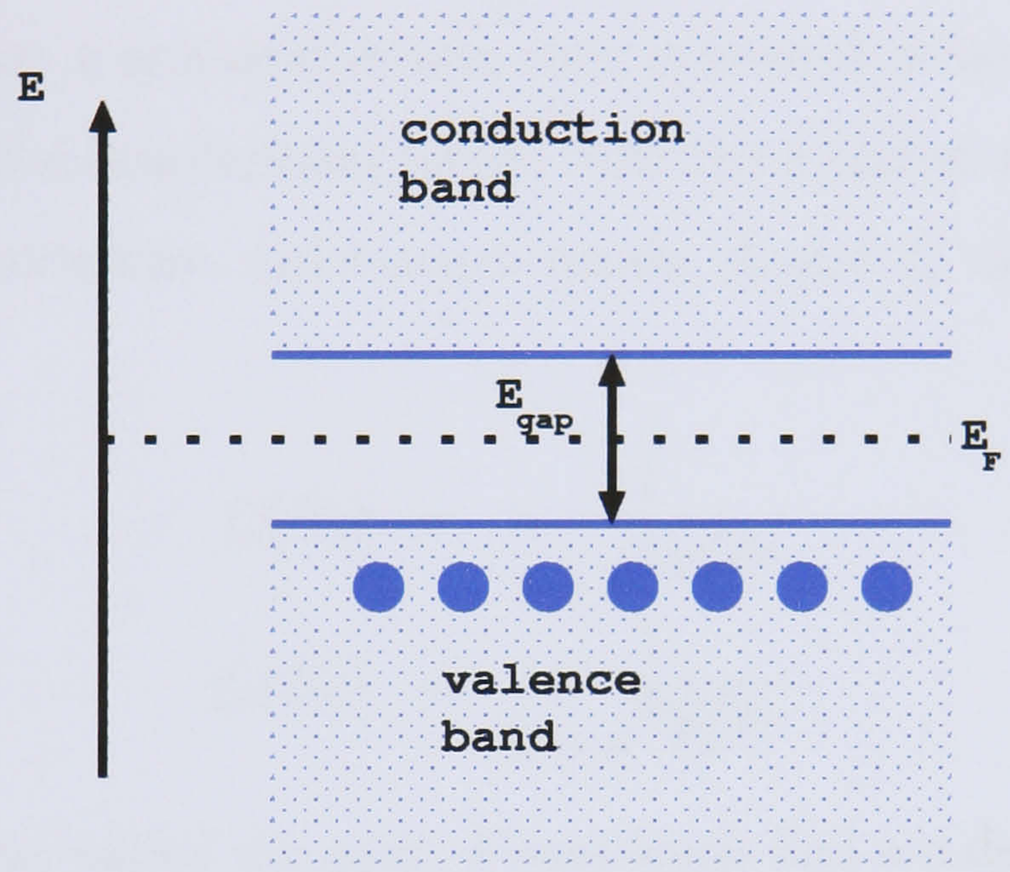

Figure 1.2: Schematic representation of the energy bands within a semiconductor where the difference between bands is called the bandgap labelled as E_{gap}. In an equilibrium situation the Fermi level, E_F, represents the energy at which, for zero temperature, all energy states below it are occupied and all above are empty.

band in an equilibrium state is given by

$$f_c(E_e) = \frac{1}{1+\mathrm{e}^{\frac{E_e-E_F}{K_BT}}} \tag{1.20}$$

$$f_v(E_h) = \frac{1}{1+\mathrm{e}^{\frac{E_h-E_F}{K_BT}}} \tag{1.21}$$

where the Fermi level is the same for electrons and holes.

Under carrier injection, a non-equilibrium state is formed, where electrons/holes are injected into the conduction/valence band. Now the electron and hole distribution probability in the conduction and valence bands, f_c and f_v respectively, are given by

$$f_c(E_e) = \frac{1}{1+\mathrm{e}^{\frac{E_e-E_{Fc}}{K_BT}}} \tag{1.22}$$

$$f_v(E_h) = \frac{1}{1+\mathrm{e}^{\frac{E_h-E_{Fv}}{K_BT}}} \tag{1.23}$$

where E_{Fc} and E_{Fv} are called the *quasi-Fermi levels* and are defined as the energies at which, for zero temperature, all energy states below them are occupied and all above are empty, within the conduction and valence bands respectively, as can be seen in Figure 1.3b).

1.2.2 Effective mass approximation

Each electron (or hole) within the crystal has associated a spatial wavefunction which defines the motion and the total energy. The electron wavefunction within the valence or the conduction band, Ψ, may be obtained solving the Schrödinger equation where the Hamiltonian, $\hat{H}$, and its energy are related as

$$\hat{H}\Psi \equiv \left[\frac{\hat{\mathbf{p}}^2}{2m} + V(\mathbf{r})\right]\Psi = E\Psi \tag{1.24}$$

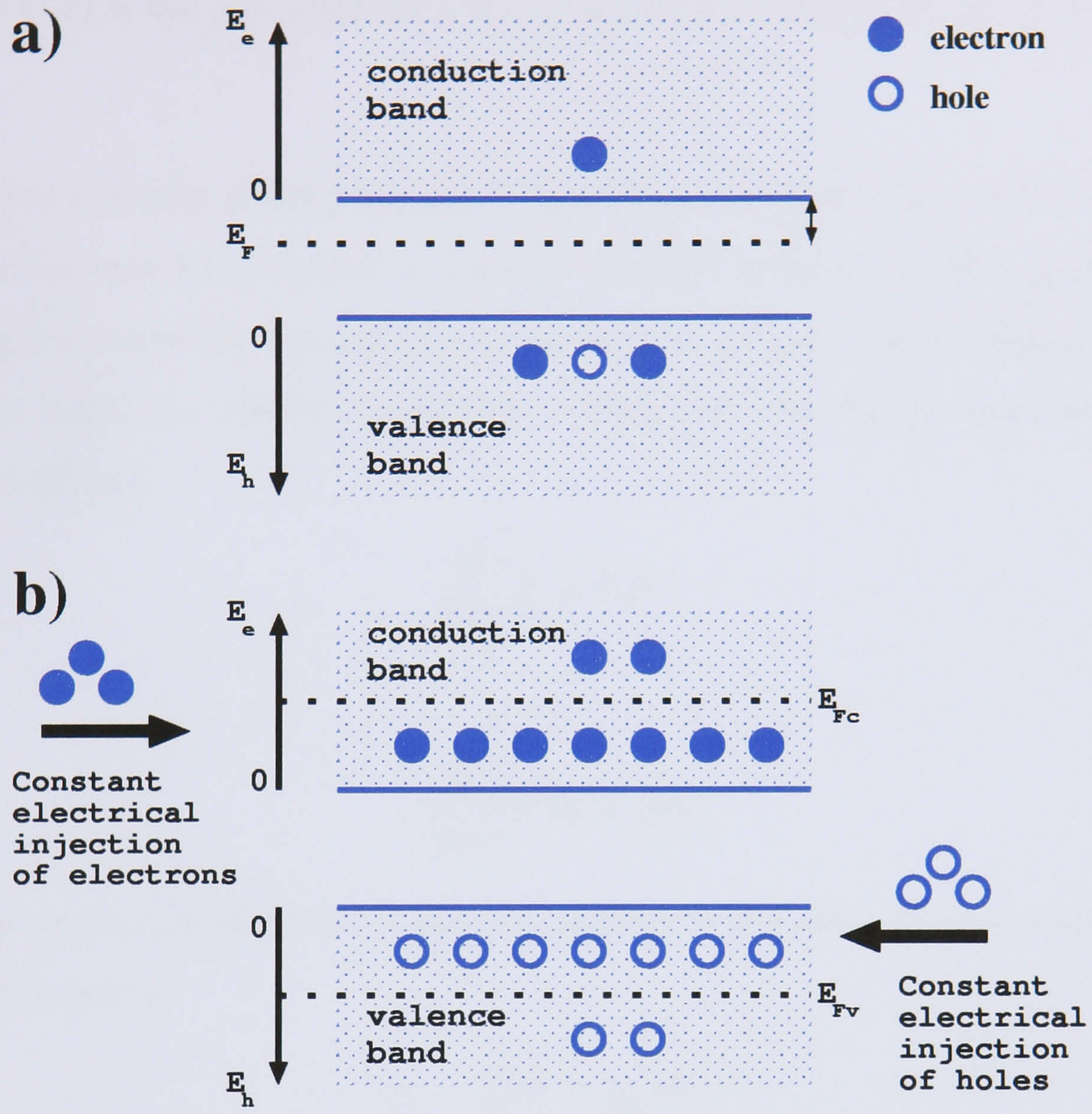

Figure 1.3: Schematic representation of the energy bands within a semiconductor in **a)**an equilibrium situation. **b)**a non-equilibrium situation. Electrons/holes are injected into the conduction/valence band. This process creates the 'Quasi-Fermi' levels, E_{Fc} and E_{Fv}, which represent the energy at which, for zero temperature, all energy states below them are occupied and all above are empty within the conduction (electrons) and valence (holes) bands respectively. It has taken zero energy of the electrons/holes at the bottom/top of the conduction/valence band and the energy sign positive into the band

.

where $\mathbf{r}$ is the position vector, $\hat{\mathbf{p}}$ is the the momentum operator, m is the electron mass and $V(\mathbf{r})$ is the potential the electron experiences due to the periodic array of atoms.

Due to the complexity of the potential V, the above equation is very difficult to solve. This problem may be simplified using the so-called 'effective mass approximation' which approximates the potential to a constant by introducing an empirical fitting parameter called the effective mass, m^*. Then the Schrödinger equation can be written as follows

$$\frac{p^2}{2m^*}\Psi = E\Psi \tag{1.25}$$

or

$$-\frac{\hbar^2}{2m^*}\nabla^2\Psi = E\Psi \tag{1.26}$$

where the general solution for Ψ may be written as the sum of two counter propagating plane waves

$$\Psi = A\mathrm{e}^{\mathbf{ikr}} + B\mathrm{e}^{-\mathbf{ikr}} \tag{1.27}$$

Therefore the solution for the energy E is given by

$$E = \frac{\hbar^2 k^2}{2m^*} \tag{1.28}$$

Figure 1.4 represents the energy bands structure against the modulus of the k-vector, where the valence band is inverted, i.e. lowest energy hole states are at the top of the band. The convention is to put the zero of the energy at the top of the valence band.

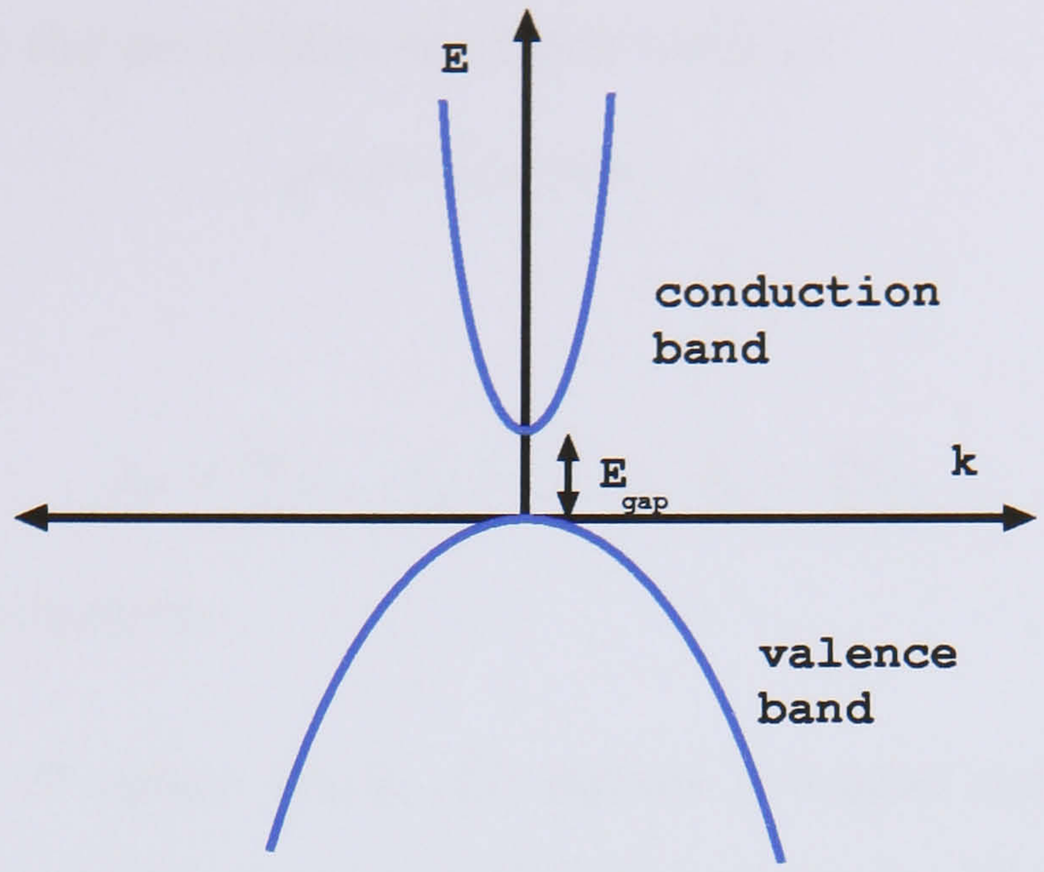

Figure 1.4: The energy versus wave vector curves for an electron in the conduction band and a hole in the valence band of a typical semiconductor.

1.2.3 Density of states

A carrier may occupy one of the allowed energy level states within the band structure. In order to obtain the number of electrons within a band, it is necessary to determine the number of allowed states an electron can occupy within the energy distribution. On using the effective mass approximation, the electron wavefunction within a bulk semiconductor may be described by Equation 1.27. Considering the crystal formed by units cells of side (L_x, L_y, L_z), the wavefunction must display periodicity within the lattice. Therefore

$$\psi(x, y, z) = \psi(x + L_x, y + L_y, z + L_z) \tag{1.29}$$

Writing the normalised wavefunction as $\psi = 1/\Omega \mathrm{e}^{\mathbf{ikr}}$ leads to

$$\psi(x, y, z) = \frac{1}{\Omega} \mathrm{e}^{\mathrm{i}(k_x x + k_y y + k_z z)} \mathrm{e}^{\mathrm{i}(k_x L_x + k_y L_y + k_z L_z)} \tag{1.30}$$

Taking into account the periodicity condition leads to

$$e^{i(k_x L + k_y L_y + k_z L_z)} = 1 \tag{1.31}$$

which implies that

$$k_x = \frac{2\pi}{L_x} n_x \quad k_y = \frac{2\pi}{L_y} n_y \quad k_z = \frac{2\pi}{L_z} n_z \tag{1.32}$$

where n_x, n_y, n_z are integers.

Therefore, each set of values (k_x, k_y, k_z) defines a unique state that an electron within a bulk semiconductor crystal is allowed to occupy. The volume of **k**-space occupied by a state is $(2\pi)^3/(L_x L_y L_z)$.

The density of states (DOS) is defined as the number of states per energy per unit volume of the cell[2]:

$$\rho(E) = \frac{dN}{dE} \tag{1.33}$$

where N in **k**-space is equal to the volume of the sphere of radius $|\mathbf{k}|$ divided by the volume occupied by one state $(2\pi)^3/(L_x L_y L_z)$ and divided again by the cell volume $V = L_x L_y L_z$. Note that a factor 2 has to be included in order to take account of the spin.

$$N = 2\frac{4\pi k^3}{3}\frac{1}{(2\pi)^3/V}\frac{1}{V} \tag{1.34}$$

$$= 2\frac{4\pi k^3}{3(2\pi)^3} \tag{1.35}$$

Returning to Equation 1.33 the density of states may be written as

$$\rho(E) = \frac{dN}{dk}\frac{dk}{dE} \tag{1.36}$$

Making use of Equation 1.28 leads to

$$\frac{dk}{dE} = \left(\frac{2m^*}{\hbar^2}\right)^{1/2} \frac{E^{-1/2}}{2} \tag{1.37}$$

and therefore the density of states of states in bulk semiconductor per unit energy and volume may be written as

$$\rho(E) = \frac{1}{2\pi^2}\left(\frac{2m^*}{\hbar^2}\right)^{3/2} E^{1/2} \tag{1.38}$$

1.3 Semiconductor laser

In order to obtain lasing action from a semiconductor three things are required

- **Gain medium**. A semiconductor region where stimulated emission occurs. Examples in modern semiconductor lasers are quantum wells, wires or dots.

- **Optical resonant cavity**. It provides photon confinement in order to allow the number of photons created by stimulated emission to exceed all other mechanisms. It can be achieved by bounding the gain medium in a resonator. Hence photons created by stimulated emission can reflect back and forward, creating more recombinations events.

- **Population inversion**. A mechanism to pump electrons into the conduction band is needed in order to obtain more electrons in upper bands and holes in lower bands which increases the number of stimulated emission processes. A forward biased p-n junction structure is the most commonly used method to achieved this.

1.3.1 Optical transitions in a semiconductor

So far, the electronic distribution of a semiconductor has been described by a two-level energy band structure composed of a conduction and a valence band. This

simple model will be used in order to describe optical transitions in a semiconductor although in reality the energy distribution structure is more complicated.

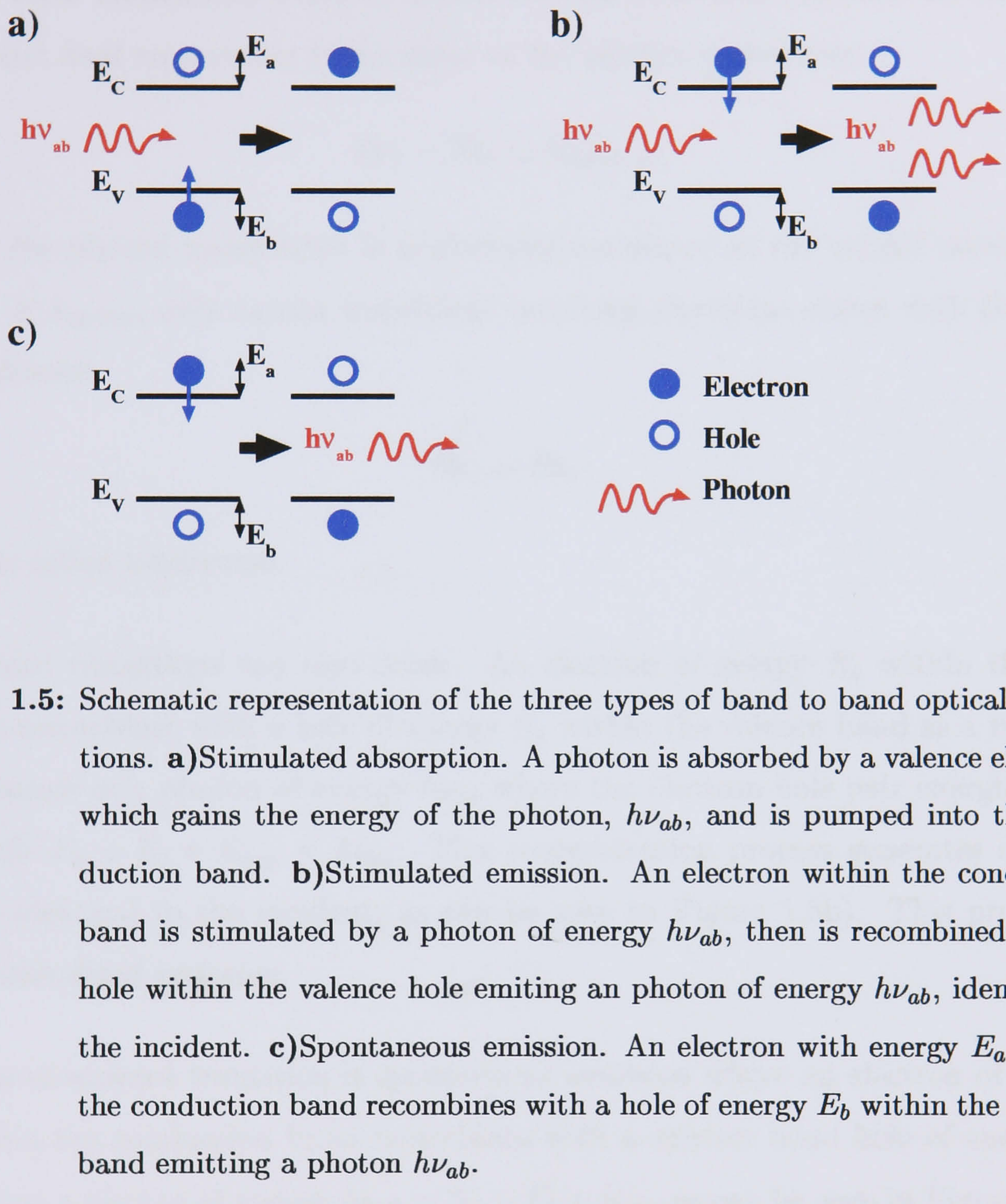

Figure 1.5: Schematic representation of the three types of band to band optical transitions. **a)**Stimulated absorption. A photon is absorbed by a valence electron, which gains the energy of the photon, $h\nu_{ab}$, and is pumped into the conduction band. **b)**Stimulated emission. An electron within the conduction band is stimulated by a photon of energy $h\nu_{ab}$, then is recombined with a hole within the valence hole emiting an photon of energy $h\nu_{ab}$, identical to the incident. **c)**Spontaneous emission. An electron with energy E_a within the conduction band recombines with a hole of energy E_b within the valence band emitting a photon $h\nu_{ab}$.

In the absence of thermal or other energy pumping processes, the conduction band appears empty, while the valence band remains full of electrons. If an electron within the valence band absorbs a photon of light and the energy of the photon, $h\nu_{ab}$, is larger than the bandgap $(E_C - E_V)$, it is excited into the empty conduction band to a state of energy E_a creating a hole in the valence band of energy E_b where

$E_a + E_b + E_{\text{gap}} = h\nu_{ab}$, as can be seen in Figure 1.5a).

As the total momentum must be conserved, the difference between an electron's initial and final momentum is the same as the photon momentum.

$$\hbar\mathbf{k}_f - \hbar\mathbf{k}_i = \hbar\mathbf{k}_{\text{photon}} \tag{1.39}$$

But as the photon momentum is neglectable compared to the carrier momentum, $k_{\text{photon}} \ll k_{\text{carrier}}$, only carrier transitions involving electronic states with the same $\mathbf{k}$ are allowed

$$\hbar\mathbf{k}_f = \hbar\mathbf{k}_i \tag{1.40}$$

which is called k-selection.

Downward transitions can also occur. An electron of energy E_a within the conduction recombines with a hole of energy E_b within the valence band as a result of the presence of a photon of energy $h\nu_{ab}$ where the electron-hole pair energies have to satisfy $E_a + E_b + E_{\text{gap}} = h\nu_{ab}$. This recombination process generates another photon identical to the incident, as can be seen in Figure 1.5b). This process is called *stimulated emission.*

Another downward transition is *spontaneous emission* where an electron of energy E_a within the conduction band recombines with a valence band hole of energy E_b generating a photon of energy $h\nu_{ab} = E_a + E_b + E_{\text{gap}}$ as can be seen in Figure 1.5c). This process can occur with no inducement of a radiation field.

1.3.2 Gain and absorption

Taking into account the processes studied in the last section, stimulated and spontaneous emission rates, called R_{ab}^{stim} and R_{ab}^{spont} respectively, are proportional to the

probability of finding an electron at energy level E_a in the conduction band and a hole (unoccupied state) at E_b in the valence band. The absorption rate is proportional to the probability of finding an electron and a hole at the energy levels E_b in the valence and at E_a in the conduction band, respectively. As explained in Section 1.2.1, the electron and hole distribution probability in the conduction and valence band, respectively, at T are given by Fermi distribution

$$f_c(E_e) = \frac{1}{1+\mathrm{e}^{\frac{E_e-E_{Fc}}{K_BT}}} \tag{1.41}$$

$$f_v(E_h) = \frac{1}{1+\mathrm{e}^{\frac{E_h-E_{Fv}}{K_BT}}} \tag{1.42}$$

Within the valence/conduction band an electron/hole can be seen as an absence of a hole/electron. Then the probability of finding an electron/hole with energy E within the valence/conduction band at temperature T is given by

$$f_v^{\text{electron}}(E) = 1 - f_v(E) \tag{1.43}$$

$$f_c^{\text{hole}}(E) = 1 - f_c(E) \tag{1.44}$$

Then the absorption and emission rates are given by

$$R_{ba}^{\text{absor}} \propto f_v^{\text{electron}}(E_b) f_c^{\text{hole}}(E_a) = [1 - f_v(E_b)][1 - f_c(E_a)] \tag{1.45}$$

$$R_{ab}^{\text{stim}} \propto f_c(E_a) f_v(E_b) \tag{1.46}$$

$$R_{ab}^{\text{spont}} \propto f_c(E_a) f_v(E_b) \tag{1.47}$$

In the case of stimulated emission and absorption the presence of a photon is also required. Calling $\rho_{\text{phot}}(h\nu_{ab})$ the photon density of the optical mode of energy $h\nu_{ab}$ last rates can be rewritten as:

$$R_{ba}^{\text{absor}} \propto f_v^{\text{electron}}(E_b) f_c^{\text{hole}}(E_a) \rho_{\text{phot}}(h\nu_{ab}) \tag{1.48}$$

$$R_{ab}^{\text{stim}} \propto f_c(E_a) f_v(E_b) \rho_{\text{phot}}(h\nu_{ab}) \tag{1.49}$$

$$R_{ab}^{\text{spont}} \propto f_c(E_a) f_v(E_b) \tag{1.50}$$

It has to be underlined that R_{ab}^{stim} and R_{ba}^{absor} are competing processes as R_{ab}^{stim} generates a photon, while R_{ab}^{stim} takes it away, hence another rate needs to be mentioned, i.e. the net_{ba} given by

$$\text{net}_{ba} = R_{ba}^{\text{absor}} - R_{ab}^{\text{stim}} \tag{1.51}$$

Hence, the *absorption* of photons into the mode $h\nu_{ab}$ in a semiconductor material can be described as [3]

$$\alpha(h\nu_{ab}) = \frac{\text{net}_{ab}}{\rho_{\text{phot}}(h\nu_{ab})} \tag{1.52}$$

and the *gain* of the semiconductor is the *negative absorption.*

1.3.3 Threshold gain

As it has been underlined before, population inversion is required in order to obtain lasing which can be achieved by pumping. A carrier current is applied which injects electrons and holes to any allowed energy state within the bands according to their density of states. Electrons populate higher energy levels, and they can be excited by photons and undergo a downward transition producing photons. It is also necessary to have a *resonator*, consisting of two parallel mirrors separated by a distance L in order to enforce the propagating field to traverse repeatedly the amplifying medium. This cavity causes optical losses, which have to be added to the losses due to the absorption.

The gain necessary to overcome the cavity losses is known as the *threshold gain.* It is also defined as *threshold current* the necessary current to reach the threshold gain. Hence, lasing appears when the value of the gain of the cavity is bigger than the threshold gain, as can be seen in Figure 1.6. It can also be seen that at low injection levels the spectra shows the device is absorbing at all energies above the

band-edge but at higher injection levels there is gain at energies near the band-edge.

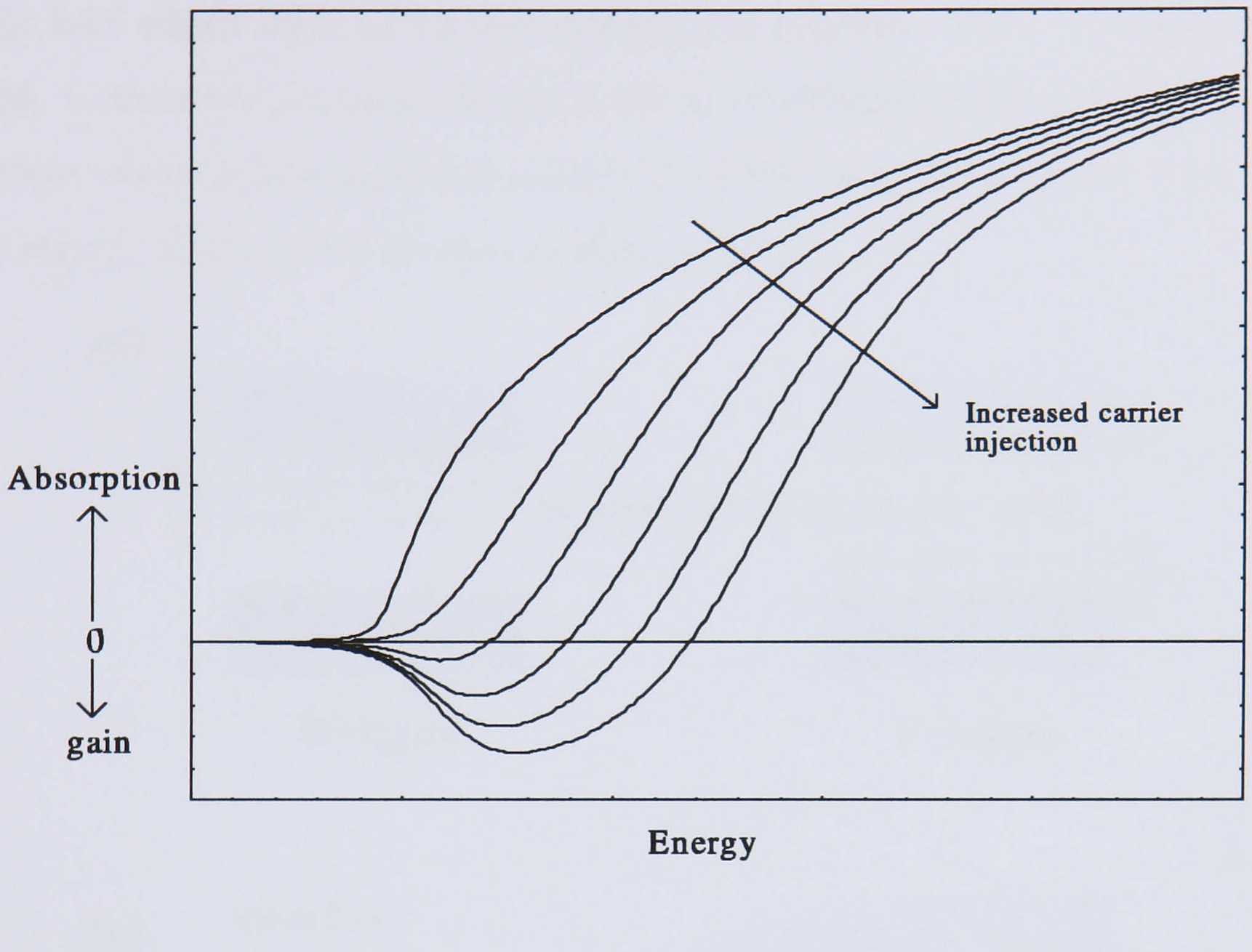

Figure 1.6: The typical absorption spectra of a bulk semiconductor shown for increasing carrier injection.

1.3.4 p-n junction

A p-n junction is formed by bringing a p-type and n-type semiconductors (doped with acceptors and donors respectively) together. The Fermi level changes when a material is doped. In the case of a p-type, the Fermi level is below the undoped Fermi level and the n-type is above it, as can be seen in Figure 1.7a). Once both materials are brought together, electrons from n-type diffuse to p-type material whereas holes do the opposite diffusing to n-type material. Due to this process a

depletion zone is created in the vicinity of the junction between the two materials. The positively and negatively charged n-side and p-side, respectively, generate an electric field which opposes further diffusion of carriers. Once a steady state is reached, a chemical potential (Fermi level) is established which is independent of position in the structure achieving a thermal equilibrium, which results in a bending of the energy bands as can be seen in Figure 1.7b).

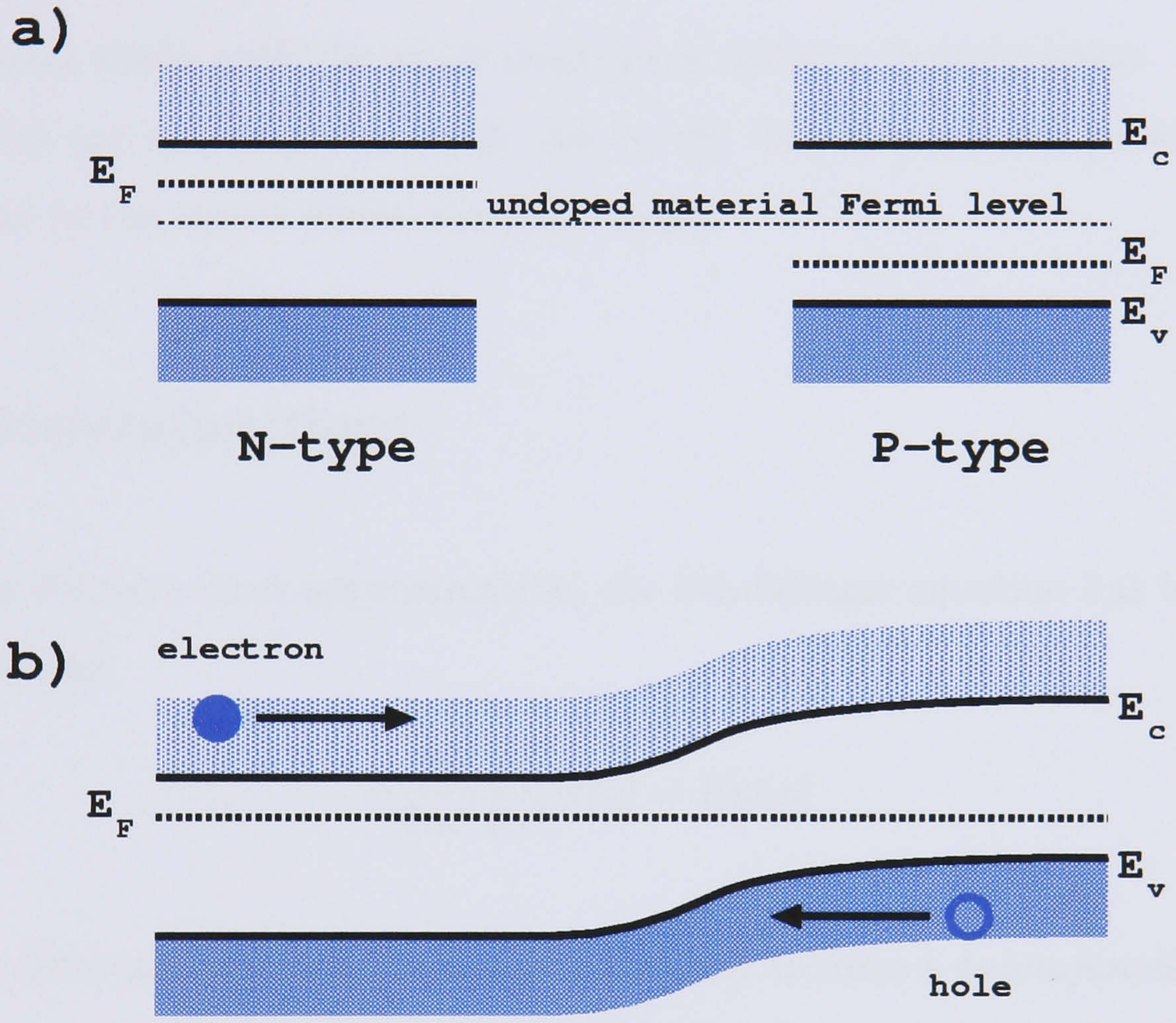

Figure 1.7: a)n- and p-type semiconductor before bringing them together. In the case of n-type(p-type), the Fermi level is above(below) the undoped Fermi level. **b)**Bringing both materials together results in a bending of the energy bands so that the Fermi level can remain flat through the junction.

An externally applied voltage may be used to control the diffusion of carriers. In forward bias, where the positive voltage is applied to the p-side of the junction, the

built-in potential is reduced allowing further diffusion and narrowing the depletion region. In reverse bias, the positive voltage is applied to the n-side of the junction increasing the opposition to diffusion and widening the depletion region. Electron and holes can recombine in this region to produce photons with the same energy as the band gap of the material. For a sufficiently high voltage, a population inversion can be achieved and optical gain can be produced.

A pn-junction made with the same material is called a homojunction. This kind of structures are not very successful due to the fact they do not provide carrier confinement in the region where the gain occurs.

1.3.5 Heterojunctions

Within the effective mass approximation, the Schrödinger equation has been found to be as follows:

$$-\frac{\hbar^2}{2m^*}\frac{\partial^2}{\partial z^2}\psi(z) = E\psi(z) \tag{1.53}$$

When two different materials are brought together to form a *heterojunction*, taking into account that the effective mass could be a function of position, last equation is valid within each. However the bandgaps of the materials can also be different, see Figure 1.8.

The discontinuity in either the conduction or the valence band can be represented by a constant potential term. Therefore the Schrödinger equation for any one of the bands, taking the effective mass to be the same in each material, would be generalised to

$$-\frac{\hbar^2}{2m^*}\frac{\partial^2}{\partial z^2}\psi(z) + V(z)\psi(z) = E\psi(z) \tag{1.54}$$

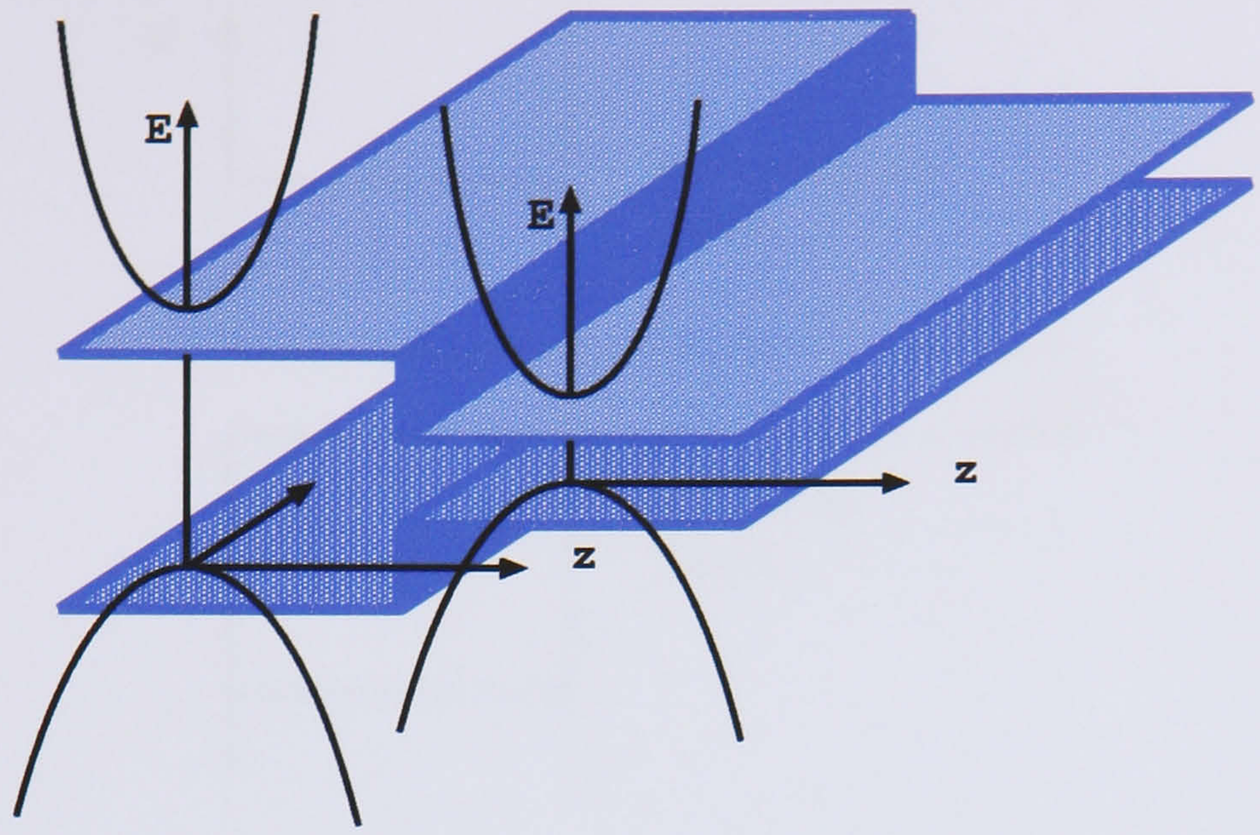

Figure 1.8: Two semiconductors with different bandgaps joined to form a heterojunction; the curves represent the unrestricted motion parallel to the interface.

In the above example, the one-dimensional $V(z)$ representing the band discontinuities at the heterojunction would have the form shown in Figure 1.9, noting that increasing hole energy in the valence band is measured downwards.

1.3.6 Heterostructures

Multiple heterojunctions joined together create *heterostructures*. One type of these structures is the double heterojunction, where a narrower-bandgap material 'A' say, is sandwiched between two layers of a wider-bandgap 'B', as illustrated in Figure 1.10. If the layer 'A' thickness is of the order of the de Broglie wavelength (is sufficiently thin for *quantum properties* to be exhibited), then such a band alignment is called a *single quantum well*, where a carrier inside this structure is said to be *confined* in the perpendicular direction to the heterojunction. When confinement is applied in other directions leads to create *quantum wires* or *quantum dots* which

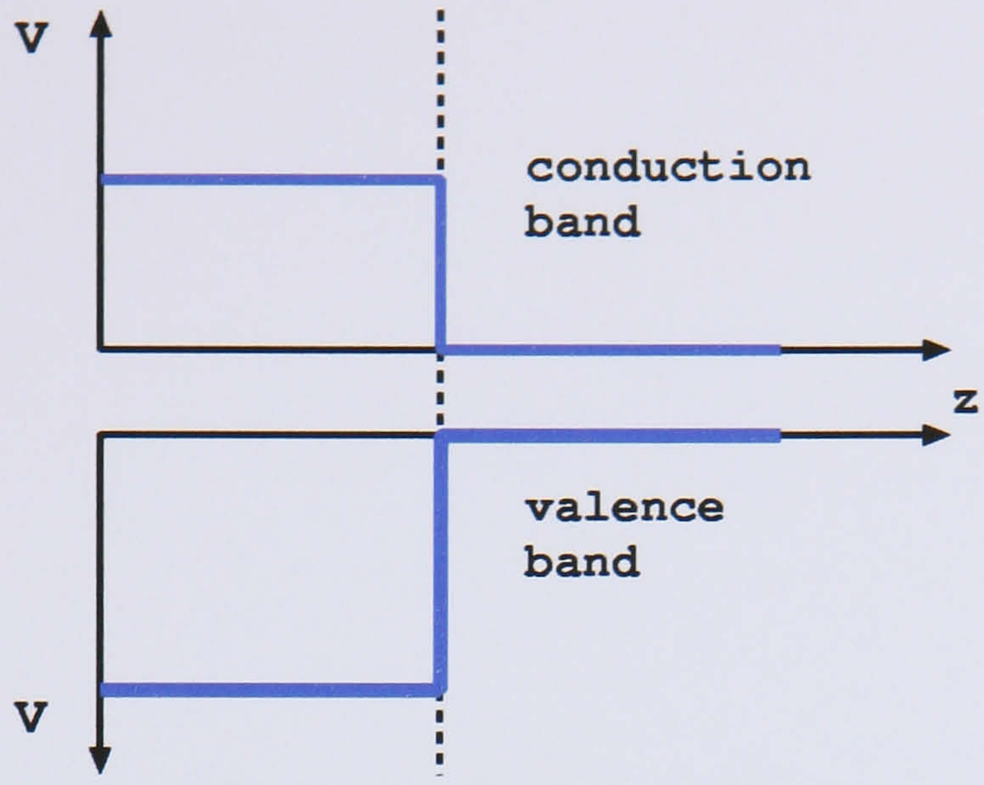

Figure 1.9: The one-dimensional potentials $V(z)$ in the conduction and valence band as might occur at a heterojunction (marked with a dashed line) between two different materials.

have two and three direction confinements respectively.

1.4 Quantum Well

Quantum wells are formed in semiconductors by having a material, like GaAs sandwiched between two layers of a material with a wider bandgap, like AlAs. Improvements in semiconductor growth technology allow control of the layer thickness and hence where the population inversion occurs down to such dimensions that a carrier in this region is confined within the growth direction and it is only allowed to move within the perpendicular plane.

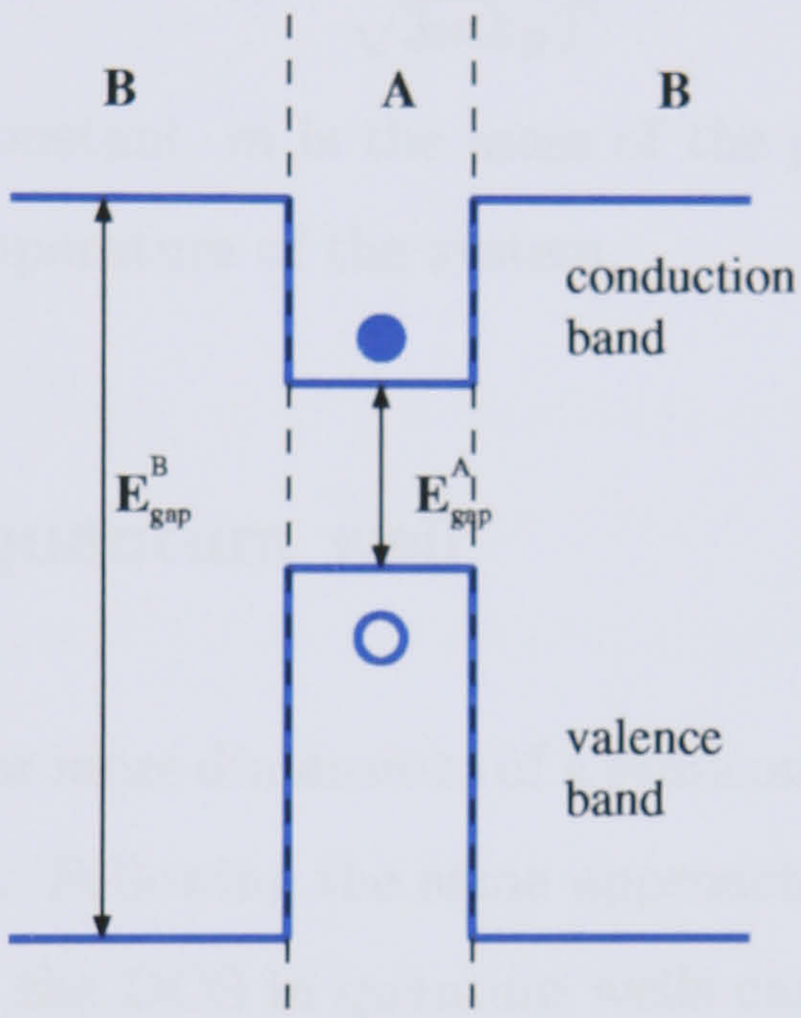

Figure 1.10: The one-dimensional potentials $V(z)$ in the conduction and valence band as might occur at a heterojunction (marked with a dashed line) between two different materials.

1.4.1 Quantisation effects

When the size of one or more dimension of a semiconductor is of the order of the de Broglie wavelength of carriers in the material quantum effects are observed. The de Broglie wavelength is a manifestation of the wave-particle duality of matter, the empirical formulation of which is given by

$$\lambda = \frac{h}{\sqrt{3mk_BT}} \tag{1.55}$$

where h is the Planck's constant, m is the mass of the particle, k_B is Boltzmann's constant and T is the temperature of the system.

1.4.2 DOS for a quantum well

A reduction in size of one or more dimensions of a semiconductor crystal significantly alters its density of states. Following the same approach described in Section 1.2.3 for a bulk semiconductor, the DOS in quantum wells can be calculated taking into account that an electron has free movement within a two dimensional **k**-space. Hence the total number of states, N^{2D}, per energy and area is given by the area of a circle of radius **k** divided by the area occupied by each state and multiply by a factor of 2 due to the spin. Considering that the confinement is in z direction the DOS can by written as

$$N^{2D} = 2\pi k^2 \frac{1}{(2\pi)^2/(L_xL_y)} \frac{1}{L_xL_y} \tag{1.56}$$

In analogy to the bulk three-dimensional case, the quantum well DOS is given by

$$\rho^{2D}(E) = \frac{\mathrm{d}N^{2D}}{\mathrm{d}E} = \frac{\mathrm{d}N^{2D}}{\mathrm{d}k}\frac{\mathrm{d}k}{\mathrm{d}E} \tag{1.57}$$

$$= \frac{m^*}{\pi\hbar^2} \tag{1.58}$$

The quantum well DOS is illustrated in Figure 1.11b).

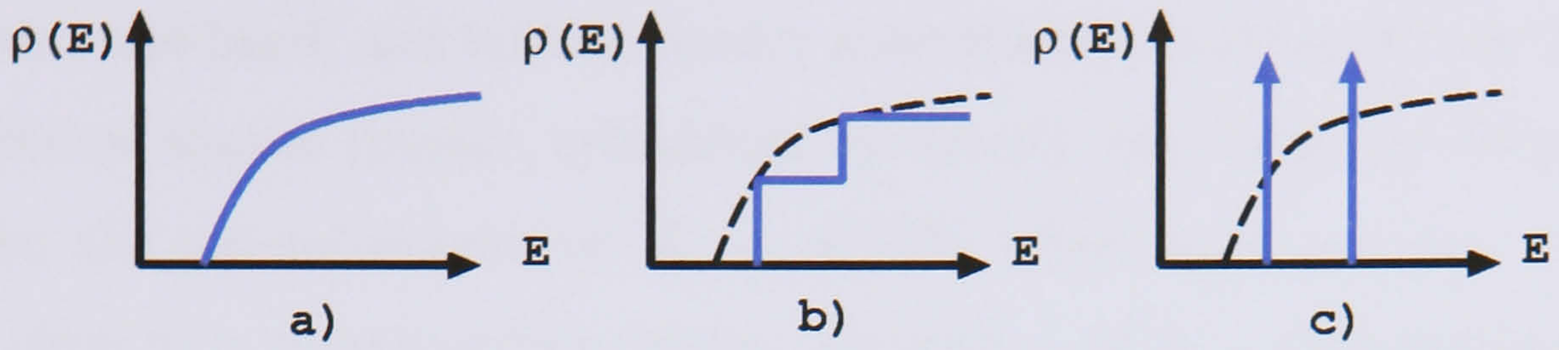

Figure 1.11: Density of states for **a)**Bulk material. **b)**Quantum Well. **c)**Quantum Dot.

1.5 Quantum dots

One of the most important features of low-dimensional semiconductor structures is the quantisation of energy spectrum of charge carriers. Three-dimensional confinement in QD's leads to a discrete (atomic-like) lower part of the energy spectrum. In order to predict novel physical phenomena and suggest new technical applications, researchers investigate manifestations of quantum-size effects in nanostructures both theoretically and experimentally. Recently, significant attention has been attracted to QD's due to their promise for applications as basic elements for semiconductor lasers, nonlinear transformers of light, computer memory, and elements of quantum logic gates. Some of the most effective methods of investigation of carrier energy spectra in QD's are optical ones. They include absorption of light, photoluminescence excitation, Raman scattering, etc. The key problem in the investigation of optical properties of QD's is finding the energy spectrum of confined charge carriers and the corresponding wavefunctions.

Coupled QD systems, which may be seen as 'molecules' have been investigated for their possible application in quantum computing. An understanding of how dots couple in quantum dot molecules is needed so that the possibilities for this system to be used as a quantum gate can be explored.

In parabolic, one-band, and infinite barrier approximations for structures with simple geometrical shapes (planar, cylindrical, spherical), the energy spectrum can be found from the general expression $E_n \sim \alpha_n^2/R^2$, where $\alpha_n (n = 1, 2, \dots)$ are real numbers close to a corresponding integer number n, R is a characteristic dimension of the system, e.g., thickness of the layer, radius of the cylinder, or radius of the sphere. The nonparabolicity of energy bands, degeneracy of valence bands and finiteness of potential barriers strongly complicate the structure of the size-quantised energy spectrum. In this case, the detailed solution of the Schrödinger equation is needed even for spherical QD's.

The crystal structure and the shape of QD's depends mainly on the growth conditions. For instance, colloidal CdSe QD's with hexagonal crystallinity, as well as CdSe, CdS_xSe_{1-x}, PbS, and PbSe QD's grown in glasses, have a nearly spherical shape. Electrochemically self-assembled CdS QD's in the Al_2O_3 matrix have a quasi-cylindrical shape. InAs/GaAs QD's are pyramidal with square base, and wurtzite GaN/AlN QD's are truncated hexagonal pyramids. Using colloidal growth technique it is possible to obtain both alloys and multilayer quantum-dot structures, where are formed as free particles in a liquid medium.

1.5.1 Density of states

Quantum dots are nanometro-scale structures that provide carriers confinement in three spatial dimensions. In these structures the carrier momentum is also quantised in all three directions and therefore a carrier confined within a QD can only occupy certain discrete energy levels, which depend on various factors like the potential barrier depth or the shape of the structure.

Figure 1.11c) shows the resulting density of states when 3D quantisation is achieved in semiconductor quantum dots. The density of states is now a delta function-

like, and in fact should be referred to as number of states rather than density. The kinetic energy of the electrons (and holes) is quantised in all three spatial directions, producing discrete atom-like electronic states. Providing the dot size, and therefore the confinement potential is of the right order, very few confined states will be allowed in the dots. It is the discrete nature of these energy states what makes quantum dots highly attractive for quantum computation. In Chapter 2, the electronic structure of a carrier within a quantum dot is calculated for different shapes of quantum dots.

1.5.2 Gain in quantum dots

As described previously, electron confinement within sufficiently narrow region of semiconductor material can significantly change the DOS and hence the energy spectrum. Quantum dots can provide much more favourable DOS from the point of view of lasing applications. In order to achieve lasing in a semiconductor, a current is applied to reach the population inversion. Electrons are injected into the conduction band, whereas holes are injected into the valence band, being distributed according to the DOS. So the broader the DOS, the more spread the carriers are over the energy axis. As recombinations of all these carriers contribute to the threshold current, it means that energy levels which do not contribute to the gain, are also going to be occupied by carriers.

Therefore, in order to construct an efficient lasing device it is necessary to collect a significant carrier density within limited energy interval. In the case of a QD, as the DOS is a delta-function like, the density of carriers accumulated at the energy of the working transition is significantly enhanced reducing the threshold current of the laser.

1.5.3 Fabrication of Quantum Dots

Early attempts at fabricating quantum dot structures involved complicated growth and lithographic techniques and were largely unsuccessful[4]. However an important breakthrough came with the development of the self-assembled growth technique [5].

There are several techniques for the epitaxial growth of self-assembled quantum dots. A typical growth method known as the Stranski-Krastanov (SK) technique [6] relies on the growth of a highly strained epitaxial layer onto the surface of a semiconductor substrate. The strain between the substrate and the grown film leads to an instability which results in a transition from an uniform layer to clusters of material in order to minimise the energy of the system. These clusters are small enough to confine electrons in three dimensions if surrounded by a material of higher bandgap.

The three dimensional quantum confinement of carriers gives rise to discrete energy level analogous to an atom. The resulting discrete density of states gives rise to high gain in semiconductor devices using these structures. However, in contrast to atoms, quantum dots can be electrically pumped, giving rise to a wide range of applications for optoelectronic devices. Consequently, the use of quantum dots for semiconductor lasers is expected to have superior operational characteristics, in contrast to other less confined structures, such as quantum wells ($1D$ confinement) and quantum wires ($2D$ confinement).

The thin epitaxial layer used to form the quantum dots is called the wetting layer (WL) and itself acts as a quantum well to confine carriers in two dimensions.

Quantum dots can also be produced by colloidal synthesis, which are very popular as fluorescent markers in biological imaging[7].

1.5.4 Self-Assembled Quantum Dot Lasers

Due to the improvements in their fabrication, the interest of self-assembled quantum dot lasers have been increased. The advantages of placing the quantum dots in a quantum well as in self-assembled quantum dot structures (SAD's) [8, 9] has been investigated . Self-assembled In(Ga)As quantum dots can be formed via Stranski-Krastanov [6] epitaxial growth[10] on a single-crystal GaAs substrate.

In this structure, the highly strained quantum well, known as the wetting layer, aids the capture of charge carriers into the dot. Dots are grown on top of the wetting layer while the whole structure is covered by bulk material, as can be seen in Figure 1.12. The confining potential of the carriers in the wetting layer (of the $2D$ carriers) results from the different bandgaps between the wetting layer material and the surrounding bulk material. Initially, carriers diffuse in the lower-bandgap $2D$ wetting layer before either recombining or being captured by the SAD's, where they can either relax into lower energy levels or re-excited back to the wetting layer, where they can diffuse and be captured by other quantum dots within the ensemble. Hence the wetting layer supplies the quantum dots with carriers, appearing as a carrier reservoir.

The role of the wetting layer

As has been explained before, in order to achieve population inversion in semiconductor lasers, carriers are injected into the active region by the forward biasing of a pn-junction. Due to the discreteness of the energy levels, carriers need to gain/lose a discrete amount of energy to be captured into a quantum dot. In the case of a self-assembled quantum dot, the carriers first populate the layer and then they are captured into the quantum dot, which make this process much faster. In this case

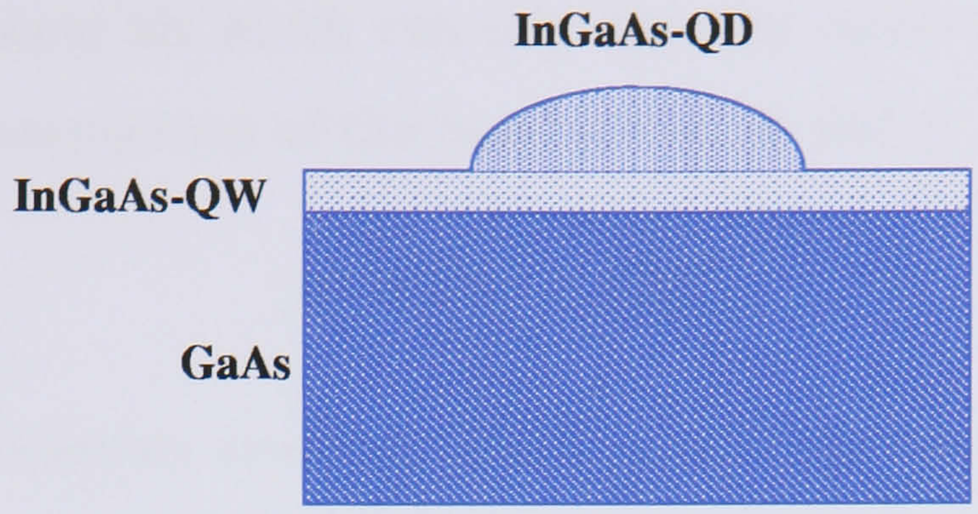

Figure 1.12: Illustration of a self-assembled quantum dot on top of the wetting layer, both embedded in bulk material.

the wetting layer behaves like a reservoir supplying the quantum dots with carriers and determines the population statistics. One of the process which can generates electron captures into the quantum dot is the interaction with LO-phonons, which is studied in Chapter 5.

In Section 2.5 this SAD model is studied and the electronic structure of an electron within a SAD is calculated under the adiabatic approximation.

1.6 Quantum computation

The interest in quantum dots for their possible application in quantum computing has been increased. In this thesis the electronic structure of two coupled quantum dots is studied. The coupling between dots has been proposed as a mechanism to create a quantum gate.

A quantum computer is a device that can process quantum states coherently. Its memory is therefore a quantum system, which is usually thought of a collection of quantum two-level systems, named quantum bits, or qubits. In contrast to a

classical two-state system bit which can take the two values 0 and 1, a qubit can exist in any linear superposition of the basis states $|0\rangle$ and $|1\rangle$

$$|\psi\rangle = \alpha|0\rangle + \beta|1\rangle \tag{1.59}$$

where α and β are complex numbers which satisfy the normalisation condition $|\alpha|^2 + |\beta|^2 = 1$ and the squares of the complex coefficients $|\alpha|^2$ and $|\beta|^2$ represent the probabilities for finding the particle in the corresponding states.

A simple quantum system is the two-level spin $-1/2$ particle. Its basis states, spin-down $|\downarrow\rangle$ and spin-up $|\uparrow\rangle$, may represent the binary zero and one, i.e. $|0\rangle$ and $|1\rangle$ respectively. In the case of an electron within a coupled quantum dot system the localisation of the electron can be used as a qubit, i.e. $|0\rangle$ if the electron is localised in the first dot and $|1\rangle$ in the second one.

Several qubits, say n, may be combined creating a 2^n states basis, called *pure states*. Therefore any state can be written as a linear combination of this basis elements.

$$\sum_{x=0}^{2^n-1} \alpha_x |x\rangle \tag{1.60}$$

where $|x\rangle$ is the product basis vector defined by the binary representation of x. For example, in the case of $n = 2$, state $|3\rangle = |11\rangle = |1\rangle|1\rangle$.

Roughly, a quantum computation works as follows

- Initially, some product state $|x\rangle$ is prepared, e.g. $|00\rangle$
- Then, somehow each state element has to be able to be manipulated or interact with other elements. This is reached using the so called quantum gates. Combinations of one-bit and two-bit operations are sufficient to construct any unitary operation on a finite number of bits. The classical analogy for quantum gates are the boolean logic gates such as NOR (for a single qubit operation),

XOR, NAND, etc. During the period when an operation is performed, the quantum register will usually be in non-trivial quantum superpositions, and has therefore to stay phase coherent.

- At the end of the computation, the final state of the quantum register is measured by measuring each qubit one-by-one, i.e. each qubit is projected in the basis $|0\rangle$, $|1\rangle$. Hence, the outcome of the quantum computation consists of n classical bits.

1.6.1 Requirements

Five basic steps required for the physical realisation of quantum information processing[11].

- Quantum phase coherence needs to be maintained over a long time compared to the length of an elementary step in the computation, in order to allow for quantum error correction.

- As a further requirement, it has to be possible to couple pairs of qubits in a controlled manner in order to carry out elementary quantum logic.

- The ability to initialise the state of the qubits to a simple fiducial state is required.

- Operations on single qubits need to be implemented, and at the end of a computation, the qubits have to be read out by performing a quantum measurement.

- The design of the quantum computer should be scalable to a large number of qubits.

1.6.2 Coherence

In an ideal quantum system there is no external factor which can alter a register or an operation between them. In reality every quantum system is coupled to non-desirable external degrees of freedom which creates decoherence (loss of coherence). In quantum computation what is aimed is having the qubits maximally coupled to each other, which enables one to *entangle* qubits, and minimally to the outside world. Hence, phase coherence is one of the vital ingredients for quantum computation.

Therefore the *coherence* time is defined as the time over which the phase of a superposition of states is well defined and the modification of this phase by an external factor is called *decoherence.*

In the case of a single qubit (e.g. a spin 1/2) one commonly describes decoherence by two times : T_1 describes how fast the spin is depolarised, while T_2 is the characteristic time after which the phase information is lost. The main source of decoherence is the one with the smaller decoherence time, $T_d = \min(T_1, T_2)$.

In Chapter 5 the LO-phonon - carrier interaction is studied as a source of decoherence in coupled self-assembled quantum dot systems.

1.6.3 Why semiconductor Quantum Dots?

Semiconductor quantum dots are structures where charge carriers are confined in all three spatial directions. Due to the fact that dots are of the order of the de Broglie wavelength, the carrier density of states is discrete. It is also possible to isolate a single carrier within a quantum dot and then use, for instance, its spin or orbital state to represent a qubit[12].

One of the requirements for the realization of a quantum computer is the *scalability* which means that it is possible to increase the number of fundamental units of a device (e.g. the number of transistors on a chip) once it is known how a single unit can be fabricated. The use of ion traps for a complete quantum computer[13] has been proposed, but it is unclear whether such atomic-physics implementations could ever be scaled up to do truly large-scale quantum computation[14].

The scalability of conventional electronic solid-state devices suggests that solid-state realizations of quantum computation have the potential for being scalable to large numbers of qubits, that makes quantum dots good candidates.

The use of coupled quantum dots in quantum computation [15, 14, 16] where the coupling between dots plays an important rule in order to implement a quantum gate has been proposed . The aim of this thesis is not to propose a candidate for quantum computer model, but to study the coupling between dots (Chapter 4) and a possible source of decoherence due to LO-phonon interaction (Chapter 5).

Bibliography

[1] Hartmut Haug and Stepphan W. Koch. *Quantum theory of the optical and electronic properties of semiconductors.* World Scientific, 1990.

[2] Paul Harrison. *Quantum Wells, Wires and Dots.* Wiley, 2000.

[3] Scott W. Corzine and Larry A. Coldren. *Diode Lasers and Photonic Integrated Circuits.* 1995.

[4] L. Jacack, P. Hawrylak, and A. Wojs. *Quantum Dots.* Springer, 1997.

[5] P. M. Petroff and S. P. Denbaars. MBE and MOCVD growth and properties of self-assembling quantum dot arrays in III-V semiconductor structures. *Superlattices and Microstructures*, 15:15, 1994.

[6] I. N. Stranski and L. von Krastanov. *Akd. Wiss. Lit. Mainz Abh. Math. Naturwiss. Kl.*, 146:797, 1939.

[7] Benoit Dubertyret, Paris Skourides, David J. Norris, Vincent Noireaux, Ali H. Brivanlou, and Albert Libchaber. In vivo imaging of quantum dots encapsulated in phospholipid micelles. *Science*, page 15, 2002.

[8] P. M. Petroff and S. P. DenBaars. *Superlattices Microstruct.*, 15:15, 1994.

[9] F. Adler, M. Geiger, A. Bauknecht, F. Scholz, H. Schweizer, and M. H. Pilkuhn. *Appl. Phys.*, 80:4019, 1996.

[10] S. Guha, A. Madukar, and K. C. Rajkumar. *Appl. Phys. Lett.*, 57:2110, 1990.

[11] IBM David P. DiVincenzo. The physical implementation of quantum computation. *quant-ph/0002077*, 2000.

[12] Guido Burkard, Daniel Loss, and David P. DiVincenzo. Coupled quantum dots as quantum gates. *Phys. Rev. B*, 59:2070, 1999.

[13] T. Pellizzari, S. A. Gardiner, J. I. Cirac, and P. Zoller. Decoherence, continuous observation and quantum computing: a cavity QED model. *Phys. Rev. Lett.*, 75:3788, 1995.

[14] Daniel Loss and David P. DiVincenzo. Quantum computation with quantum dots. *Phys. Rev. A*, 57:120, 1998.

[15] M. Bayer, P. Hawrylak, K. Hinzer, S. Fafard, M. Korkusinski, Z. R. Wasilewski, O. Stern, and A. Forchel. Coupling and entangling of quantum states in quantum dot molecules. *Science*, 291:451, 2001.

[16] Tetsufumi Tanamoto. Quantum gates by coupled aymmetric quantum dots and controlled-NOT-gate operation. *Phys. Rev. A*, 61:022305, 2000.

Chapter 2

Carrier energy levels within a Quantum Dot

Contents

2.1 Introduction

As described in Chapter 1, quantum dots are nanometer-scale structures that provide carrier confinement in three spatial dimensions. In these structures the carrier momentum is then also quantised in all three directions and hence a carrier confined within a QD can only occupy certain discrete energy levels, which depend on various factors like the potential barrier depth or the shape of the structure.

The energy levels in QD structures may be obtained analytically if the potential barriers are of infinite height and the structures have simple geometry such as cubes, cylinders or spheres.

Before calculating phonon scattering and coupling between two QD's we need to determine their wavefunctions and energies, which satisfy the time-independent Schrödinger equation $\hat{H}\Psi = E\Psi$. In order to study QD structures with spherical and cylindrical symmetry, the Schrödinger equation in spherical and cylindrical coordinates is solved.

In order to obtain the QD electronic structure, it is first introduced the Schrödinger equation is first introduced and its solutions for a free particle moving in three directions. General properties are developed through examination of the free-particle problem. Then the energy levels and wavefunctions of colloidal quantum dots (using spherical symmetry) and self assembled semiconductor quantum dots (using cylindrical symmetry) are calculated.

2.2 The free particle

In order to calculate wavefunctions of quantum dots with spherical symmetry, the free-particle problem needs to be understood. The Hamiltonian of a free-particle of mass m in spherical coordinates (r, θ, ϕ) is given by[1]:

$$\hat{H} = \frac{\hat{p}_r^2}{2m} + \frac{\hat{L}^2}{2mr^2} \tag{2.1}$$

where $\hat{p}_r$ is the radial component of the particle's momentum and $\hat{L}$ the angular momentum. Then $\psi(r, \theta, \phi)$, the solution of the time-independent Schrödinger equation in spherical coordinates given by

$$\frac{1}{2m}\left(\hat{p}_r^2 + \frac{\hat{L}^2}{r^2}\right)\psi = E\psi \tag{2.2}$$

The expressions for operators $\hat{p}_r$ and $\hat{L}^2$ are given by

$$\hat{p}_r = -\mathrm{i}\hbar\frac{1}{r}\frac{\partial}{\partial r}r \tag{2.3}$$

$$\hat{L}^2 = -\hbar^2\left[\frac{1}{\sin\theta}\frac{\partial}{\partial\theta}\left(\sin\theta\frac{\partial}{\partial\theta}\right) + \frac{1}{\sin^2\theta}\frac{\partial^2}{\partial\phi^2}\right] \tag{2.4}$$

The eigenfunctions ψ_{lm} of the operator $\hat{L}^2$ may obtained solving the following equation

$$\hat{L}^2\psi_{lm} = \hbar^2 l(l+1)\psi_{lm} \tag{2.5}$$

the solutions are called *spherical harmonics* and are universally denoted by the symbol $Y_l^m(\theta, \phi)$.

$$Y_l^m(\theta, \phi) = \left[\frac{2l+1}{4\pi}\frac{(l-m)!}{(l+m)!}\right]^{1/2} P_l^m(\cos\theta)\mathrm{e}^{\mathrm{i}m\phi} \tag{2.6}$$

The first few normalised spherical harmonics can be seen in Table 2.1.

As $\hat{p}_r^2$ is a function only of r and $\hat{L}^2$ is a function only of the angle variables (θ, ϕ) it is assumed that the solution of equation 2.2 my be separated in two components

$$\psi_{lm}(r, \theta, \phi) = R(r)Y_l^m(\theta, \phi) \tag{2.7}$$

Spherical Harmonics Functions

$$\mathbf{Y_l^m}(\theta,\phi) = \left[\frac{\mathbf{2l+1}}{\mathbf{4\pi}}\frac{\mathbf{(l-m)!}}{\mathbf{(l+m)!}}\right]^{\mathbf{1/2}} \mathbf{P_l^m}(\cos\theta)\mathrm{e}^{\mathbf{im}\phi}$$

Spherical Harmonics			**Legendre polynomials**		
Y_l^{-l}	$=$	$\frac{1}{2^l l!}\sqrt{\frac{(2l+1)!}{4\pi}}\sin^l\theta\mathrm{e}^{-il\phi}$	P_0	$=$	1
Y_l^0	$=$	$\sqrt{\frac{2l+1}{4\pi}}P_1(\cos\theta)$	P_1^1	$=$	$-\sin\theta$
Y_l^{-m}	$=$	$(-1)^m(Y_l^m)^*$	P_1^0	$=$	$-\cos\theta$
Y_0^0	$=$	$\left(\frac{1}{4\pi}\right)^{1/2}$	P_1^{-1}	$=$	$\frac{1}{2}\sin\theta$
Y_1^1	$=$	$-\frac{1}{2}\left(\frac{3}{2\pi}\right)^{1/2}\sin\theta\mathrm{e}^{i\theta}$			
Y_1^0	$=$	$\frac{1}{2}\left(\frac{3}{\pi}\right)^{1/2}\cos\theta$			

Table 2.1: The first few normalised spherical harmonics and corresponding associated Legendre polynomials.

Substituting ψ_{lm} in Equation 2.2 leads to

$$\left[-\left(\frac{1}{r}\frac{\mathrm{d}^2}{\mathrm{d}r^2}r\right)+\frac{l(l+1)}{r^2}\right]R_l(r)=\frac{2mE}{\hbar^2}R_l r \tag{2.8}$$

where due to the dependence on the quantum number l the radial wavefunction $R(r) \rightarrow R_l(r)$ is introduced. With the substitution

$$E = \frac{\hbar^2 k^2}{2m} \tag{2.9}$$

$$x = kr \tag{2.10}$$

Equation 2.8 becomes the *spherical Bessel differential equation*

$$\frac{\mathrm{d}^2}{\mathrm{d}x^2}R_l(x)+\frac{2}{x}\frac{\mathrm{d}R_l(x)}{\mathrm{d}x}+\left[1-\frac{l(l+1)}{x^2}\right]R_l(x)=0 \tag{2.11}$$

This equation for the radial function R_l has two linearly independent solutions called spherical Bessel and Neumann functions and denoted by the symbols j_l and y_l respectively. Then R_l is given by

$$R_l(x) = Aj_l(x) + By_l(x) \tag{2.12}$$

where Table 2.2 shows the solutions j_l and y_l.

As Figure 2.1 shows, only the spherical Bessel function j_l is finite at the origin. The spherical Neumann function y_l is not a valid solution of the radial component.

Due to the dependence of the radial wavefunction and the energy solution on the variable k, the subscript k is introduced, defining $R_l(r) \rightarrow R_{kl}(r)$ and $E_l \rightarrow E_{kl}$. Therefore the radial solution of the Schrödinger equation may now be written as $R_{kl}(r) = j_l(kr)$ and the eigenvalues and eigenstates of the free-particle Hamiltonian in spherical coordinates are

$$\psi_{klm}(r,\theta,\phi) = R_{kl}(r)Y_l^m(\theta,\phi) \tag{2.13}$$

$$E_{kl} = \frac{\hbar^2 k^2}{2m} \tag{2.14}$$

Spherical Bessel and Neumann functions

Equation

$$f'' + \frac{2}{x} f + \left[1 - \frac{l(l+1)}{x^2}\right] f = 0$$

Spherical Bessel	Spherical Neumann
$j_l(kr) = \left(-\frac{r}{k}\right)^l \left(\frac{1}{r}\frac{\mathrm{d}}{\mathrm{d}r}\right)^l j_0(kr)$	$y_l(kr) = \left(-\frac{r}{k}\right)^l \left(\frac{1}{r}\frac{\mathrm{d}}{\mathrm{d}r}\right)^l y_0(kr)$
$j_0(kr) = \frac{\sin(kr)}{kr}$	$y_0(kr) = -\frac{\cos(kr)}{kr}$

Table 2.2: Properties of spherical Bessel and Neumann functions.

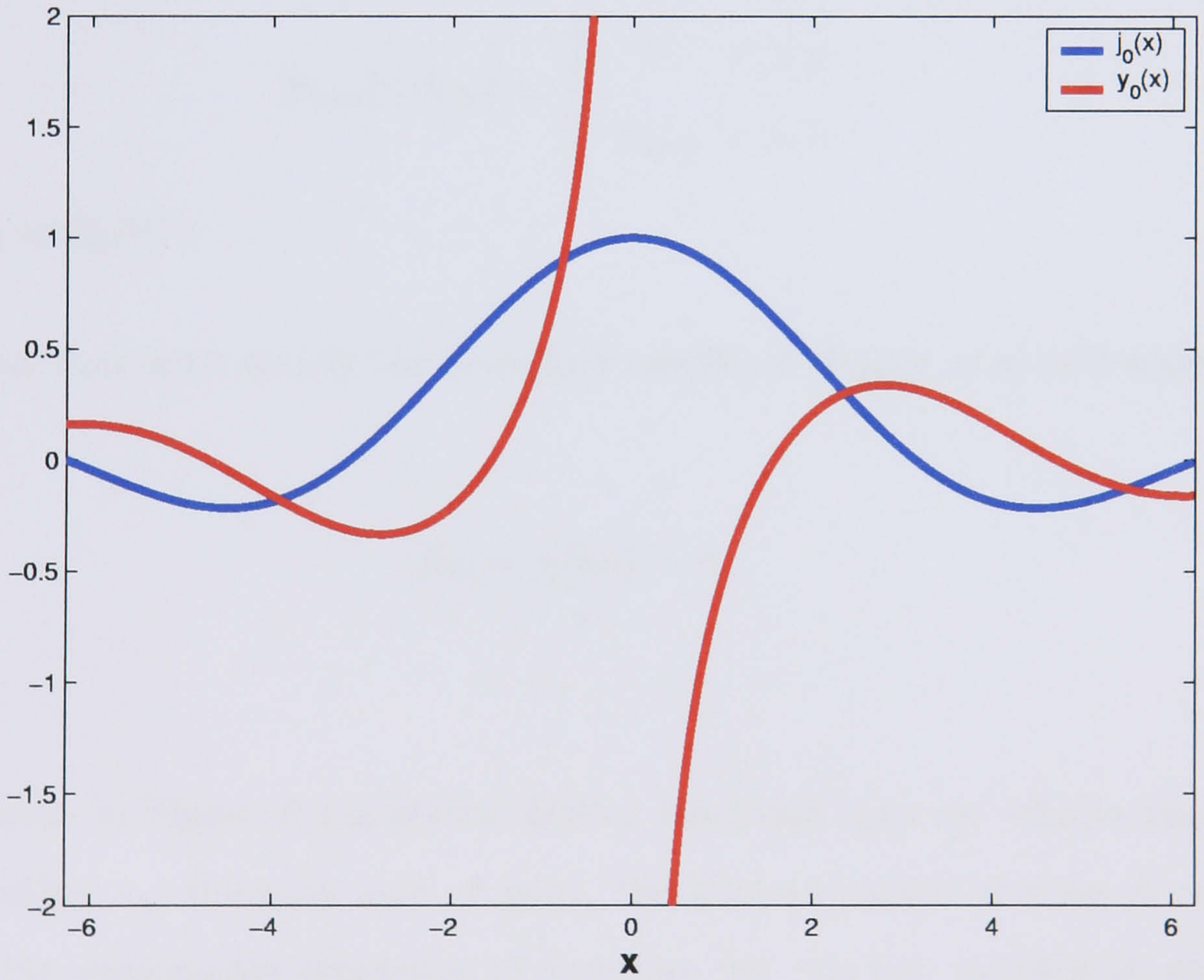

Figure 2.1: Spherical Bessel and Neumann functions of first order.

2.3 Spherical Quantum Dot

2.3.1 Infinite barrier potential

Now that we have obtained the free particle solution of the Schrödinger equation we are in a position to study the quantum confined energy levels of a quantum dot.

A particle of effective mass m^* is considered to be confined to the interior of a spherical infinite potential well of radius a with impenetrable walls. In the domain $r \geq a$ the wavefunction vanishes. When $r < a$ the particle behaves like a free-particle and the wavefunction may be obtained from Equation 2.13. Therefore the wavefunction within those two regions may be written as

$$\Psi_{klm}(r,\theta,\phi) = \begin{cases} 0 & r \geq a \\ \psi_{klm} & r < a \end{cases} \tag{2.15}$$

where $\psi_{klm} = R_{kl}Y_l^m$.

The wavefunction must satisfy the boundary condition $\Psi_{klm}(r = a) = 0$ which leads to

$$R_{kl} = j_l(ka) = 0 \tag{2.16}$$

As can be seen in Figure 2.2 spherical Bessel functions have an infinite number of zeros. Denoting x_{nl} the n-th zero of $j_l(x)$, the allowed values of k are $k = x_{nl}/a$. Note that the continuous spectrum of k values for the free particle in spherical coordinates translates to the discrete spectrum of the quantum number n, therefore the radial wavefunction $R_{kl} \rightarrow R_{nl}$ is defined and the wavefunction $\psi_{klm} \rightarrow \psi_{nlm}$.

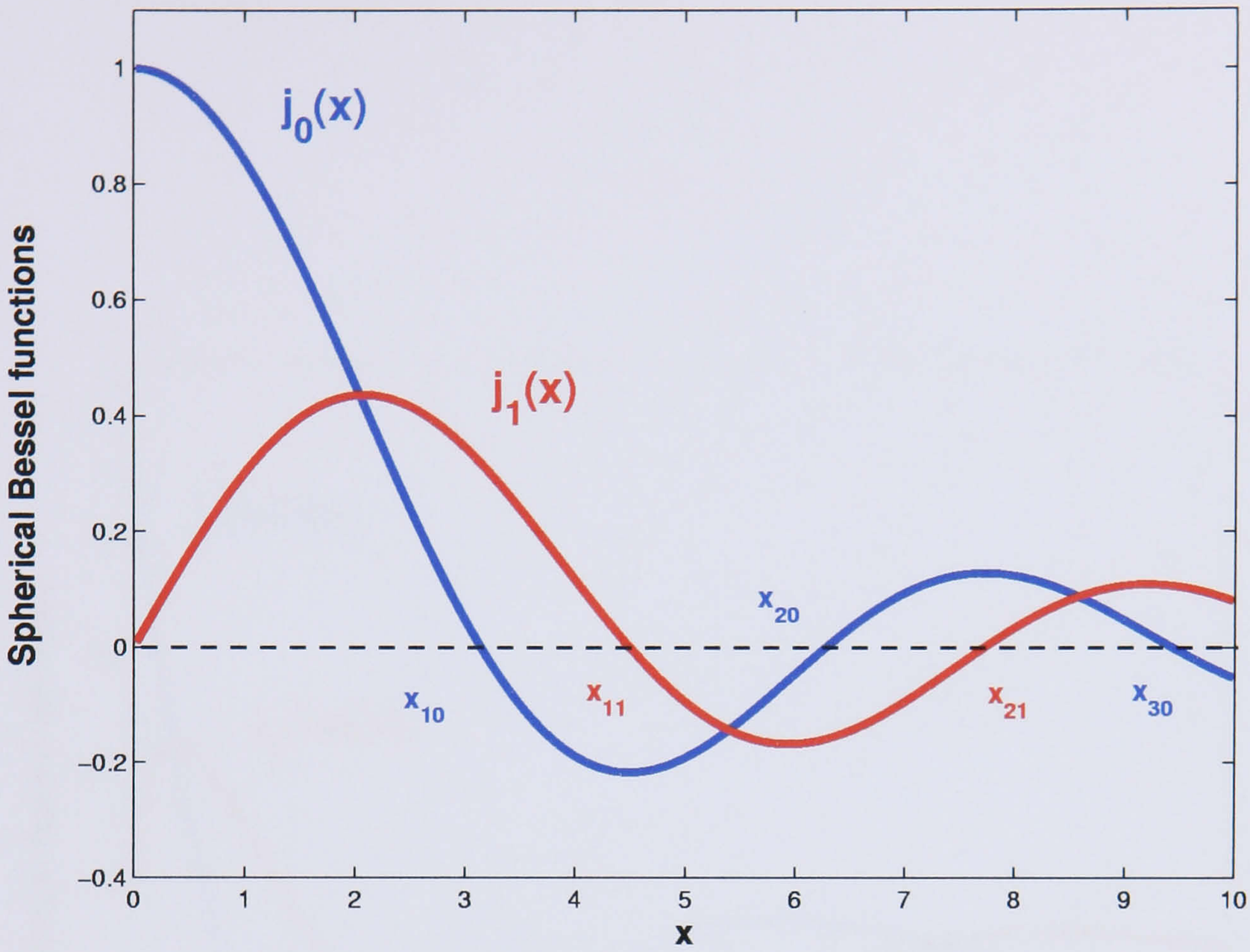

Figure 2.2: Representation of Spherical Bessel functions $j_0(x)$ and $j_1(x)$.

Energy levels

E_{nl} (eV)	$n=1$	$n=2$	$n=3$
$l=0$	0.2555	1.0219	2.2992
$l=1$	0.5226	1.4547	3.0776

Table 2.3: First energy levels of an electron of effective mass $m^* = 0.023m_0$ within an infinite potential barrier spherical quantum dot of radius $a = 8$ nm. Only $l = 0, 1$ has been taken into account.

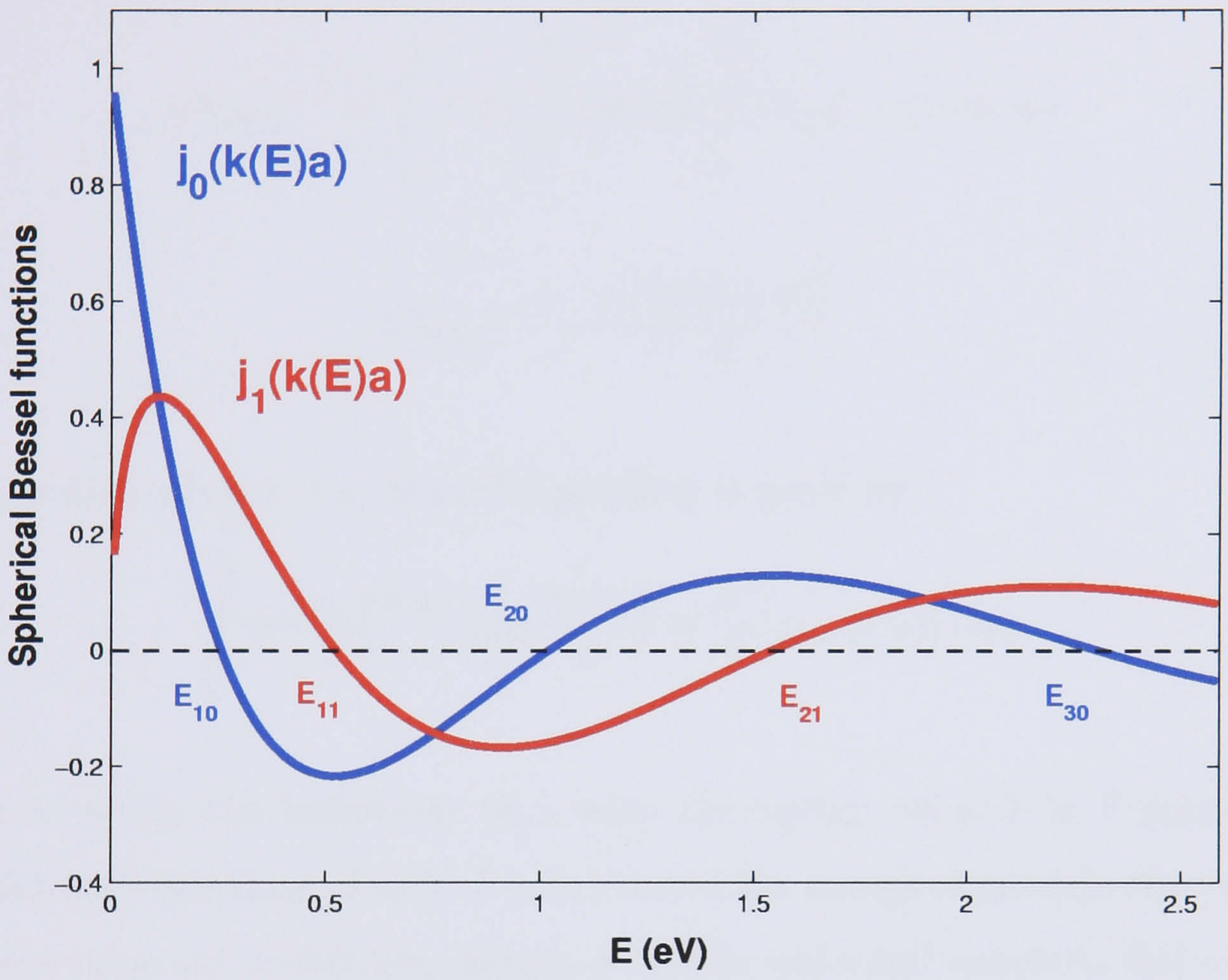

Figure 2.3: Representation of Spherical Bessel functions $j_0(k(E)a)$ and $j_1(k(E)a)$ versus E, which is the energy of an electron of effective mass $m^* = 0.023m_0$ within an infinite potential barrier spherical QD of radius $a = 8$ nm.

Now the eigenfunctions and eigenvalues for the spherical dot are then given by

$$\psi_{nlm}(r,\theta,\phi) = A_{nlm} j_l\left(\frac{x_{ln} r}{a}\right) Y_l^m(\theta,\phi) \tag{2.17}$$

$$E_{nl} = \frac{\hbar^2 {x_{ln}}^2}{2m^* a^2} \tag{2.18}$$

where A_{nlm} is the normalisation factor given by

$$\left(A_{nlm}\right)^{-2} = \int_0^\infty r^2 \mathrm{d}r \int_0^\pi \sin\theta \mathrm{d}\theta \int_0^{2\pi} |\Psi_{nlm}(r,\theta,\phi)|^2 \mathrm{d}\phi \tag{2.19}$$

$$\left(A_{nlm}\right)^{-2} = \frac{a^3 \left[j_l'(k_{lm}a)\right]^2}{2} \tag{2.20}$$

As Ψ_{nlm} is zero when $r \geq a$, the orthogonality is given by

$$\int_0^a \mathrm{d}r r^2 j_l\left(\frac{x_{ln} r}{a}\right) j_l\left(\frac{x_{ln'} r}{a}\right) = \frac{a^3}{2}\left[j_{l+1}(x_{ln})\right]^2 \delta_{nn'} \tag{2.21}$$

In order to study the behaviour of j_l with the energy we plot in Figure 2.3 the spherical Bessel functions of order $l = 0, 1$ versus the energy of particle of an electron of effective mass $m^* = 0.023 m_0$ within a infinite potential spherical QD of radius $a = 8$ nm. The radial equation R_{nl} has an infinite number of solutions, but only orders $l = 0, 1$ are plotted for convenience. The allowed energies, E_{lm}, are the ones which satisfy $j_l(ak(E)) = 0$. These zeros are calculated applying the Newton-Raphson method [2]. Table 2.3 shows the first energies for $l = 0, 1$. Their associated radial wavefunctions R_{nl} are shown in Figure 2.4.

2.3.2 Finite barrier potential

The electronic structure of a particle within spherical structures with infinite confinement may be obtained analytically as has been explained in the last section.

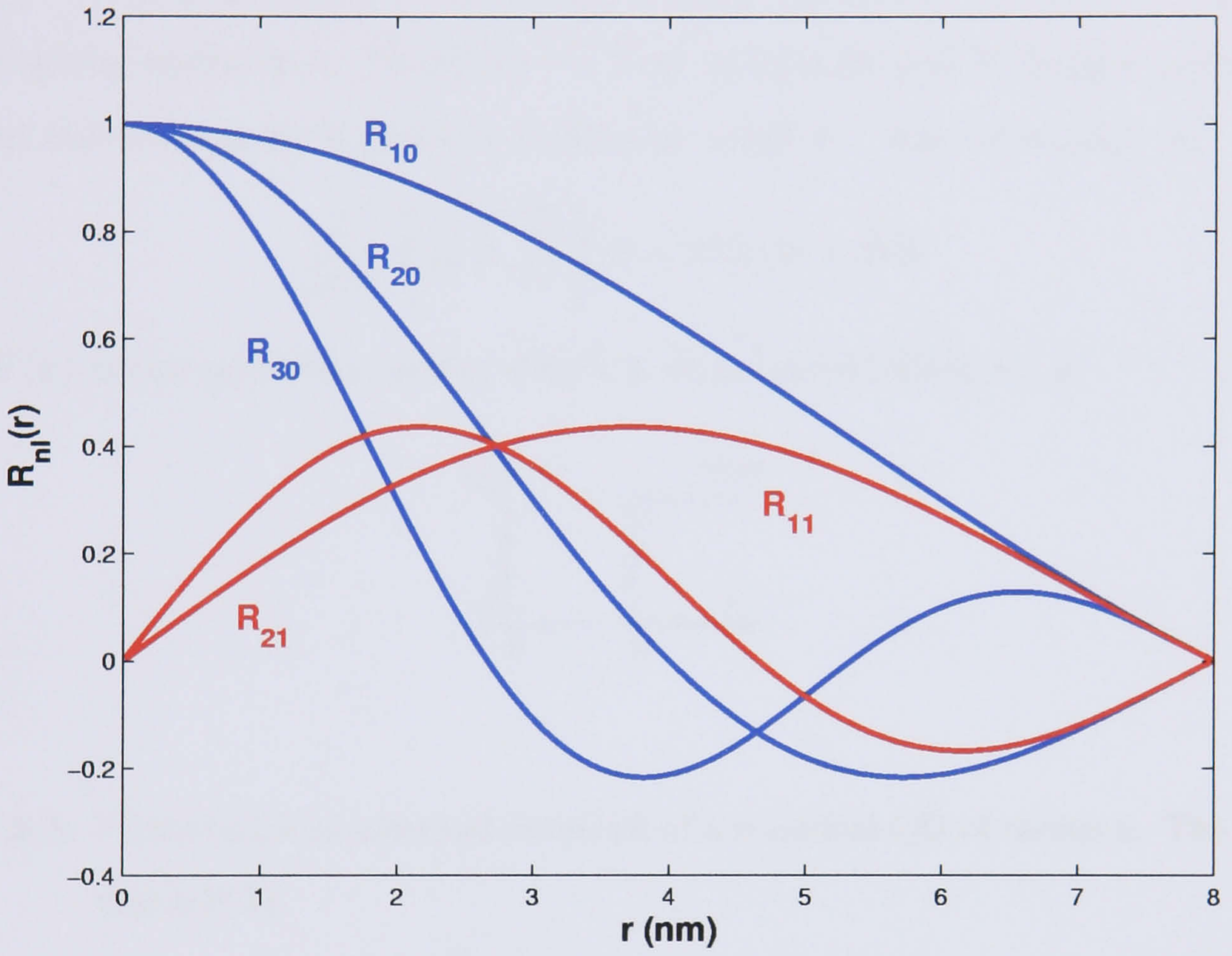

Figure 2.4: Representation of the first few radial wavefunctions of order $l = 0, 1$ of an electron of mass $m^* = 0.023m_0$ within an infinite potential barrier spherical QD of radius $a = 8$ nm.

Although in reality the barrier height is the energy difference between QD and surrounding material conduction/valence bands which is finite.

To find the energy levels for a finite barrier potential the Schrödinger equation must be solved satisfying the boundary conditions imposed by the geometry of the structure. It is assumed that the 3D quantum-confinement structure is spherical and the sphere radius is a. Therefore the time independent Schrödinger equation in spherical coordinates for a particle of effective mass m^* may be written as

$$\frac{1}{2m^*}\left(\hat{p}_r^2 + \frac{\hat{L}^2}{r^2}\right)\Psi + V(\mathbf{r})\Psi = E\Psi \tag{2.22}$$

where $V(\mathbf{r})$ is the potential barrier which is described in Figure 2.5.

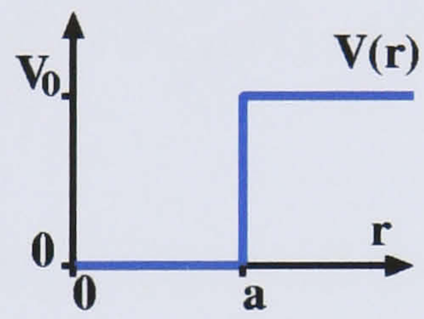

Figure 2.5: Finite barriers spherical potential of a spherical QD of radius a. The barrier depth is V_0.

The confining potential is constant within the region $0 < r < a$ and the region $a < r$, and a particle within these two regions behaves as a free-particle. As discussed in Section 2.2, the solution of the Schrödinger Equation in spherical coordinates is

$$\psi_{klm}(r,\theta,\phi) = R_{kl}(r)Y_l^m(\theta,\phi) \tag{2.23}$$

where $Y_l^m(\theta,\phi)$ is the normalised spherical harmonics and R_{kl} is the radial wave-function. The normalised spherical harmonics are given by

$$Y_l^m(\theta,\phi) = \left[\frac{2l+1}{4\pi}\frac{(l-m)!}{(l+m)!}\right]^{1/2} P_l^m\big(\cos(\theta)\big)\mathrm{e}^{\mathrm{i}m\theta} \tag{2.24}$$

The confining potential only depends on r, therefore it can be assumed that the angular component of the wavefunction of our model is $Y_l^m(\theta, \phi)$. The wavefunction is defined as

$$\Psi_{lm}(r, \theta, \phi) = R(r)Y_l^m(\theta, \phi) \tag{2.25}$$

where

$$R(r) = \begin{cases} R^W & r < a \\ R^B & r > a \end{cases} \tag{2.26}$$

Substituting this spherical harmonics expression into Equation 2.22 gives

$$\frac{\hbar^2}{2m*}\left[-\left(\frac{1}{r}\frac{\partial^2}{\partial r^2}r\right) + \frac{l(l+1)}{r^2} + V(r)\right]R(r) = ER(r) \tag{2.27}$$

Depending on the distance from the centre of the sphere, the potential takes two different values:

- $\mathbf{r < a \rightarrow V(r) = 0}$

  Equation 2.27 may be written as

  $$\frac{\hbar^2}{2m}\left[-\left(\frac{1}{r}\frac{\partial^2}{\partial r^2}r\right) + \frac{l(l+1)}{r^2}\right]R^W(r) = E_l R^W(r) \tag{2.28}$$

  with the substitution

  $$\begin{aligned} E_l &= \tfrac{\hbar^2 k_W^2}{2m} \\ x &= k_W r \end{aligned} \tag{2.29}$$

  equation 2.28 becomes the *spherical Bessel differential equation*

  $$\frac{\mathrm{d}^2}{\mathrm{d}x^2}R^W(x) + \frac{2}{x}\frac{\mathrm{d}R^W(x)}{\mathrm{d}x} + \left[1 - \frac{l(l-1)}{x^2}\right]R^W(x) = 0 \tag{2.30}$$

  and it can be solved analytically.

The general solution is:

$$R^W(x) = A_W j_l(x) + B_W y_l(x) \tag{2.31}$$

where $l = 0, 1, 2, ...$ is the angular momentum quantum number, $j_l(x)$ is the spherical Bessel function and $y_l(x)$ the spherical Neumann function (also called $n_l(x)$). In this case the constant B_W term must be zero because $y_l(0) \to \infty$ and $R_W(x)$ must be finite when $x = 0$.

- $\mathbf{r > a \to V(r) = V_0}$

  Equation 2.27 may be written as

$$\frac{\hbar^2}{2m}\left[-\left(\frac{1}{r}\frac{\partial^2}{\partial r^2}r\right) + \frac{l(l+1)}{r^2}\right] R^B(r) = -|V_0 - E| R^B(r) \tag{2.32}$$

  with the substitution

$$\begin{aligned} |V_0 - E| &= \tfrac{\hbar^2 k_B^2}{2m} \\ x &= k_B r \end{aligned} \tag{2.33}$$

  the last equation becomes the *modified spherical Bessel differential equation* and the general solution is:

$$R_l^B(x) = A_B i_l(x) + B_B k_l(x) \tag{2.34}$$

  The wavefunction in this region must be conserved finite, therefore $A_B = 0$ because the function $i_l(x)$ diverges when $x \to \infty$ as can be seen in Figure 2.6.

Therefore the radial wavefunction may be expressed as

$$R_l(r) = \begin{cases} R_l^W(r) = A_W j_l(k_W r) & r \leq a \\ R_l^B(r) = B_B k_l(k_B r) & r > a \end{cases} \tag{2.35}$$

The Radial wavefunction is required to satisfy the following boundary conditions

$$R_l^B(a) = R_l^W(a) \tag{2.36}$$

$$\left.\frac{\mathrm{d}R_l^B}{\mathrm{d}r}\right|_{r=a} = \left.\frac{\mathrm{d}R_l^W}{\mathrm{d}r}\right|_{r=a} \tag{2.37}$$

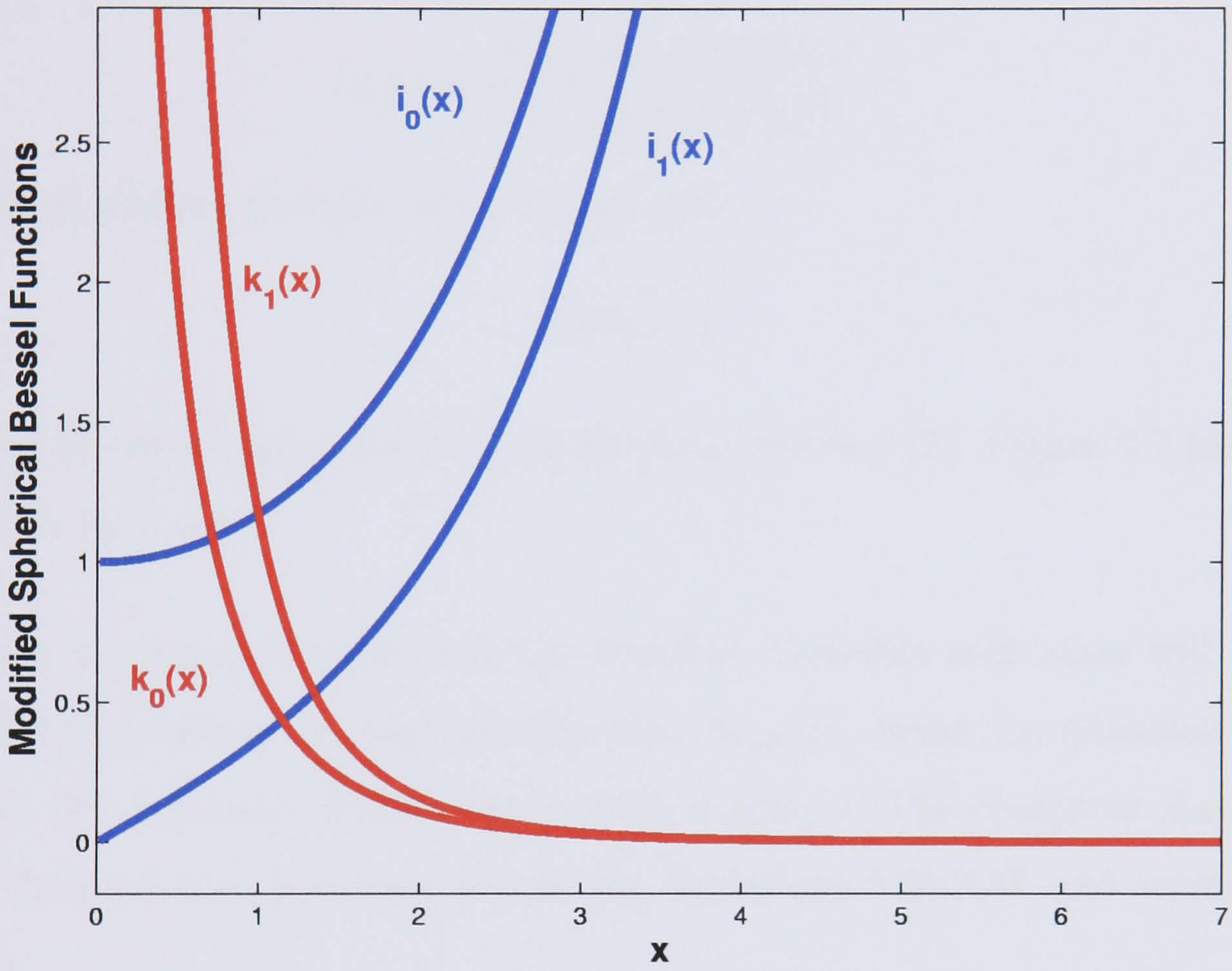

Figure 2.6: Modified Spherical Bessel functions of the first kind $i_l(x)$ and second kind $k_l(x)$ for $l = 0, 1$.

Then the equation giving the eigenvalues of energy is found to be

$$\frac{j_l(k_W a)k_l'(k_B a)}{j_l'(k_W a)k_l(k_B a)} = \frac{k_W}{k_B} \tag{2.38}$$

where $f_l' = \frac{\partial f_l}{\partial r}$.

Rewriting as

$$F_l(E) = \frac{k_B}{k_W}\frac{j_l(k_W a)k_l'(k_B a)}{j_l'(k_W a)k_l(k_B a)} - 1 \tag{2.39}$$

the confined allowed energies will be given with

$$F_l(E) = 0 \tag{2.40}$$

which can be solved using the Newton-Raphson method [2]. Figure 2.7 plots functions $F_l(E)$ for $l = 0, 1$.

Equation 2.40 may give more than one solution, therefore each state will be characterised by its energy E_{nl} and wavefunction $\Psi_{nlm}(\mathbf{r})$, being the quantum number $n = 1, 2...$ the n-th zero of Equation 2.39 for a given l. The constants A_W and B_B may be obtained from boundary conditions, Equations 2.36-2.37, and normalisation condition

$$\int_0^\infty R_{nl}^2(r)r^2 \mathrm{d}r = 1 \tag{2.41}$$

Now, for a given allowed energy E_{nl} and using the boundary condition described in Eq. 2.36, A_W can be written as

$$A_W = B_B \frac{k_l(k_B a)}{j_l(k_W a)} \tag{2.42}$$

and applying normalisation condition leads to

$$(B_B)^{-2} = \frac{{k_l}^2(k_B a)}{{j_l}^2(k_W a)} \int_0^a r^2 {j_l}^2(k_W r)\mathrm{d}r + \int_a^\infty r^2 {k_l}^2(k_B r)\mathrm{d}r \tag{2.43}$$

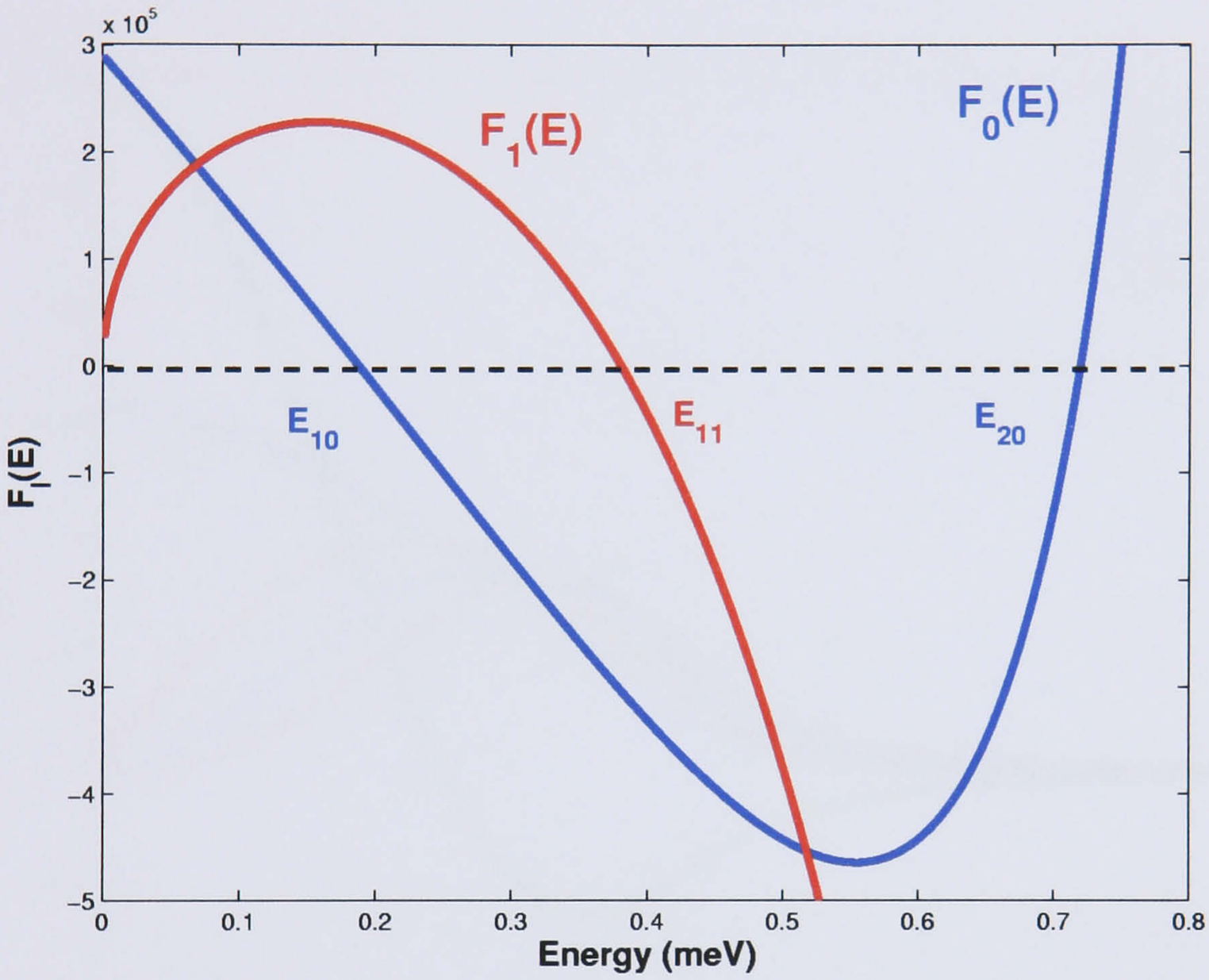

Figure 2.7: Functions $F_l(E)$ for $l = 0, 1$. Points where $F_l(E) = 0$ are the allowed confined energy levels of a particle of mass effective $m^* = 0.023m_0$ within a finite potential barrier ($V_0 = 1$ eV) spherical QD of radius $a = 8$ nm. E_{nl} is the n-th zero of $F_l(E)$.

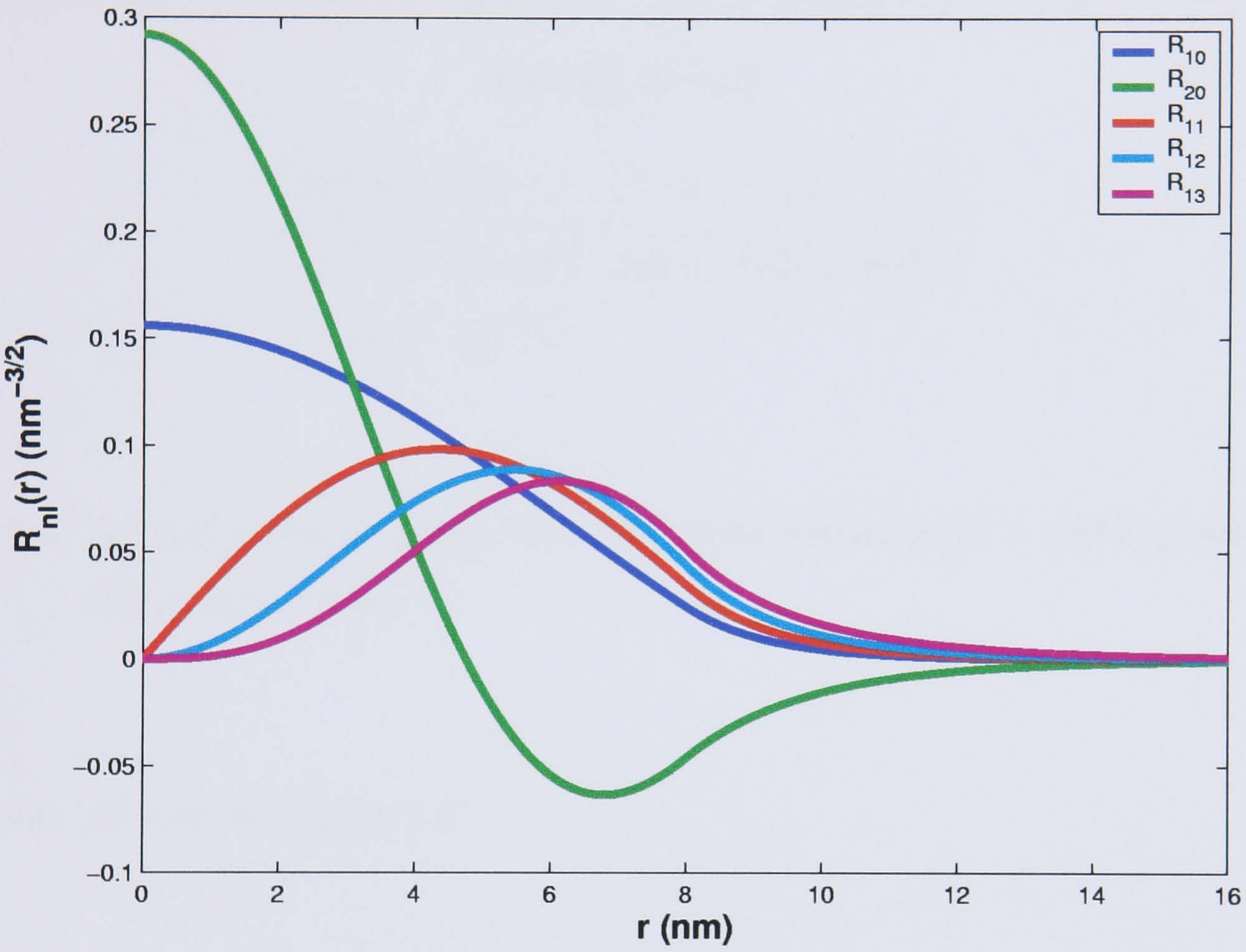

Figure 2.8: Radial wavefunctions of an electron of mass effective $m^* = 0.023m_0$ within a finite potential ($V_0 = 1$ eV) spherical QD of radius $a = 8$ nm.

2.3.3 An example of the energy levels calculation. Finite barrier SQD.

Our model consists of an electron of mass $m^* = 0.023m_0$ within a spherical QD of radius $a = 8$ nm. The potential barrier height is $V_0 = 1$ eV. This model has five allowed energies shown in Table 2.4. Their corresponding radial wavefunctions

Energy levels

E_{nl} (eV)	$l=0$	$l=1$	$l=2$	$l=3$
$n=1$	0.188	0.381	0.618	0.893
$n=2$	0.719			

Table 2.4: Allowed confined Energy levels of a finite potential ($V_0 = 1$ eV) spherical QD of radius $a = 8$ nm.

$R_{nl}(r)$ can be seen in Figure 2.8.

2.3.4 Colloidal Quantum Dot. Capped Quantum Dots.

Semiconductor nanocrystal quantum dots have been the subject of great scientific and technological interest, with promising applications such as biological tagging materials[3]. The colloidal synthesis of QD's is well suited to the fabrication of engineered heterostructure nanoparticles such as CdSe/ZnS (core/shell)[4]. Overcoating nanocystallites with higher band gap inorganic materials has been shown to improve the photoluminescence quantum yields by passivating surface non-radiative recombination sites.

We now illustrate the calculation of the electronic structure of a capped spherical quantum dot. The understanding of this model is necessary in order to investigate the coupling between two capped colloidal QD's, which will be studied later in Chapter 4.

Model

In this model it is assumed that the QD consists of a spherical CdSe core surrounded by a concentric shell of ZnS where the band offsets are such that the conduction band of the shell is of higher energy than that of the core. As a result, a carrier is mostly confined in the core.

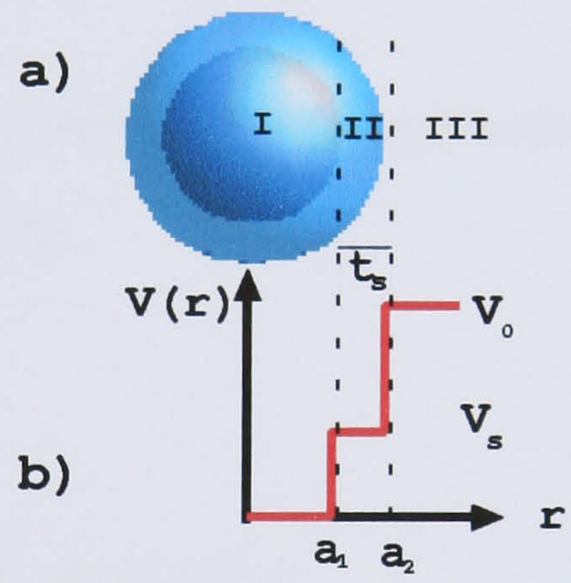

Figure 2.9: **a)**Schematic picture of a core-shell quantum dot and **b)**the band-edge potential where region I corresponds to the core of the dot (CdSe), region II to the capping layer (ZnS) and region III to the surrounding material

Figure 2.9a) shows the picture of a CdSe/ZnS core-shell quantum dot with core radius a_1 and shell thickness $t_s = a_2 - a_1$. The confining potential of the dot is represented in spherical coordinates in Figure 2.9b). The energy levels of a spherical QD with finite barriers potential may be obtained by solving the Schrödinger

Equation:

$$\hat{H}\Psi = E\Psi \tag{2.44}$$

Due to the spherical symmetry of the QD, and following Section 2.3.2 the spatial wavefunction $\Psi = \langle \mathbf{r}|\Psi\rangle$ may be written as

$$\Psi(r,\theta,\phi) = R_{nl}(r)Y_l^m(\theta,\phi) \tag{2.45}$$

where $Y_l^m(\theta,\phi)$ are the normalised spherical harmonics given in Table 2.1 and R_{nl} is the radial wavefunction which may be expressed in terms of $j_l(i_l)$ and $k_l(y_l)$, which are the spherical Bessel functions and modified spherical Bessel functions of first(second) order, respectively.

Assuming that E is an eigenfunction of the Hamiltonian in Equation 2.44, the radial component may be expressed as

- If $0 < E < V_s$

$$R_{nl} = \begin{cases} A_1 j_l(K_1 r) & \text{region I} \\ A_2 i_l(K_2 r) + B_2 k_l(K_2 r) & \text{region II} \\ B_3 k_l(K_3 r) & \text{region III} \end{cases} \tag{2.46}$$

- If $V_s < E < V_0$

$$R_{nl} = \begin{cases} A_1 j_l(K_1 r) & \text{region I} \\ A_2 j_l(K_2 r) + B_2 y_l(K_2 r) & \text{region II} \\ B_3 k_l(K_3 r) & \text{region III} \end{cases} \tag{2.47}$$

where $K_1 = \sqrt{2m^*E}/\hbar$, $K_2 = \sqrt{2m^*|V_s - E|}/\hbar$, $K_3 = \sqrt{2m^*|V_0 - E|}/\hbar$ and A_1, A_2, B_2 and B_3 are parameters which can be obtained satisfying the boundary conditions

given by

$$\begin{aligned} R_{nl}(a_1{}^-) &= R_{nl}(a_1{}^+) \\ R_{nl}(a_2{}^-) &= R_{nl}(a_2{}^+) \\ R'_{nl}(a_1{}^-) &= R'_{nl}(a_1{}^+) \\ R'_{nl}(a_2{}^-) &= R'_{nl}(a_2{}^+) \end{aligned} \tag{2.48}$$

In region II, coefficients A_2 and B_2 are non zero for the case $0 < E < V_s$ and $V_s < E < V_0$, respectively because spherical Bessel functions i_l and y_l are finite within the interval. We substitute R_{nl} in Equation system 2.48, where the energy $0 < E < V_s$ giving

$$\begin{cases} A_1 j_l(K_1 a_1) &= A_2 i_l(K_2 a_1) + B_2 k_l(K_2 a_1) \\ A_1 K_1 j'_l(K_1 a_1) &= A_2 K_2 i'_l(K_2 a_1) + B_2 K_2 k'_l(K_2 a_1) \\ B_3 k_l(K_3 a_2) &= A_2 i_l(K_2 a_2) + B_2 k_l(K_2 a_2) \\ B_3 K_3 k'_l(K_3 a_2) &= A_2 K_2 i'_l(K_2 a_2) + B_2 K_2 k'_l(K_2 a_2) \end{cases} \tag{2.49}$$

then

$$\begin{cases} A_1 j_{11} - A_2 i_{21} - B_2 k_{21} = 0 \\ A_1 K_1 j'_{11} - A_2 K_2 i'_{21} - B_2 K_2 k'_{21} = 0 \\ A_2 i_{22} + B_2 k_{22} - B_3 k_{32} = 0 \\ A_2 K_2 i'_{22} + B_2 K_2 k'_{22} - B_3 K_3 k'_{32} = 0 \end{cases} \tag{2.50}$$

where $f_{ij} = f_l(K_i a_j)$ and $f'_{ij} = f'_l(K_i a_j)$, where $f_l = j_l, i_l, k_l$. Last system of equations (Equations 2.50) may be written in terms of matrices as

$$\begin{pmatrix} j_{11} & i_{21} & -k_{21} & 0 \\ K_1 j'_{11} & K_2 i'_{21} & -K_2 k'_{21} & 0 \\ 0 & i_{22} & k_{22} & -k_{32} \\ 0 & K_2 i'_{22} & K_2 k'_{22} & -K_3 k'_{32} \end{pmatrix} \begin{pmatrix} A_1 \\ A_2 \\ B_2 \\ B_3 \end{pmatrix} = 0 \tag{2.51}$$

or

$$\mathcal{M}\mathcal{C} = 0 \tag{2.52}$$

The only non-trivial solution of the last expression occurs when the determinant of the matrix $\mathcal{M}$ is zero. Therefore

$$\det(\mathcal{M}) = \begin{vmatrix} j_{11} & i_{21} & -k_{21} & 0 \\ K_1 j'_{11} & K_2 i'_{21} & -K_2 k'_{21} & 0 \\ 0 & i_{22} & k_{22} & -k_{32} \\ 0 & K_2 i'_{22} & K_2 k'_{22} & -K_3 k'_{32} \end{vmatrix} = 0 \tag{2.53}$$

This last equation may be solved using the Newton-Raphson method [2] to give the allowed energies of the system.

2.3.5 An example of the energy levels calculation. Capped SQD.

Equation 2.53 is solved and the energy levels of a electron of mass $m^* = 0.1m_0$ within a CdSe/ZnS core/shell QD of radius $a_1 = 3$ nm and shell thickness $a_2 - a_1 = t_s = 0.5$ nm obtained, where m_0 is the electron resting mass. We set the potential inside the CdSe core $V = 0$. The band offset between core and shell is $V_s = 0.9$ eV and between core and surrounding material(liquid) is $V_0 = 3$ eV as is represented in Figure 2.9b). All the parameters have been taken from [5, 4]. The energy values obtained within the range $0 < E < V_s$ are $E_{10} = 0.303$ eV and $E_{11} = 0.616$ eV, as can be seen in Figure 2.10. Figure 2.11 shows their corresponding radial wavefunctions R_{10} and R_{11}. These calculations will be used later in Chapter 4 in order to study the electronic structure of coupled capped colloidals QD's.

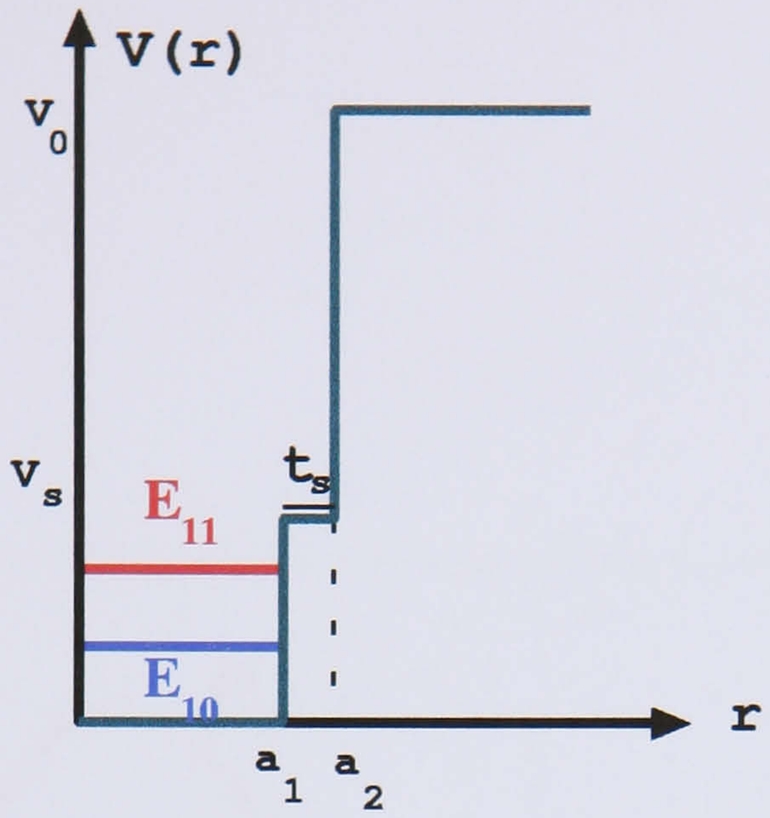

Figure 2.10: Two lowest energy levels of an electron within a CdSe/CdS core/shell colloidal QD and representation of its potential $V(r)$ where $V_s = 0.9$ eV and $V_0 = 3$ eV.

2.4 Cylindrical Quantum Dot

Cylindrical QD's are studied because they provide a basis to investigate the electronic structure of self-assembled semiconductor quantum dots with cylindrical symmetry, which will be described later in Section 2.5. This symmetry will be used in the full diagonalisation of the system Hamiltonian method, studied in Chapter 3.

2.4.1 Free particle in Cylindrical coordinates

As for the earlier case of the spherical QD, first we need to solve the Schrödinger equation for a free particle, but in this case in cylindrical coordinates. These results will then be used to study confined structures with cylindrical symmetry.

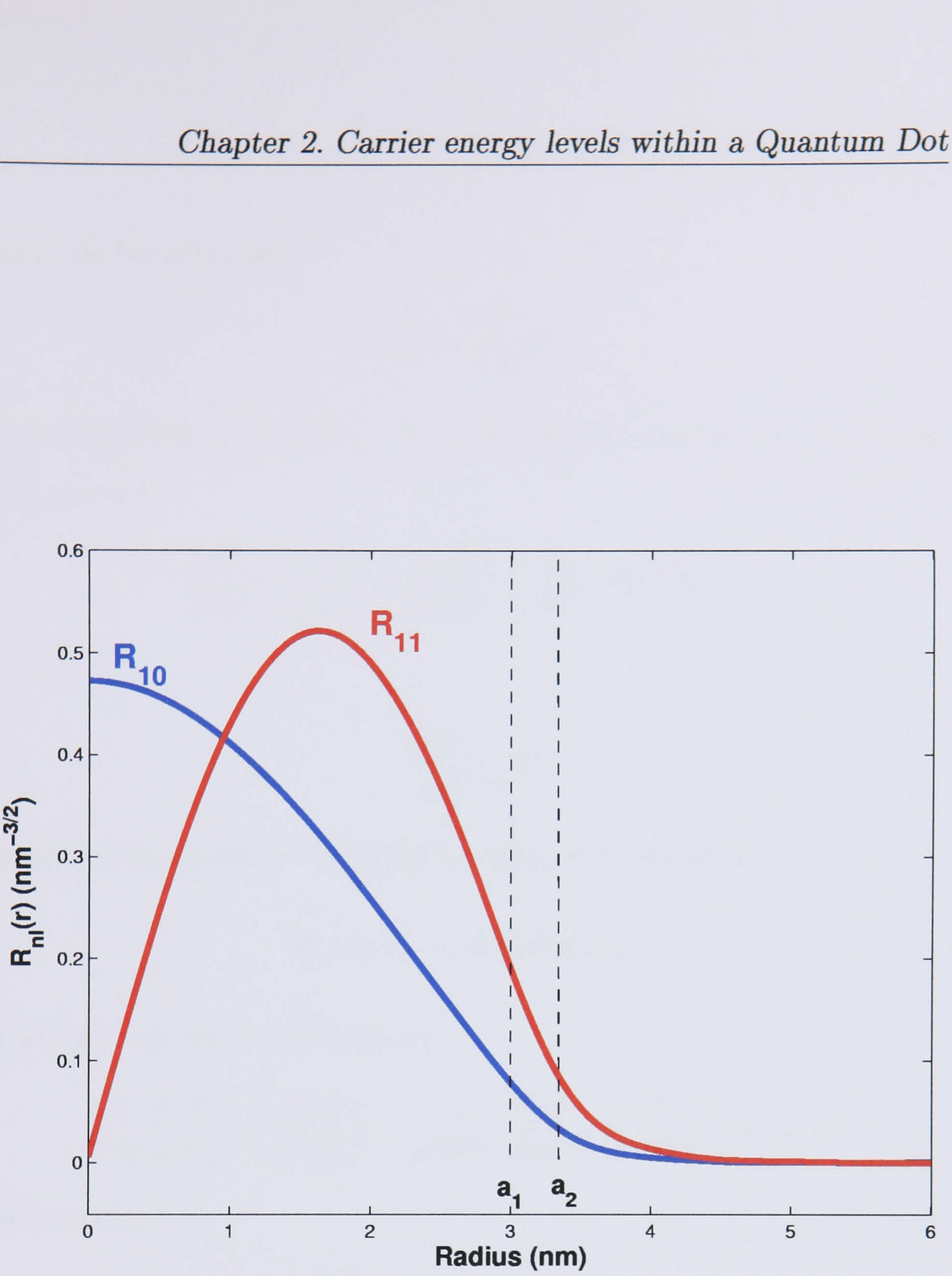

Figure 2.11: Two lowest radial wavefunctions of an electron of mass $m^* = 0.1m_0$ within a CdSe/ZnSe core/shell colloidal QD where the core radius is $a_1 = 3$ nm and the shell thickness is $a_2 - a_1 = 0.3$ nm.

Employing the Hamiltonian

$$\hat{H} = -\frac{\hbar^2}{2M}\nabla^2 \tag{2.54}$$

written in cylindrical coordinates, the Schrödinger equation for a free particle of mass M is given by

$$\left[\frac{\partial^2}{\partial\rho^2} + \frac{1}{\rho}\frac{\partial}{\partial\rho} + \frac{1}{\rho^2}\frac{\partial^2}{\partial\phi^2} + \frac{\partial^2}{\partial z^2} + k^2\right]\Psi = 0 \tag{2.55}$$

where

$$\frac{\hbar^2 k^2}{2M} = E \tag{2.56}$$

is the energy of the particle. With the separation of variables

$$\Psi(\rho,\phi,z) = R(\rho)\Phi(\phi)Z(z) \tag{2.57}$$

the Schrödinger equation 2.55 becomes

$$\frac{1}{R}\left(\frac{\partial^2 R}{\partial\rho^2} + \frac{1}{\rho}\frac{\partial R}{\partial\rho}\right) + \frac{1}{\rho^2\Phi(\phi)}\frac{\partial^2\Phi}{\partial\phi^2} + \frac{1}{Z}\frac{\partial^2 Z}{\partial z^2} + k^2 = 0 \tag{2.58}$$

and it follows that

$$\frac{1}{Z}\frac{\mathrm{d}^2 Z}{\mathrm{d}z^2} = \text{constant} \equiv -{k_z}^2 \tag{2.59}$$

$$\frac{1}{\Phi}\frac{\mathrm{d}^2\Phi}{\mathrm{d}\phi^2} = \text{constant} \equiv -m^2 \tag{2.60}$$

Taking into account that $\Phi(\phi) = \Phi(\phi + 2\pi)$, components $Z(z)$ and $\Phi(\phi)$ may be written as

$$Z(z) = A\mathrm{e}^{\mathrm{i}k_z z} + B\mathrm{e}^{-\mathrm{i}k_z z} \tag{2.61}$$

$$\Phi(\phi) = C\mathrm{e}^{\mathrm{i}m\phi} \tag{2.62}$$

where A, B are constants, $m = 0, \pm1, \pm2, \ldots$ and $C = 1/\sqrt{2\pi}$ is the angular component normalisation constant.

Substituting Equations 2.59 and 2.60 into 2.58 and denoting prime as the differentiation with respect to ρ lead to

$$\frac{1}{R}(\rho^2 R'' + \rho R') + \rho^2(k^2 - {k_z}^2) = m^2 \tag{2.63}$$

Now, labelling

$$k^2 - {k_z}^2 \equiv K^2 \tag{2.64}$$

$$x \equiv K\rho \tag{2.65}$$

leads to

$$x^2 R'' + xR' + (x^2 - m^2)R = 0 \tag{2.66}$$

which is known as Bessel's equation. General solutions to this equation are given by

$$R(x) = C_1 J_m(x) + C_2 Y_m(x) \tag{2.67}$$

where C_1 and C_2 are constants and $J_m(x)$ and $Y_m(x)$ are called Bessel and Neumann (also called $N_m(x)$) functions of the first kind, respectively. Figure 2.12 shows functions $J_{l=0}(x)$ and $Y_{l=0}(x)$.

2.4.2 Infinite barrier potential

First the energy levels and wavefunctions of an infinite cylindrical barrier are calculated which provides a useful introduction to the coordinate system before investigating more complicated cylindrical structures. The results of the infinite barrier calculation will also be used in the Full Diagonalisation of the system Hamiltonian method explained in Chapter 3.

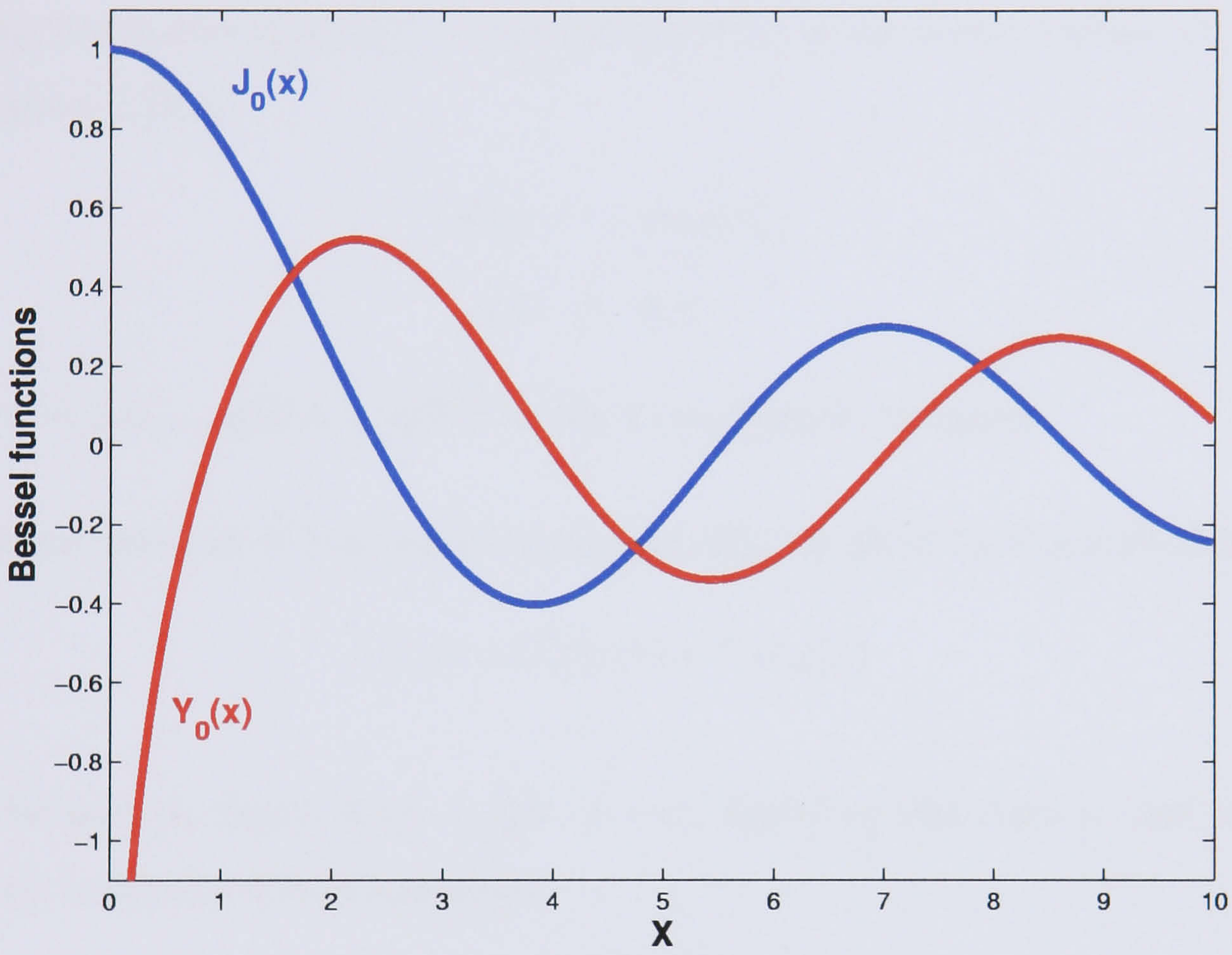

Figure 2.12: Bessel functions of the first kind of the first order ($l = 0$).

In the model it is considered the case of a particle of mass m^* confined to a cylindrical box of radius a and length L. Expressed in cylindrical coordinates, the potential of this configuration is given by

$$V(\rho,\phi,z) = \begin{cases} 0 & \rho < a \wedge 0 < z < L \\ \infty & \text{outside the cylinder} \end{cases} \tag{2.68}$$

Applying the potential given by 2.68, the solution of the z-component $Z(z)$, given by Equation 2.59, is

$$Z(z) = A \sin k_z z \tag{2.69}$$

$$k_z L = n_z \pi \tag{2.70}$$

where $n_z = 1, 2, ...$ and $A = \sqrt{2/L}$ is the normalisation constant.

The general solution of the radial component $R(\rho)$ is given by Equation 2.67

$$R(x) = C_1 J_m(x) + C_2 Y_m(x) \tag{2.71}$$

As can be seen in Figure 2.12, $Y_m(0) \to -\infty$, therefore this term is omitted. The remaining boundary conditions gives

$$R(\rho = a) = 0 = C_1 J_m(aK) \tag{2.72}$$

Denoting x_{ms} the s-th zero of $J_m(x)$ leads to

$$K = x_{ms}/a \tag{2.73}$$

Therefore the eigenenergies are given by

$$E = \frac{\hbar^2 k^2}{2m^*} = \frac{\hbar^2}{2m^*}(K^2 + {k_z}^2) = \frac{\hbar^2}{2m^*}\left[K^2 + \left(\frac{n_z \pi}{L}\right)^2\right] \tag{2.74}$$

substituting $K = x_{ms}/a$ the last equation becomes

$$E = \frac{\hbar^2}{2m^*}\left[\left(\frac{x_{ms}}{a}\right)^2 + \left(\frac{n_z \pi}{L}\right)^2\right] \tag{2.75}$$

and the corresponding eigenfunctions are given by

$$\psi_{n_z ms}(\rho, \phi, z) = A_{ms} J_m \left(\frac{x_{ms}}{a^2}\rho\right) \sin\left(\frac{n_z \pi}{L} z\right) \mathrm{e}^{\mathrm{i}m\phi} \tag{2.76}$$

Orthogonality of the Bessel functions is given by

$$\int_0^a \mathrm{d}\rho\rho J_m \left(\frac{\rho x_{ms}}{a}\right) J_m \left(\frac{\rho x_{ms'}}{a}\right) = \frac{a^2}{2}[J_{m+1}(x_{ms})]^2 \delta_{ss'} \tag{2.77}$$

The normalisation constant A_{ms} is given by

$$(A_{ms})^{-2} = \frac{\pi L[aJ_m{}'(K_{ms}a)]^2}{2} \tag{2.78}$$

2.5 Self-assembled Quantum Dot (SAD)

In Chapter 1 the growth of self-assembled semiconductor quantum dots was discussed. The self-assembled dot studied in this section is composed of a dot formed on a quantum well wetting layer of thickness t_w, and modelled as a part of an ellipsoid of a short axis of length h (height) and two long axis of length R (radius) as can be seen in Figure 2.13. Electrons(holes) are confined in the narrow wetting-layer quantum well due to the step in the conduction(valence)-band edge at the interface, and they are further localised in the area of the dot due to the increased thickness of the layer.

Following [6], the parameters of the two materials that make up the QD and the barrier appear in the model through the effective units of energy and length, R_y^* and a_B^* respectively, which take into account all the effects due to stress, discontinuity of the effective mass and dielectric constant at the interface, etc.

$$R_y{}^* = \frac{\mathrm{e}^2}{2\epsilon a_B{}^*} \equiv 1 \tag{2.79}$$

$$a_B{}^* = \frac{\epsilon \hbar^2}{m^* \mathrm{e}^2} \equiv 1 \tag{2.80}$$

We use a three-dimensional potential $V(\rho, z)$, which has the same geometry as a SAD (Figure 2.14), that acts on the electrons (holes) confined within the dot. Thus carriers localised inside the dot must satisfy the Schrödinger Equation (cylindrical coordinates):

$$[H_z^0 + H_{\rho\phi}^0 + V(\rho, z)]\Psi^{\mathrm{D}} = E^{\mathrm{D}}\Psi^{\mathrm{D}} \tag{2.81}$$

where

$$H_z^0 = -\frac{\partial^2}{\partial z^2} \tag{2.82}$$

$$H_{\rho\phi}^0 = -\frac{1}{\rho^2}\left(\rho\frac{\partial}{\partial\rho}\rho\frac{\partial}{\partial\rho} + \frac{\partial^2}{\partial\phi^2}\right) \tag{2.83}$$

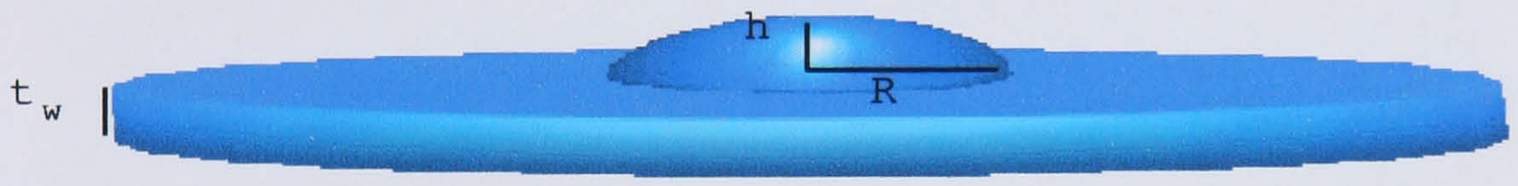

Figure 2.13: Schematic representation of a self-assembled quantum dot, where the wetting layer thickness is t_w and the dot is a semi-ellipsoidal of height h and radius R.

2.5.1 Wave function and energy within the quantum dot

A carrier inside the QD is confined in all directions by the potential V shown in Figure 2.14 and described by:

$$V = \begin{cases} 0 & \text{inside the SAD} \\ V_0 & \text{outside the SAD} \end{cases} \tag{2.84}$$

where V_0 is the difference between the conduction(valence)-band energies in the two materials, including the effect of strain. Due to the cylindrical symmetry of the QD and the fact that the radius is much bigger than its height, the Hamiltonian may be solved using the adiabatic approximation. This method takes advantage of the fact that the carrier wavefunctions are strongly confined to the lowest sub-band in the narrow wetting-layer quantum well [6]. Thus we can write:

$$\Psi^{\mathrm{D}}(\rho,\phi,z) = \frac{e^{im\phi}}{\sqrt{2\pi}} g_{n\rho}(z) f_m(\rho) \tag{2.85}$$

where $g_{n\rho}(z)$ is a slowly varying function of ρ.

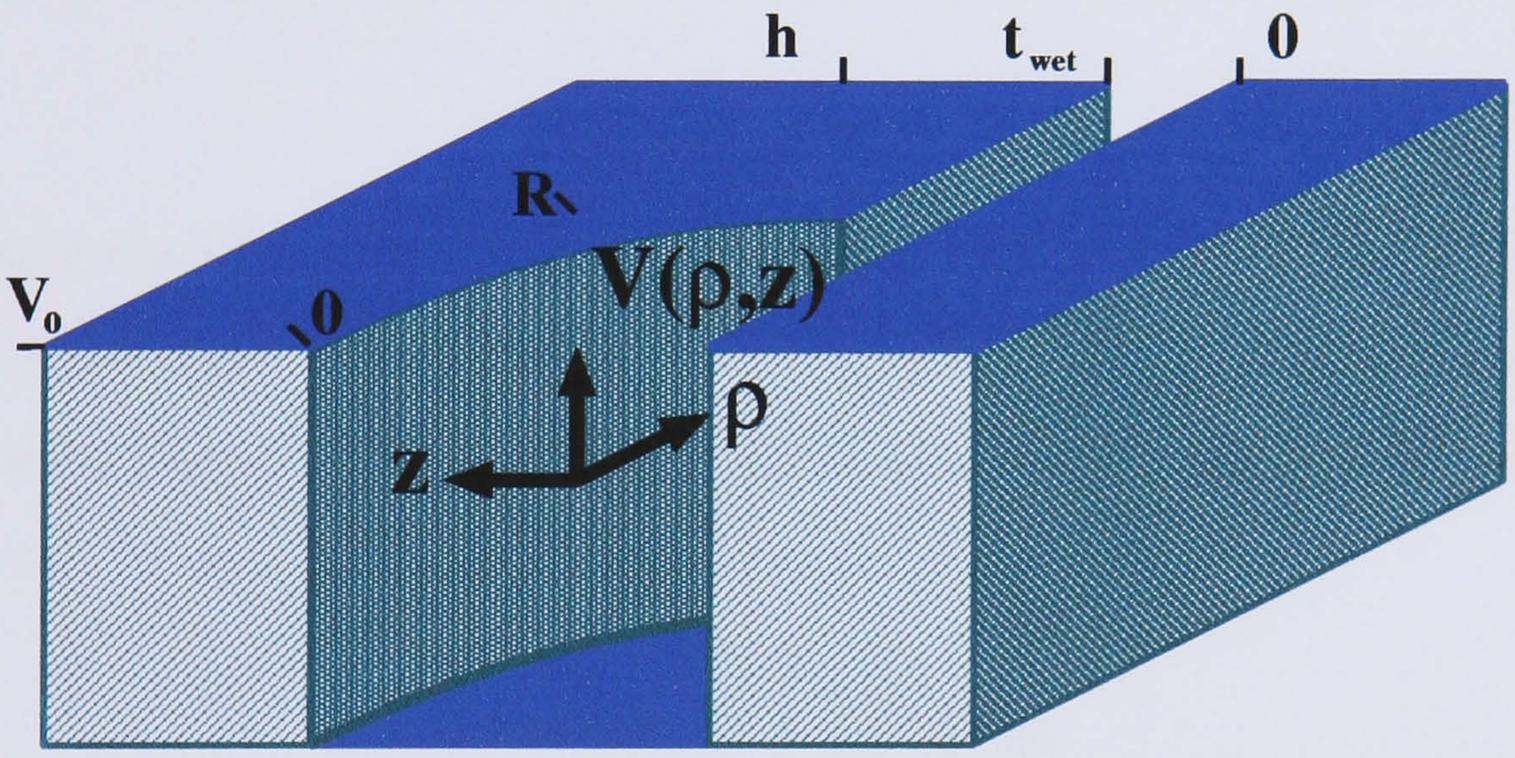

Figure 2.14: Schematic picture of the SAD effective potential in cylindrical coordinates, $V(\rho,z)$. The potential inside the SAD is $V=0$, whereas outside is $V=V_0$.

In the subspace of functions with integer angular momentum m, functions $g_{n\rho}$ and f_m need to satisfy the system of equations:

$$\Big[-\frac{\partial^2}{\partial z^2} + V(z,\rho)\Big] g_{n\rho}(z) = E_n(\rho) g_{n\rho}(z) \tag{2.86}$$

$$\Big[-\frac{1}{\rho^2}\Big(\rho\frac{\partial}{\partial\rho}\rho\frac{\partial}{\partial\rho} - m^2\Big) + E_n(\rho)\Big] f_m(\rho) = E^{\mathrm{D}} f_m(\rho) \tag{2.87}$$

where $E_n(\rho)$, $n=1,\ldots,$ is the effective lateral confining potential. In order to solve Equations 2.86 and 2.87 numerical methods need to be used.

The z component (finite potential Quantum Well)

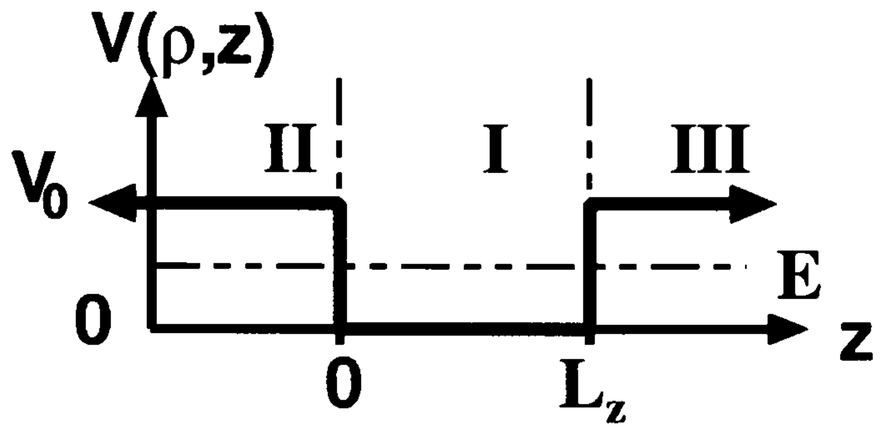

Figure 2.15: Schematic representation of quantum well potential with finite barriers.

The z component of the Hamiltonian, Equation 2.86, describes the finite potential well in a one dimension problem, shown in Figure 2.15. Due to the fact that the dot radius is much bigger than the height, the width of the well, $L_z(\rho)$, varies slowly with ρ, as can be seen in Figure 2.16a), satisfying:

$$L_z = h\sqrt{1 - \left(\frac{\rho}{R}\right)^2} + t_{\text{wet}} \tag{2.88}$$

This is simply the classic problem of quantum mechanical confinement by a finite potential in one dimension. Following [1], the ground state energy (in effective units) is given by:

$$k_I \tan(k_I L_z(\rho)/2) = k_{II} \tag{2.89}$$

where

$$L_z(\rho) = t_w + h\sqrt{1 - (\rho/R^2)} \tag{2.90}$$

describes the shape of the SAD and

$$k_I^2 = E \tag{2.91}$$

$$k_{II}^2 = V_0 - E \tag{2.92}$$

Equation 2.89 may be solved numerically and it gives several solutions for the energy E_n. The corresponding wavefunction is given by:

$$g_{n=1\rho}(z) = \begin{cases} A_\rho \cos(k_I L_z/2) \mathrm{e}^{k_{II} z} & \text{region II} \\ A_\rho \cos(k_I (z - L_z/2)) & \text{region I} \\ A_\rho \cos(k_I L_z/2) \mathrm{e}^{-k_{II}(z-L_z)} & \text{region III} \end{cases} \tag{2.93}$$

where the normalisation condition $\int_{-\infty}^{\infty} |g_{1\rho}|^2 \mathrm{d}z = 1$ determines the constant A_ρ.

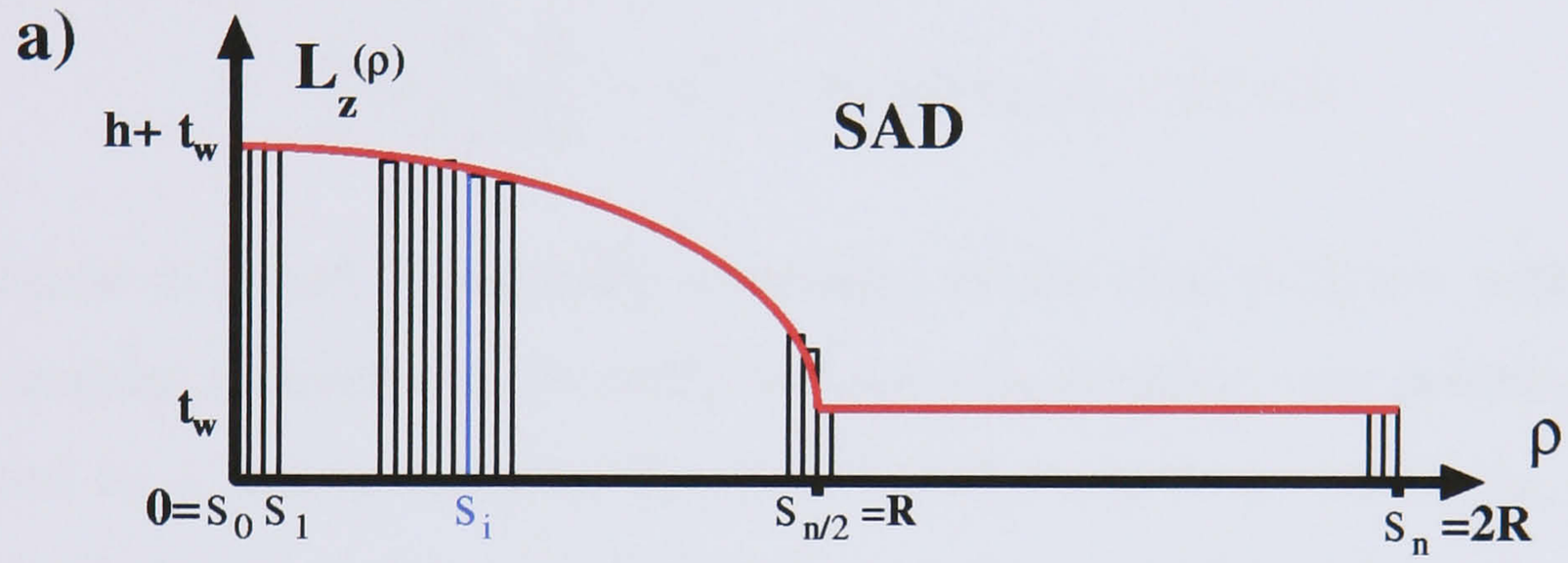

Figure 2.16: a)SAD height versus radius in cylindrical coordinates. **b)**Radial Schrödinger equation *effective potential* V_{eff}.

Radial component

We can now insert the energy $E_n(\rho)$ into the radial Schrödinger Equation 2.87 as an *effective potential.* Taking into account that the electron wavefunctions are strongly confined to the lowest sub-band in the narrow wetting-layer quantum well, we can assume that this effective potential is $E_{n=1}(\rho)$.

Substituting this potential into 2.87 leads to

$$\Big[-\frac{1}{\rho^2}\Big(\rho\frac{\partial}{\partial\rho}\rho\frac{\partial}{\partial\rho}-m^2\Big)+E_1(\rho)\Big]f_m(\rho)=Ef_m(\rho) \tag{2.94}$$

This equation is solved numerically separately within each subspace with a fixed value of angular momentum. In order to solve this equation, the potential is approximated by a n-step function $E_1(\rho) = V_{\text{eff}}(\rho) = v_i$ if $s_i < \rho < s_{i+1}$, where $v_{i+1} > v_i$, s_i is a vector of $n+1$ values from $s_0 = 0$ to $s_n = 2R$ and $s_{i+1} > s_i$ as can be seen in Figure 2.16b). Due to the fact that the radial wavefunction practically vanishes for $\rho > 2R$, the element $s_n = 2R$ has been chosen as the ρ axis limit.

The wavefunction that corresponds to the energy E and angular momentum m can be written as

$$f_m(r) = A_iF(k_ir) + B_iG(k_ir) \tag{2.95}$$

if $s_i \leq r \leq s_{i+1}$ where $k_i^2 = |E - v_i|$ and (F, G) is the appropriate pair of cylindrical Bessel functions: (J_m, Y_m) for $E > v_i$ and (K_m, I_m) for $E < v_i$. The wavefunctions must be continuous and smooth at each interface:

$$A_{i-1}F_i^L + B_{i-1}G_i^L = A_iF_i^R + B_iG_i^R \tag{2.96}$$

$$A_{i-1}\nabla F_i^L + B_{i-1}\nabla G_i^L = A_i\nabla F_i^R + B_i\nabla G_i^R \tag{2.97}$$

In the above equations we use the followings notation:

$$\begin{aligned} P_i^L &\equiv P(k_{i-1}s_i) \quad & \nabla P_i^L &\equiv k_{i-1}P'(k_{i-1}s_i) \\ P_i^R &\equiv P(k_is_i) & \nabla P_i^R &\equiv k_iP'(k_is_i) \end{aligned} \tag{2.98}$$

where $P = F, G$. The coefficients (A, B) are related to the transfer matrix T_j by

$$\begin{bmatrix} A_j \\ B_j \end{bmatrix} = T_j \begin{bmatrix} A_{j-1} \\ B_{j-1} \end{bmatrix} \tag{2.99}$$

where T_j may be written as

$$T_j = \begin{pmatrix} F_j^R & G_j^R \\ \nabla F_j^R & \nabla G_j^R \end{pmatrix}^{-1} \begin{pmatrix} F_j^L & G_j^L \\ \nabla F_j^L & \nabla G_j^L \end{pmatrix} \tag{2.100}$$

Solving the system of equations 2.96-2.97 is equivalent to finding the total transfer matrix T, defined as

$$\begin{bmatrix} A_n \\ B_n \end{bmatrix} = \left(\prod_{i=1}^{n} T_i \right) \begin{bmatrix} A_0 \\ B_0 \end{bmatrix} \equiv T \begin{bmatrix} A_0 \\ B_0 \end{bmatrix} \tag{2.101}$$

The wavefunctions and derivatives must be finite in the centre of the dot, hence this condition must be met by

$$B_0 = 0 \tag{2.102}$$

The energies of the bound states E_b are obtained from the condition that the wavefunctions vanish in the limit of infinite radius. This additional condition

$$B_n = 0 \tag{2.103}$$

is equivalent to the vanishing of the corresponding element of the total transfer matrix,

$$T_{21}(E_b) = 0 \tag{2.104}$$

for the discrete set of energies E_b. This condition may give more than one solution, therefore we include a subscript, $l = 1, 2, \ldots$, to denote that E_{ml} is the l-th allowed energy associated to the quantum number m. Therefore the eigenfunction of the Hamiltonian may be written as:

$$\Psi^{\mathrm{D}}_{1ml}(\rho, \phi, z) = \frac{e^{im\phi}}{\sqrt{2\pi}} g_{1\rho}(z) f_{ml}(\rho) \tag{2.105}$$

2.5.2 An example of the energy levels calculation. SAD.

Our model consists of a InAs self-assembled ellipsoidal QD whose height $h = 2$ nm, radius $R = 8$ nm and wetting layer thickness $t_w = 0.5520$ nm surrounded by GaAs (taken from [7]). We want to obtain the electronic structure of an electron of mass $m^* = 0.023m_0$ within the SAD. The barrier potential height for the electron is set to $V_0 = 1$ eV and $\epsilon = 13\epsilon_0$. All the parameters have been taken from [8].

The allowed confined energies, E_{ml}, we obtain are

$$\begin{aligned} E_{01} &= 0.706 \text{ eV} \\ E_{11} &= 0.876 \text{ eV} \end{aligned}$$

Their associated wavefunctions, the ground state Ψ_{101} and the first excited state Ψ_{111} may be seen in Figure 2.17 and Figure 2.18, respectively.

2.6 Summary

In this chapter the Schrödinger equation has been solved for an electron within different shaped semiconductor QD's applying the effective mass approximation. First, the free particle problem has been solved in spherical coordinates and the results used to obtain the solution for spherical symmetric step-like potentials. Both finite and infinite potential barriers have been considered. The solution of the Schrödinger equation for a capped QD has been also obtained, where the QD is capped by a layer of higher bandgap material. The Schrödinger equation for a free particle in cylindrical coordinates has been solved analytically in order to obtain the solution of an infinite step-like barrier potential QD. These results will be used in Chapter 3. Due to the cylindrical symmetry of the SAD's we study in this

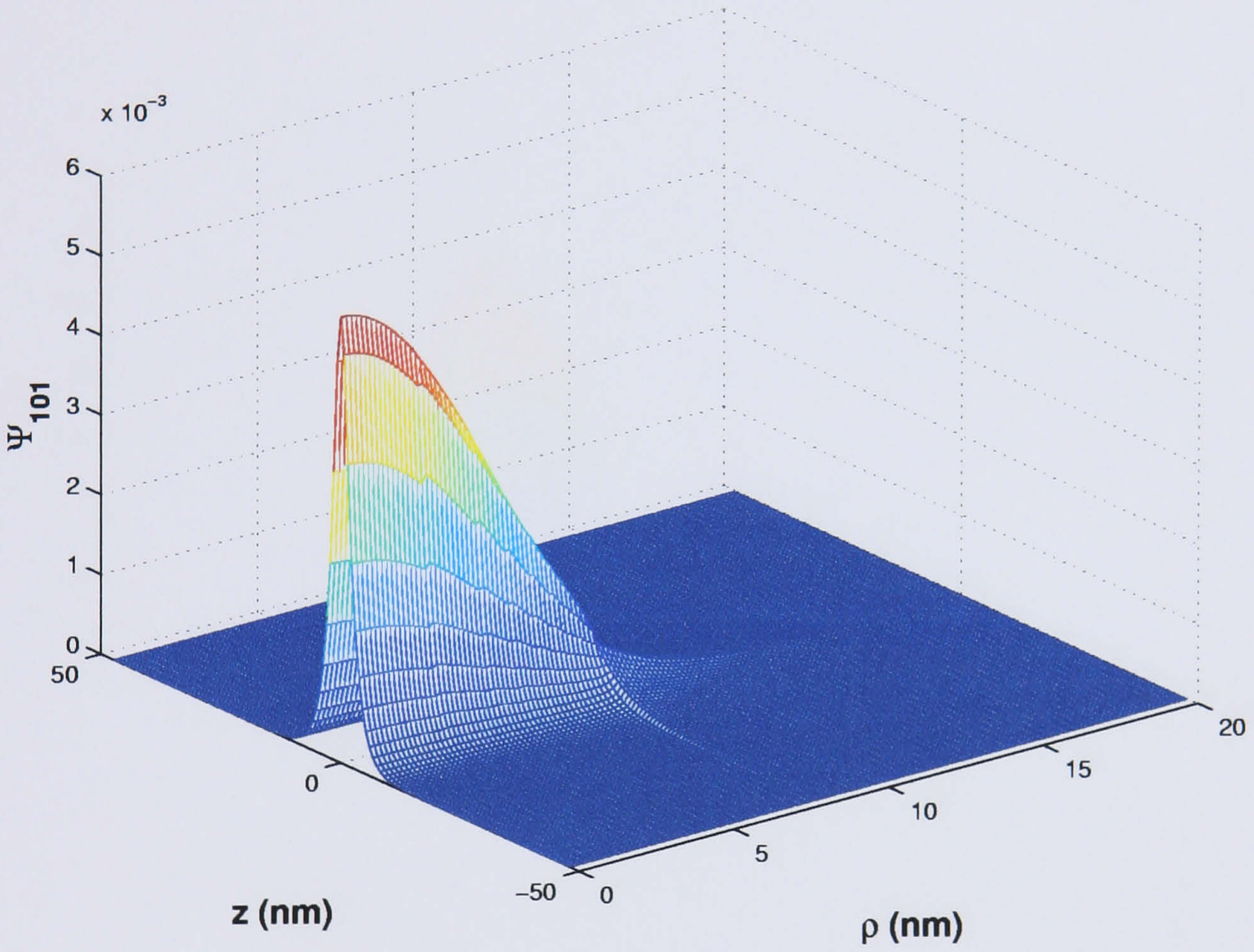

Figure 2.17: SAD ground state wavefunction Ψ_{101}.

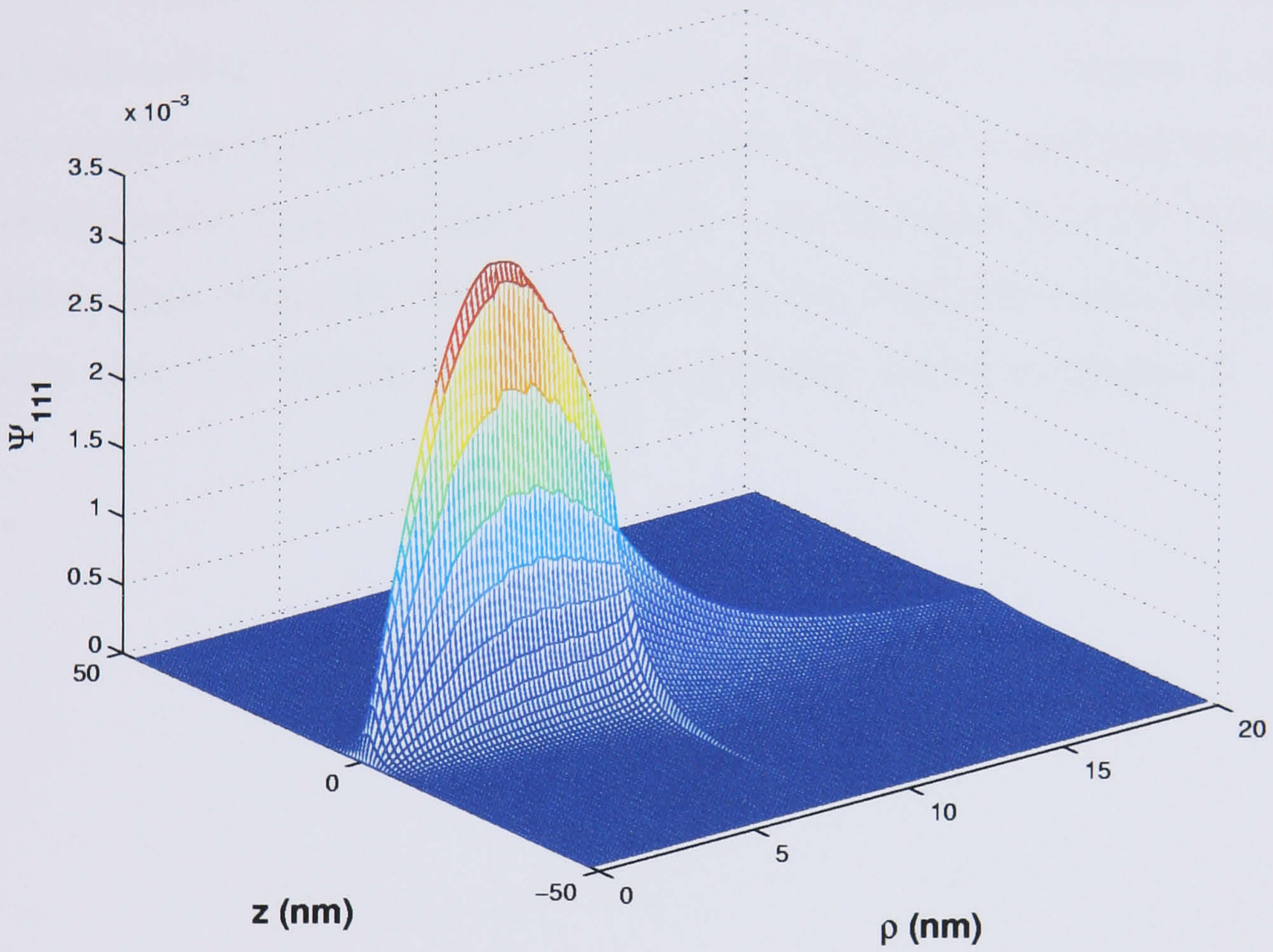

Figure 2.18: SAD first excited state wavefunction $|\Psi_{111}|$.

thesis, these results will be used in Chapter 5 where the LO-phonon interaction in SAD's is investigated. Finally the Schrödinger equation is solved for a self-assembled quantum dot applying an adiabatic method. This kind of quantum dots will be studied later in Chapters 4 and 5.

This chapter has described the calculation of energy levels and wavefunctions of several QD geometries. This work forms the basis for the investigation of the numerical method proposed in Chapter 3, the coupling between QD's in Chapter 4 and the electron scattering due to LO-phonon in Chapter 5. Special consideration has been taken of cylindrical symmetry structures, due to the fact that the SAD's have been modelled as semi-ellipsoids. The SAD wavefunctions obtained in this chapter will be used in order to calculate the scattering processes studied in Chapter 5.

Bibliography

[1] Richard L. Liboff. *Introductory Quantum Mechanics.* Addison Wesley, 1931.

[2] Lorenzo Abellanas Murray R. Spiegel. *Mathematical handbook of formulas and tables.* Mc Graw Hill, 1988.

[3] H. Mattoussi, J. Matthew Mauro, Ellen R. Goldman, George P. Anderson, Vikram C. Sundar, Frederic V. Mikulec, and Moungi G. Bawendi. Self-assembly of `CdSe-ZnS` quantum dot bioconjugates using an engineered recombinant protein. *J. Am. Chem. Soc*, 122:12142, 2000.

[4] B. O. Dabbousi, J. Rodríguez-Viejo, F. V. Mikulec, J. R. Heine, H. Mattoussi, R. Obera, K. F. Jensen, and M. G. Bawendi. `(CdSe)ZnS` core-shell quantum dots: Synthesis and characterization of a size series of highly luminescent nanocrystallites. *J. Phys. Chem. B*, 101:9463, 1997.

[5] Todd D. Krauss and Luouis E. Brus. Electronic properties of single semiconductor nanocyrstals: optical and electrostatic force microscopy measurements. *Materials Science and Engineering B69-70*, page 289, 2000.

[6] L. Jacack, P. Hawrylak, and A. Wojs. *Quantum Dots.* Springer, 1997.

[7] Craig Pryor. Quantum wires formed from coupled `InAs/GaAs` strained quantum dots. *Physical Review Letters*, 80(16):3579, 1998.

[8] Marek Korkusiński and Pawel Hawrylak. Electronic structure of vertically stacked self-assembled quantum disks. *Phys. Rev. B*, 63:195311, 2001.

Chapter 3

Full diagonalisation of the System Hamiltonian

Contents

3.1 Introduction

In the previous chapter we have calculated the electronic energy levels and wavefunctions for quantum dots with simple geometric shapes. In this chapter we introduce two methods for solving the electronic energy levels and wavefunctions for quantum dots with cylindrical symmetry. The first method involves the diagonalisation of the discretised system Hamiltonian and the second is the well known finite difference method. We check the validity of these two methods by comparison with the exact solution of a finite potential spherical quantum dot.

3.2 Cylindrical structures

In order to calculate the energy levels for a 3D quantum-confinement structure with finite barrier height, the Schrödinger equation must be solved satisfying the boundary conditions imposed by the geometry of the structure. These solutions may be obtained analytically only for spherical structures. In all other cases, numerical methods must be applied.

In this chapter we solve the Schrödinger equation for finite barrier potentials with cylindrical symmetry, such as cylinder, sphere and ellipsoid, by diagonalasing the

system Hamiltonian expanded in a chosen basis. This method may be applied to other structures, but assuming a cylindrical symmetry model reduces the three dimensions problem into two dimensional and requires less computational time.

3.2.1 Full diagonalisation of the system Hamiltonian method

First we introduce the method by solving the energy levels and wavefunctions of a simple structure, such as a cylinder, as represented in Figure 3.1a). We assume that the QD is a cylinder of radius a and height h. The Hamiltonian of a particle of effective mass m^* is given by:

$$\hat{H} \equiv -\frac{\hbar^2}{2m^*}\nabla^2 + V = \hat{H}^0 + V \tag{3.1}$$

where V is the band-edge energy described by:

$$V(\mathbf{r}) = \begin{cases} 0 & \text{inside the QD} \\ V_0 & \text{outside the QD} \end{cases} \tag{3.2}$$

and shown in Figure 3.1a).

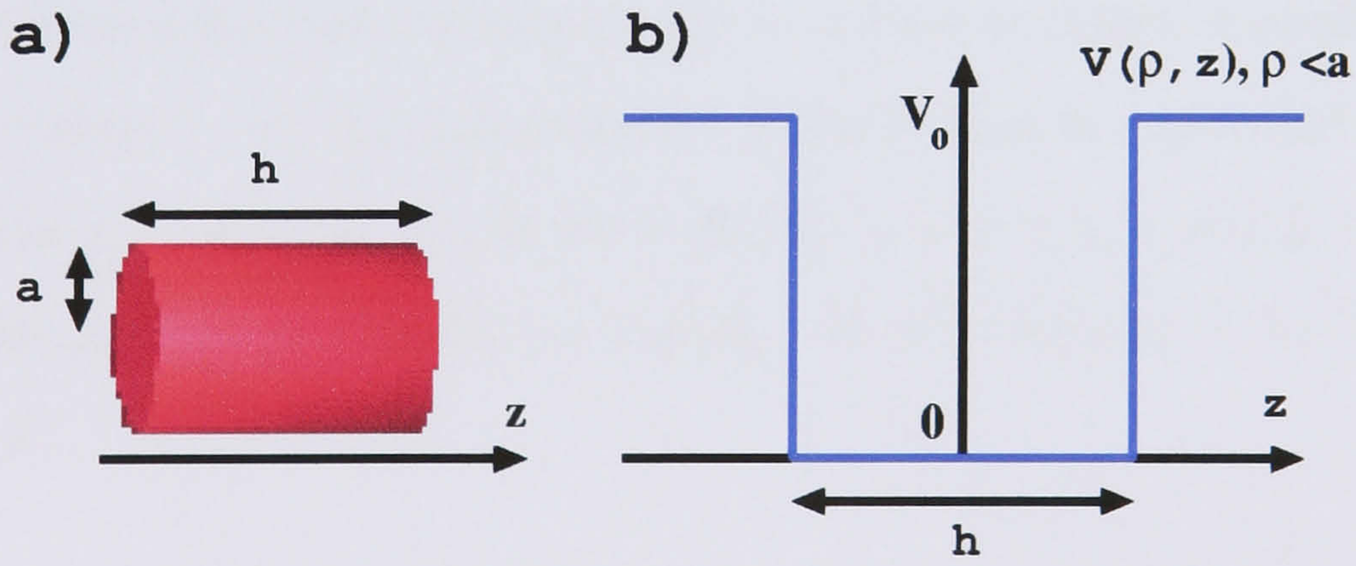

Figure 3.1: **a)**Cylindrical quantum dot of radius a and height h. **b)**Schematic representation of the band-edge potential.

The Schrödinger equation for a finite barrier potential with cylindrical symmetry cannot be solved analytically and therefore must be solved by applying numerical methods. Let the space of eigenfunctions of the Hamiltonian $\hat{H}$ be called $\mathfrak{H}$, the set of functions

$$\mathfrak{B} = \{\Psi_i\}$$

be a basis of $\mathfrak{H}$ and $\{E_i\}$ their corresponding eigenvalues which satisfy

$$\hat{H}\Psi_i = E_i\Psi_i \tag{3.3}$$

In this method each function Ψ_i is expanded in terms of a complete orthonormal set of functions. This set of functions, $\{\phi_j\}$ has to be able to generate the space of eigenfunctions $\mathfrak{H}$.

$$\Psi_i = \sum_j a_{ij}\phi_j \tag{3.4}$$

The set of functions we consider are the eigenfunctions of the Hamiltonian of an infinite potential with similar symmetry as the model we are studying. Similar methods have been proposed expressing the solutions as series of periodic functions like sine and cosine [1, 2]. In this case the Hamiltonian is expanded in terms of a set of functions $\psi = \psi_x\psi_y\psi_z$ where $\psi_l = \sin(k_{l_i}l)$, $l = x, y, z$ and $l_i = l_1, l_2, \ldots, l_{n_l}$ creating a Hamiltonian of dimension $n_x n_y n_z$. In the case $n_x = n_y = n_z = n$ the dimension is n^3.

In this chapter, cylindrical symmetric structures are treated and the Hamiltonian is expanded in terms of a set of functions $\psi = \psi_z\psi_{\rho,\phi}$, which are the eigenfunctions of the Hamiltonian of a particle within an infinite barrier cylindrical potential. The components of the expanded Hamiltonian $\hat{H}$ are easier to calculate using this set of functions due to the cylindrical symmetry of the QD.

Calling $\mathfrak{H}^{\infty}$ the space of eigenfunctions of the Hamiltonian $\hat{H}^{\infty}$ described by

$$\hat{H}^{\infty} = \hat{H}^{0} + V^{\infty} \tag{3.5}$$

where the potential V^{∞} is an infinite barrier cylinder of radius R and height L 'larger' than the QD (wavefunctions should be zero at the boundaries of this cylinder) , as it can be seen in Figure 3.2a). The potential V^{∞} is represented in Figure 3.2b) for values of $\rho < R$ and is written as

$$V^{\infty}(\mathbf{r}) = \begin{cases} 0 & \text{inside the cylinder} \\ \infty & \text{outside the cylinder} \end{cases} \tag{3.6}$$

Let the set of functions

$$\mathfrak{B}^{\infty} = \{\Psi^{\infty}_{nlm}\}$$

be called a basis of $\mathfrak{H}^{\infty}$.

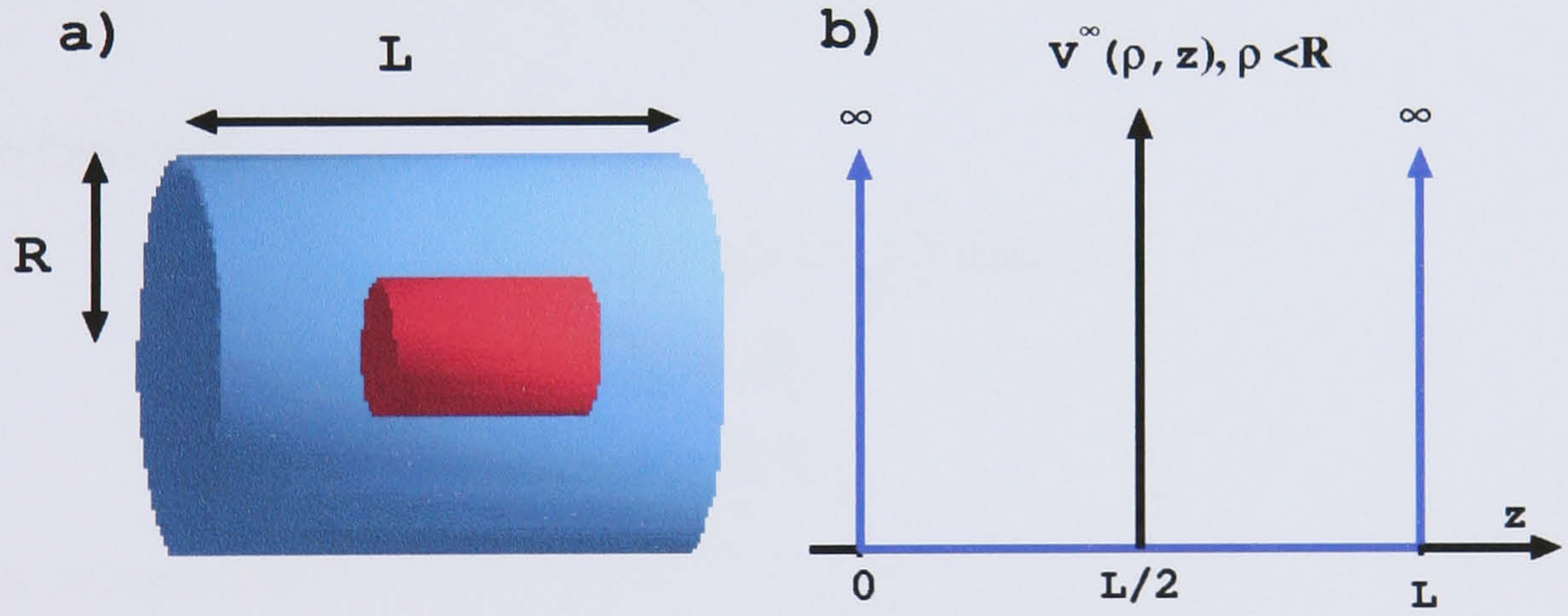

Figure 3.2: **a)**QD inside the infinite potential cylinder. **b)**Representation of the potential V^{∞} for values of $\rho < R$.

In this method we assume that any wavefunction Ψ which belongs to $\mathfrak{H}$ may be expanded in terms of the new basis $\mathfrak{B}^{\infty}$.

$$\Psi = \sum_{nlm} a_{nlm} \Psi^{\infty}_{nlm} \tag{3.7}$$

or, equivalently,

$$|\Psi\rangle = \sum_{nlm} a_{nlm}|nlm\rangle \tag{3.8}$$

where $|nlm\rangle = |\Psi^{\infty}_{nlm}\rangle$.

The solution of the Schrödinger equation for an infinite cylindrical barrier can be obtained analytically as has been explained in Section 2.4.2. The wavefunction can be split in z and (ρ, ϕ) components. Energy levels and wavefunctions solution of $\hat{H}^{\infty}\Psi^{\infty} = E^{\infty}\Psi^{\infty}$ are given by:

$$E^{\infty}_{nlm} = \frac{\hbar^2}{2m^*}(k_n^2 + k_{lm}^2) \tag{3.9}$$

$$\Psi^{\infty}_{nlm} = \psi^{\infty}_n(z)\psi^{\infty}_{lm}(\rho)\frac{e^{il\phi}}{\sqrt{2\pi}} \tag{3.10}$$

Expressing the wavefunction components as:

- z component

$$\psi^{\infty}_n(z) = \sqrt{\tfrac{2}{L}}\sin(k_n z)$$
$$k_n = \tfrac{\pi n}{L} \tag{3.11}$$
$$n = 1, 2, ...$$

- ρ, ϕ component

$$\psi^{\infty}_{lm}(\rho, \phi) = \chi^{\infty}_{lm}(\rho)\frac{e^{il\phi}}{\sqrt{2\pi}} \tag{3.12}$$

where

$$\chi^{\infty}_{lm}(\rho) = A_{lm}J_l(k_{lm}\rho) \tag{3.13}$$

$$k_{lm} = x_{lm}/R$$

and

$$(A_{lm})^{-2} = \begin{cases} \frac{a^2}{8}\big(J_{l-1}(x_{lm}) - J_{l+1}(x_{lm})\big)^2 & l \neq 0 \\ \big[-J_1(x_{lm})\big]^2\frac{a^2}{2} & l = 0 \end{cases} \tag{3.14}$$

$l = 0, 1, 2, ...$

$m = 1, 2, 3...$

where J_l is the Bessel function or order l and x_{lm} is its m-th zero.

Now we expand the Hamiltonian $\hat{H}$ in terms of the basis of functions $\mathfrak{B}^\infty = \{|nlm\rangle\}$, which may be written as:

$$\hat{H}^{\mathfrak{B}^\infty} = \sum_{\substack{nlm \\ n'l'm'}} |n'l'm'\rangle(\hat{H}^0 + V)\langle nlm|$$

Adding a null term $V^\infty - V^\infty$ to the Hamiltonian leads to

$$\begin{aligned}
\hat{H}^{\mathfrak{B}^\infty} &= \sum_{\substack{nlm \\ n'l'm'}} |n'l'm'\rangle(\hat{H}^0 + V + V^\infty - V^\infty)\langle nlm| && (3.15)\\
&= \sum_{\substack{nlm \\ n'l'm'}} \Big[|n'l'm'\rangle(\hat{H}^0 + V^\infty)\langle nlm| + |n'l'm'\rangle(V - V^\infty)\langle nlm|\Big] && (3.16)\\
&= \sum_{nlm} |nlm\rangle E^\infty_{nlm}\langle nlm| + \sum_{\substack{nlm \\ n',l',m'}} |n'l'm'\rangle M_{nn'll'mm'}\langle nlm| && (3.17)
\end{aligned}$$

where $M_{nn'll'mm'} = \langle nlm|(V - V^\infty)|n'l'm'\rangle$ and may be obtained solving the integral

$$M_{nn'll'mm'} = \iiint_{\text{cylinder}} [\Psi^\infty_{nlm}]^* \Psi^\infty_{n'l'm'}(V - V^\infty)\mathrm{d}\mathbf{r} \qquad (3.18)$$

over the infinite potential barrier cylinder.

Taking into account that $V^\infty = 0$ within the cylinder leads to

$$M_{nn'll'mm'} = \iiint_{\text{cylinder}} [\Psi^\infty_{nlm}]^* \Psi^\infty_{n'l'm'} V \mathrm{d}\mathbf{r} \qquad (3.19)$$

Substituting Ψ^∞_{nlm} and $\Psi^\infty_{n'l'm'}$, Equation 3.19 may be written as

$$\begin{aligned}
M_{nn'll'mm'} &= \iint_{\text{cylinder}} \rho[\psi^\infty_n \chi^\infty_{lm}]^* V \psi^\infty_{n'} \chi^\infty_{l'm'} \mathrm{d}z\mathrm{d}\rho \int_0^{2\pi} \frac{\mathrm{e}^{\mathrm{i}(l'-l)\phi}}{2\pi}\mathrm{d}\phi && (3.20)\\
&= \delta_{ll'} \iint_{\text{cylinder}} \rho[\psi^\infty_n \chi^\infty_{lm}]^* V \psi^\infty_{n'} \chi^\infty_{l'm'} \mathrm{d}z\mathrm{d}\rho && (3.21)
\end{aligned}$$

Therefore element $M_{nn'll'mm'}$ is nonzero when $l = l'$. Taking into account that ψ_n^∞ and χ_{lm}^∞ are real functions and suppressing the index l', the last equation may be written as

$$\langle nlm|(V - V^\infty)|n'lm'\rangle \equiv M_{nn'lmm'} = \iint_{\text{cylinder}} \rho\psi_n^\infty \chi_{lm}^\infty V \psi_{n'}^\infty \chi_{l'm'}^\infty \mathrm{d}z\mathrm{d}\rho \tag{3.22}$$

therefore

$$\langle nlm|(V - V^\infty)|n'lm'\rangle = \langle n'lm'|(V - V^\infty)|nlm\rangle \tag{3.23}$$

Substituting $M_{nn'lmm'}$ into Equation 3.17 leads to

$$\hat{H} = \sum_{nlm} |nlm\rangle E_{nlm}^\infty \langle nlm| + \sum_{\substack{nlm \\ n'm'}} |n'lm'\rangle M_{nn'lmm'} \langle nlm| \tag{3.24}$$

and hence we can say that $\hat{H}$ is a symmetric matrix. With this representation, the Hamiltonian is written as a block matrix, where each block has the same quantum number l.

$$\hat{H}^{\mathfrak{B}^\infty} = \begin{pmatrix} H_{l=0} & 0 & 0 & \dots \\ 0 & H_{l=1} & 0 & \dots \\ 0 & 0 & H_{l=2} & \dots \\ \vdots & \vdots & \vdots & \ddots \end{pmatrix} \tag{3.25}$$

The eigenvalues may be obtained diagonalasing this matrix block by block, giving our model energy levels $E_0, E_1, \dots$.

$$\hat{H}^D = \begin{pmatrix} E_0 & 0 & 0 & \dots \\ 0 & E_1 & 0 & \dots \\ 0 & 0 & E_2 & \dots \\ \vdots & \vdots & \vdots & \ddots \end{pmatrix} \tag{3.26}$$

Due to the fact the matrix $\hat{H}^{\mathfrak{B}^\infty}$ is symmetric, all the diagonal elements in the diagonalised Hamiltonian $\hat{H}^D$ have to be real, but we only consider energies below the potential barrier, $E_i < V_0$, which correspond to confined states.

We have approximated the energy levels of a cylindrically symmetric QD expanding the Hamiltonian in terms of $\mathfrak{B}^{\infty} = \{\Psi^{\infty}_{nlm}\}$, which is the basis of space of functions $\mathfrak{H}^{\infty}$ and whose dimension is infinite. However realistically we must use a finite set of functions

$$\mathfrak{F} = \{|nlm\rangle\}^{N_n, N_l - 1, N_m}_{n,l,m=1,0,1} \tag{3.27}$$

and write the Hamiltonian as

$$\hat{H}^{\mathfrak{F}} = \sum_{nlm}^{N_n N_{l-1} N_m} |nlm\rangle E^{\infty}_{nlm} \langle nlm| + \sum_{\substack{nlm \\ n'm'}}^{N_n N_{l-1} N_m} |n'lm'\rangle M_{nn'lmm'} \langle nlm| \tag{3.28}$$

where $n = 1, 2, ..., N_n$, $l = 0, 2, ..., N_{l-1}$ and $m = 1, 2, ..., N_m$. Later in this chapter we study examples of structures where this technique is applied and we determine the number of elements in the expansion, $N = N_n N_l N_m$, which gives sufficiently accurate results.

3.2.2 Matrix M

In this section we calculate the elements of the matrix M given by:

$$M_{nn'lmm'} = \iiint_{\text{cylinder}} [\Psi^{\infty}_{nlm}]^* \Psi^{\infty}_{n'lm'} V \, \mathrm{d}\mathbf{r} \tag{3.29}$$

Adding the term $V_0 - V_0$ to the potential, the last equation may be written as

$$M_{nn'lmm'} = \iiint_{\text{cylinder}} [\Psi^{\infty}_{nlm}]^* \Psi^{\infty}_{n'lm'} V' \mathrm{d}\mathbf{r} + V_0 \iiint_{\text{cylinder}} [\Psi^{\infty}_{nlm}]^* \Psi^{\infty}_{n'lm'} \mathrm{d}\mathbf{r} \tag{3.30}$$

where $V'(\mathbf{r}) = V(\mathbf{r}) - V_0$.

As may be seen in Figure 3.3, the value of V' within the limits of the cylinder is zero outside the QD and $-V_0$ inside it, therefore the limits of the first term in

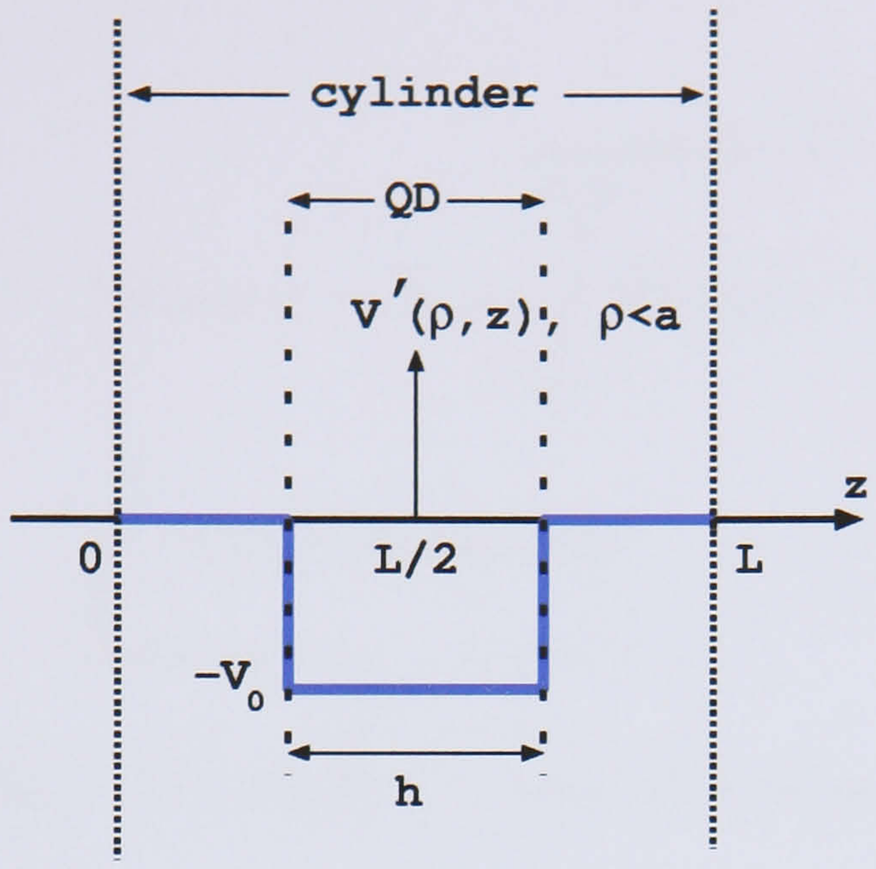

Figure 3.3: Potential $V'(\rho, z) = V(\rho, z) - V_0$ for $\rho < a$.

Equation 3.30 are given by the structure of the QD. The second term is zero unless $nlm = n'lm'$. Therefore Equation 3.30 may be written as

$$M_{nn'lmm'} = V_0 \left[\delta_{nn'}\delta_{mm'} - \iiint_{\mathrm{QD}} [\Psi^{\infty}_{nlm}]^* \Psi^{\infty}_{n'lm'} \mathrm{d}\mathbf{r} \right] \tag{3.31}$$

Substituting the expression of Ψ^{∞}_{nlm} in cylindrical coordinates from Equation 3.10

$$\Psi^{\infty}_{nlm} = \sqrt{\frac{2}{L}} \sin(k_n z) A_{lm} J_l(k_{lm}\rho) \frac{\mathrm{e}^{il\phi}}{\sqrt{2\pi}} \tag{3.32}$$

and denoting

$$\delta_{nn'mm'} = \delta_{nn'}\delta_{mm'}$$

leads to

$$M_{nn'lmm'} = V_0\delta_{nn'mm'} - A_{lmm'}\overbrace{\int_{\frac{L-h}{2}}^{\frac{L+h}{2}} \mathrm{d}z \sin(k_n z)\sin(k_{n'} z)}^{I_z} \times \underbrace{\int_0^a J_l(k_{lm'}\rho)J_l(k_{lm}\rho)\mathrm{d}\rho\rho}_{I_\rho} \tag{3.33}$$

where $A_{lmm'} = \frac{2V_0}{L}A_{lm}A_{lm'}$. The integral I_ρ may be written as

- $k_{lm} \neq k_{l'm}$

$$I_\rho = \frac{a}{k_{lm}^2 - k_{l'm}^2}\left[k_{lm'}J_l(k_{lm}a)J_l'(k_{l'm}a) - k_{lm}J_l(k_{l'm}a)J_l'(k_{lm}a)\right] \tag{3.34}$$

- $k_{lm} = k_{l'm}$

$$I_\rho = \frac{a^2}{2}\left[[J_l'(k_{lm}a)]^2 + (1 - \frac{l^2}{k_{lm}^2 a^2})[J_l(k_{lm}a)]^2\right] \tag{3.35}$$

and the integral I_z may be easily solved applying

$$\sin A \sin B = \frac{1}{2}\left[\cos(A-B) - \cos(A+B)\right] \tag{3.36}$$

Calling $k^\pm = k_n \pm k_{n'}$ and $L^\pm = (L \pm h)/2$, the integral I_z may be written as

- $k_n = k_{n'}$

$$I_z = \int_{L^-}^{L^+} \frac{1-\cos(2k_n z)}{2}\mathrm{d}z \tag{3.37}$$

$$= \frac{2k_n h - \cos(2k_n L^+) + \cos(2k_n L^-)}{4} \tag{3.38}$$

- $k_n \neq k_{n'}$

$$I_z = \int_{L^-}^{L^+} \frac{\left[\cos(k^- z) - \cos(k^+ z)\right.}{2}\mathrm{d}z \tag{3.39}$$

$$= \frac{\sin(k^- L^+) - \sin(k^- L^-)}{2k^-} - \frac{\sin(k^+ L^+) - \sin(k^+ L^-)}{2k^+} \tag{3.40}$$

3.3 Cylindrical symmetry structures

The method explained in the last section takes into account the cylindrical symmetry, thus it may be applied to any structure or cluster of dots which preserve this symmetry.

First we will test and check the basis set by calculating the eigenvalues of a finite barrier potential spherical quantum dot Hamiltonian; an example we have studied in Section 2.3.2 and may be solved analytically.

3.3.1 Spherical Quantum Dot

Spherical Quantum Dots have cylindrical symmetry, and therefore their energy levels can be estimated using the FDH method described in the last section.

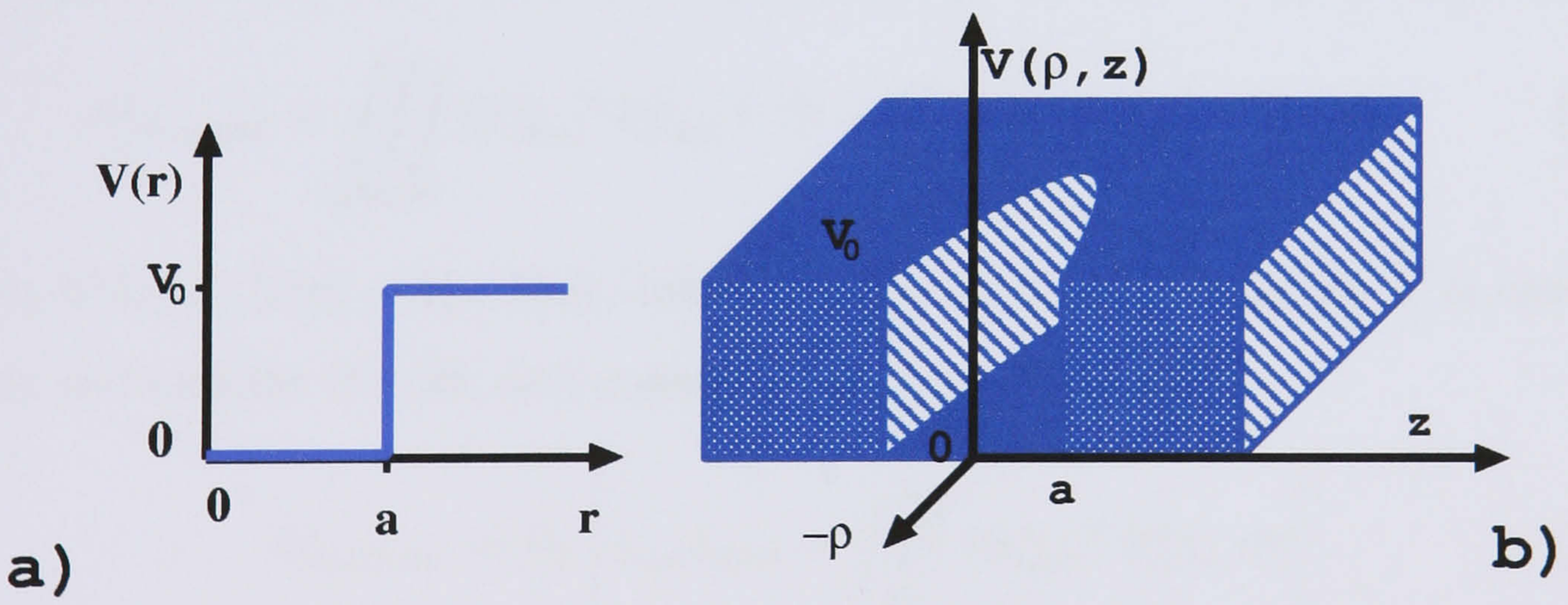

Figure 3.4: Schematic representation of the finite barrier potential of a spherical QD, **a)**in spherical coordinates **b)**in cylindrical coordinates.

Our model consists of a spherical quantum dot of radius a within a finite potential

barrier height. Proceeding as in the previous section, following Equation 3.28, we expand the Hamiltonian in terms of the functions of $\mathfrak{F}$ given by Equation 3.27. The Hamiltonian may be written as:

$$\hat{H}^{\mathfrak{F}} = \sum_{\substack{n,m=1 \\ l=0}}^{\substack{N_n,N_m \\ N_{l-1}}} |nlm\rangle E^{\infty}_{nlm} \langle nlm| + \sum_{\substack{n,m=1 \\ n',m'=1 \\ l=0}}^{\substack{N_n,N_m \\ N_n,N_m \\ N_{l-1}}} |n'lm'\rangle M_{nn'lmm'} \langle nlm| \tag{3.41}$$

where the matrix element $M_{nn'lmm'}$ is given by equation 3.19

$$M_{nn'lmm'} = \iiint_{\text{cylinder}} [\Psi^{\infty}_{nlm}]^* \Psi^{\infty}_{n'lm'} V \mathrm{d}\mathbf{r} \tag{3.42}$$

and potential V is given by

$$V(\mathbf{r}) = \begin{cases} 0 & \text{inside the QD} \\ V_0 & \text{outside the QD} \end{cases} \tag{3.43}$$

Adding a null term $V_0 - V_0$ to the potential V the matrix M may be expressed as:

$$M_{nn'lmm'} = \iiint_{\text{cylinder}} [\Psi^{\infty}_{nlm}]^* \Psi^{\infty}_{n'lm'} V' \mathrm{d}\mathbf{r} + V_0 \iiint_{\text{cylinder}} [\Psi^{\infty}_{nlm}]^* \Psi^{\infty}_{n'lm'} \mathrm{d}\mathbf{r} \tag{3.44}$$

where $V'(\mathbf{r}) = V(\mathbf{r}) - V_0$. Now, taking into account that potential V is constant inside and outside the dot, last equation may be written as

$$M_{nn'lmm'} = V_0 \left[\delta_{nn'}\delta_{mm'} - \iiint_{\text{QD}} [\Psi^{\infty}_{nlm}]^* \Psi^{\infty}_{n'lm'} \mathrm{d}\mathbf{r} \right] \tag{3.45}$$

Substituting the expression of Ψ^{∞}_{nlm} in cylindrical coordinates from Equation 3.10

$$\Psi^{\infty}_{nlm} = \sqrt{\frac{2}{L}} \sin(k_n z) A_{lm} J_l(k_{lm}\rho) \frac{\mathrm{e}^{il\phi}}{\sqrt{2\pi}} \tag{3.46}$$

and denoting

$$\delta_{nn'mm'} = \delta_{nn'}\delta_{mm'}$$

lead to

$$M_{nn'lmm'} = V_0\delta_{nn'mm'} - A_{lmm'}\int_{\frac{L-h}{2}}^{\frac{L+h}{2}} \mathrm{d}z \sin(k_n z)\sin(k_{n'} z) \times \underbrace{\int_0^{f(z)} J_l(k_{lm'}\rho)J_l(k_{lm}\rho)\mathrm{d}\rho\rho}_{I_\rho(z)} \tag{3.47}$$

where $A_{lmm'} = \frac{2V_0}{L}A_{lm}A_{lm'}$ and $f(z)$ describes the the spherical quantum dot surface in cylindrical coordinates as shown in Figure 3.5.

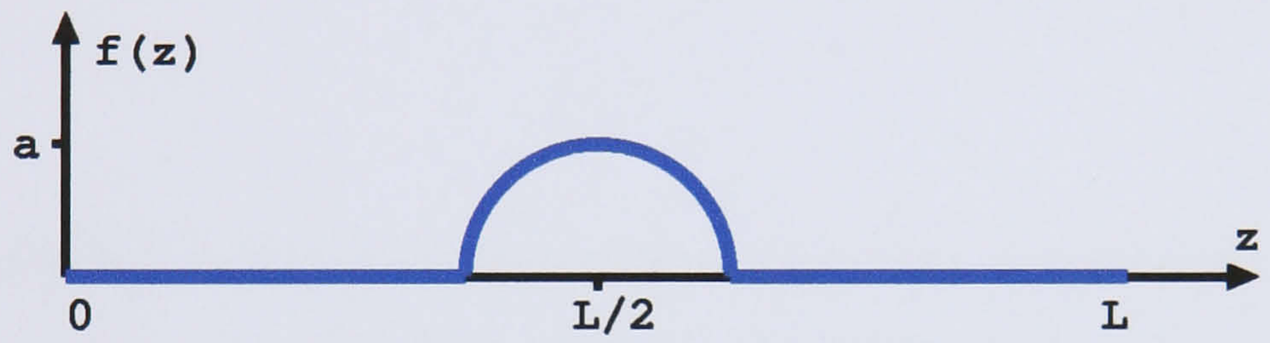

Figure 3.5: Spherical QD surface equation in cylindrical coordinates.

$$f(z) = \begin{cases} \sqrt{a^2 - (z - L/2)^2} & |z - L/2| < a \\ 0 & |z - L/2| \geq a \end{cases} \tag{3.48}$$

Again the integral $I_\rho(z)$ may be solved giving:

- $k_{lm} \neq k_{l'm}$

$$I_\rho(u) = u\frac{k_{lm'}J_l(k_{lm}u)J_l'(k_{l'm}u) - k_{lm}J_l(k_{l'm}u)J_l'(k_{lm}u)}{k_{lm}^2 - k_{l'm}^2} \tag{3.49}$$

- $k_{lm} = k_{l'm}$

$$I_\rho(u) = \frac{u^2}{2}\left[[J_l'(k_{lm}u)]^2 + (1 - \frac{l^2}{k_{lm}^2u^2})[J_l(k_{lm}u)]^2\right] \tag{3.50}$$

where $u = f(z)$.

Therefore matrix M is given by

$$M_{nn'lmm'} = V_0 \delta_{nn'mm'} - A_{lmm'} \int_{\frac{L-h}{2}}^{\frac{L+h}{2}} \mathrm{d}z \sin(k_n z) \sin(k_{n'} z) I_\rho(z) \tag{3.51}$$

and this integral may be solved numerically.

3.3.2 An example of the energy levels calculation. Spherical QD

As we have explained in Section 2.3.2, energy levels of a Spherical QD with finite barrier potentials can be calculated analytically. This allows us to verify the FDH method. In this section we compare the exact ground and first excited state energy level with the ones obtained using the FDH method.

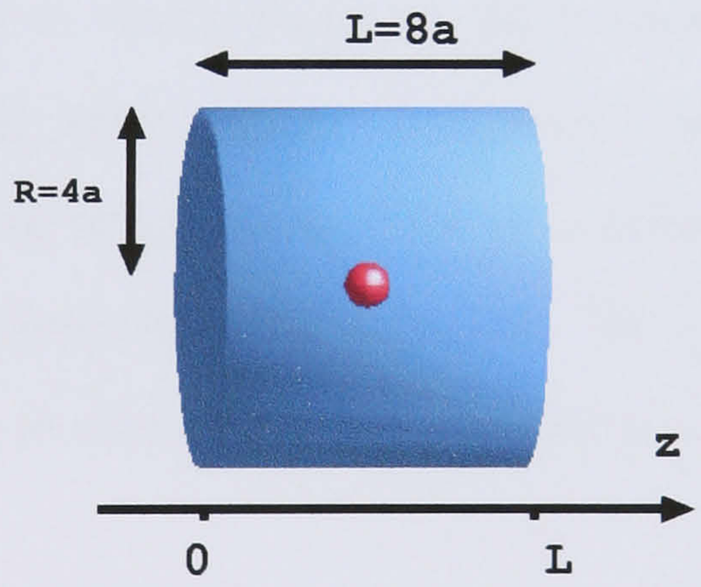

Figure 3.6: Spherical QD within an infinite barrier potential cylinder.

Our model consists in a spherical QD of radius $a = 3 - 9$ nm. The QD is composed of InAs and the surrounding material is GaAs. The potential barrier depth is $V_0 = 1$

eV and $m = 0.023m_0$ is the electron effective mass. In order to make a qualitative study of the method we have taken those parameters from [3] for self-assembled quantum dots. The radius of the infinite cylinder is $R = 4a$ and the height $L = 8a$ as can be seen in Figure 3.6.

In this model we expand the Hamiltonian in terms of the basis $\mathfrak{B}^{\infty} = \{\Psi^{\infty}_{nlm}\}$, but only taking a finite number of functions, i.e. $n = 1, 2, ..., N_n$, $l = 0, 1, ..., N_l - 1$ and $m = 1, 2, ..., N_m$. If $\mathfrak{F} = \{\mathfrak{F}_l\}_{l=0,...,N_l-1}$ is this finite set of functions, where each $\mathfrak{F}_l = \{\Psi^{\infty}_{nlm}\}_{n=1,...,N_n, m=1,...,N_m}$ is a subset of functions, the Hamiltonian is given by

$$\hat{H}^{\mathfrak{F}} = \sum_{\substack{n,m=1 \\ l=0}}^{\substack{N_n,N_m \\ N_{l-1}}} |nlm\rangle E^{\infty}_{nlm} \langle nlm| + \sum_{\substack{n,m=1 \\ n',m'=1 \\ l=0}}^{\substack{N_n,N_m \\ N_n,N_m \\ N_{l-1}}} |n'lm'\rangle M_{nn'lmm'} \langle nlm| \tag{3.52}$$

This Hamiltonian is a matrix of dimension $N = N_n N_l N_m$ and for this case we take $N_n = 50$, $N_l = 1$ and $N_m = 25$.

The Hamiltonian is l-number block diagonal, as expressed in Equation 3.25, thus blocks do not interfere with each other. Therefore the addition of more l-blocks in the Hamiltonian may give more eigenvalues or increase the degeneracy of them, but does not make the eigenvalues more accurate. We discuss later the inclusion of more l-blocks and why we assume that $H_{l=0}$ is the block which makes the results more accurate.

We express the Hamiltonian eigenfunctions as series of functions of $\mathfrak{F}$. These functions, $\Psi^{\infty}_{nlm} = \psi^{\infty}_{n}(z)\psi^{\infty}_{lm}(\rho, \phi)$, may be split in z and (ρ, ϕ) components. Therefore, we have a finite set of functions in z-direction, $\psi^{\infty}_{n}(z)$, and another finite set of functions in the plane (ρ, ϕ), $\psi^{\infty}_{lm}(\rho, \phi)$ to generate the spatial function Ψ in cylindrical coordinates, where $n = 1, 2, ..., N_n = 50$ and $m = 1, ..., N_m = 25$.

For a given l, we define a finite set of functions $\mathfrak{F}_l = \{|k, l\rangle\}_{k=1,...,N}$, where $N = N_l N_m$

and

$$|k = (n-1)N_m + m, l\rangle = |nlm\rangle \tag{3.53}$$

or equivalently

$$\chi_{kl} = \Psi^{\infty}_{nlm} \tag{3.54}$$

In order to expand the Hamiltonian we need N_l sets of functions. In our case we only need one, but for l-blocks of $l > 1$ the process is the same. Then a l-block Hamiltonian, $\hat{H}_l$, expanded in terms of $\mathfrak{F}_l$ may be written as

$$\hat{H}_l^{\mathfrak{F}_l} = \sum_{ij=1}^{N} |il\rangle a_{ijl} \langle jl| \tag{3.55}$$

or as a matrix of dimension $N = 50 \times 25 = 1250$.

$$\hat{H}_l^{\mathfrak{F}_l} = \begin{pmatrix} a_{11}^l & a_{12}^l & \dots & a_{1N}^l \\ a_{21}^l & a_{22}^l & \dots & a_{2N}^l \\ \vdots & \vdots & \ddots & \vdots \\ a_{N1}^l & a_{N2}^l & \dots & a_{NN}^l \end{pmatrix} \tag{3.56}$$

In our case $N_l = 1$ and only $l = 0$ is taking into account, thus $\mathfrak{F} = \mathfrak{F}_0$ and the Hamiltonian is composed of one l-block Hamiltonian, $\hat{H}^{\mathfrak{F}} = \hat{H}_{l=0}^{\mathfrak{F}_0}$. Therefore the Hamiltonian expanded in terms of function of $\mathfrak{F}$ is given by

$$\hat{H}^{\mathfrak{F}} = \hat{H}_0^{\mathfrak{F}_0} = \begin{pmatrix} a_{11}^0 & a_{12}^0 & \dots & a_{1N}^0 \\ a_{21}^0 & a_{22}^0 & \dots & a_{2N}^0 \\ \vdots & \vdots & \ddots & \vdots \\ a_{N1}^0 & a_{N2}^0 & \dots & a_{NN}^0 \end{pmatrix} \tag{3.57}$$

where elements a_{ij}^0 are obtained from Equation 3.41.

We want to obtain the eigenvalues and eigenfunctions of matrix $\hat{H}^{\mathfrak{F}}$ which obey

$$\hat{H}^{\mathfrak{F}}\Psi_i = E_i\Psi_i \tag{3.58}$$

where E_i is an energy level, Ψ_i is its associated wavefunction and $i = 0, ..., N-1$. The eigenfunctions are given by

$$\Psi_i = \sum_{j=1}^{N} c_{ij}|j0\rangle \tag{3.59}$$

or changing notation $|kl> \rightarrow |nlm>$ where $k = N_m(n-1)+m$

$$\Psi_i = \sum_{n,m=1}^{N_n,N_m} c_{i(N_m(n-1)+m)}|n0m\rangle \tag{3.60}$$

In order to obtain the eigenvalues and eigenfunctions of the Hamiltonian, we use NAG-library mathematical software, where the time taken by the routine is approximately proportional to N^3[4].

Applying these numerical libraries to the Hamiltonian of a spherical QD of radius $a = 9$ nm, we obtain the eigenvalues, E_i, and the coefficients c_{ij} for $i = 0, N-1, j = 1, N$. Only energy values below the potential barrier, $E_i < V_0$, are the allowed confined energies.

We compare the results obtained from the FDH method with the analytical solution calculated in Section 2.3.2. Figure 3.7 shows the two first energy levels against QD's radius. The error is the order of 0.01 %. Therefore the set of functions we have taken is good enough to estimate the energy levels.

Assuming that the energies are sorted increasingly, the eigenfunction associated with the lowest energy, E_0, is given by:

$$\Psi_0 = \sum_{j=1}^{N} c_{0j}|j0\rangle \tag{3.61}$$

or

$$\Psi_0 = \sum_{n=m=1}^{N_n,N_m} c_{0((n-1)N_n+m)}\Psi^{\infty}_{n0m} \tag{3.62}$$

Functions Ψ^{∞}_{nlm} are given by Equation 3.10 in cylindrical coordinates.

$$\Psi^{\infty}_{nlm} = \psi^{\infty}_{n}(z)\psi^{\infty}_{lm}(\rho)\frac{e^{il\phi}}{\sqrt{2\pi}} \tag{3.63}$$

Substituting these functions into Equation 3.62 gives the ground state wavefunction in cylindrical coordinates, which can be seen in Figure 3.8.

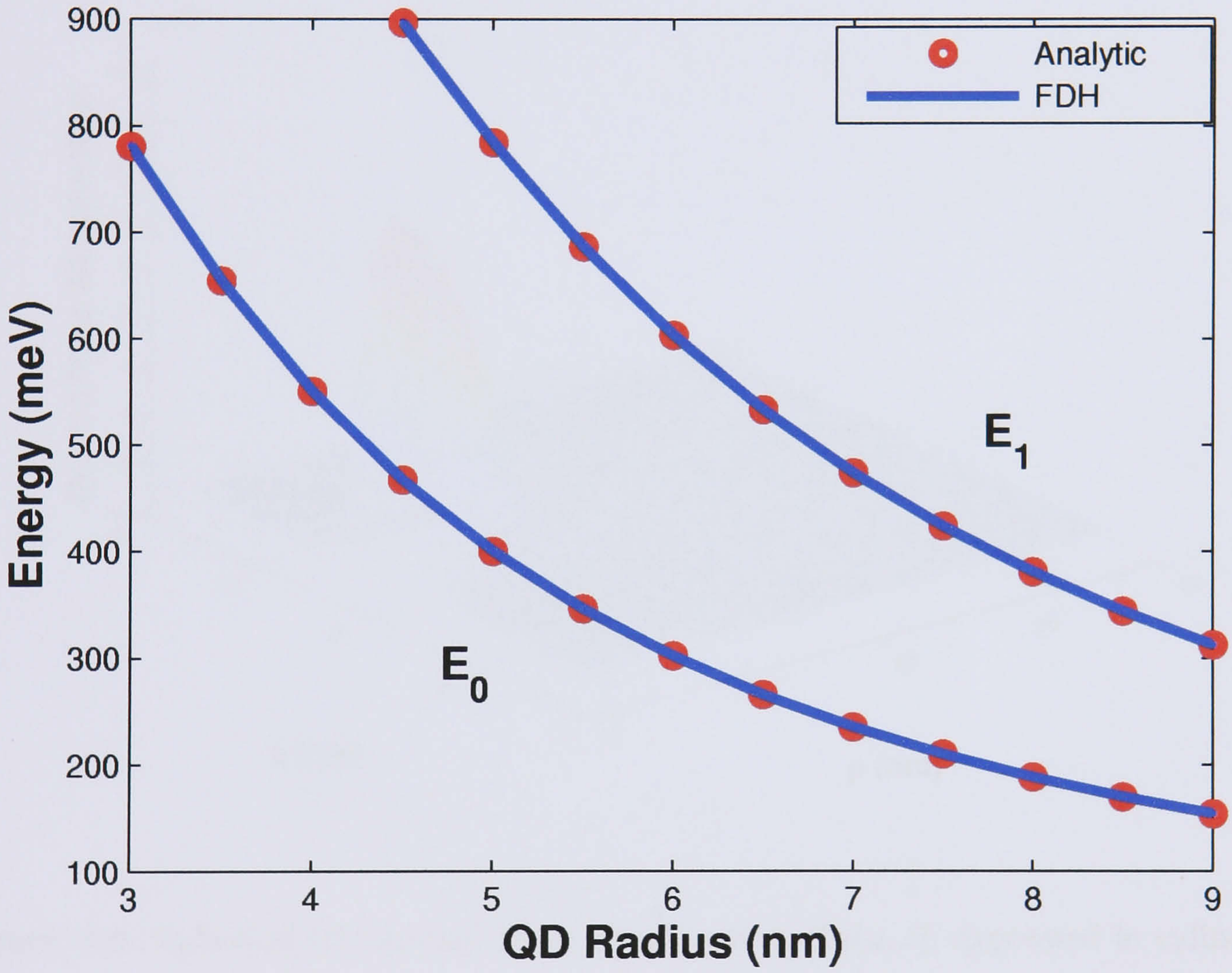

Figure 3.7: Two first energy levels of a Spherical QD calculated analytically and using the FDH method versus QD radius.

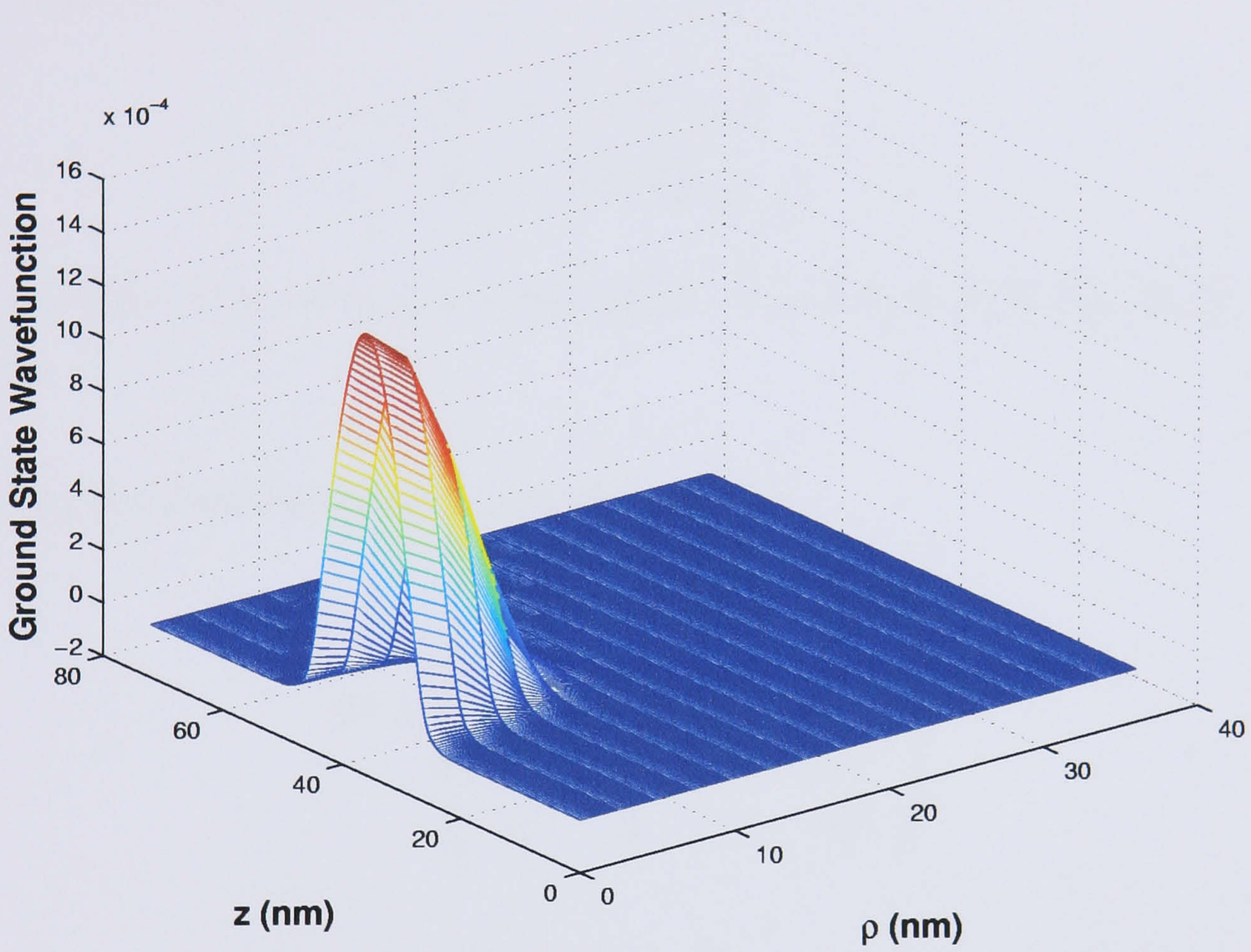

Figure 3.8: Spherical QD ground state wavefunction, $\Psi_0(\rho, z)$, expressed in cylindrical coordinates.

Choosing the set of functions $\mathfrak{F}$

We have estimated the ground state energy expanding the Hamiltonian in terms of $\mathfrak{F} = \mathfrak{F}_0$, where only functions with $l = 0$ have been taken into account. Now, in order to demonstrate that the accuracy of the solution does not change including more subsets of functions $\mathfrak{F}_l$, we take

$$\mathfrak{F} = \{\mathfrak{F}_l\}_{l=0,1,2,3} \tag{3.64}$$

$$\mathfrak{F}_l = \{|k,l\rangle\}_{k=1,\ldots,N} \tag{3.65}$$

where $|k = (n-1)N_m + m, l\rangle = |nlm\rangle$ and $l = 0,1,2,3$, $N = N_n N_m$, $N_n = 50$ and $N_m = 25$.

Expanding the Hamiltonian in terms of $\mathfrak{F}$ leads to

$$\hat{H}^{\mathfrak{F}} = \begin{pmatrix} \hat{H}_0^{\mathfrak{F}_0} & 0 & 0 & 0 \\ 0 & \hat{H}_1^{\mathfrak{F}_1} & 0 & 0 \\ 0 & 0 & \hat{H}_1^{\mathfrak{F}_2} & 0 \\ 0 & 0 & 0 & \hat{H}_2^{\mathfrak{F}_3} \end{pmatrix} \tag{3.66}$$

Proceeding as described in the previous section we calculate the eigenvalues and eigenfunctions of each block $\hat{H}_l^{\mathfrak{F}_l}$. In Table 3.1 we compare the lowest eigenvalues of each block with the energies calculated analytically.

Table 3.1 shows that the eigenvalues of the matrix $\hat{H}_0^{\mathfrak{F}_0}$ ($l = 0$) of dimension $N = 1250$ reproduce with good accuracy all the energies calculated analytically. Obtaining the eigenvalues of other l-blocks, $l = 1,2,3$, gives accurate energies but only for energies where the spherical m-number is non-zero, like E_{11}, E_{12} and E_{13}, as seen in Table 3.1. The reason for this is that the analytical solution wavefunctions for $m = 0$, are non-zero at the origin $R_{n,m=0}(0) \neq 0$, as can be seen in Figure 3.9. Therefore for $l \neq 0$, the set of functions $\{\mathfrak{F}_l\}_{l\neq 0}$, cannot solely be used as a

	Energy (eV)				
E_{nm}	Analytically				
	E_{10}	E_{11}	E_{12}	E_{20}	E_{13}
	0.153440	0.311839	0.508806	0.596511	0.739963
50×50	FDH				
$l = 0$	0.153484	0.311963	0.508968	0.596678	0.740050
$l = 1$	0.311905	0.508993	0.740335	0.874207	0.999456
$l = 2$	0.508891	0.740157	0.999349	1.036726	1.046420
$l = 3$	0.740069	0.999162	1.055364	1.064734	1.080549
25×50					
$l = 0$	0.153558	0.312015	0.509145	0.596969	0.740335
$l = 1$	0.312106	0.509148	0.740563	0.874724	0.999820
$l = 2$	0.509248	0.740446	0.999672	1.036733	1.046420
$l = 3$	0.740560	0.999600	1.055364	1.064735	1.080550
12×24					
$l = 0$	0.154517	0.313882	0.513045	0.601627	0.748319
$l = 1$	0.314182	0.511881	0.746244	0.882448	1.009234
$l = 2$	0.512249	0.744700	1.005995	1.036801	1.046421
$l = 3$	0.745881	1.005966	1.055365	1.064742	1.080551

Table 3.1: Energies levels of an electron of mass $m = 0.023m_0$ within a finite potential barrier ($V_0 = 1$ eV) spherical QD of radius $a = 9$ nm calculated analytically and using the FDH method. Analytical results E_{nm} are ordered increasingly. The FDH method has been applied to each Hamiltonian block, $H_l^{\mathfrak{F}l}$, for $l = 0, 1, 2, 3$ and with different matrix dimensions $N = 2500$, $N = 1250$ and $N = 300$.

valid basis to calculate the system wavefunctions which are not zero at the origin ($\Psi(0) \neq 0$) because all the functions of the set vanish at the origin, $\Psi^{\infty}_{nl\neq 0m}(0) = 0$.

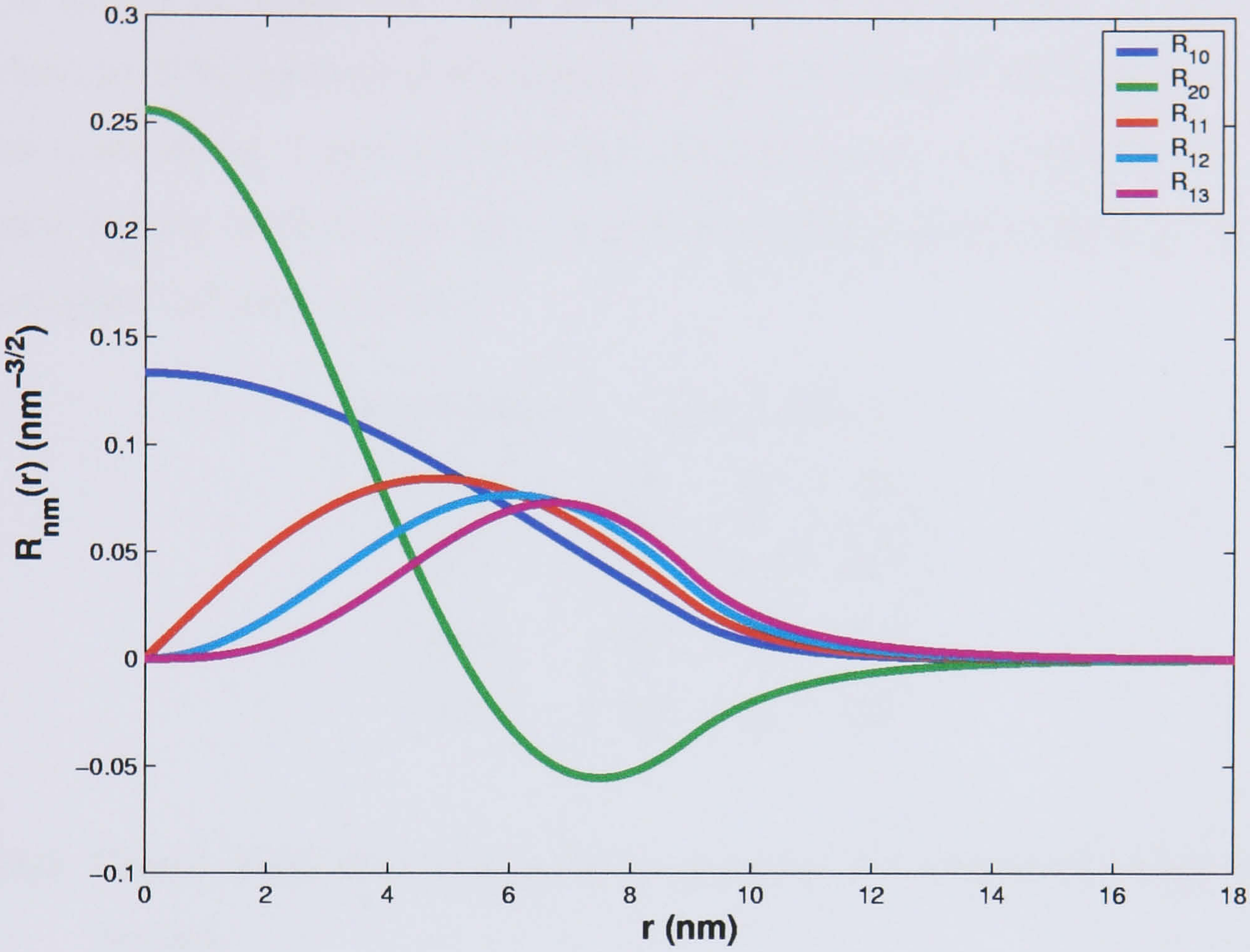

Figure 3.9: Spherical radial wavefunctions, $R_{nm}(r)$, of the five lowest energy levels of a spherical QD of radius $a = 9$ nm obtained analytically.

In order to obtain the eigenvalues of the Hamiltonian, the set of functions $\{\mathfrak{F}_l\}_{l>0}$ only contribute to increase the degeneracy of the energies obtained using $\mathfrak{F}_0$ and not increasing the accuracy due to the fact that functions with different l number do not interfere with each other within the Hamiltonian $\hat{H}^{\mathfrak{F}}$. Therefore choosing $\mathfrak{F} = \mathfrak{F}_0$ gives the method a good accuracy in order to calculate the energy levels.

We also calculate the eigenvalues of different Hamiltonian matrix sizes. Increasing the dimension of the Hamiltonian makes the result more accurate, but also requires more computational time. Therefore we want to demonstrate that the dimension

we have taken ($N = 1250$) gives accurate energies without using big matrixes. We calculate the relative energy error of the ground state and two first excited states, which is shown in Table 3.2. The relative error in all the cases is very small. Using fortran NAG-numerical libraries on a *SUNW,UltraSPARC-III+, 900 MHz* machine takes about 2 minutes to obtain the eigenvalues and eigenfunctions of a symmetric matrix of dimension 1250, which we consider gives enough accuracy for the computational time required.

Hamiltonian	**Error (%)**		
Dimension	E_0	E_1	E_2
2500	0.02	0.04	0.03
1250	0.07	0.06	0.07
300	0.7	0.7	0.8

Table 3.2: Energy levels error of a spherical quantum dot calculated using the FDH method.

3.3.3 Spherical capped Colloidal QD

The energy levels and wavefunctions of spherical capped colloidal QD's have been calculated previously in Chapter 2. Again we study the FDH method by checking against an analytic solution in order to study the accuracy of the method.

A capped core/shell colloidal QD of radius a_1 and shell thickness t_s is 'inserted' within an infinite barrier cylinder of radius $R = 4a_1$ and height $L = 8a_1$. As before, following Equation 3.28, we expand the Hamiltonian in terms of the functions of

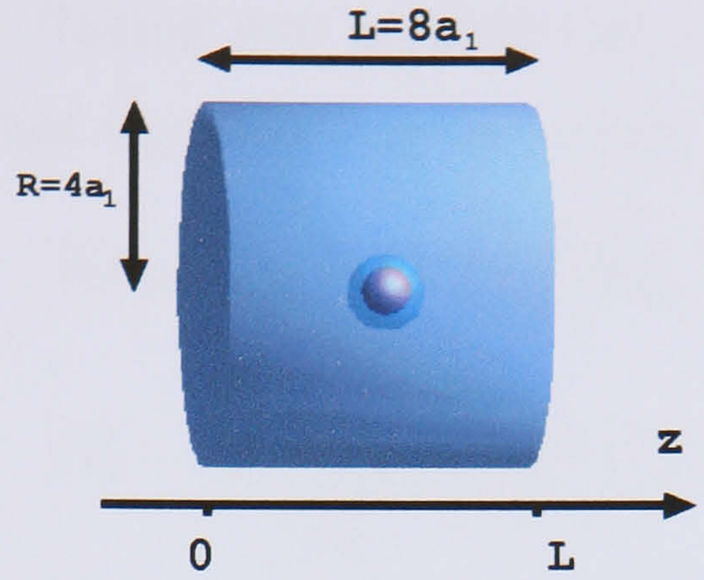

Figure 3.10: Capped Colloidal QD of core radius a_1 and shell thickness t_s within an infinite barrier potential cylinder of radius $R = 4a_1$ and height $L = 8a_1$.

$\mathfrak{F} = \{|nlm\}$.

$$\hat{H}^{\mathfrak{F}} = \sum_{nlm} |nlm\rangle E^{\infty}_{nlm} \langle nlm| + \sum_{\substack{nlm \\ n'm'}} |n'lm'\rangle M_{nn'lmm'} \langle nlm| \tag{3.67}$$

where $n, n' = 1, \ldots, N_n; m, m' = 1, \ldots, N_m; l = 0, \ldots, N_l - 1$ and the matrix element $M_{nn'lmm'}$ is given by Equation 3.19

$$M_{nn'lmm'} = \iiint_{\text{cylinder}} [\Psi^{\infty}_{nlm}]^* \Psi^{\infty}_{n'lm'} V \mathrm{d}\mathbf{r} \tag{3.68}$$

where the potential V is given by

$$V(\mathbf{r}) = \begin{cases} 0 & \text{inside the core} \\ V_s & \text{inside the shell} \\ V_0 & \text{outside the QD} \end{cases} \tag{3.69}$$

Adding a null term $V_0 - V_0$ to the potential V the matrix M may be expressed as:

$$M_{nn'lmm'} = V_0 \iiint_{\text{cylinder}} [\Psi^{\infty}_{nlm}]^* \Psi^{\infty}_{n'lm'} \mathrm{d}\mathbf{r} + \iiint_{\text{cylinder}} [\Psi^{\infty}_{nlm}]^* \Psi^{\infty}_{n'lm'} V' \mathrm{d}\mathbf{r} \tag{3.70}$$

where $V'(\mathbf{r}) = V(\mathbf{r}) - V_0$. Taking into account that the potential V is constant within all the regions, the last equation may be written as

$$M_{nn'lmm'} = V_0\delta_{nn'}\delta_{mm'} - V_0 \underset{\text{core}}{\iiint} [\Psi^{\infty}_{nlm}]^* \Psi^{\infty}_{n'lm'} \mathrm{d}\mathbf{r} - (V_0 - V_s) \underset{\text{shell}}{\iiint} [\Psi^{\infty}_{nlm}]^* \Psi^{\infty}_{n'lm'} \mathrm{d}\mathbf{r} \tag{3.71}$$

Substituting the expression of Ψ^{∞}_{nlm} in cylindrical coordinates

$$\Psi^{\infty}_{nlm} = \sqrt{\frac{2}{L}} \sin(k_n z) A_{lm} J_l(k_{lm}\rho) \frac{\mathrm{e}^{il\phi}}{\sqrt{2\pi}} \tag{3.72}$$

and denoting

$$\delta_{nn'mm'} = \delta_{nn'}\delta_{mm'}$$

leads to

$$M_{nn'lmm'} = V_0\delta_{nn'mm'} - A_{lmm'} \int_{\frac{L-a_1-2t_s}{2}}^{\frac{L+a_1+2t_s}{2}} \mathrm{d}z \sin(k_n z) \sin(k_{n'} z) \times \left[V_0 \int_0^{f_c(z)} J_l(k_{lm'}\rho) J_l(k_{lm}\rho) \mathrm{d}\rho\rho + V_s \int_{f_c(z)}^{f_s(z)} J_l(k_{lm'}\rho) J_l(k_{lm}\rho) \mathrm{d}\rho\rho \right] \tag{3.73}$$

where $A_{lmm'} = \frac{2}{L} A_{lm} A_{lm'}$ and $f_c(z)(f_s(z))$ describes the surface of the QD core(shell) in cylindrical coordinates, as can be seen in Figure 3.11.

$$f_c(z) = \begin{cases} \sqrt{a_1^2 - (z - L/2)^2} & |z - L/2| < a_1 \\ 0 & |z - L/2| \geq a_1 \end{cases} \tag{3.74}$$

$$f_s(z) = \begin{cases} \sqrt{(a_1 + t_s)^2 - (z - L/2)^2} & a_1 < |z - L/2| < a_1 + t_s \\ 0 & |z - L/2| \geq a_1 + t_s \end{cases} \tag{3.75}$$

The integral

$$I_\rho(u) = \int^{u} J_l(k_{lm'}\rho) J_l(k_{lm}\rho) \mathrm{d}\rho\rho \tag{3.76}$$

again may be solved analytically giving:

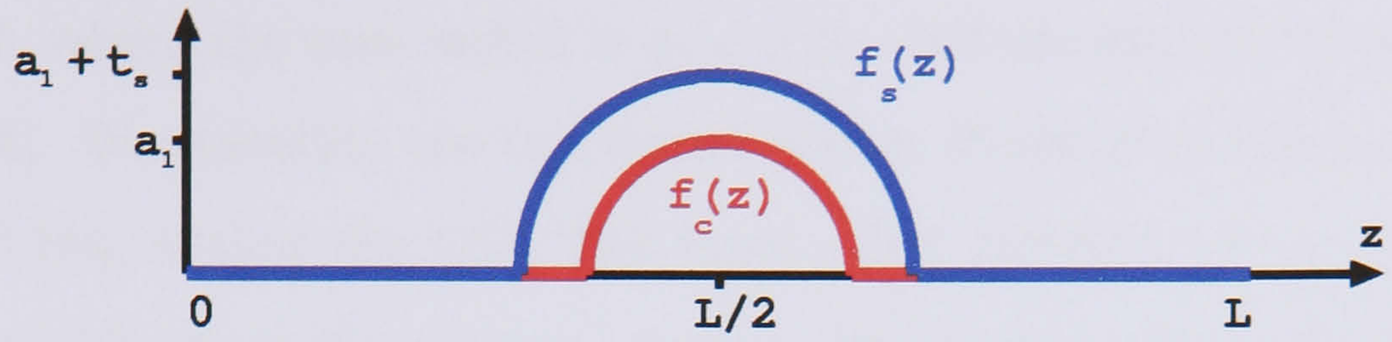

Figure 3.11: Shape of core, $f_c(z)$, and shell, $f_s(z)$, boundaries.

- $k_{lm} \neq k_{l'm}$

$$I_\rho(u) = u\frac{k_{lm'}J_l(k_{lm}u)J_l'(k_{l'm}u) - k_{lm}J_l(k_{l'm}u)J_l'(k_{lm}u)}{k_{lm}^2 - k_{l'm}^2} \tag{3.77}$$

- $k_{lm} = k_{l'm}$

$$I_\rho(u) = \frac{u^2}{2}\left[[J_l'(k_{lm}u)]^2 + (1 - \frac{l^2}{k_{lm}^2u^2})[J_l(k_{lm}u)]^2\right] \tag{3.78}$$

Substituting $I_\rho(u)$ into Equation 3.71 leads to

$$\begin{aligned} M_{nn'lmm'} &= V_0\delta_{nn'mm'} - A_{lmm'}\int_{\frac{L-a_1-2t_s}{2}}^{\frac{L+a_1+2t_s}{2}} \mathrm{d}z\sin(k_nz)\sin(k_{n'}z)\times \\ &\quad \left[V_0I_\rho\big(f_c(z)\big) + V_s\big[I_\rho\big(fs(z)\big) - I_\rho\big(f_c(z)\big)\big]\right] \end{aligned} \tag{3.79}$$

This expression may be calculated numerically.

3.3.4 An example of the energy levels calculation. Spherical capped QD

The colloidal quantum dots most often used to date in fundamental or applied studies are spherical nanocrystals with core sizes that vary between 1.5 and 12 nm in diameter. For this example we consider a core-shell (CdSe/ZnS) spherical

quantum dot, where the core radius is $a_1 = 1.5 - 2.0$ nm and the shell thickness is $t_s = 0.3$ nm[5]. We calculate the two lowest energy levels of an electron of effective mass $m = 0.1m_0$ within the QD. The band offset between the core and shell is $V_s = 0.9$ eV and between the core and surrounding material(liquid) is $V_0 = 3$ eV[6]. The infinite potential cylinder radius and height are $R = 12$ nm and $L = 24$ nm, respectively.

In this model we expand the Hamiltonian in terms of the finite set of functions $\mathfrak{F} = \{|nlm\rangle\}$ where $n = 1, 2, ..., N_n$, $l = 0, 1, ..., N_l - 1$ and $m = 1, 2, ..., N_m$. The dimension of $\mathfrak{F}$ is given by $N = N_n N_l N_m$ and for our case we take $N_n = 50$,$N_l = 1$ and $N_m = 25$, thus $\mathfrak{F} = \mathfrak{F}_0$. Expanding the Hamiltonian using this basis set creates a symmetric matrix of dimension $N = 50 \times 25 = 1250$. In order to diagonalise the Hamiltonian of the system we use NAG-library routines.

We calculate the ground and first state energy levels for different core radii $a_1 = 1.5 - 2$ nm and the results are shown in Figure 3.12. These are compared with the analytical solutions, obtained in Section 2.3.4. It can be seen that energy levels obtained using the FDH method agree very well with the analytical solution.

The ground state wavefunction may be obtained calculating the eigenfunction associated with the lowest energy level. Figure 3.13 shows the ground state wavefunction, $\Psi_0(\rho, z)$, in cylindrical coordinates. This wavefunction vector will be used in order to calculate the electronic structure of coupled colloidal QD's in Section 4.5.3.

We have tested the FDH method against the analytical solution for spherical QD's and capped spherical QD's. In both cases the approximation agrees well with analytical solution, making the FDH method a good candidate for use with other structures with cylindrical symmetry, such as ellipsoidal QD's, as will be studied in Section 3.3.5.

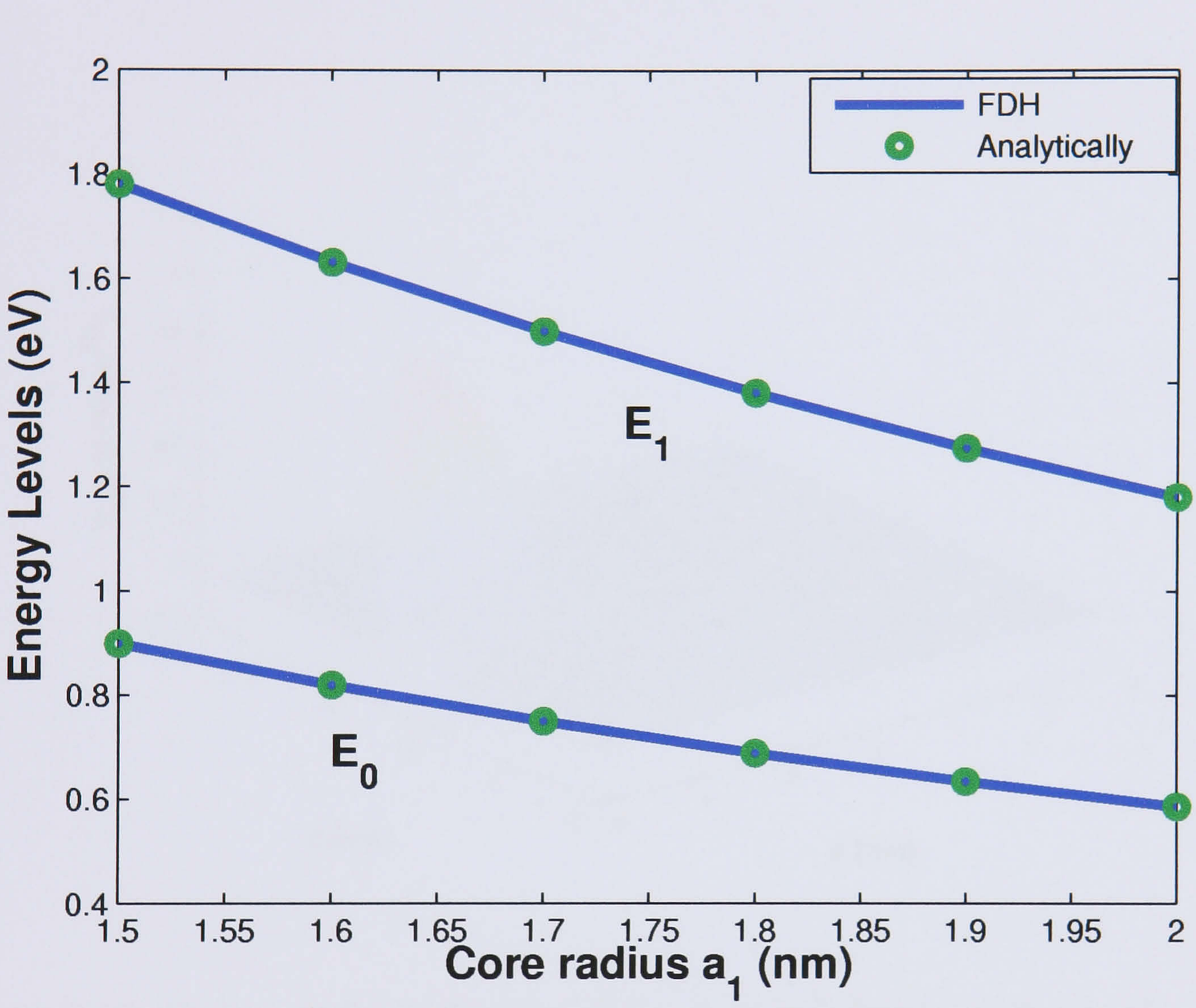

Figure 3.12: Ground and first excited state of an electron within a CdSe/ZnS spherical QD of radius $a_1 = 1.5 - 2.0$ nm. Solid line corresponds to the results obtained using the FDH method and circles lines to the analytical solution.

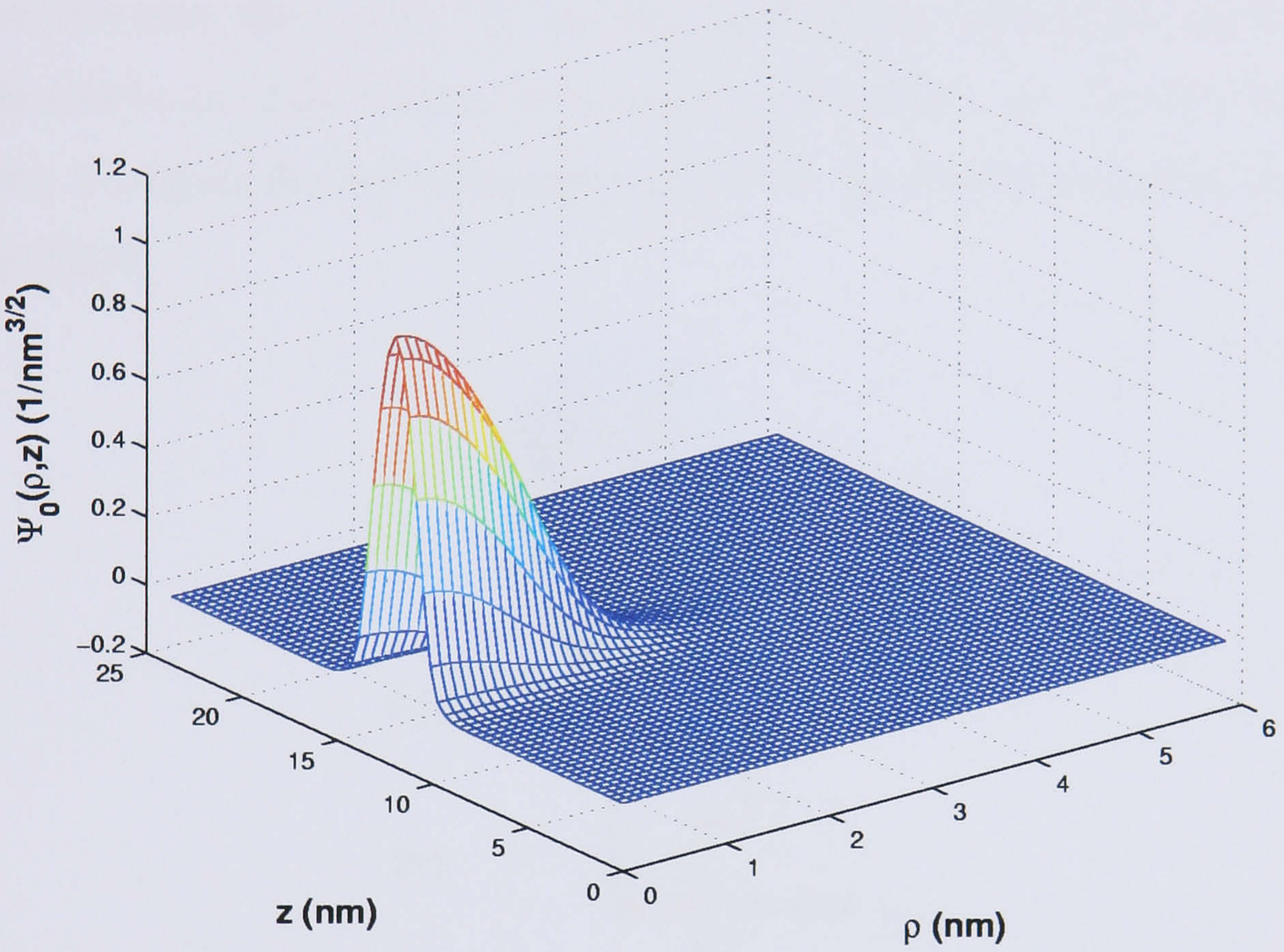

Figure 3.13: Ground state wavefunction, $\Psi_0(\rho, z)$, in cylindrical coordinates of an electron of mass $m = 0.1m_0$ within a capped spherical QD of radius $a_1 = 3$ nm and capping layer thickness $t_s = 0.3$ nm. Energy band offsets are $V_0 = 3$ eV and $V_s = 0.9$ eV[6].

3.3.5 Ellipsoidal Quantum Dot

In last section electronic structure of a CdSe/ZnS type spherical QD was studied. The II-VI semiconductor nanocrystals are well characterised structurally and several studies have shown that CdSe crystallites are elongated along the unique wurtzite axis[7], in our case the z axis. It has also been shown that electronic and optic properties can be strongly dependent on nanocrystal shape, as well as on size[8]. In this section we apply the full diagonalisation of the system Hamiltonian method to ellipsoidal QD's.

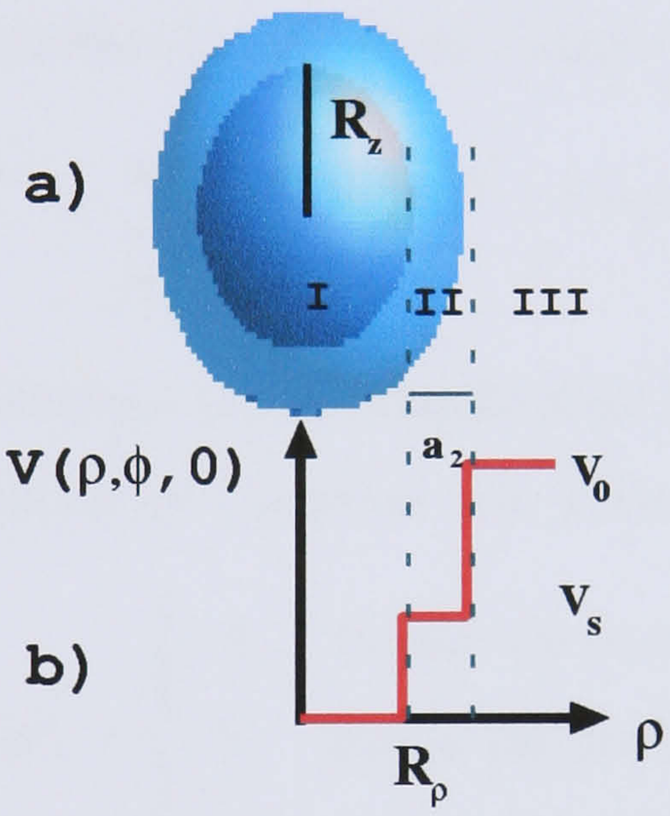

Figure 3.14: **a)**Schematic picture of a core-shell ellipsoidal quantum dot. **b)**Representation of the QD potential in cylindrical coordinates at $z = 0$.

The eigenfunctions of an ellipsoidal QD Hamiltonian, Figure 3.14a), cannot be expressed in spherical coordinates, therefore they must be obtained using other methods. In this section we obtain the energy levels using the full diagonalisation of the

effective mass Hamiltonian $\hat{H}$

$$\hat{H} \equiv -\frac{\hbar^2}{2m^*}\nabla^2 + V = \hat{H}^0 + V \tag{3.80}$$

where V is the band-edge energy described by Figure 3.14b).

$$V(\mathbf{r}) = \begin{cases} 0 & \text{inside the QD core} \\ V_s & \text{inside the QD shell} \\ V_0 & \text{elsewhere} \end{cases} \tag{3.81}$$

As before, we insert our QD within an infinite barrier potential cylinder (see Figure 3.15) and we expand the Hamiltonian in terms of basis $\mathfrak{B}^\infty$ functions.

$$\hat{H}^{\mathfrak{B}^\infty} = \sum_{\substack{nlm \\ n'l'm'}} |n'l'm'\rangle(\hat{H}^0 + V)\langle nlm|$$

where $|nlm\rangle$ are the eigenfunctions of the Hamiltonian of the empty infinite barrier potential cylinder H^∞ described by Equation 3.5. Potential V is given by

$$V(\mathbf{r}) = \begin{cases} 0 & \text{inside the core} \\ V_s & \text{inside the shell} \\ V_0 & \text{outside the QD} \end{cases} \tag{3.82}$$

Proceeding as in Section 3.3.3 for a capped spherical QD, the Hamiltonian $\hat{H}^{\mathfrak{B}^\infty}$ may be written as:

$$\hat{H}^{\mathfrak{B}^\infty} = \sum_{nlm} |nlm\rangle E^\infty_{nlm}\langle nlm| + \sum_{\substack{nlm \\ n'm'}} |n'lm'\rangle M_{nn'lmm'}\langle nlm| \tag{3.83}$$

where the matrix element $M_{nn'lmm'}$ is given by Equation 3.71

$$\begin{aligned} M_{nn'lmm'} &= V_0\delta_{nn'}\delta_{mm'} - V_0 \iiint_{\text{core}} [\Psi^\infty_{nlm}]^* \Psi^\infty_{n'lm'} \mathrm{d}\mathbf{r} - \\ &\quad (V_0 - V_s) \iiint_{\text{shell}} [\Psi^\infty_{nlm}]^* \Psi^\infty_{n'lm'} \mathrm{d}\mathbf{r} \end{aligned} \tag{3.84}$$

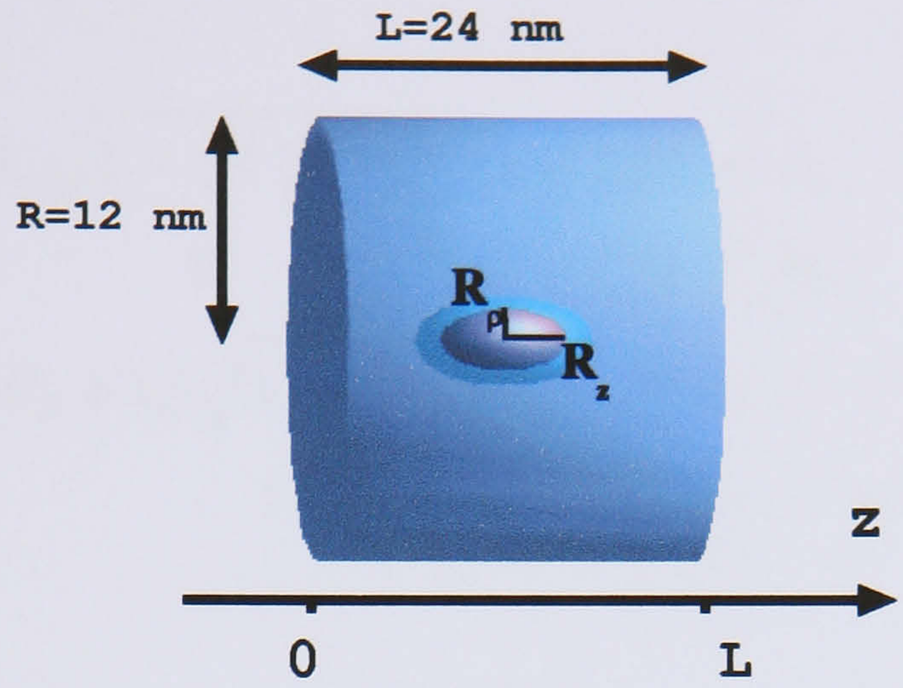

Figure 3.15: Ellipsoidal capped QD inside infinite barrier potential cylinder.

Substituting the expression of Ψ^{∞}_{nlm} in cylindrical coordinates

$$\Psi^{\infty}_{nlm} = \sqrt{\frac{2}{L}} \sin(k_n z) A_{lm} J_l(k_{lm}\rho) \frac{\mathrm{e}^{il\phi}}{\sqrt{2\pi}} \tag{3.85}$$

and denoting

$$\delta_{nn'mm'} = \delta_{nn'}\delta_{mm'}$$

lead to

$$M_{nn'lmm'} = V_0\delta_{nn'mm'} - A_{lmm'} \int_{\frac{L-R_z-2t_s}{2}}^{\frac{L+R_z+2t_s}{2}} \mathrm{d}z \sin(k_n z)\sin(k_{n'} z) \times$$

$$\left[V_0 \int_0^{f_c(z)} J_l(k_{lm'}\rho) J_l(k_{lm}\rho)\mathrm{d}\rho\rho + V_s \int_{f_c(z)}^{f_s(z)} J_l(k_{lm'}\rho) J_l(k_{lm}\rho)\mathrm{d}\rho\rho \right] \tag{3.86}$$

where $A_{lmm'} = \frac{2}{L} A_{lm} A_{lm'}$ is the normalisation constant and $f_c(z)(f_s(z))$ describes the surface of the QD core(shell) in cylindrical coordinates, as can be seen in Figure

3.16.

$$f_c(z) = \begin{cases} R_\rho\sqrt{1-\left(\frac{(z-L/2)}{R_z}\right)^2} & |z-L/2| < R_z \\ 0 & |z-L/2| \geq R_z \end{cases} \tag{3.87}$$

$$f_s(z) = \begin{cases} (R_\rho + t_s)\sqrt{1-\left(\frac{(z-L/2)}{R_z}\right)^2} & R_z < |z-L/2| < R_z + t_s \\ 0 & |z-L/2| \geq a_1 + t_s \end{cases} \tag{3.88}$$

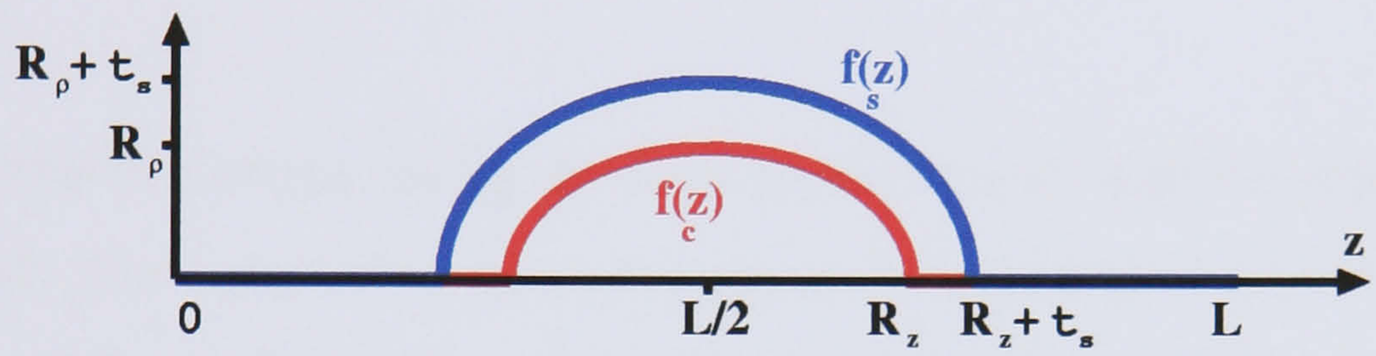

Figure 3.16: Surface equation of the core, $f_c(z)$, and the shell, $f_s(z)$, in cylindrical coordinates, where the core is an ellipsoidal of short radial axis, R_ρ and a long axis R_z along z direction. The shell thickness is t_s.

The integral

$$I_\rho(u) = \int^{u} J_l(k_{lm'}\rho)J_l(k_{lm}\rho)\mathrm{d}\rho\rho \tag{3.89}$$

has been calculated in Section 3.3.3. Then substituting this expression into Equation 3.86 leads to

$$\begin{aligned} M_{nn'lmm'} = V_0\delta_{nn'mm'} - A_{lmm'} \int_{\frac{L-R_z-2t_s}{2}}^{\frac{L+R_z+2t_s}{2}} \mathrm{d}z \sin(k_n z)\sin(k_{n'}z) \times \\ \left[V_0 I_\rho\big(f_c(z)\big) + V_s\big[I_\rho\big(fs(z)\big) - I_\rho\big(f_c(z)\big)\big]\right] \end{aligned} \tag{3.90}$$

and this expression may be calculated numerically.

3.3.6 An example of the energy levels calculation. Ellipsoidal capped QD

In this case we consider a core-shell (CdSe/ZnS) ellipsoidal quantum dot, where the core is elongated along the z axis. We consider ellipsoids of ellipticity $\mu = R_z/R_\rho - 1$, with long axis $R_z = 1.5-2.0$ nm, short axis $R_\rho = 1.5$ nm and shell thickness $t_S = 0.3$ nm.

We calculate the two lowest energy levels of an electron of effective mass $m = 0.1m_0$ within the QD. The band offset between core and shell is $V_s = 0.9$ eV and between core and surrounding material(liquid) is $V_0 = 3$ eV[6]. The infinite potential cylinder radius and height are $R = 12$ nm and $L = 24$ nm, respectively.

We expand the Hamiltonian in terms of the finite set of functions $\mathfrak{F} = \{\Psi^{\infty}_{nlm}\}$ where $n = 1, 2, ..., N_n$, $l = 0, 1, ..., N_l - 1$ and $m = 1, 2, ..., N_m$. The dimension of the set of functions is given by $N = N_n N_l N_m$ and for our case we take $N_n = 50$,$N_l = 1$ and $N_m = 25$. Expanding the Hamiltonian in terms of $\mathfrak{F}$ creates a symmetric matrix of dimension $N = 50 \times 25 = 1250$. In order to diagonalise the Hamiltonian we use NAG-library routines.

We calculate ground and first state energy levels for different core long radii $R_z = 1.5 - 2.0$ nm and short radius $R_\rho = 15$ nm diagonalising the Hamiltonian, as shown in Figure 3.17. These energies are compared with energies obtained in Section 3.3.3 for a capped spherical QD, where the radius $R = R_z$.

Again, the ground state wavefunction may be obtained calculating the eigenfunction associated with the lowest energy level. Figure 3.18 shows the ground state wavefunction, $\Psi_0(\rho, z)$, in cylindrical coordinates. This wavefunction vector will be used in order to calculate the electronic structure of coupled colloidal ellipsoidal QD's in Section 4.5.4.

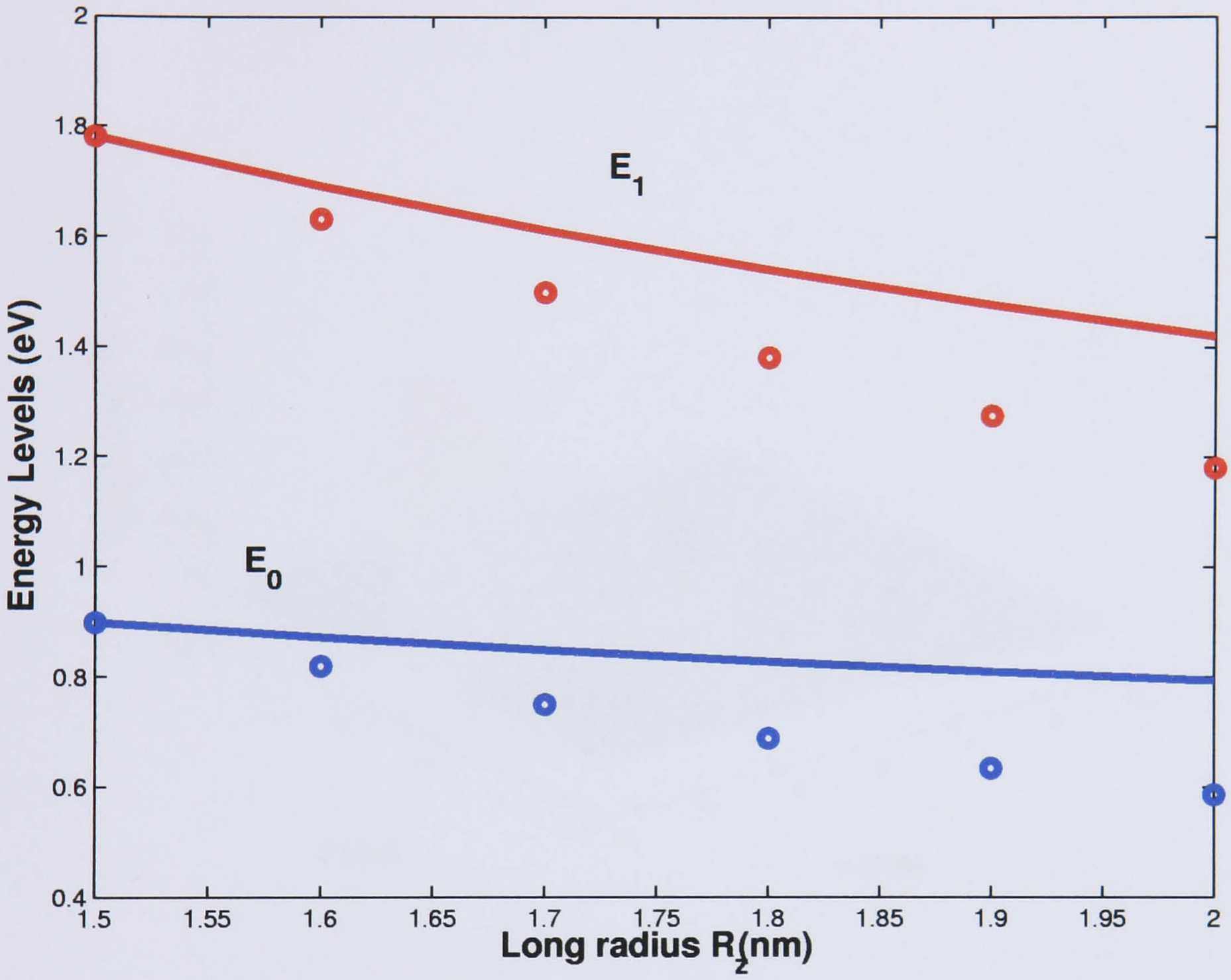

Figure 3.17: Ground and first excited state of an electron within a CdSe/ZnS ellipsoidal QD versus long radius $R_z = 1.5 - 2.0$ nm. Solid lines corresponds to the ellipsoidal QD of short radius $R_\rho = 1.5$ nm and circles lines corresponds to a spherical QD of radius $R = R_z$.

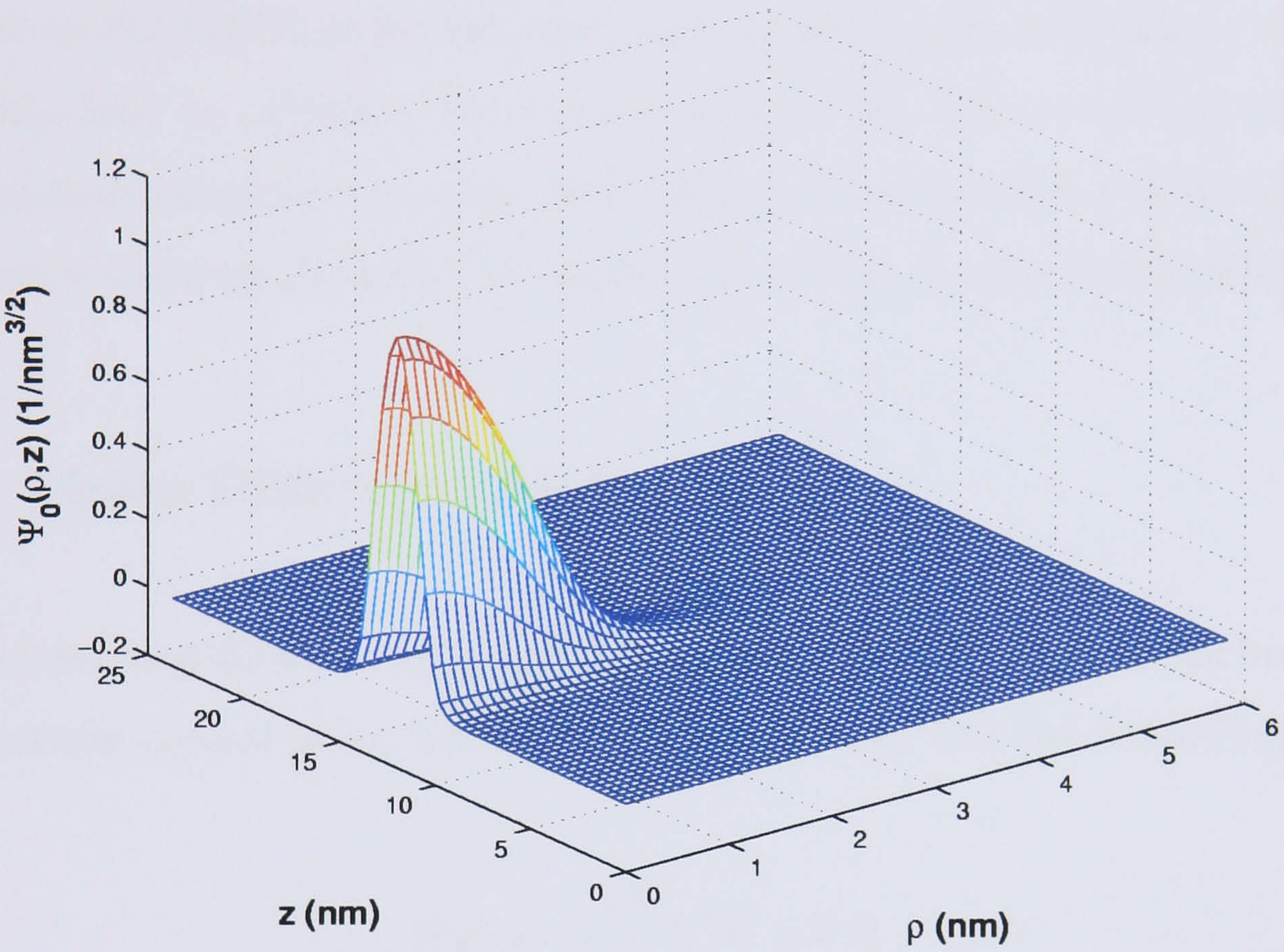

Figure 3.18: Ground state wavefunction, $\Psi_0(\rho, z)$, in cylindrical coordinates of an electron of mass $m = 0.1m_0$ within a capped ellipsoidal QD of long radius $R_z = 2$ nm, short radius $R_\rho = 1.5$ nm and capping layer thickness $t_s = 0.3$ nm. Energy band offsets are $V_0 = 3$ eV and $V_s = 0.9$ eV.

3.4 The Finite Difference Method

We have calculated analytically the Schrödinger equation for spherical structures and used the FDH method for cylindrical structures. Both methods have been compared solving the system for spherical QD's. Here we introduce the Finite Difference method (FD) as another technique for solving the Schrödinger equation. We explain how to calculate the energy levels of any cylindrical QD using this method and we calculate the energy levels of a finite barrier potential spherical QD and compare these results with the analytical solution and the FDH method.

3.4.1 Finite Difference Method

Methods involving difference quotient approximations for derivatives can be used for solving certain second-order boundary value problems, like the Schrödinger equation.

$$\hat{H}\Psi = -\frac{\hbar^2}{2m*}\nabla^2\Psi + V\Psi \tag{3.91}$$

where V is the potential of a cylindrical structure.

Due to the cylindrical shape of the potential, we have symmetry about the z-axis, thus the value of ϕ does not vary and we can write $\Psi(\rho, \phi, z)$ as the following:

$$\Psi(\rho, \phi, z) = \psi(\rho, z)\frac{1}{\sqrt{2\pi}}\mathrm{e}^{im\phi} \tag{3.92}$$

Taking the expression for a free particle, studied in Section 2.4.1, the Schrödinger equation of a particle of effective mass M written in cylindrical coordinates is given by

$$-\frac{\hbar^2}{2m*}\left[\frac{\partial^2}{\partial\rho^2} + \frac{1}{\rho}\frac{\partial}{\partial\rho} - \frac{m}{\rho^2} + \frac{\partial^2}{\partial z^2}\right]\psi + V\psi = E\psi \tag{3.93}$$

The three-dimensional problem has now been reduced to a much more simple two-dimensional problem. This solution can be solved using the finite difference method.

This method of solving partial differential equations only approximates the governing equations at a discrete number of points and not throughout the whole region. As a result, the whole domain is covered by a mesh of points. The first step in our solution is to define this domain. We use N_ρ and N_z number of points to describe ρ and z axis, respectively.

$$\begin{aligned} \rho &\rightarrow 0 = \rho_1, \rho_2, ..., \rho_{N_\rho} = \rho_{\max} \quad \text{where} \quad h = \rho_j - \rho_{j-1} \\ z &\rightarrow z_{\min} = z_1, z_2, ..., z_{N_z} = z_{\max} \quad \text{where} \quad k = z_j - z_{j-1} \end{aligned}$$

where h and k are the increments in ρ and z respectively.

We denote the value of the wavefunction $\psi(\rho, z)$ and the potential $V(\rho, z)$ at these points as:

$$\psi_{ij} = \psi(\rho_i, z_j) \tag{3.94}$$

$$V_{ij} = V(\rho_i, z_j) \tag{3.95}$$

where $i = 1, \ldots, N_\rho$ and $j = 1, \ldots, N_z$.

Now, replacing the partial derivatives with finite difference quotients and neglecting second order terms give[9]:

$$\left.\frac{\partial \psi}{\partial \rho}\right|_{(\rho_i, z_j)} = \frac{\psi_{i+1,j} - \psi_{i-1,j}}{2h} \tag{3.96}$$

$$\left.\frac{\partial^2 \psi}{\partial \rho^2}\right|_{(\rho_i, z_j)} = \frac{\psi_{i+1,j} - 2\psi_{i,j} + \psi_{i-1,j}}{h^2} \tag{3.97}$$

$$\left.\frac{\partial^2 \psi}{\partial z^2}\right|_{(\rho_i, z_j)} = \frac{\psi_{i,j+1} - 2\psi_{i,j} + \psi_{i,j+1}}{k^2} \tag{3.98}$$

Substituting the above quotients into the Schrödinger equation leads to:

$$\begin{aligned} &\frac{\psi_{ij+1} - 2\psi_{ij} + \psi_{ij-1}}{k^2} + \frac{\psi_{i+1j} - \psi_{ij-1}}{\rho_i h} + \\ &\frac{\psi_{i+1j} - 2\psi_{ij} + \psi_{i-1j}}{h^2} - \frac{m\psi_{ij}}{{\rho_i}^2} = \frac{2M}{\hbar^2}(V_{ij} - E)\psi_{ij} \end{aligned} \tag{3.99}$$

or rearranging last equation

$$\psi_{i-1j}\left[\frac{1}{h^2}-\frac{1}{2h\rho_i}\right]+\psi_{ij}\left[-\frac{2}{k^2}-\frac{2}{h^2}-\frac{m}{\rho_i^2}-\frac{2MV_{ij}}{\hbar^2}\right]+$$
$$\psi_{i+1j}\left[\frac{1}{h^2}+\frac{1}{2h\rho_i}\right]-\psi_{ij-1}\left[\frac{1}{k^2}\right]+\psi_{ij+1}\left[\frac{1}{k^2}\right]=E\psi_{ij} \tag{3.100}$$

Due to the fact that the wavefunction must be zero at infinity and defined within the range $(i = 1,\ldots,N_\rho, j = 1,\ldots,N_z)$ the following elements are zero: $\psi_{i0} = \psi_{i(N_z+1)} = \psi_{0j} = \psi_{(N_\rho+1)j} = 0$.

Substituting for all values of i and j, we can arrange the Schrödinger equation as a system of linear equations and produce a (N, N) matrix, where $N = N_\rho N_z$.

Lets denote the column vector Φ as

$$\Phi = \begin{pmatrix} \psi_{11} & \psi_{12} & \ldots & \psi_{1N_z} & \psi_{21} & \psi_{22} & \ldots & \psi_{N_\rho N_z} \end{pmatrix}^t \tag{3.101}$$

The system of linear equations may be written as

$$\mathcal{A}\Phi = E\Phi \tag{3.102}$$

where $\mathcal{A}$ is the matrix described as

$$\mathcal{A} = \begin{pmatrix} A_{11} & A_{12} & \ldots & A_{1N_\rho} \\ A_{21} & A_{22} & \ldots & A_{2N_\rho} \\ \vdots & \vdots & \ddots & \vdots \\ A_{N_\rho 1} & A_{N_\rho 2} & \ldots & A_{N_\rho N_\rho} \end{pmatrix} \tag{3.103}$$

where each element A_{ij} is another matrix defined as

$$A_{ij} = \begin{pmatrix} a_{(N_i+1)(N_j+1)} & a_{(N_i+1)(N_j+2)} & \cdots & a_{(N_i+1)(N_j+N_z)} \\ a_{(N_i+2)(N_j+1)} & a_{(N_i+2)(N_j+2)} & \cdots & a_{(N_i+2)(N_j+N_z)} \\ \vdots & \vdots & \ddots & \vdots \\ a_{(N_i+N_z)(N_j+1)} & a_{(N_i+N_z)(N_j+2)} & \cdots & a_{(N_i+N_z)(N_j+N_z)} \end{pmatrix} \tag{3.104}$$

with $N_i = N_\rho(i-1)$ and $N_j = N_\rho(j-1)$.

Substituting the Equations 3.100 into the matrix $\mathcal{A}$ leads to

$$\mathcal{A} = \begin{pmatrix} A_{11} & A_{12} & 0 & 0 & \dots & 0 \\ A_{21} & A_{22} & A_{23} & 0 & \dots & 0 \\ 0 & A_{32} & A_{33} & A_{34} & \dots & 0 \\ 0 & 0 & A_{43} & A_{44} & \dots & 0 \\ \vdots & \vdots & \vdots & \vdots & \ddots & \vdots \\ 0 & 0 & 0 & 0 & \dots & A_{N_\rho N_\rho} \end{pmatrix} \tag{3.105}$$

For a given i the non-zero elements of matrix $\mathcal{A}$ are:

$$A_{ii-1} = A_{i-1i} = \left[\frac{1}{h^2} - \frac{1}{2h\rho_i}\right] \begin{pmatrix} 1 & 0 & 0 & \dots & 0 \\ 0 & 1 & 0 & \dots & 0 \\ 0 & 0 & 1 & \dots & 0 \\ \vdots & \vdots & \vdots & \ddots & \vdots \\ 0 & 0 & 0 & \dots & 1 \end{pmatrix} \tag{3.106}$$

$$A_{ii+1} = A_{i+1i} = \left[\frac{1}{h^2} + \frac{1}{2h\rho_i}\right] \begin{pmatrix} 1 & 0 & 0 & \dots & 0 \\ 0 & 1 & 0 & \dots & 0 \\ 0 & 0 & 1 & \dots & 0 \\ \vdots & \vdots & \vdots & \ddots & \vdots \\ 0 & 0 & 0 & \dots & 1 \end{pmatrix} \tag{3.107}$$

$$\begin{aligned} A_{ii} = & \left[-\frac{2}{k^2} - \frac{2}{h^2} - \frac{m}{\rho_i^2}\right] \begin{pmatrix} 1 & 0 & 0 & \dots & 0 \\ 0 & 1 & 0 & \dots & 0 \\ 0 & 0 & 1 & \dots & 0 \\ \vdots & \vdots & \vdots & \ddots & \vdots \\ 0 & 0 & 0 & \dots & 1 \end{pmatrix} - \\ & \frac{2M}{\hbar^2} \begin{pmatrix} V_{i1} & 0 & 0 & \dots & 0 \\ 0 & V_{i2} & 0 & \dots & 0 \\ 0 & 0 & V_{i3} & \dots & 0 \\ \vdots & \vdots & \vdots & \ddots & \vdots \\ 0 & 0 & 0 & \dots & V_{iN_z} \end{pmatrix} + \\ & \frac{1}{k^2} \begin{pmatrix} 0 & 1 & 0 & \dots & 0 \\ 1 & 0 & 1 & \dots & 0 \\ 0 & 1 & 0 & \dots & 0 \\ \vdots & \vdots & \vdots & \ddots & \vdots \\ 0 & 0 & 0 & \dots & 0 \end{pmatrix} \end{aligned} \tag{3.108}$$

where $A_{i0} = A_{0i} = A_{(N_\rho+1)0} = A_{0(N_\rho+1)} = \mathbf{0}$

We have shown that $\mathcal{A}$ is a band symmetric matrix of order N. This matrix depends on the axial number m, therefore we include this number as an upper-script of the matrix $\mathcal{A} \rightarrow \mathcal{A}^m$. Using NAG-mathematical libraries, we obtain the eigenvalues, E_l, and eigenfunctions, Ψ_l, of $\mathcal{A}$ which are the energy levels and wavefunctions of the equation

$$\mathcal{A}^m \Psi_{ml} = E_{ml} \Psi_{ml} \tag{3.109}$$

In order to obtain the two-dimensional wavefunction $\Psi_{ml}(\rho, z)$ we use the transformation

$$\Phi_{ml} = \begin{pmatrix} \psi_{11}^{ml} & \psi_{12}^{ml} & \dots & \psi_{1N_z}^{ml} & \psi_{21}^{ml} & \psi_{22^{ml}} & \dots & \psi_{N_\rho N_z}^{ml} \end{pmatrix}^t \tag{3.110}$$

where

$$\Psi_{ml}(\rho_i, z_j) = \psi_{ij}^{ml} \tag{3.111}$$

3.4.2 An example of the energy levels calculation. Spherical QD

We calculate the energy levels of a finite barrier potential spherical QD. We take the same parameters as before: a spherical QD of radius $R = 9$ nm, potential barrier depth $V_0 = 1$ eV and the effective mass of the electron $m = 0.023 m_0$.

Taking different number of partitions in z and ρ directions as, N_ρ and N_z respectively, we obtain the first few energies shown in Table 3.3. We compare the results with the analytic solution.

We calculate the energies using $(N_\rho = 25, N_z = 50)$ and $(N_\rho = 50, N_z = 100)$ number of partitions in ρ and z axis. We create the matrix $\mathcal{A}$ for $m = 0, 1$. The

	Energy (eV)				
	E_0	E_1	E_2	E_3	E_4
	Analytically				
E_{nm}	E_{10}	E_{11}	E_{12}	E_{20}	E_{13}
	0.153440	0.311839	0.508806	0.596511	0.739963
	FD				
	$N_\rho = 25, N_z = 50$				
$m = 0$	0.164311	0.316626	0.508831	0.636302	0.737222
$m = 1$	0.341018	0.532979	0.752368	0.938908	1.000180
	$N_\rho = 50, N_z = 100$				
$m = 0$	0.158954	0.319300	0.517377	0.615271	0.754053
$m = 1$	0.324407	0.526052	0.756434	0.902336	1.019230

Table 3.3: Energy levels of an electron of mass $m = 0.023m_0$ within a finite potential barrier ($V_0 = 1$ eV) spherical QD of radius $R = 9$ nm calculated analytically and using the FD method. Analytical results E_{nm} are ordered increasingly. The FD method has been applied for different axial numbers $m = 0, 1$ and using two different dimension matrixes: $N = N_\rho N_z = 25 \times 50$ and $N = N_\rho N_z = 50 \times 100$.

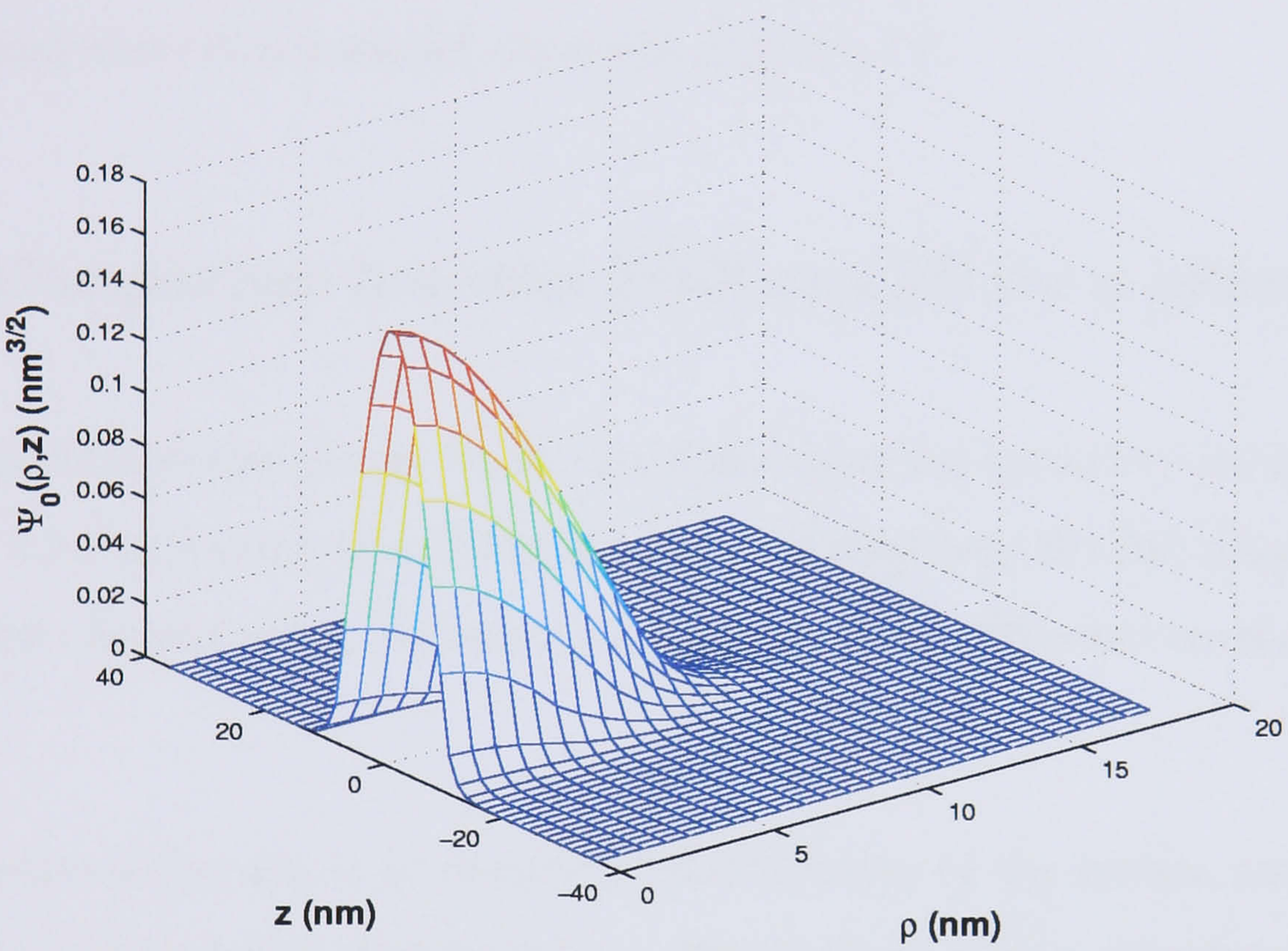

Figure 3.19: Ground state wavefunction of a finite potential barrier spherical QD calculated using the FD method.

range of z axis we have taken into account is $[z_{\min}, z_{\max}] = [-36, 36]$ nm, and the range of ρ $[\rho_{\min}, \rho_{\max}] = [0, 18]$ nm.

As shown in Table 3.3, using functions with axial number $m = 0$, Ψ_0, to generate the matrix $\mathcal{A}$ gives more accurate results for the energy levels. As it happens in the FDH method, functions of axial number $m \geq 1$ vanish at the origin, thus they cannot reproduce any wavefunction which is not zero at the origin, which is the case of the ground state of our model, shown in Figure 3.19.

3.4.3 Comparison between FDH and FD for a spherical QD

We have calculated the energy levels of a finite spherical quantum dot analytically in Section 2.3.2 and using two different numerical methods: the full diagonalisation of the system Hamiltonian, Section 3.3.1, and the finite difference method, Section 3.4.2.

In both methods the aim is to create the Hamiltonian of the system and then calculate its eigenvalues and eigenfunctions. We compare both methods constructing equal size Hamiltonians and we use numerical libraries in order to obtain the eigenfunctions and eigenvalues.

Table 3.4 shows the five lowest energies obtained analytically and using both methods for a spherical QD of radius $a = 9$ nm. Both methods have been used to solve cylindrically symmetric structures, where the three-dimensional Hamiltonian is reduced to two dimensions. Then comparing energies in Table 3.4 we can state that the results obtained using the FDH method are more accurate than the ones obtained using FD, making the former technique a good candidate to calculate the energy levels of cylinder symmetric QD's.

	Energy (eV)				
	E_0	E_1	E_2	E_3	E_4
	Analytically				
	0.153440	0.311839	0.508806	0.596511	0.739963
	FDH				
$N = 1250$	0.153484	0.311963	0.508968	0.596678	0.740050
	FD				
$N = 1250$	0.164311	0.316626	0.508831	0.636302	0.737222

Table 3.4: Energies levels of an electron of mass $m = 0.023m_0$ within a finite potential barrier ($V_0 = 1$ eV) spherical QD of radius $R = 9$ nm calculated analytically and using the FDH and the FD numerical methods. Analytical results E_{nm} are ordered increasingly. In both numerical methods a matrix of dimension $N = 25 \times 50 = 1250$ has been used in order to write the Hamiltonian.

3.5 Summary

In this chapter the Schrödinger equation has been solved for an electron within a cylindrical symmetric quantum dot. For QD structures the analytical solution is only available for certain cases like spheres or infinite potential cylinders. In other cases numerical methods must be applied. The full diagonalisation of the system Hamiltonian method has been used in order to obtain the electronic structure and the wavefunctions of the particle.

Firstly, the FDH method has been explained and applied for a spherical QD and a spherical capped colloidal QD. In both cases the results have been checked against the analytical solution calculated in Chapter 2. Using the example of a spherical QD we estimate the size of the basis set which is used to expand the Hamiltonian in order to determine accurate results for structures where the analytical solution is not possible to obtain. Therefore, using the same basis as for the spherical QD, the solution is obtained for an ellipsoidal QD and an ellipsoidal capped QD.

Another numerical method, the finite difference method, is studied and applied for the case of a spherical QD. This method is checked against the solutions obtained analytically and using the FDH method. It has been found that the FDH method is much faster and accurate than the FD method.

Bibliography

[1] S. Gangopadhyay and B.R. Nag. Energy levels in three-dimensional quantum-confinement structures. *Nanotechnology*, 8, 1997.

[2] D. Gershoni, H. Temkin, G.J. Dolan, J. Dunsmuir, S.N.G. Chu, and M.B. Panish. Effects of two-dimensional confinement on the optical properties of `InGaAs/InP` quantum wire structures. *Appl. Phys. Lett*, 53, 1988.

[3] Marek Korkusiński and Pawel Hawrylak. Electronic structure of vertically stacked self-assembled quantum disks. *Phys. Rev. B*, 63:195311, 2001.

[4] *NAG Fortran Library Manual.* http://www.nag.co.uk/numeric/fl/manual.

[5] B. O. Dabbousi, J. Rodríguez-Viejo, F. V. Mikulec, J. R. Heine, H. Mattoussi, R. Obera, K. F. Jensen, and M. G. Bawendi. `(CdSe)ZnS` core-shell quantum dots: Synthesis and characterization of a size series of highly luminescent nanocrystallites. *J. Phys. Chem. B*, 101:9463, 1997.

[6] Todd D. Krauss and Luouis E. Brus. Electronic properties of single semiconductor nanocyrstals: optical and electrostatic force microscopy measurements. *Materials Science and Engineering B69-70*, page 289, 2000.

[7] C. B. Murray, D. J. Norris, and M. G. Bawendi. Synthesis and characterization of nearly monodisperse `CdE(E=S, Se, Te)` semiconductor nanocrystallites. *J. Am. Chem. Soc.*, 115:8706, 1993.

[8] S. Pokrant and K. B. Whaley. Tight-binding studies of surface effects on electronic structure of cdse nanocrystals: the role of organic ligands, surface reconstruction, and inorganic capping shells. *Eur. Phys. J. D*, 6:255, 1999.

[9] John H. Mathews. *Numerical methods for mathematics, science and engineering.* Prentice-Hall, 1992.

Chapter 4

Coupling between two QD's

Contents

4.1 Introduction

Coupled QD systems have been investigated for their possible application in quantum computing. In [1] the spin degree of freedom of the electrons within a coupled QD has been used to describe a qubit. In contrast, [2] proposes to use the individual carrier localisation within a pair of vertically aligned SAD's to define a qubit. In both cases the coupling between QD's is used to create a quantum gate, which is the key to building a quantum processor. A mechanism which makes it possible to switch the coupling on and off is also required.

Vertically coupled quantum dots in multilayer self-assembled structures have also attracted large interest for device application as light emitters. Self-assembled QD's are structures which have well-defined excited state transitions, but a blue-shift or red-shift of the fundamental transition energy can be observed under different coupling conditions[3]. It has also been demonstrated that stacks of SAD's can increase the gain in the active region[4].

Therefore an understanding of how dots couple in quantum dot molecules is needed so that the possibilities for the use of coupled QD's as quantum gates can be explored. In this chapter it the electronic structure of coupled QD's for two types of dots will be studied: SAD's and colloidal QD's. For simplicity in terms of computation time, only systems with cylindrical symmetry have been taken into account.

In order to calculate the lowest energy level, the linear combination of QD states approximation (LCQDSA) method is used and it is compared with the full diagonalisation of the system Hamiltonian (FDH) method explained in Section 3.2, which can solve systems with cylindrical symmetry but requires more computational time.

The coupling between dots will be studied varying the shape of the dots, the inter-dot distance and the potential barrier.

4.2 Linear combination of QD states approximation

The linear combination of QD states approximation (LCQDSA) method is employed to estimate the states of a coupled quantum dot system. This method uses linear combination of isolated QD states and has been applied to estimate the states of a molecule in terms of a linear combination of quantum states of isolated constituent atoms [5].

This method estimates the confined energy levels of a single charge carrier within two coupled QD systems. In this present analysis the LCQDSA method is employed with the potential shown in Figure 4.1c), which is a one-dimensional representation of two aligned spherical QD's, where each well should represent the spherical-shape potential of each QD (the system is of course solved full in 3-D).

The electronic structure of an isolated spherical QD has been calculated previously in Section 2.3. Therefore the normalised wavefunctions and the energy of each isolated QD may be obtained, being $|\psi_1\rangle(|\psi_2\rangle)$ the wavefunction and $E_1(E_2)$ the energy of the left(right) QD. Using the effective mass Hamiltonian those functions

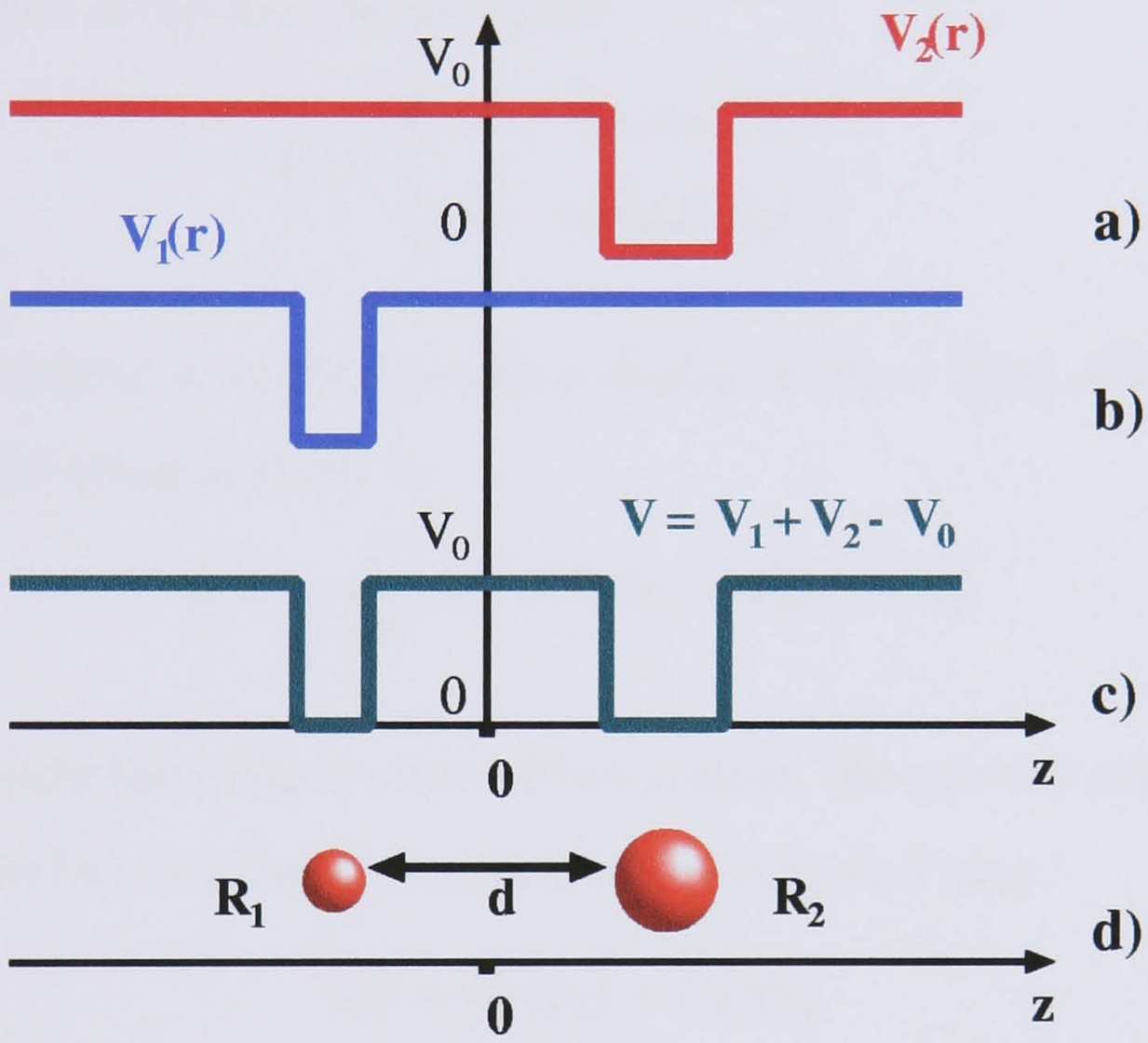

Figure 4.1: Schematic representation of the potentials of **a)**isolated QD 2, **b)**isolated QD 1 and **c)**two coupled QD's. **d)**Representation of two QD's of radius R_1 and R_2 separated by a distance d between surfaces.

have to satisfy

$$\left(\hat{H}^0 + V_1(\mathbf{r})\right)|\psi_1\rangle = E_1|\psi_1\rangle \tag{4.1}$$

$$\left(\hat{H}^0 + V_2(\mathbf{r})\right)|\psi_2\rangle = E_2|\psi_2\rangle \tag{4.2}$$

where $\hat{H}^0 = -\frac{\hbar^2}{2m^*}\nabla^2$ is the free charge effective mass Hamiltonian and $V_1(\mathbf{r})$ and $V_2(\mathbf{r})$ are the confining potential of QD 1 and QD 2, respectively, which are shown in Figure 4.1a) and 4.1b) and described by:

$$V_i = \begin{cases} 0 & \text{inside QD}\, i \\ V_0 & \text{outside QD}\, i \end{cases} \tag{4.3}$$

The LCQDSA method is applied to the potential $V(\mathbf{r}) = V_1(\mathbf{r}) + V_2(\mathbf{r}) - V_0$. Then the system Hamiltonian is given by:

$$\hat{H} = -\frac{\hbar^2}{2m^*}\nabla^2 + V_1(\mathbf{r}) + V_2(\mathbf{r}) - V_0 \tag{4.4}$$

In order to estimate the ground-state of the system, the ground-state wavefunction will be approximated to a linear combination of $|\psi_1\rangle$ and $|\psi_2\rangle$:

$$|\psi\rangle = C_1|\psi_1\rangle + C_2|\psi_2\rangle \tag{4.5}$$

where C_1 and C_2 are constants. Therefore $|\psi\rangle$ must obey the Hamiltonian $\hat{H}|\psi\rangle = E|\psi\rangle$.

The energy expectation value is defined as $\langle E\rangle$ which is the average value of the Hamiltonian $\hat{H}$ in an arbitrary normalised state $|\Phi\rangle$. In Dirac notation this equation appears as

$$\langle E\rangle = \int \Phi^*(\mathbf{r})\hat{H}\Phi(\mathbf{r})\mathrm{d}\mathbf{r} = \langle\Phi|\hat{H}|\Phi\rangle \tag{4.6}$$

Following [5], the energy expectation value $\langle E\rangle$ in any normalised state $|\Phi\rangle$, is stationary and is minimum in the ground state. Then

$$\langle E\rangle_{\text{minimum}} = \langle E_G\rangle = \frac{\langle\Phi_G|\hat{H}|\Phi_G\rangle}{\langle\Phi_G|\Phi_G\rangle} \tag{4.7}$$

Therefore minimising the energy expected value in the state $|\psi\rangle$ leads to:

$$\langle E\rangle = \frac{\langle\psi|\hat{H}|\psi\rangle}{\langle\psi|\psi\rangle} \tag{4.8}$$

where the normalisation condition is included. Substituting Equation 4.5 into last expression leads to:

$$\langle E\rangle = \frac{{C_1}^2 H_{11} + {C_2}^2 H_{22} + C_1 C_2 (H_{12} + H_{21})}{C_1^2 + {C_2}^2 + C_1 C_2 (S + S^*)} \tag{4.9}$$

where S, which is the overlap integral between $|\psi_1\rangle$ and $|\psi_2\rangle$, and H_{ij} are given by

$$S = \langle\psi_1|\psi_2\rangle \tag{4.10}$$

$$H_{ij} = \langle\psi_i|\hat{H}|\psi_j\rangle \tag{4.11}$$

Elements H_{11}, H_{22}, H_{12} and H_{21} may be obtained using Equation 4.4. QD's with cylindrical symmetry, whose ground state spatial wavefunctions are real vectors, are going to be investigated. Therefore it can be assumed that $S = S^*$ and $H_{12} = H_{21}$. The expression for H_{11} is

$$\begin{aligned} H_{11} &= \langle\psi_1|\overbrace{\hat{H}^0 + V_1(\mathbf{r})}^{\hat{H}_1} + V_2(\mathbf{r}) - V_0|\psi_1\rangle && (4.12)\\ &= \langle\psi_1|\hat{H}_1 - V_0|\psi_1\rangle + \langle\psi_1|V_2(\mathbf{r})|\psi_1\rangle && (4.13)\\ &= (E_1 - V_0) + \langle\psi_1|V_2(\mathbf{r})|\psi_1\rangle && (4.14) \end{aligned}$$

Proceeding in the same way for H_{22}, H_{12} and H_{21} leads to

$$\begin{aligned} H_{11} &= (E_1^0 - V_0) + \langle\psi_1|V_2|\psi_1\rangle && (4.15)\\ H_{21} = H_{12} &= (E_2^0 - V_0)S + \langle\psi_1|V_1|\psi_2\rangle && (4.16)\\ H_{22} &= (E_2^0 - V_0) + \langle\psi_2|V_1|\psi_2\rangle && (4.17) \end{aligned}$$

then the average energy may be written as

$$\langle E\rangle = \frac{{C_1}^2 H_{11} + {C_2}^2 H_{22} + 2C_1 C_2 H_{12}}{C_1^2 + {C_2}^2 + 2C_1 C_2 S} \tag{4.18}$$

Now the condition which minimises $\langle E \rangle$ over a variable u is $\partial\langle E \rangle / \partial u = 0$. In this case it is wanted to obtain which values of C_1 and C_2 minimise the energy. Therefore the conditions which minimise $\langle E \rangle$ over C_1 and C_2 are the followings:

$$\frac{\partial\langle E \rangle}{\partial C_1} = \frac{\partial\langle E \rangle}{\partial C_2} = 0 \tag{4.19}$$

Developing the first condition leads to

$$\begin{aligned} \frac{\partial\langle E \rangle}{\partial C_1} &= \frac{(2C_1H_{11} + 2C_2H_{12})({C_1}^2 + {C_2}^2 + 2C_1C_2S)}{({C_1}^2 + {C_2}^2 + 2C_1C_2S)^2} \\ &\quad - \frac{({C_1}^2H_{11} + {C_2}^2H_{22} + 2C_1C_2H_{12})(2C_1 + 2C_2S)}{(C_1^2 + {C_2}^2 + 2C_1C_2S)^2} \\ &= 2\frac{C_1H_{11} + C_2H_{22} - \langle E \rangle(C_1 + C_2S)}{{C_1}^2 + {C_2}^2 + 2C_1C_2S} = 0 \end{aligned}$$

Then

$$C_1H_{11} + C_2H_{22} - \langle E \rangle(C_1 + C_2S) = 0 \tag{4.20}$$

Developing the derivative with respect to C_2 in a similar way leads to:

$$\begin{aligned} C_1(H_{11} - \langle E \rangle) &+ C_2(H_{12} - \langle E \rangle S) = 0 \\ C_1(H_{12} - \langle E \rangle S) &+ C_2(H_{11} - \langle E \rangle) = 0 \end{aligned} \tag{4.21}$$

With $\mathcal{C}$ representing a column vector with components (C_1, C_2), the preceding equations may be written in the matrix form $\mathcal{RC} = 0$, where $\mathcal{R}$ is the implied coefficient matrix.

$$\begin{matrix} & \mathcal{R} & & \mathcal{C} \end{matrix}$$
$$\begin{pmatrix} H_{11} - \langle E \rangle & H_{12} - \langle E \rangle S \\ H_{12} - \langle E \rangle S & H_{22} - \langle E \rangle \end{pmatrix} \begin{pmatrix} C_1 \\ C_2 \end{pmatrix} = \begin{pmatrix} 0 \\ 0 \end{pmatrix} \tag{4.22}$$

Solving this matrix equation leads to $\mathcal{C} = 0$ unless both equations are linear-dependent. Therefore a nontrivial solution occurs when Equations 4.21 are linear-

dependent, which is the same as saying $\det \mathcal{R} = 0$,

$$\begin{vmatrix} H_{11} - \langle E \rangle & H_{12} - \langle E \rangle S \\ H_{12} - \langle E \rangle S & H_{22} - \langle E \rangle \end{vmatrix} = 0 \tag{4.23}$$

which gives

$$\langle E \rangle_{\pm} = \frac{-b \mp \sqrt{b^2 - 4ac}}{2a} \tag{4.24}$$

where $a = 1 - S^2$, $b = 2H_{12}S - H_{11} - H_{22}$ and $c = H_{11}H_{22} - {H_{11}}^2$. The normalised eigenfunctions $|\psi_{\pm}\rangle$ which corresponds to the energy levels $\langle E \rangle_{\pm}$ are

$$|\psi_{\pm}\rangle = A_{\pm}(C_{1\pm}|\psi_1\rangle + C_{2\pm}|\psi_2\rangle) \tag{4.25}$$

where

$$C_{1\pm} = \langle E \rangle_{\pm} S - H_{12} \tag{4.26}$$

$$C_{2\pm} = H_{11} - \langle E \rangle_{\pm} \tag{4.27}$$

$$(A_{\pm})^{-2} = (C_{2\pm})^2 + (C_{1\pm})^2 + 2C_{2\pm}C_{1\pm}S \tag{4.28}$$

4.3 Two Finite Potential Identical Spherical QD's

In this section we study the ground and first excited states of two identical coupled spherical QD's applying the LCQDSA method. This is an ideal system to illustrate the technique to the reader.

The model is composed of two identical spherical QD's of radius a separated by a distance d as shown in Figure 4.2.

Finite potential spherical QD's have been studied previously in Section 2.3.2. Energies and wavefunctions of isolated spherical QD's are obtained solving the effective

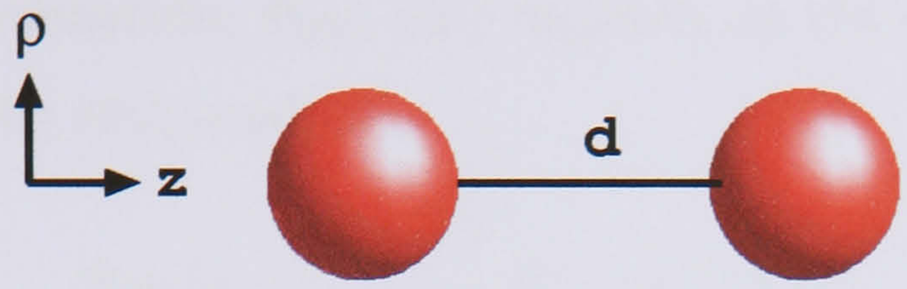

Figure 4.2: Two identical spherical quantum dots aligned in z direction and separated by a distance d.

mass Hamiltonian described in Equation 2.22. The wavefunction of a particle confined within a finite potential isolated spherical QD is given by Equation 2.23

$$\Psi_{nlm}(\mathbf{r}) = R_{nl}(r)Y_l^m(\theta,\phi) \tag{4.29}$$

where the ground state wavefunction is given by

$$\Psi_{000}(\mathbf{r}) = \sqrt{\frac{1}{4\pi}}R_{00}(r) \tag{4.30}$$

being $R_{nl}(r)$ the radial solution of the Schrödinger equation in spherical coordinates for a spherical finite barrier potential given in Section 2.3.2 by Equation 2.35.

$$R_l(r) = \begin{cases} Aj_l(k_W r) & r \leq a \qquad k_W = \sqrt{2mE}/\hbar \\ Bk_l(k_B r) & r > a \qquad k_B = \sqrt{2m(V_0 - E)}/\hbar \end{cases} \tag{4.31}$$

where a is the QD radius and A, B are parameters which can be obtained from Equations 2.42 and 2.43.

The potential of an isolated QD has spherical symmetry $V(\mathbf{r}) = V(r)$, but once another QD is added, the system symmetry changes to cylindrical (Figure 4.3). It will be convenience to express the wavefunctions Ψ_{nlm} in cylindrical coordinates taking z coordinate parallel to the axis which joins both QD's. The wavefunctions may be written as

$$\Psi_{nlm}(\rho,\phi,z) = R_{nl}(\sqrt{z^2+\rho^2})Y_l^m(\arctan(\rho/z),\phi) \tag{4.32}$$

The ground state wavefunction, Ψ_{000}, only depends on the modulus of the position vector $\mathbf{r}$, then it may be expressed as

$$\Psi_{000}(\rho, z) = \sqrt{\frac{1}{4\pi}} R_{00}(\sqrt{z^2 + \rho^2}) \tag{4.33}$$

QD's 1 and 2 are referred as the lower and the upper dot respectively. The ground state wavefunction of each isolated QD in cylindrical coordinates are:

$$\psi_1(\rho, z) = \Psi_{000}(\rho, z + z_0) \tag{4.34}$$

$$\psi_2(\rho, z) = \Psi_{000}(\rho, z - z_0) \tag{4.35}$$

where $z_0 = (d+a)/2$ is the distance from each QD centre to the origin of coordinates $\mathbf{r} = (0, 0, 0)$.

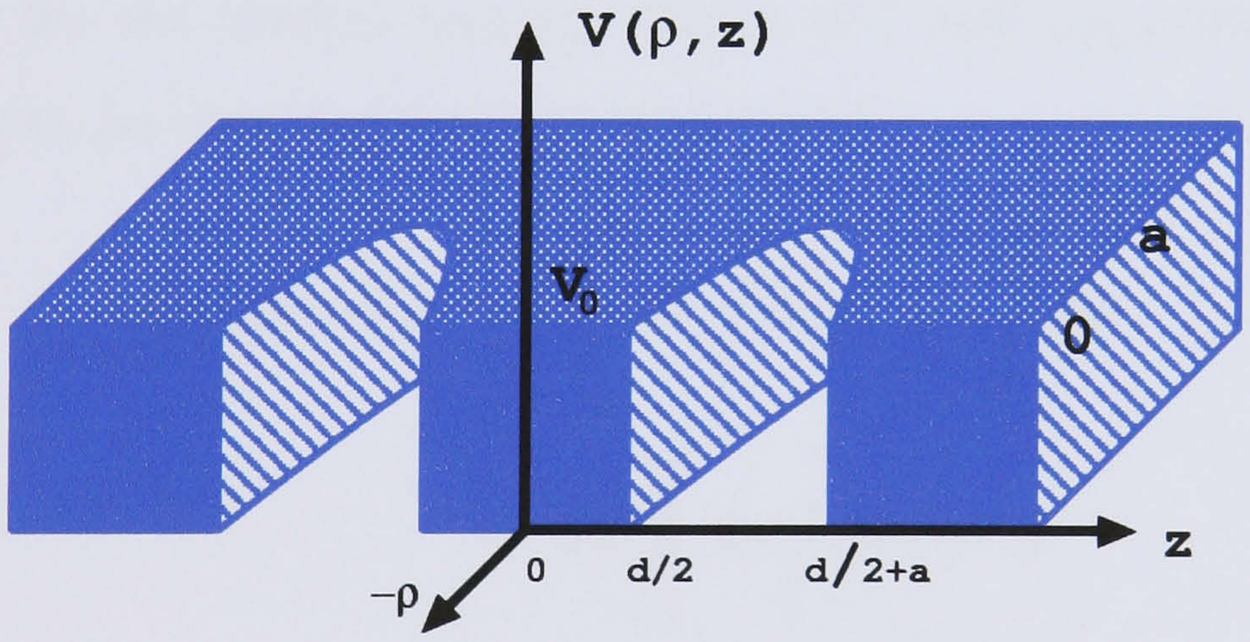

Figure 4.3: Two spherical QD potential in cylindrical coordinates.

Now, the LCQDSA method explained in Section 4.2 is applied in order to estimate the two lowest energies of two identical QD's. Taking the ground-state energy of an isolated QD from Equation 2.38, $E_0 = E_{n=0,l=0}$, and solving Equation 4.22 taking into account that $H_{11} = H_{22}$, the approximated solution for the energies and

wavefunctions of the system may be written as

$$\psi_{\pm} = \frac{A_{\pm}}{\sqrt{2}}(\psi_1 \pm \psi_2) \tag{4.36}$$

$$E_{\pm} = \frac{H_{11} \pm H_{12}}{1 \pm S} \tag{4.37}$$

where

$$A_{\pm} = \tfrac{1}{\sqrt{1 \pm S}} \tag{4.38}$$

$$S = \langle \psi_1 | \psi_2 \rangle \tag{4.39}$$

$$H_{ij} = \langle \psi_i | \hat{H} | \psi_j \rangle \tag{4.40}$$

4.3.1 Calculation of the overlap S and H_{ij} elements

The expression for the overlap between states $|\psi_1\rangle$ and $|\psi_2\rangle$, which is given by Equation 4.39, can be obtained solving the integral

$$S \equiv \langle \psi_1 | \psi_2 \rangle = \int_{-\infty}^{\infty} \mathrm{d}z \int_{0}^{\infty} \mathrm{d}\rho \rho \psi_1 \psi_2 \int_{0}^{2\pi} \mathrm{d}\phi \tag{4.41}$$

$$= 2\pi \int_{-\infty}^{\infty} \mathrm{d}z \int_{0}^{\infty} \mathrm{d}\rho \rho \psi_1 \psi_2 \tag{4.42}$$

where wavefunctions ψ_1 and ψ_2 are given by Equations 4.34 and 4.35 respectively. The last integral may be calculated using the trapezoidal rule. The fact that both dots are identical spheres leads to $H_{11} = H_{22}$. Using Equations 4.15 and 4.17, elements H_{12} and H_{22} can be expressed as:

$$H_{12} = H_{21} = (E_1^0 - V_0)S + 2\pi \int_{-\infty}^{\infty} \mathrm{d}z \int_{0}^{\infty} \mathrm{d}\rho \rho \psi_1(\rho, z) V_1(\rho, z) \psi_2(\rho, z) \tag{4.43}$$

$$H_{22} = H_{11} = (E_2^0 - V_0) + 2\pi \int_{-\infty}^{\infty} \mathrm{d}z \int_{0}^{\infty} \mathrm{d}\rho \rho \psi_2(\rho, z) V_1(\rho, z) \psi_2(\rho, z) \tag{4.44}$$

where E_0 is the ground state energy level of isolated dots 1 and 2. Potential $V_1(\rho, z)$ is the potential of the isolated dot 1 described in cylindrical coordinates as:

$$V_1(\rho,z) = \begin{cases} 0 & \rho^2 < a^2 - (z+z_0)^2 \quad \text{(inside dot 1)} \\ V_0 & \rho^2 > a^2 - (z+z_0)^2 \quad \text{(outside dot 1)} \end{cases} \tag{4.45}$$

Discretising V_1 and taking the discrete representation of ψ_i, all those integrals may be calculated using the trapezoidal rule.

4.3.2 Ground and first excited estate

Once S and H_{ij} are calculated, the ground and first excited energy state can be obtained. The energy difference between odd and even state energies, E_+ and E_- respectively, is

$$\Delta E = E_- - E_+ = 2\frac{SH_{11} - H_{12}}{1 - S^2} \tag{4.46}$$

In this section the two lowest energy levels are calculated for different dot radii $a = 3 - 8$ nm and for different potential barriers $V_0 = 1 - 10$ eV. The electron effective mass m^* used is $m^* = 0.023m_0$. Parameters for InAs/GaAs self-assembled quantum dots have been taken from [6]. Self-assembled QD's are not spheres, but the aim of this section is to introduce this technique to the reader and more realistic models will be presented later in other sections.

Figure 4.4 shows the energy values and the shape of the wavefunctions for the ground and first excited state for a fixed radius and varying the distance between dots. The plot reveals that E_+ is the ground-state energy, thus the ground-state wavefunction

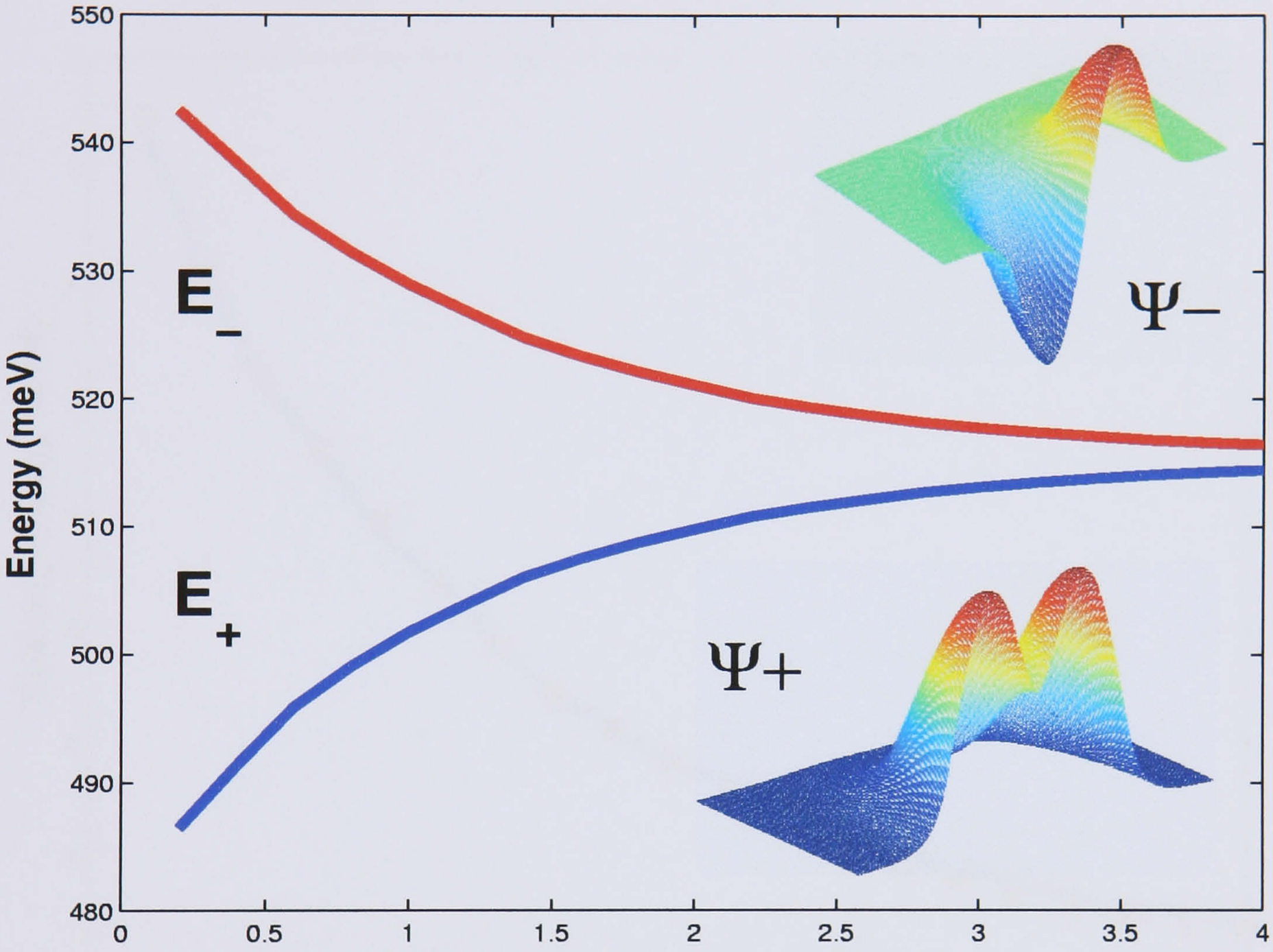

Figure 4.4: Ground and first excited states of an electron of effective mass $m^* = 0.023m_0$ within two identical coupled spherical quantum dots of radius $a = 8$ nm where the confinement potential barrier $V_0 = 1$ eV. The ground state Ψ_+ is a symmetric function whereas the first excited state Ψ_- is antisymmetric.

is Ψ_+.

$$\begin{aligned} \Psi_G &= \Psi_+ \\ E_G &= E_+ \end{aligned} \tag{4.47}$$

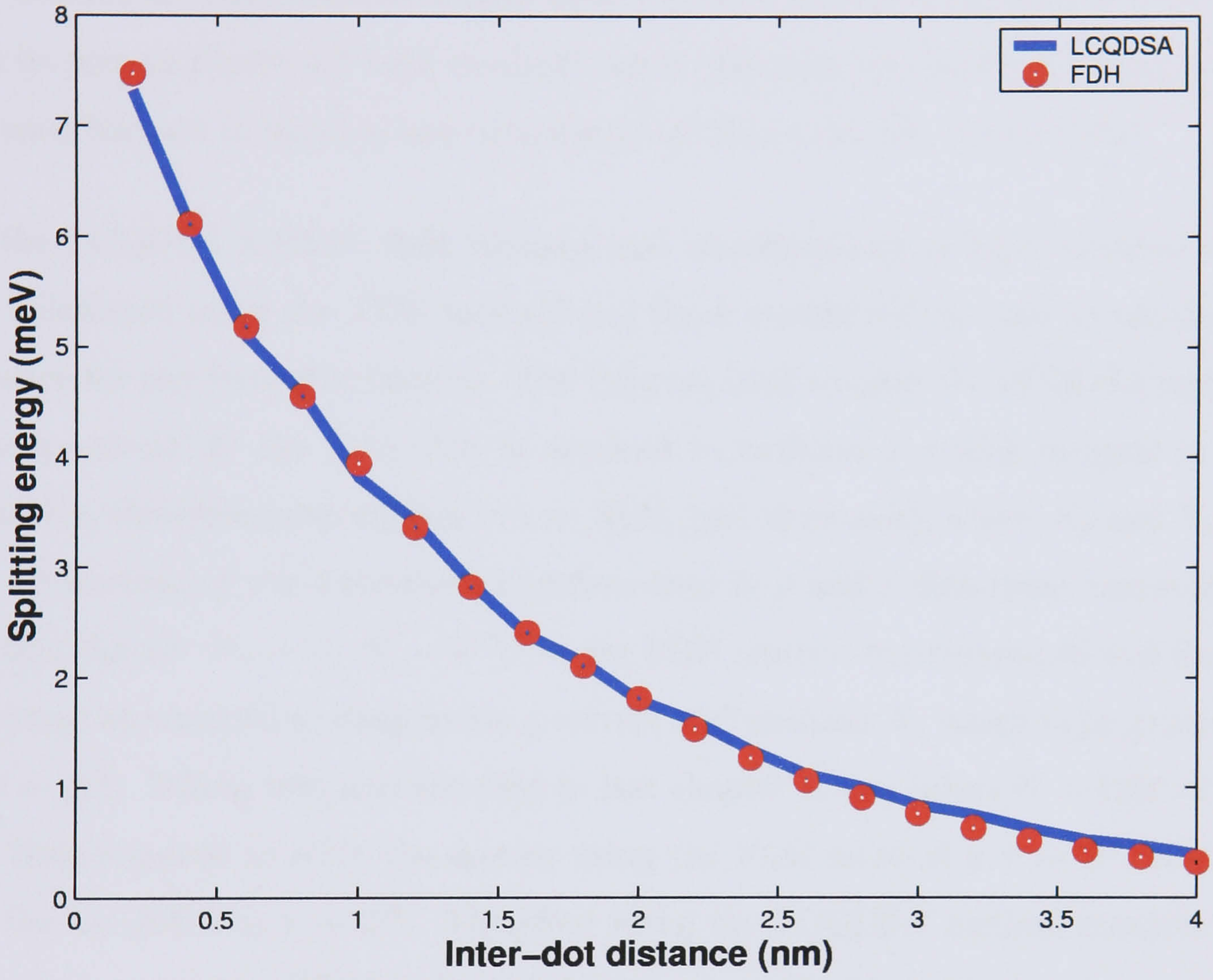

Figure 4.5: Splitting energy of an electron of effective mass $m^* = 0.023m_0$ within two identical coupled spherical quantum dots of radius 8 nm where the confinement potential barrier $V_0 = 1$ eV. The results obtained using the LCQDSA method has been contrasted with the values obtained applying the full diagonalisation of the system Hamiltonian method to the coupled system.

In order to compare the method with another one, the energy splitting between

the ground and first excited states is calculated applying the FDH method to the coupled system and both results are shown in Figure 4.5. The model consists of two spheres which possess cylindrical symmetry with respect to the z axis, as is shown in Figure 4.2. Energies has been calculated for an electron of effective mass $m^* = 0.023m_0$, the potential barrier $V_0 = 1$ eV and the QD's radius $a = 8$ nm. As can be seen in Figure 4.5 both methods agree. However, the LCQDSA method will be used because it requires less computational time than the FDH method.

In the LCQDSA method, first energies and wavefunctions of both isolated QD's are calculated using the FDH method and those results will be used to obtain the solution for any inter-dot distance. The time required to solve the LCQDSA method is proportional to the time that is required to perform a double integral in z, ρ variables, therefore proportional to $\tau \sim N_\rho N_z$ (per time unit), where N_ρ and N_z are the dimensions of the discretised wavefunctions in ρ and z directions, respectively (in this chapter $N_\rho = 2^8$, $N_z = 2^{10}$). In the FDH method the computational time is the same as required to diagonalise a matrix of dimension N, which is proportional to $\tau \sim N^3$. Taking into account that in last chapter it was taken $N = 1250 \approx 2^{10}$, the time required to solve the system using the FDH method is $\tau \sim 2^{30}$, whereas for the LCQDSA is $\tau \sim 2^{18}$. Therefore using the LCQDSA method requires less time than using the FDH method if the former method is applied more than two times (the LCQDSA method uses the FDH method twice in order to obtain the isolated QD energies and wavefunctions). The calculations have been realized on a *SUNW, UltraSPARC-III+, 900 MHz* machine and the time required to apply the FDH method is one minute, whereas the time required to apply the LCQDSA method (after calculating the energy and the wavefunctions of isolated QD's) is a second.

For inter-dot distances much greater than the QD radius, the difference between energies tends to zero. In this case the ground state is doubly degenerate. Bring-

ing the QD's in close proximity makes tunnelling possible between the dots and removes the degeneracy. Figure 4.4 shows how the degenerate ground state splits into two different energies, where the lowest value (E_+) corresponds to the even (symmetric) state (Ψ_+) and the first excited energy level (E_-) corresponds to an odd (antisymmetric) state (Ψ_-).

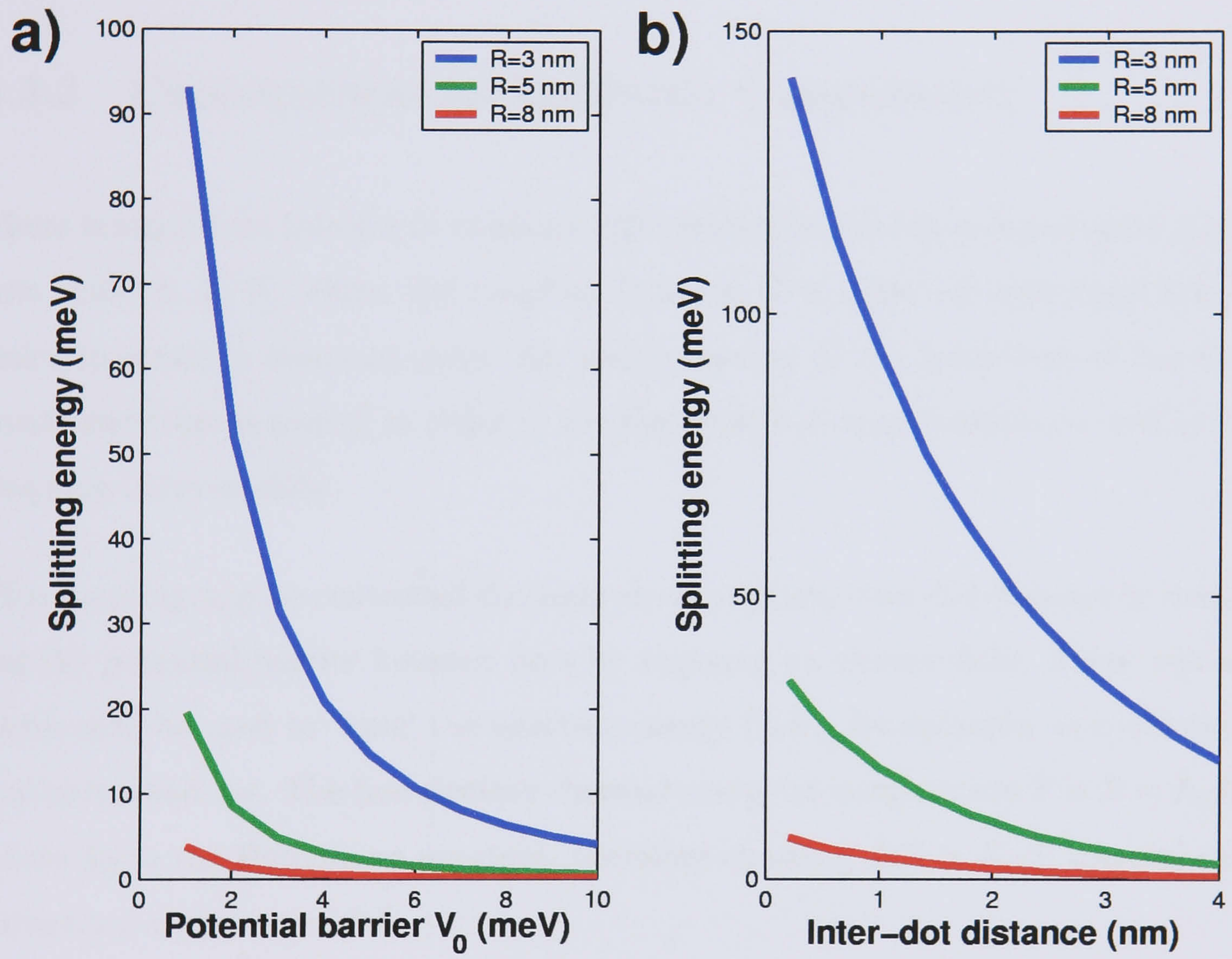

Figure 4.6: **a)**Splitting energy when the inter-dot distance is $d = 1$ nm for different dot radii changing the barrier potential V_0. **b)**Splitting energy for different dot radii changing the inter-dot distance when the potential barrier is $V_0 = 1$ eV.

Figure 4.6a) shows the splitting energy between the ground and first excited states for different potential barriers, V_0. Due to charge tunneling, which increases when the dot radius is decreased, the coupling between dots (splitting energy) at the same inter-dot distance decreases when the dot radius is increased, as can be seen in Figure 4.6b).

4.3.3 Consequences for Quantum Computation

There is significant interest in quantum information processing using coupled quantum dots [2, 1, 7], where the coupling between dots plays an important role in order to create a quantum gate. An understanding of the behaviour of the electronic structure is needed in order to use this system as a mechanism to control the coupling between dots.

This coupling may be controlled choosing an appropriate inter-dot distance or changing the potential barrier between dots by applying an electric field. These mechanisms may be used to 'tune' the splitting energy (ΔE), for example, to avoid thermal perturbations. The free electron thermal energy at temperature T is $E = K_B T$, where k_B is the Boltzmann constant, therefore choosing $\Delta E > K_B T$ thermal perturbations may be avoided.

4.4 Two vertically aligned SAD's

Vertically ordered quantum dots in multi-layer InAs/GaAs structures have attracted large interest for device application as light emitters and for their possible application in quantum computing.

In [1, 8] the spin of a single electron confined in a QD has been proposed as a qubit, and coupled self-assembled QD's as candidates to perform quantum operations. It has also been proposed the localisation of a carrier within a two SAD system as a qubit and the coupling between QD's as a mechanism to perform quantum operation [2]. These results have opened the possibility of using coupled SAD's for quantum information applications.

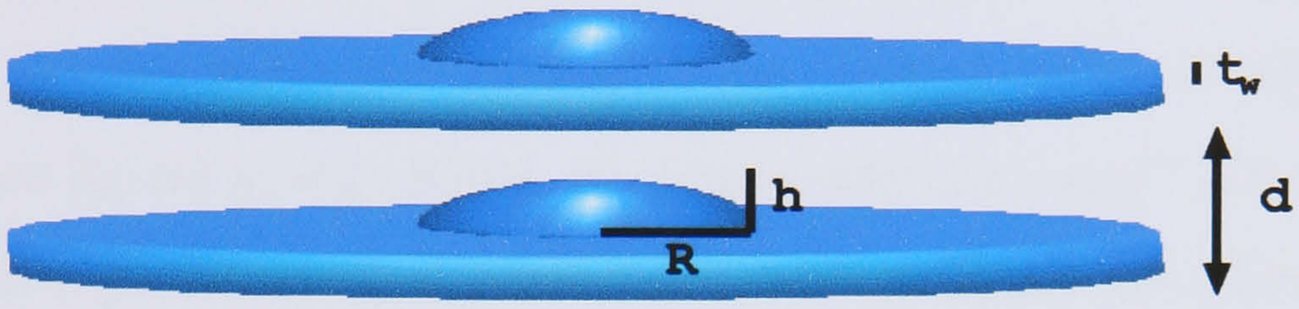

Figure 4.7: Representation of two vertically aligned elliptical SAD's. The dot is represented by a semi-ellipsoid of height h and radius at the base R. The wetting layer thickness is represented by t_w and d is the distance between wetting layers tops.

The electronic structure of vertically stacked self-assembled quantum disks[6] and pyramidal-shape quantum dots[3] has been studied. In this section the coupling between two ellipsoidal-shaped SAD's is studied and how this coupling changes is investigated when the inter-dot distance, the confining potential and the dimensions of the dots are varied.

The model consists of two vertically stacked ellipsoidal-shaped InAs/GaAs SAD's as is shown in Figure 4.7. Each dot is formed on a wetting layer of thickness t_w and covered by GaAs barrier material. Both QD's have the same height h and radius R and they are separated by a distance d, which is the distance between the top of both wetting layers, resulting in a QD tunneling barrier of thickness $d - h - t_w$ at $\rho = 0$ (see Figure 4.8). The difference in the conduction band offsets for the

QD(InAs) and surrounding material(GaAs) gives rise to the confining potential V_0.

4.4.1 Energies and Wavefunctions

The simplest model to illustrate the QD system is an envelope function approximation using a Hamiltonian with constant effective masses, and a three-dimensional potential that has the same geometrical shape of two coupled SAD's. In order to calculate the two lowest energy levels, the linear combination of QD's states approximation method explained before is used. In order to obtain the ground energy and wavefunction of each isolated SAD, the *adiabatic approximation* method is used. Dots 1 and 2 are referred as the dot at the bottom and the top respectively. The material parameters of quantum dot and wetting layers appears through the following effective units of energy and length: Rydberg $E_R = m_e e^4/2\epsilon^2\hbar^2$ and the effective Bohr radius, $a_B = \epsilon\hbar^2/m_e e^2$; where $m_e = 0.023m_0$, m_0 and $\epsilon = 13\epsilon_0$ are the effective mass of an electron, the electron rest mass and the dielectric constant, respectively.

The ground wavefunctions of the isolated dots 1 and 2; Ψ_1 and Ψ_2 respectively, may be obtained from Equation 2.85.

$$\Psi^{\mathrm{D}}(\rho,\phi,z) = \frac{e^{im\phi}}{\sqrt{2\pi}} g_{n\rho}(z) f_m(\rho) \tag{4.48}$$

Due to the shape of the SAD, ψ_1 and ψ_2 have cylindrical symmetry and may be expressed in cylindrical coordinates.

$$\psi_1(\rho,\phi,z) = \psi_1(\rho,z) = \frac{g_{n=0\rho}(z+z_0) f_{m=0}(\rho)}{\sqrt{2\pi}} \tag{4.49}$$

$$\psi_2(\rho,\phi,z) = \psi_2(\rho,z) = \frac{g_{n=0\rho}(z-z_0) f_{m=0}(\rho)}{\sqrt{2\pi}} \tag{4.50}$$

where $z_0 = (d+t_w+h)/2$. Two vertically aligned SAD's have cylindrical symmetry, therefore the potential may be expressed in cylindrical coordinates as is illustrated in Figure 4.8.

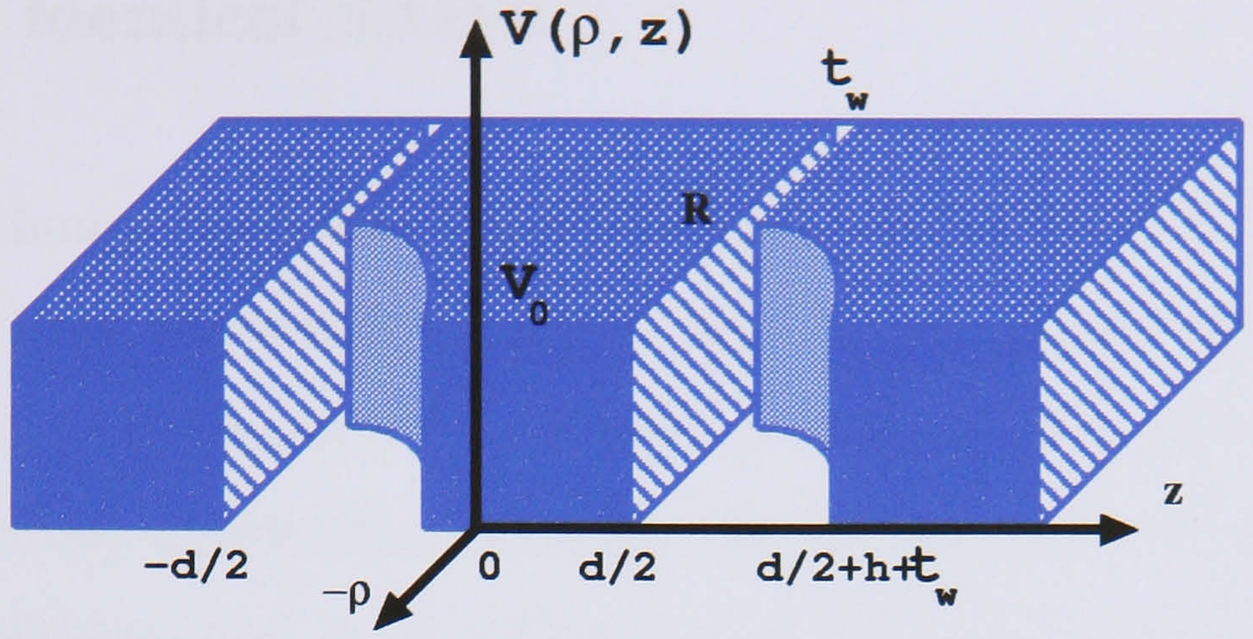

Figure 4.8: Schematic representation of the potential of two vertically aligned SAD's of radius R, height h and the wetting layers tops are separated by a distance d.

$$V(\rho,\phi,z) = \begin{cases} 0 & \text{inside both SAD's} \\ V_0 & \text{outside them} \end{cases} \tag{4.51}$$

Due to SAD's cylindrical symmetry, the potential V does not depend upon the angular variable ϕ. Therefore $V(\rho,\phi,z) = V(\rho,z)$. Introducing V_1 and V_2 as the confining potential of isolated SAD 1 and SAD 2 respectively, $V(\rho,z)$ may be expressed as $V = V_1+V_2-V_0$. Now using the LCQDSA method and following Equation 4.25, the ground and first excited, Ψ_+ and Ψ_- respectively, may be written as:

$$\Psi_+ = A_+(C_{1+}\psi_1 + C_{2+}\psi_2) \tag{4.52}$$

$$\Psi_- = A_-(C_{1-}\psi_1 + C_{2-}\psi_2) \tag{4.53}$$

where C_{1+}, C_{2+} and $A_\pm$ are given by Equations 4.26-4.28 and their energies are given by Equation 4.24

$$\langle E\rangle_\pm = \frac{-b \mp \sqrt{b^2-4ac}}{2a} \tag{4.54}$$

where $a = 1-S^2$, $b = 2H_{12}S - H_{11} - H_{22}$ and $c = H_{11}H_{22} - {H_{11}}^2$.

4.4.2 Two identical SAD's

In this case, although both SAD's are identical, due to the fact that neither the potential $V(\rho, z)$ nor the wavefunctions ψ_1 and ψ_2 are y-axis symmetric, H_{11} and H_{22} are not equal. Also Ψ_+ and Ψ_- are no longer strictly even and odd functions as they were in the case of two spherical QD's. But we use this notation to emphasise that Ψ_+ is an addition and Ψ_- a subtraction of functions ψ_1 and ψ_2. Parameters a, b and c are given by $a = 1 - S^2$, $b = 2H_{12}S - H_{11} - H_{22}$ and $c = H_{11}H_{22} - {H_{11}}^2$. Once again ψ_1 and ψ_2 are real functions thus $H_{21} = H_{12}$ and $S = S^*$. Elements H_{ij} may be obtained from Equations 4.15-4.17 which leads to

$$H_{11} = (E_1 - V_0) + 2\pi \int_{-\infty}^{\infty} \mathrm{d}z \int_{0}^{\infty} \mathrm{d}\rho\rho V_1(\rho, z){\psi_1}^2(\rho, z) \tag{4.55}$$

$$H_{22} = (E_2 - V_0) + 2\pi \int_{-\infty}^{\infty} \mathrm{d}z \int_{0}^{\infty} \mathrm{d}\rho\rho V_2(\rho, z){\psi_2}^2(\rho, z) \tag{4.56}$$

$$H_{12} = (E_1 - V_0) + 2\pi \int_{-\infty}^{\infty} \mathrm{d}z \int_{0}^{\infty} \mathrm{d}\rho\rho V_2(\rho, z)\psi_1(\rho, z)\psi_2(\rho, z) \tag{4.57}$$

The overlap between ψ_1 and ψ_2, $S = \langle\psi_1|\psi_2\rangle$, is given by

$$S = 2\pi \int_{-\infty}^{\infty} \mathrm{d}z \int_{0}^{\infty} \mathrm{d}\rho\rho\psi_1(\rho, z)\psi_2(\rho, z) \tag{4.58}$$

Once all the parameters have been described, the ground and first excited energy levels can be calculated. Figure 4.9 shows the dependence of the electronic states on the inter-dot distance d for two identical SAD's of radius $R = 8$ nm, height $h = 2$ nm, wetting layer thickness $t_w = 0.552$ nm and potential barrier height $V_0 = 1$ eV. All the parameters have been taken from [6]. It is important to remark that at small inter-dot distances, i.e. $d = 3$ nm, the energy level of the first excited state is higher than the confinement barrier potential, $E_- > V_0$. In these cases the first excited state is not considered to be confined to the SAD.

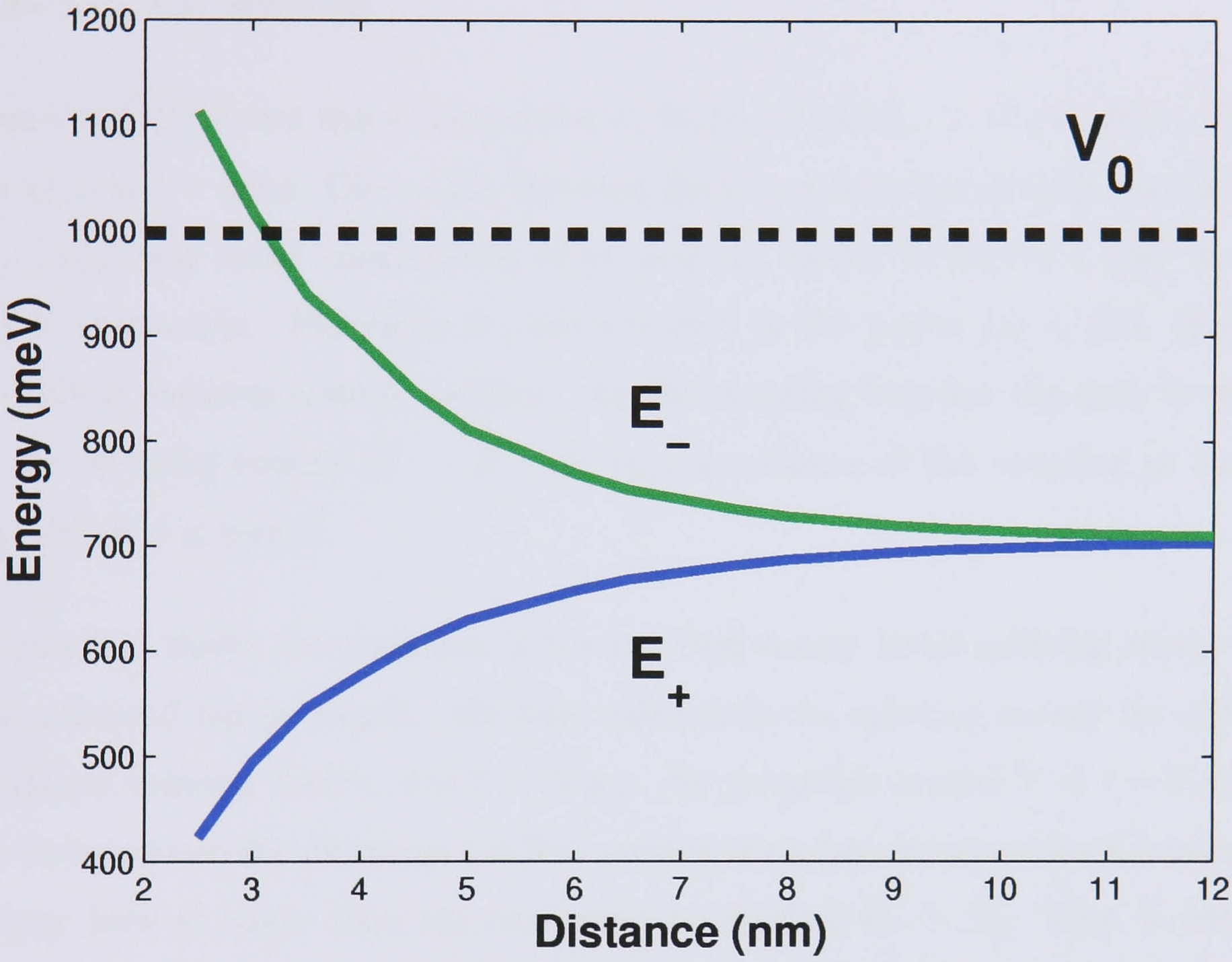

Figure 4.9: Energy levels evolution of an electron within two identical vertically aligned SAD's against inter-dot distance d. The radius and the height of the SAD are $R = 8$ nm and $h = 2$ nm, respectively; the wetting layer thickness $t_w = 0.552$ nm and potential barrier height $V_0 = 1$ eV.

The wavefunctions associated with energies $E_\pm$ are given by Equation 4.25

$$\Psi_\pm = A_\pm(C_{1\pm}\psi_1 + C_{2\pm}\psi_2) \tag{4.59}$$

where parameters $C_{1\pm}, C_{2\pm}, A_\pm$ may be obtained by substituting H_{ij}, S into Equations 4.26, 4.27 and 4.28.

Figure 4.10b) shows the z-component of $\Psi_\pm(\rho, z)$ when $\rho = 0$ and the inter-dot distance is $d = 4$ nm. Due to the fact that the potential is not strictly symmetrical, $\Psi_\pm$ which are linear combination of ψ_1 and ψ_2, shown in Figure 4.10a), are not y-axis symmetric. Functions $\Psi_\pm$ are non-zero in the region $|z| < d/2$, therefore tunnelling between dots is possible. As the coupling between the dots is related to the splitting energy $|E_- - E_+|$ we have a measure of the coupling as the dot separation d is varied.

Figure 4.11 shows the evolution of the two first energy levels splitting energy with the potential barrier depth. We have calculated the splitting energy for different distances between SAD's, $d = 3 - 12$ nm. At potentials around $V = 1 - 2$ eV and for certain inter-dot distances the first excited state become unconfined because its energy level is larger than the confinement potential $E_- > V_0$. That is why the splitting energy at 3 nm of inter-dot distance in Figure 4.11 is shown starting from $V_0 \approx 2$ eV. Therefore these plots represent the splitting energy between two confined states, and can be observed that the splitting energy decreases with V_0.

Taking QD heights as constants, $h_1 = h_2 = h = 2$ nm, the energies are calculated varying the radius. In Figure 4.12a) the splitting energy is plotted versus the distance for different QD radii, $R = 8 - 9$ nm, and it can be seen that the variations are minimal. Also plotting the splitting energy versus QD radius for different distances $d = 3 - 13$ nm, as can be seen in Figure 4.12b), which shows that the splitting energy is more or less constant. Widening both SAD's radii changes the energy level E_0 and expands wavefunctions ψ_1 and ψ_2 within the lateral direction. This

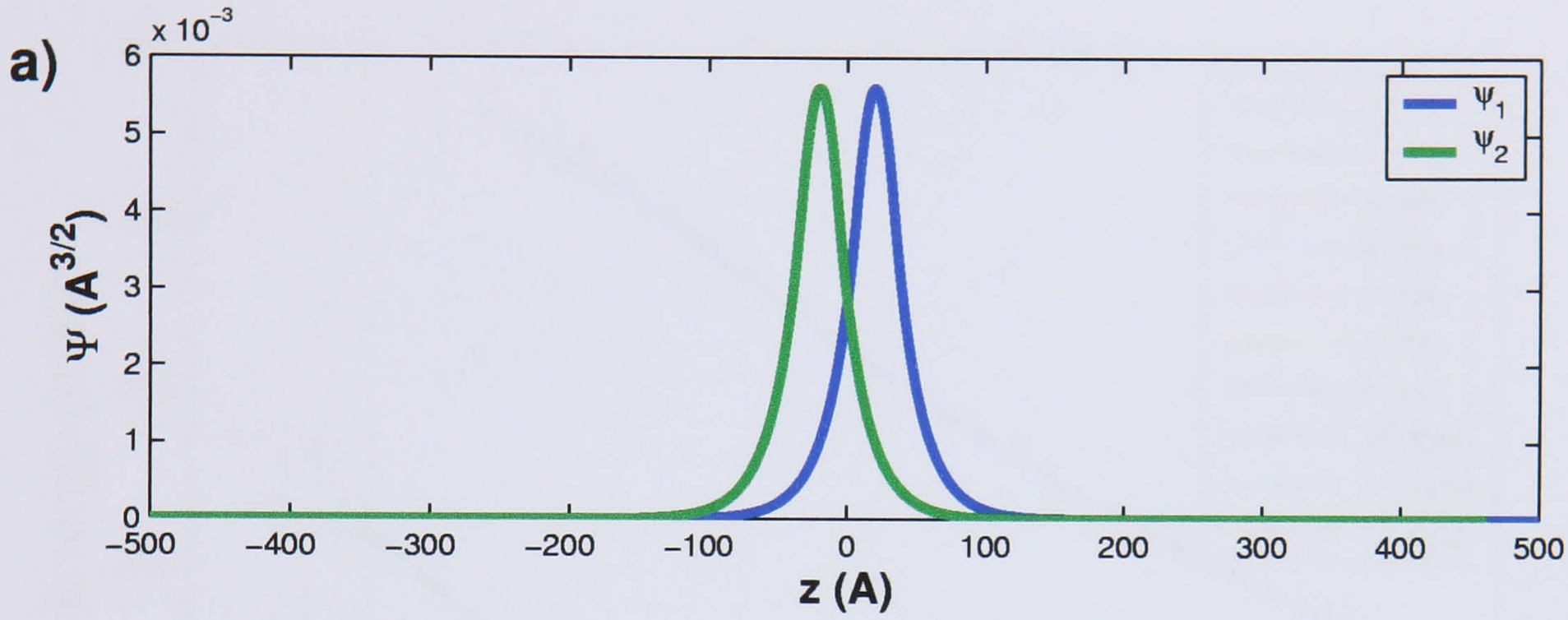

Figure 4.10: **a)**z-projection of ψ_1 and ψ_2 wavefunctions for $\rho = 0$. Dots 1 and 2 are separated by a distance $d = 4$ nm. **b)**z-projection of Ψ_+ and Ψ_-.

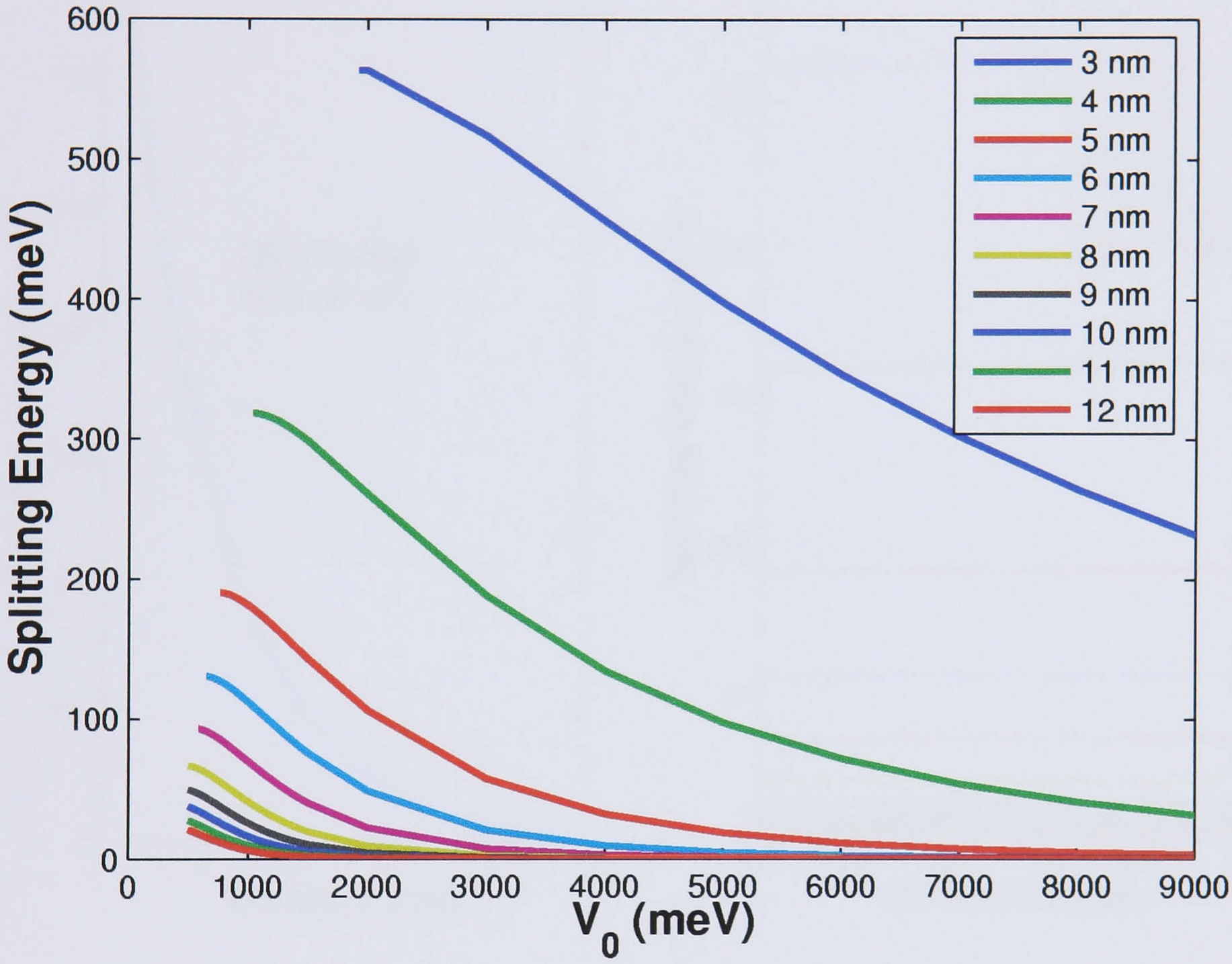

Figure 4.11: Splitting energy evolution versus potential barrier depth V_0 for different distances $d = 3 - 12$ nm for two identical SAD's of radius $R = 8$ nm and height $h = 2$ nm. The legend shows the distance between wetting layers.

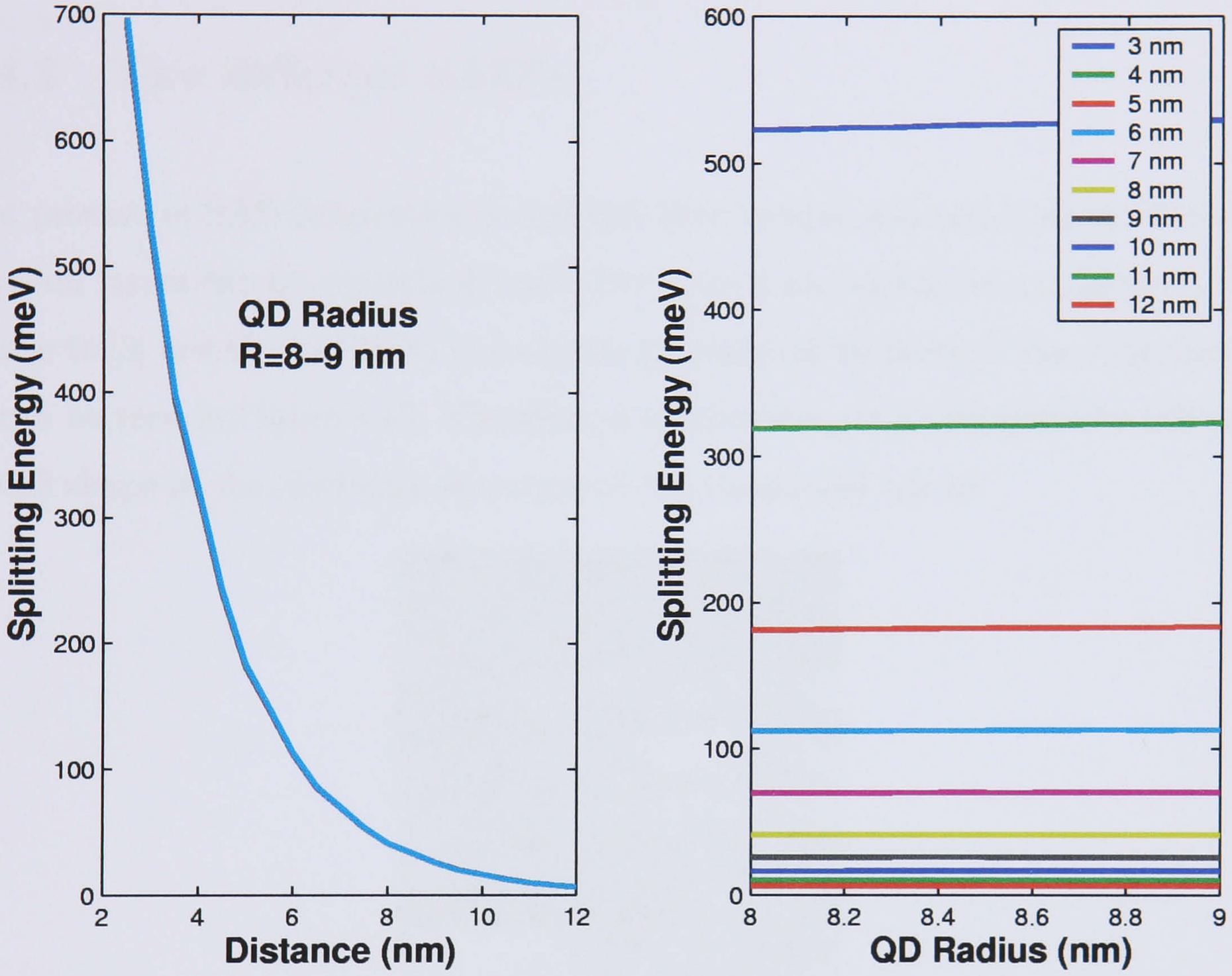

Figure 4.12: Splitting energy versus **a)**wetting layers distance for different QD radii. **b)**QD radius for different distances between layers. The legend shows the distance between lower and upper wetting layer. QD's height and potential depth remain constant: $h = 2$ nm, $V_0 = 1$ eV.

slightly alters the overlap S, which mainly depends on the vertical component of ψ_1 and ψ_2. Therefore the coupling between two vertically aligned SAD's remains almost invariable under changes on the lateral size of both of them.

4.4.3 Two different SAD's

The process of SAD fabrication is still not very precise and although the distance between layers can be controlled, both dots cannot be considered as identical. Reference to [3] reveals that QD's size slightly increases as we move to the upper layers, as can be seen in Figure 4.13. Therefore it is interesting to investigate the influence of QD shape in the electronic structure of the considered model.

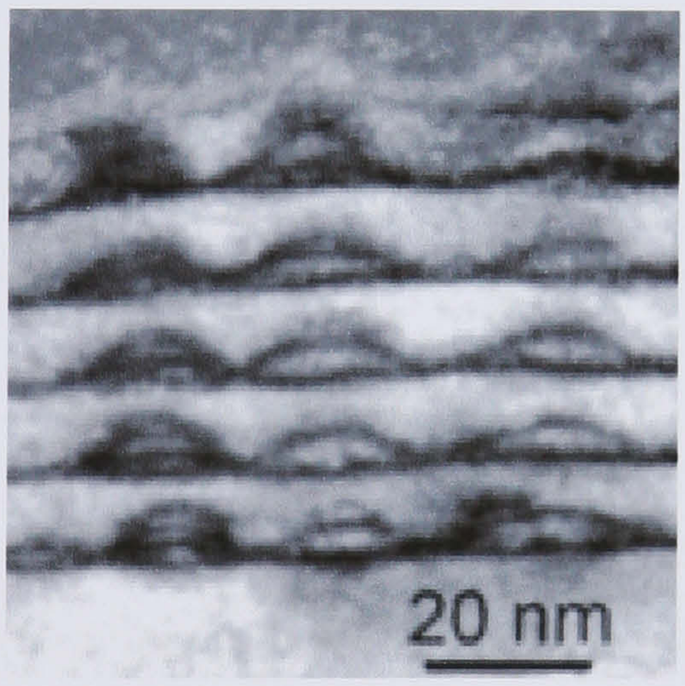

Figure 4.13: Structure consisting of 5 embedded layers of InAs QD's, separated by 10-nm thick GaAs spacers (taken from [3]).

In [6] the electronic structure of two different radius vertically stacked self-assembled quantum disks is studied. In order to compare the model with that described in reference [3] we calculate the two lowest energies of two different radius ellipsoidal SAD's taking as parameters the same height and radius that appears in [6]: QD's

height $h_1 = h_2 = 2$ nm and QD's radius $R_1 = 8$ and $R_2 = 8.5$ nm.

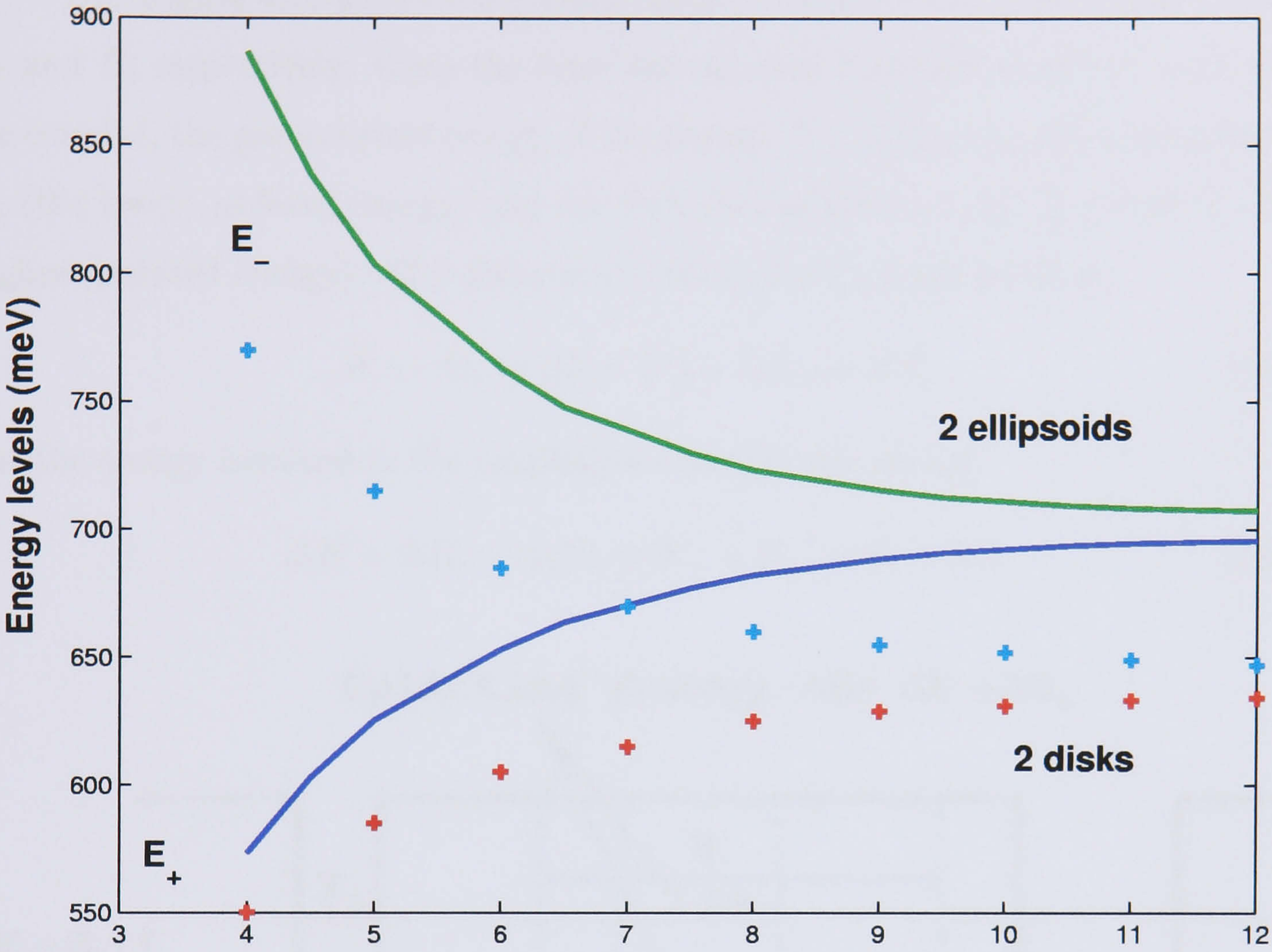

Figure 4.14: Two lowest energy levels for two vertically aligned ellipsoidal SAD's and self-assembled quantum disks of different radius at the base, $R_1 = 8$ and $R_2 = 8.5$ (taken from [6]), versus wetting layer distance.

Figure 4.14 shows the comparison between the two models. The volume of the ellipsoidal structure is smaller than the volume of the disk and hence a particle within the ellipsoid is more confined and has higher energies. But apart from that there is no significant difference between both models.

Unlike the case of identical QD's, the splitting energy of two different QD's, ΔE, is

not the same as the difference between first excited state and ground state energies $E_- - E_+$. Figure 4.15 shows the ground states of isolated dot 1 and 2 (solid lines), E_1 and E_2 respectively. Once the inter-dot distance becomes small and both dots are coupled, the ground state energy of the system, E_+, splits from the lowest energy E_2 (the lowest isolated energy) and the first excited state energy, E_-, from E_1 (the highest isolated energy). The difference between both energy levels is

$$E_- - E_+ = |E_2 - E_1| + \Delta E_+ + \Delta E_- \tag{4.60}$$

but the energy involved in the coupling is the splitting energy

$$\Delta E = \Delta E_- + \Delta E_+ = E_- - E_+ - |E_2 - E_1| \tag{4.61}$$

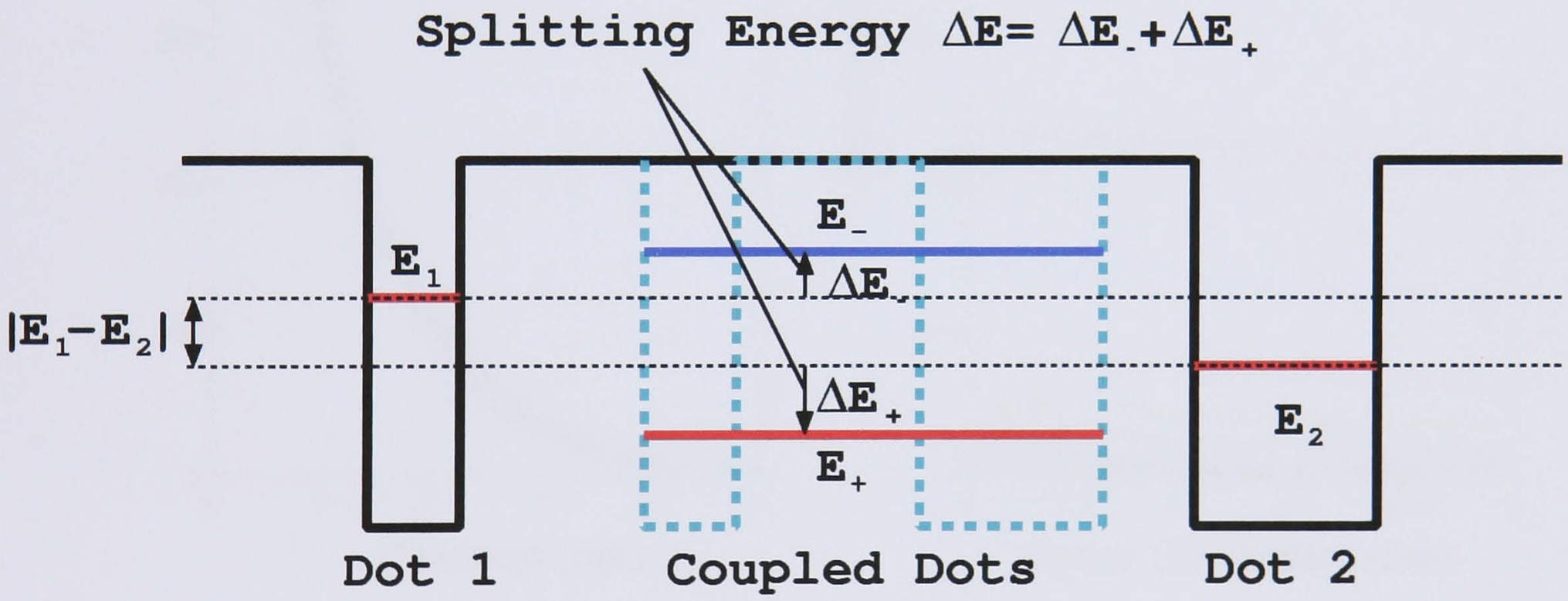

Figure 4.15: Ground state energy level of isolated dot 1 and 2 (solid lines) and coupled QD system two first energy levels (dashed lines).

The evolution in splitting energy will now be calculated as the upper QD radius is varied but keeping the QD heights constant at, $h = 2$ nm, and lower QD radius, $R = 8$ nm. Figure 4.16a) shows that the splitting energy changes slowly with the upper QD radius. Only for short distances, $d = 3-5$ nm, there is a marked decrease, as can be seen in Figure 4.16b).

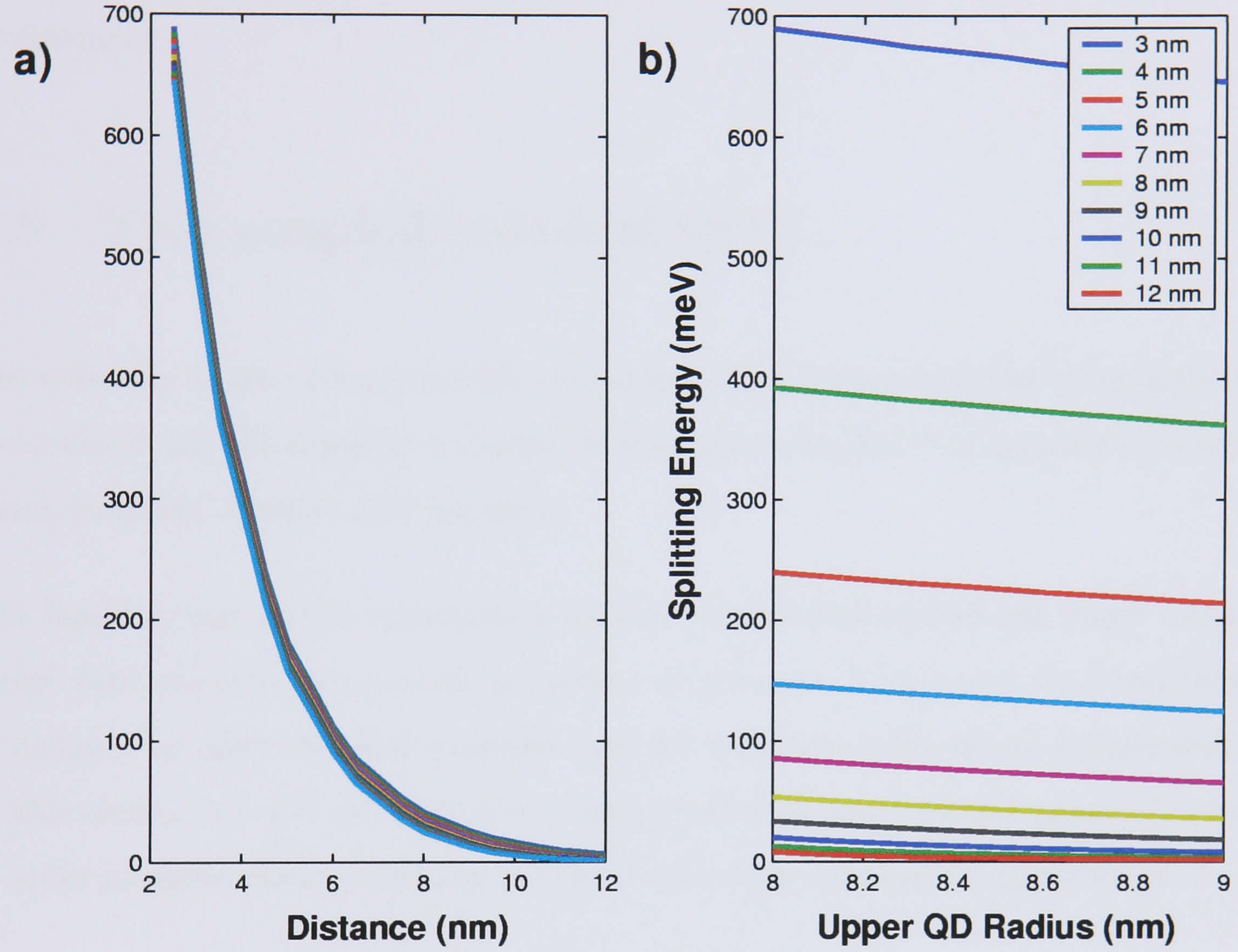

Figure 4.16: Splitting energy versus **a)**wetting layers distance for different upper QD radii. **b)**upper QD radius for different distances between layers. The legend shows the distance between wetting layers. The QD's height and potential depth remain constant: $R = 8$ nm, $V_0 = 1$ eV.

The splitting energy dependence upon changes in the upper QD height is shown in Figure 4.17a). It shows that the system is more sensitive to changes in the height than in the radius of one dot. It is because tunneling between dots occurs vertically and the vertical confinement plays a more important role than the lateral confinement.

4.5 Two coupled colloidal QD's

The assembly of two or more colloidal quantum dots has been achieved using protein molecules[9, 10]. As it has been studied before, when the inter-dot distance becomes small, coupling between dots appears.

The liquid nature of the surrounding material makes this system less likely to interact with external factors such as carriers or phonons. This opens the possibility of using of coupled colloidal quantum dots for quantum information applications. In this section we will calculate the coupling between two colloidal quantum dots in order to assess their suitability for use in quantum information applications.

A simple method is presented here to calculate the shift between the ground and first excited energy levels of two coupled colloidal QD's using the linear combination of QD state approximation (LCQDSA) method explained in Section 4.2, where single colloidal QD states have been obtained solving the effective mass approximation Hamiltonian. The spin effects have not been taken into account. There are more sophisticated theoretical approaches to calculate the energy levels of small colloidal QD's like tight-binding method [11], but the aim of this section is to make a qualitative study of the QD's.

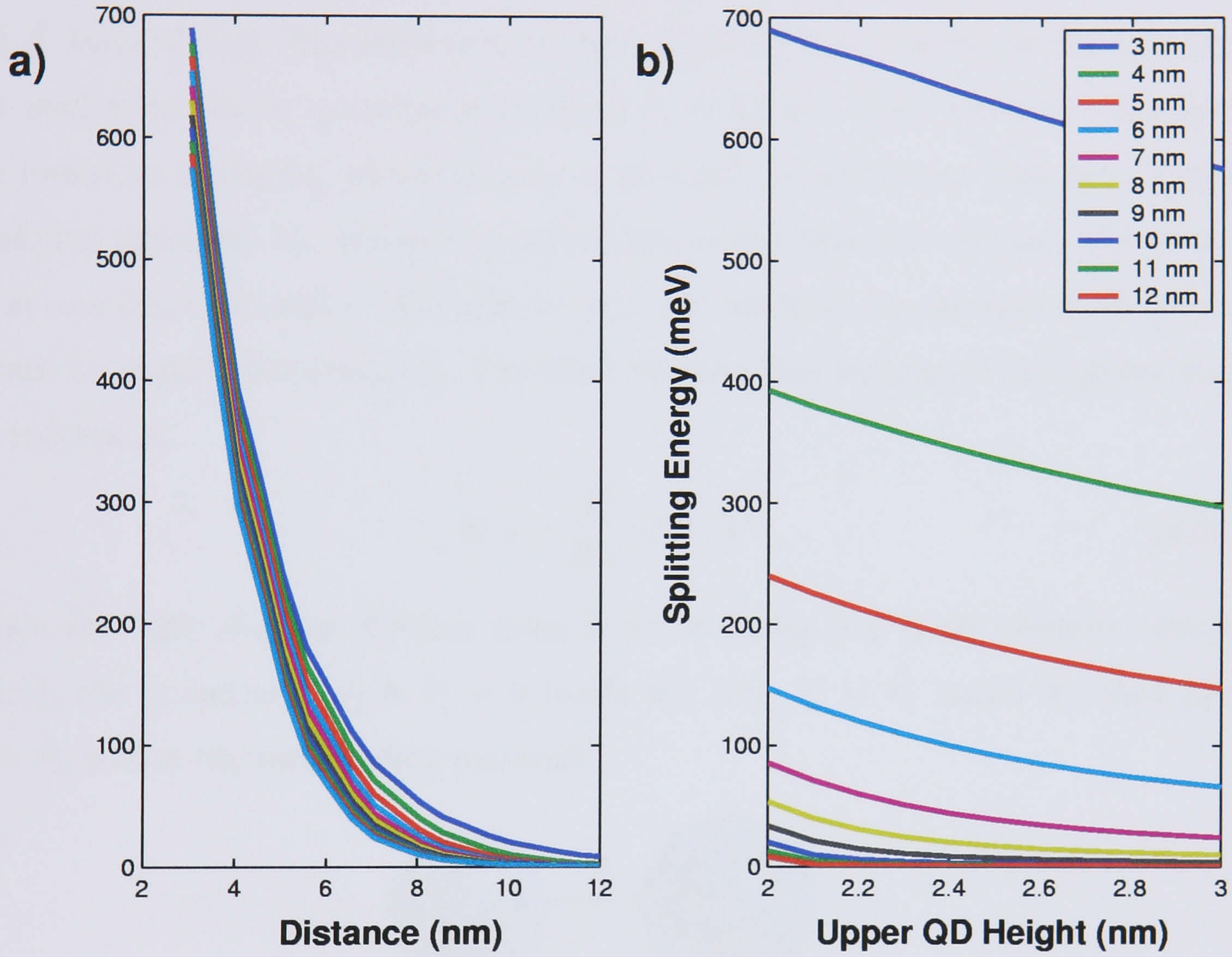

Figure 4.17: Splitting energy versus **a)**wetting layers distance for different upper QD height. **b)**upper QD height for different distances between layers. The legend shows the distance between lower and upper wetting layer. QD's radius and potential depth remain constant: $h = 2$ nm, $V_0 = 1$ eV.

4.5.1 Model

The system is composed of two core-shell spherical quantum dots (Figure 4.18). Both dots are formed by a core of CdSe of radii R_1 and R_2 (15-20 Å) covered by a 3 Å layer of ZnS. The difference in the conduction band offsets of the core and the shell gives rise to a confining potential $V_s = 0.9$ eV. We assume that the dots are linked by a protein, which behaves as an insulator and hence they have a high confining potential V_0. However a probability exists that the electron will tunnel from one dot to another. We take $V_0 = 3$ eV which is representative of typical values for organic materials[12]. The effective mass Hamiltonian of the system may be written as

$$\hat{H} = -\frac{\hbar^2}{2m^*}\nabla^2 + V \tag{4.62}$$

where the light electron effective mass is $m^* = 0.1m_0$ (m_0 is the electron resting mass), the potential $V(\mathbf{r})$ is $V = 0$ inside the core, $V = V_s$ inside the shell and $V = V_0$ within the surrounding material.

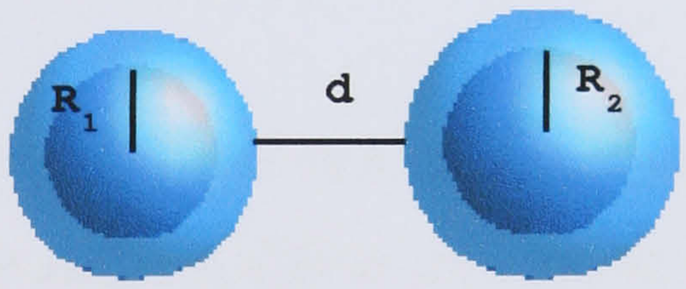

Figure 4.18: Picture of two coupled colloidal QD's where d is the distance between surfaces.

When the two dots are far apart, the solutions of each isolated quantum dot are eigenvalues of the system Hamiltonian. When the inter-dot distance becomes small, tunneling between dots appears and the energy levels of the system becomes inter-dot distance-dependent.

In this section it is shown how the coupling between QD's changes with the inter-dot distance for spherical QD's. It is noted that increasing the distance is physically equivalent to raising the inter-dot potential barrier, which can be achieved experimentally by e.g. applying a gate voltage between the dots [1]. Therefore the effect of such gate voltages is described in the model simply by a change of the inter-dot distance d.

4.5.2 Energies and Wavefunctions

As before for the two vertically aligned SAD's, a Hamiltonian with constant effective masses and a three dimensional potential that has the same geometry as the two coupled colloidal QD's will be used. The potential is represented schematically in Figure 4.19d). In order to calculate the two lowest energy levels we use the LCQDSA method described previously. We will also use the FDH method explained in Section 3.3.3 in order to obtain the ground-state energy and wavefunction of each isolated QD.

Referring to dot 1 and dot 2 as the left and right dot respectively (Figure 4.18), the ground state energy of each isolated QD is denoted as E_1 and E_2 and their wavefunction ψ_1 and ψ_2 can be obtained from Equation 2.45. Now using the LCQDSA method and following Equation 4.25, the ground and first excited, Ψ_+ and Ψ_- respectively, may be written as:

$$\Psi_+ = A_+(C_{1+}\psi_1 + C_{2+}\psi_2) \tag{4.63}$$

$$\Psi_- = A_-(C_{1-}\psi_1 + C_{2-}\psi_2) \tag{4.64}$$

where C_{1+}, C_{2+} and $A_\pm$ are given by Equations 4.26-4.28 and their energies are given by Equation 4.24

$$\langle E\rangle_\pm = \frac{-b \mp \sqrt{b^2 - 4ac}}{2a} \tag{4.65}$$

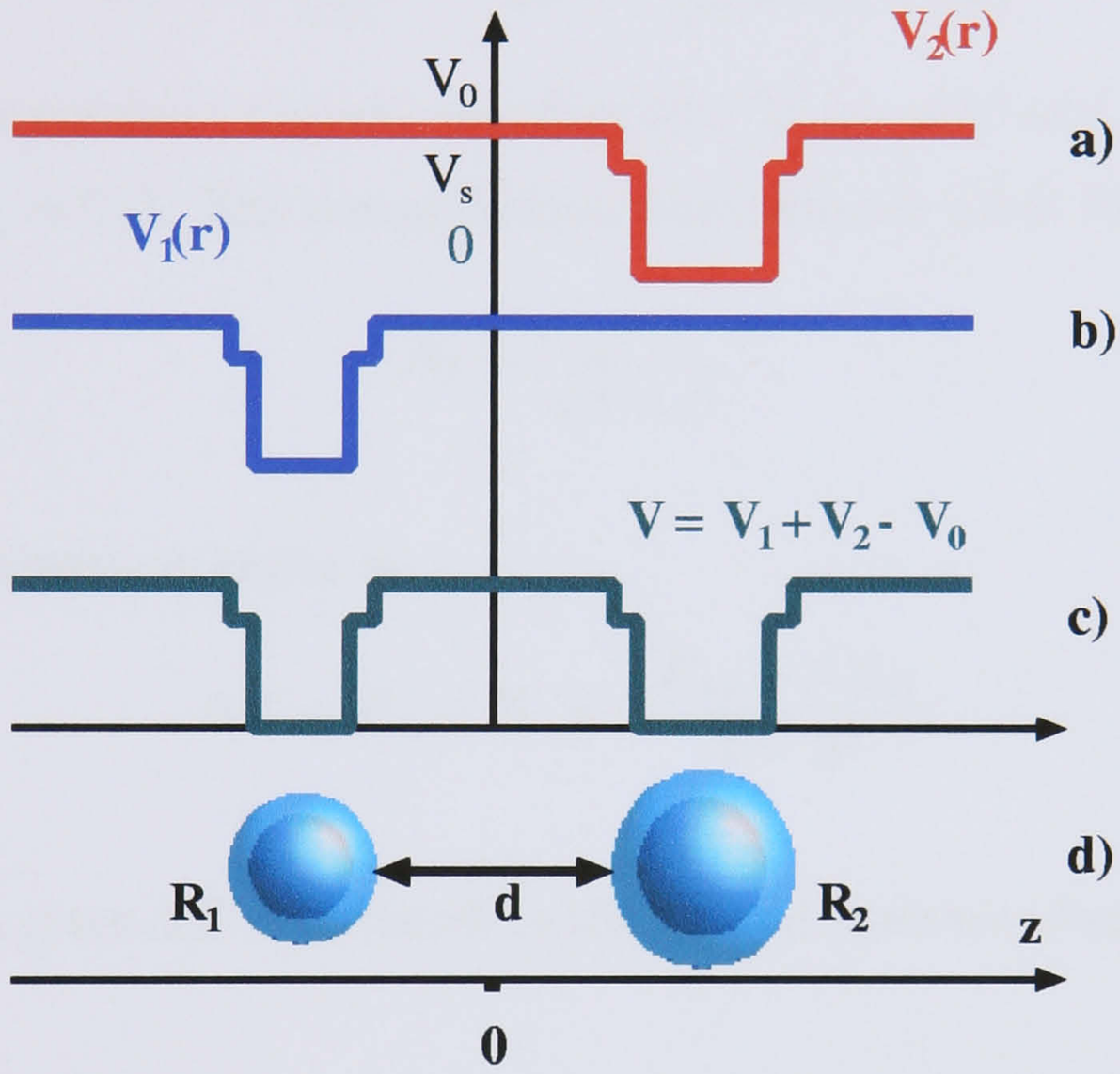

Figure 4.19: **a),b)**Schematic representation of isolated colloidal QD potentials. **c)**Coupled QD potential. **d)**Representation of two coupled colloidal QD's aligned in z direction.

4.5.3 Two identical spherical QD's

In the case of two identical QD's ($H_{11} = H_{22}$) energies and wavefunctions of ground and first excited states are given by

$$\begin{aligned} E_- &= \tfrac{H_{11}-H_{12}}{1-S} \qquad |\psi_-\rangle = \tfrac{A_-}{\sqrt{2}}(|\psi_1\rangle - |\psi_2\rangle) \\ E_+ &= \tfrac{H_{11}+H_{12}}{1+S} \qquad |\psi_+\rangle = \tfrac{A_+}{\sqrt{2}}(|\psi_1\rangle + |\psi_2\rangle) \end{aligned} \tag{4.66}$$

where $\langle E\rangle_-$ corresponds to the odd wavefunction ($C_1 = -C_2$) and $\langle E\rangle_+$ to the even wavefunction ($C_1 = C_2$). The normalisation constants are given by

$$A_\pm = \frac{1}{\sqrt{1 \pm S}} \tag{4.67}$$

The difference between energies is

$$\Delta E = E_+ - E_- = 2\frac{H_{12} - SH_{11}}{1 - S^2} \tag{4.68}$$

The last equation gives $\Delta E > 0$, therefore the ground-state wavefunction and energy are

$$\begin{aligned} |\Psi_G\rangle &= |\Psi_+\rangle \\ E_G &= E_+ \end{aligned} \tag{4.69}$$

For inter-dot distances much greater than the dot radius the difference between energies tends to zero. In this case the ground state is doubly degenerate. Bringing the QD's in close proximity makes tunnelling possible between the dots and removes this degeneracy. Figure 4.20 shows how the degenerate ground state splits into two different values, where the lowest value correspond to the even state (E_+). Therefore the distance between layers might be used to "tune" the coupling of the dots. For low distances, $d \sim$ Å, choosing a temperature T such that the splitting energy is bigger than the energy $K_B T$ avoids thermal perturbations.

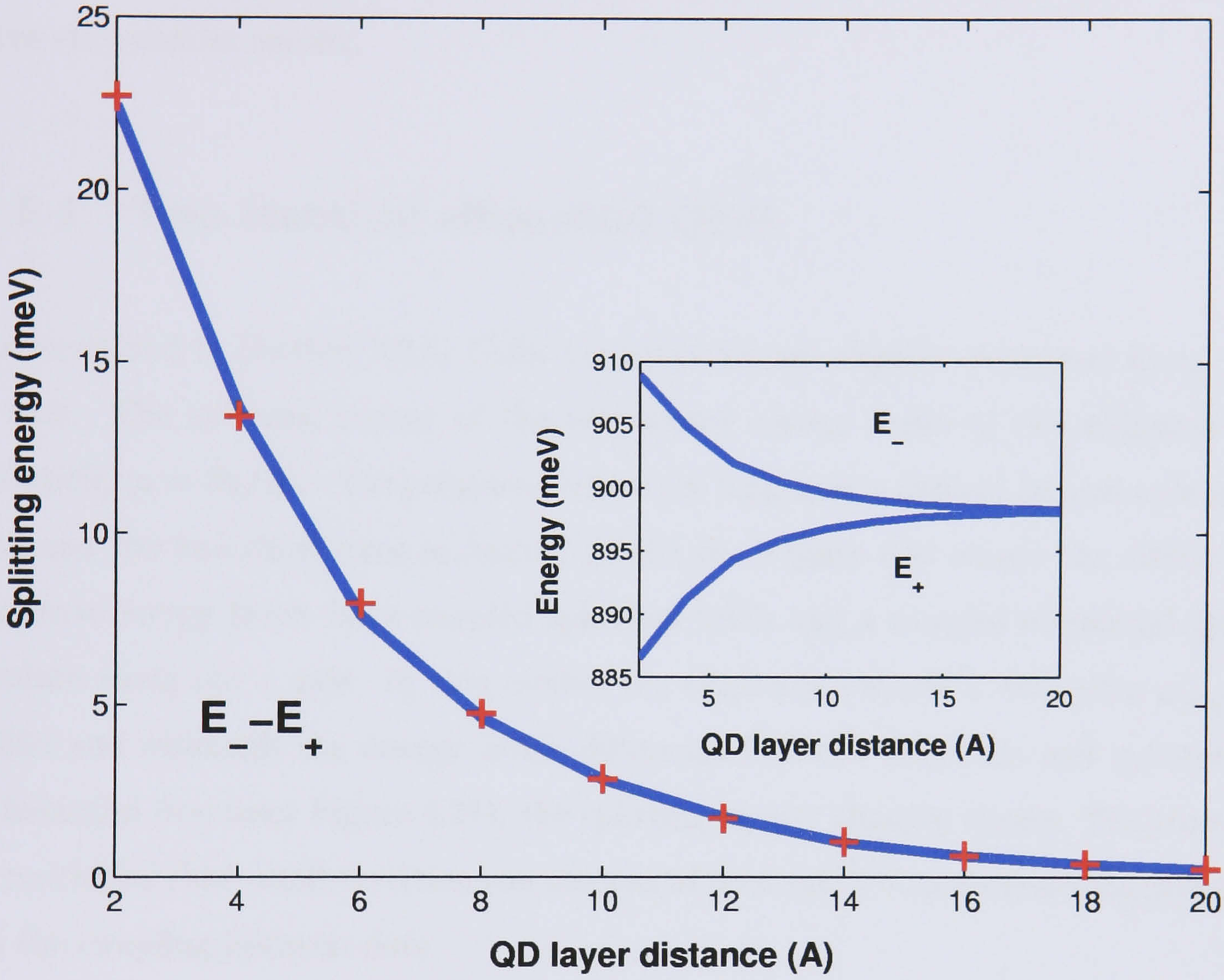

Figure 4.20: Energy difference between the first excited and the ground state of two identical spherical QD's. The QD core radius is $R = 15$ Å and the thickness of the layer $R_L = 3$ Å. The plus dot line shows the splitting energy obtained using the full diagonalisation of effective mass system Hamiltonian method.

This model has cylindrical symmetry, thus the full diagonalisation of the effective mass system Hamiltonian explained in Section 3.3 may be used in order to calculate the splitting energy between two lowest energy levels. The crosses in Figure 4.20 shows the splitting energy using the FDH method. As can be seen, both methods give very similar results.

4.5.4 Two identical ellipsoidal QD's

As explained in Section 3.3.5, CdSe nanocrystals are slightly elongated along the z axis. The splitting energy of the two lowest energy levels of two ellipsoids of ellipticity $\mu = R_z/R_0 - 1$ is presented where the long axis is defined as having length R_z, and the two short axes as having length R_0. Figure 4.21 shows the difference between energy levels for a coupled spherical QD's and a coupled ellipsoidal QD's prolate along the z axis. In this model, the ellipsoids present a ellipticity $\mu_{\text{core}} = 0.066$ and although the energy levels difference between ellipsoids and spheres is substantial (see inset Figure 4.21), the splitting energy changes slowly. Therefore it is concluded that small variations on the size of both QD's do not create big changes on the coupling between dots.

4.5.5 Variations in the shape

In this section small changes in the shape of the dots are simulated. Expanding a spherical QD z axis turns it into an ellipsoid. Now the splitting energy is studied varying the z dimension of the right QD, R_z, for two different shapes for the left QD: a sphere and an ellipsoid, as can be seen in Figures 4.22a),b). In order to calculate the two first energy levels the LCQDSA method is used, where the ground state of each isolated QD has been obtained using the FDH method described previously.

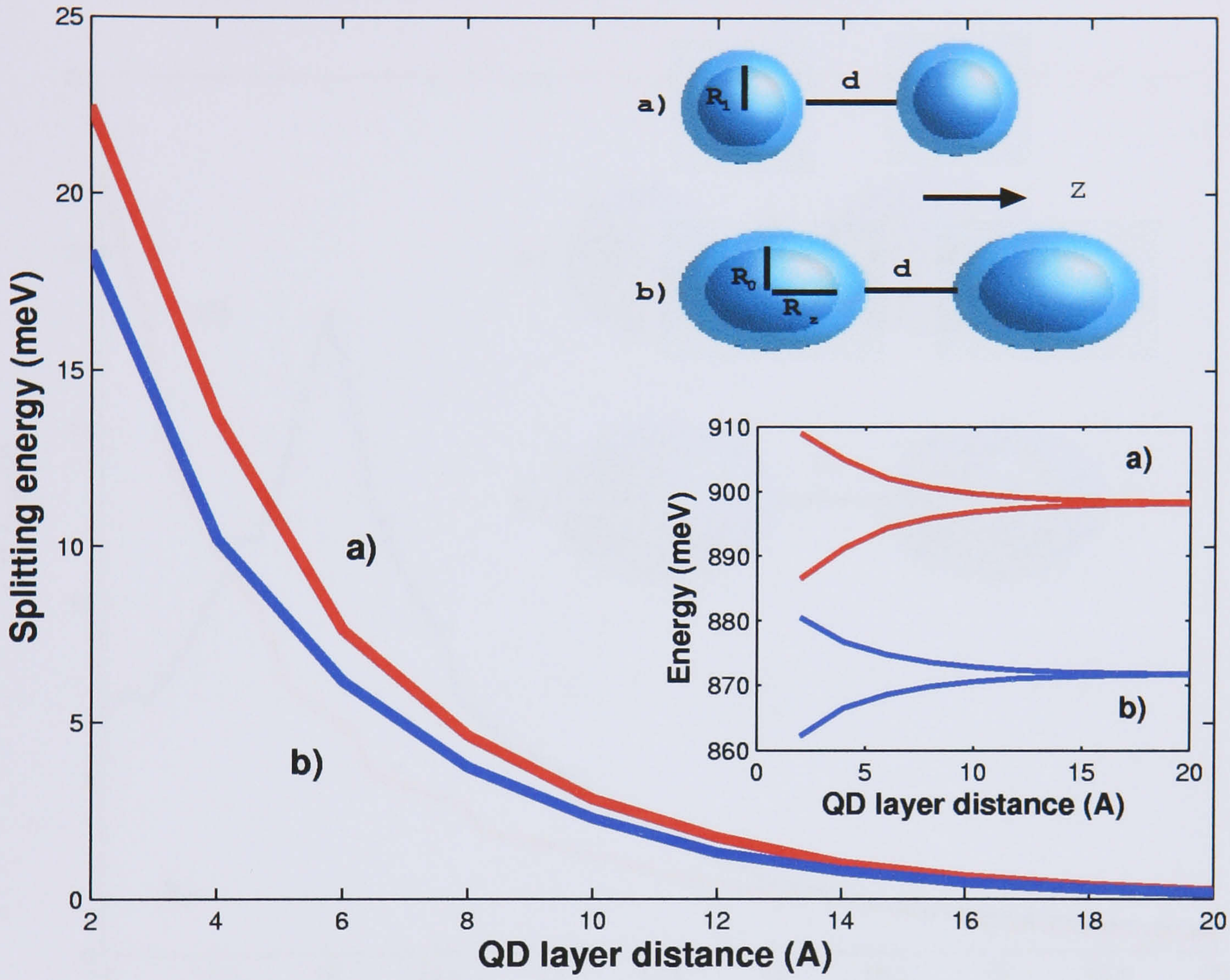

Figure 4.21: Difference between first excited and ground state energy levels of **a)**a coupled spherical QD's of radius $R_1 = 15$ Å, and **b)**a coupled ellipsoidal QD's of long axis $R_z = 16$ Å and two short axes $R_0 = 15$ Å ($\mu_{\text{core}} = 0.066$). In both cases the size of the capping layer is 3 Å and the QD's are aligned along the z axis. In the inset the ground and the first excited states are plotted for **a)**a coupled spherical QD's and **b)**a coupled ellipsoidal QD's.

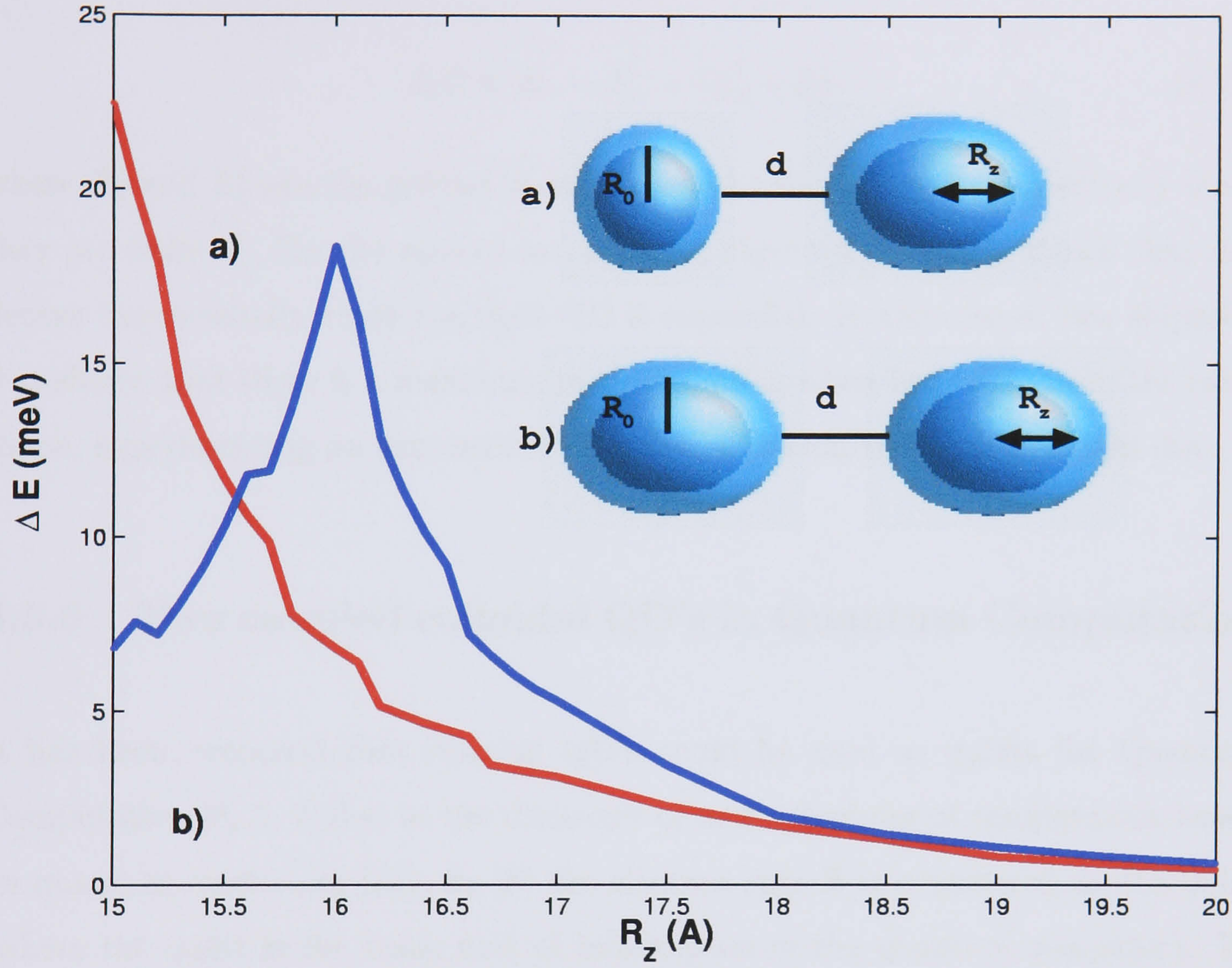

Figure 4.22: Exchange energy with inter-dot distance $d = 2$ Å where the core of the right dot is expanded in z axis. The left remains invariable and the shape of this dot is **a)**a sphere of radius $R_0 = 15$ Å and **b)**an ellipsoid of two short axis $R_0 = 15$ Å and long axis $R_z = 16$ Å.

Figure 4.22 shows the exchange energy ΔE expanding the core of the dot in z direction remaining constant the distance between surfaces $d = 2$ Å. Taking E_+ and E_- as the ground and first excited states respectively, the exchange energy is defined as

$$\Delta E = E_- - E_+ - |E_0^1 - E_0^2| \tag{4.70}$$

where E_0^1 and E_0^2 are the ground state of the left and right QD's respectively when they are isolated. For the case of two spheres, Figure 4.22a), it is shown that ΔE decays exponentially when the right QD is expanded. In the case of two ellipsoids it is shown that there is a maximum in the coupling when both dots have the same shape, experimenting an exponential decay with the expansion of the right dot.

4.5.6 Two coupled colloidal QD's in Quantum Computation

It has been proposed that coupled QD's could be used as qubits for Quantum Computation [8, 2, 7] due to the discovery of new principles of computation based on quantum mechanics [13]. In [8] the electron spin **S** is considered as the qubit (where the qubit is the basic unit of information in the quantum computer). By contrast, [2, 7] consider the localisation of an individual charge (in one dot or in the other) as a basis for qubit states. In both cases the coupling between dots is a key to preparing a quantum gate, which plays an important role as a mechanism to control a source of entanglement[14].

It is essential that during a quantum computational process, phase coherence of the qubits must be preserved. In a GaAs coupled SAD's system, the dephasing time of real spin can be on the order of microseconds [15], whereas the charge dephasing time can be of the order of nanoseconds[16], where electron-phonon scattering is known to be the primary source of dephasing [17].

Using colloidal QD systems this source of decoherence is avoided because due to the liquid nature of the surrounding material of a colloidal dot in suspension, an electron within this model has no interaction with phonons.

Using this two coupled colloidal QD's model, at distances between layers around 2-4 Å, the exchange energy is of the order of 10 meV which prevents thermal perturbations at temperatures around $T \sim 100$ K. Due to the liquid nature of the surrounding material of a colloidal dot in suspension, an electron within this model has no interaction with phonons, hence there is no dephasing time due to phonons.

4.6 Summary

In this chapter the coupling between two coupled quantum dots has been studied and its application to quantum computation discussed. The linear combination of quantum dot states approximation has been outlined and used in order to obtain the electronic structure of an electron within the coupled system. This method has been checked against the FDH method for an electron within two identical coupled QD's, showing that both methods agree. Due to the fact that the LQDSA method requires less computational time than the FDH method, it is used to calculate the two lowest energy levels of an electron within two spherical QD, two vertically aligned SAD and two colloidal QD systems.

- **Two spherical QD's**. The LCQDSA has been applied to two spherical QD's to illustrate the technique to the reader. The coupling between dots, described as the splitting energy between the first and ground state energy levels, has been calculated varying the inter-dot distance and the potential barrier showing that controlling one of these two parameters, thermal perturbations can be avoided.

- **Two vertically aligned SAD's.** The coupling between two ellipsoidal-shaped SAD's has been studied and the variation with the inter-dot distance, the confining potential and the dot dimensions investigated. Varying these parameters the coupling changes, which makes this model a good candidate to be used in quantum computation. For two identical SAD's it has been shown that changing the dot radius at the base does not alter the coupling significantly. In the case of two different SAD's the splitting energy dependence upon changes in the upper QD has been shown. Again the coupling remains nearly constant under changes on the radius, whereas it decreases when the upper dot height is increased.

- **Two colloidal QD's.** The coupling between two colloidal QD's has been studied in order to assess their suitability for use in quantum information applications. The model is composed of two spherical core-shell (CdSe-ZnS) QD's of radius around 15-20 Å and layer thickness 3 Å. The coupling has been calculated for two identical QD's varying the inter-dot distance obtaining similar results as with the FDH method. As CdSe nanocrystals are slightly prolate along the z axis, the case of two vertically aligned ellipsoidal capped QD's is investigated and compared with the two spherical QD's model. Only changes in the QD z axis has been considered in order to preserve the cylindrical symmetry. It has been found that increasing the z axis in both QD's, while the separation is constant, decreases the coupling between them. For the case of two ellipsoidal QD's, we found that the coupling reaches a maximum when both QD's have the same size.

The two-level electronic structure of the system is calculated within the effective mass approximation. The inter-dot distance affects the coupling between dots, therefore varying the separation of QD's may tune the coupling, giving a mechanism to switch it 'on' and 'off'. We observe that choosing the appropriate inter-dot

distance, the model may avoid thermal perturbations. In the case of two coupled SAD's, the exchange energy between dots is insensitive to small variations in the shape of both dots within the xy-axis. Small variations are observed changing the upper QD radius at the base. In contrast the exchange energy experiences large changes when the height of a single SAD is varied. We have also investigated the case of two aligned colloidals QD's (z-aligned in the case of ellipsoidal QD's) varying their shape. We find that without changing the separation between QD's, a maximum coupling is reached when both QD's have identical dimension and shape. Due the liquid nature of the surrounding material, the main source of decoherence, the charge-phonon scattering, can be neglected, making it a good candidate for use in quantum computation applications.

Bibliography

[1] Guido Burkard, Daniel Loss, and David P. DiVincenzo. Coupled quantum dots as quantum gates. *Phys. Rev. B*, 59:2070, 1999.

[2] M. Bayer, P. Hawrylak, K. Hinzer, S. Fafard, M. Korkusinski, Z. R. Wasilewski, O. Stern, and A. Forchel. Coupling and entangling of quantum states in quantum dot molecules. *Science*, 291:451, 2001.

[3] S. Taddei, M. Colocci, A. Vinattieri, F. Bogani, S. Franchi, P. Frigeri, L. Lazzarini, and G. Salviati. Vertical coupling and transition energies in multilayer `InAs/GaAs` quantum-dot structures. *Phys. Rev. B*, 62(15):10220, 2000.

[4] S. Fafard, Z. R. Wasilewski, C. Nì. Allen, K. Hinzer, J. P. McCaffrey, and Y. Feng. Lasing in quantum-dot ensembles with sharp adjustable electronic shells. *Applied Physics Letters*, 75(7):986, 1999.

[5] Richard L. Liboff. *Introductory Quantum Mechanics.* Addison Wesley, 1931.

[6] Marek Korkusiński and Pawel Hawrylak. Electronic structure of vertically stacked self-assembled quantum disks. *Phys. Rev. B*, 63:195311, 2001.

[7] Tetsufumi Tanamoto. Quantum gates by coupled aymmetric quantum dots and controlled-`NOT`-gate operation. *Phys. Rev. A*, 61:022305, 2000.

[8] Daniel Loss and David P. DiVincenzo. Quantum computation with quantum dots. *Phys. Rev. A*, 57:120, 1998.

[9] H. Mattoussi, J. Matthew Mauro, Ellen R. Goldman, George P. Anderson, Vikram C. Sundar, Frederic V. Mikulec, and Moungi G. Bawendi. Self-assembly of CdSe-ZnS quantum dot bioconjugates using an engineered recombinant protein. *J. Am. Chem. Soc*, 122:12142, 2000.

[10] Gregory P. Mitchell, Chad A. Mirkin, and Robert L. Letsinger. Programmed assembly of DNA functionalized quantum dots. *J. Am. Chem. Soc*, 121:8122, 1999.

[11] K. Leung, S. Pokrant, and K. B. Whaley. *Phys. Rev. B*, 57:12291, 1998.

[12] Todd D. Krauss and Luouis E. Brus. Electronic properties of single semiconductor nanocyrstals: optical and electrostatic force microscopy measurements. *Materials Science and Engineering B69-70*, page 289, 2000.

[13] D. Deutsch. *Proc. R. Soc. Lond. A*, 400:97, 1985.

[14] D. P. DiVincezo. *Phys. Rev. A*, 51:1015, 1995.

[15] J. M. Kikkawa and D. D. Awschalom. *Phys. Rev. Lett.*, 80:4313, 1998.

[16] A. G. Huibers, M. Switkes, C. M. Marcus, K. Campman, and A. C. Gossard. *Phys. Rev. Lett.*, 81:200, 1998.

[17] J. Shah. *Ultrafast Spectroscopy of Semiconductors and Semiconductor Nanostructures*. Springer, Berlin, 1996.

Chapter 5

LO-phonon - carrier capture scattering in SAD's

Contents

5.1 Introduction

Carrier transitions between different dimensionality confinement states are of relevance in a variety of modern semiconductor nanostructures. For example in devices with self-assembled quantum dots, carriers are generated in the two-dimensional wetting layer (WL) and they are then scattered into the zero-dimensional dot states. This capture process is very important in lasing devices, since it injects electron/holes into the QD conduction/valence band, therefore enhancing the population of QD states which improves laser performance. But, as discussed in the previous chapter, decoherence due to the scattering of carriers is major problem in semiconductor implementations of qubits. In this chapter the scattering rates of carriers in quantum dots due to lattice phonons are calculated in order to assess their use in optoelectronic devices and for quantum computing applications. The capture of carriers into the quantum dot from the quantum well wetting layer due to emission or absorption of a longitudinal optical (LO) phonon is investigated.

Calculations are based on the Frölich carrier - LO-phonon coupling, which is the interaction between a carrier and a LO-phonon, and the capture rate probability is calculated using Fermi's Golden Rule.

5.2 Fermi's Golden Rule

A charge carrier moving within a perfect crystal lattice free of defects and with all atoms stationary will continue *ad infinitum*. However this situation is not realistic since there are many factors that can change its state- a process which is known as *scattering*.

Quantum Mechanical scattering is usually summarised in terms of *Fermi's Golden*

Rule which states the following: if an electron (or hole) in a state $|i\rangle$ of energy E_i subjects a time-dependent perturbation $\tilde{\mathcal{H}}$ which could scatter (transfer) it into any one of the final states $|f\rangle$ of energy E_f, then the lifetime of the carrier in state $|i\rangle$ is given by:

$$\frac{1}{\tau_i} = \frac{2\pi}{\hbar} \sum_{|f\rangle} \left| \langle f|\tilde{\mathcal{H}}|i\rangle \right|^2 \delta(E_f - E_i) \tag{5.1}$$

where $\tilde{\mathcal{H}}$ is the Frölich Hamiltonian.

In this chapter we will study the case of two-dimensional carrier capture scattering process into a zero-dimensional state, due to LO-phonon interaction.

5.3 Phonons

The atoms that constitute semiconductor crystals are connected together by chemical bonds which are nominally covalent. These atoms are always in a state of continual motion, which because of the definite crystal lattice structure, is vibrational around an equilibrium position. In some ways, the vibrations of these interconnected quantum particles resembles a classical system of a series of masses connected by springs. There are basically four different modes of vibration, as illustrated in Figures 5.1 and 5.2.

The acoustic modes shown in Figure 5.1 are characterised by the neighbouring atoms being in phase. In the longitudinal mode the atomic displacements are in the same direction as the direction of energy transfer, while in the transverse mode the atomic displacements are perpendicular to this direction.

The longitudinal and transverse definitions also apply to the two types of optic phonon modes as illustrated in Figure 5.2. However, in this type of lattice vibration the displacements of neighbouring atoms are in opposite phase.

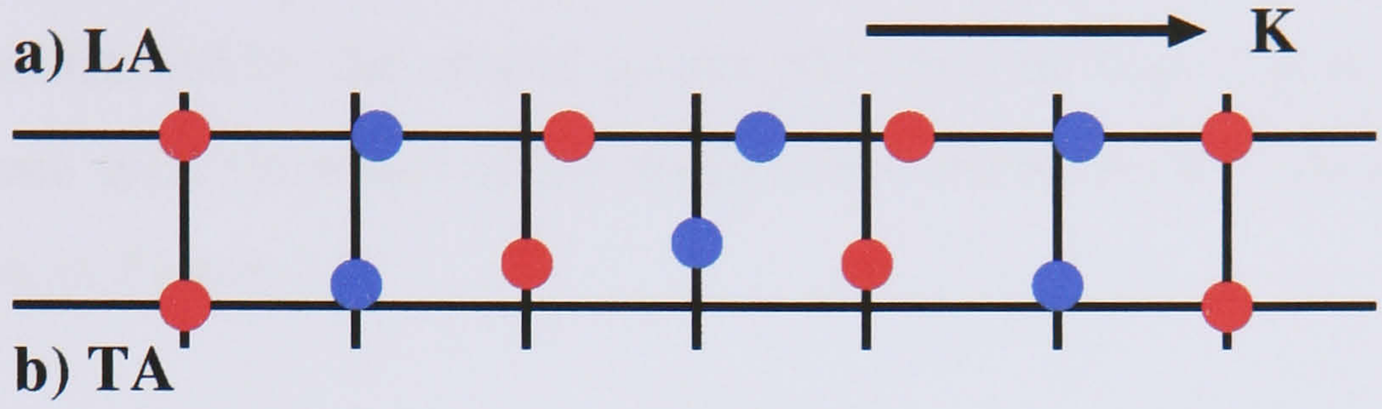

Figure 5.1: Schematic illustrations of the atomic displacements in **a)**longitudinal acoustic (LA) and **b)**transverse acoustic (TA) phonon modes.

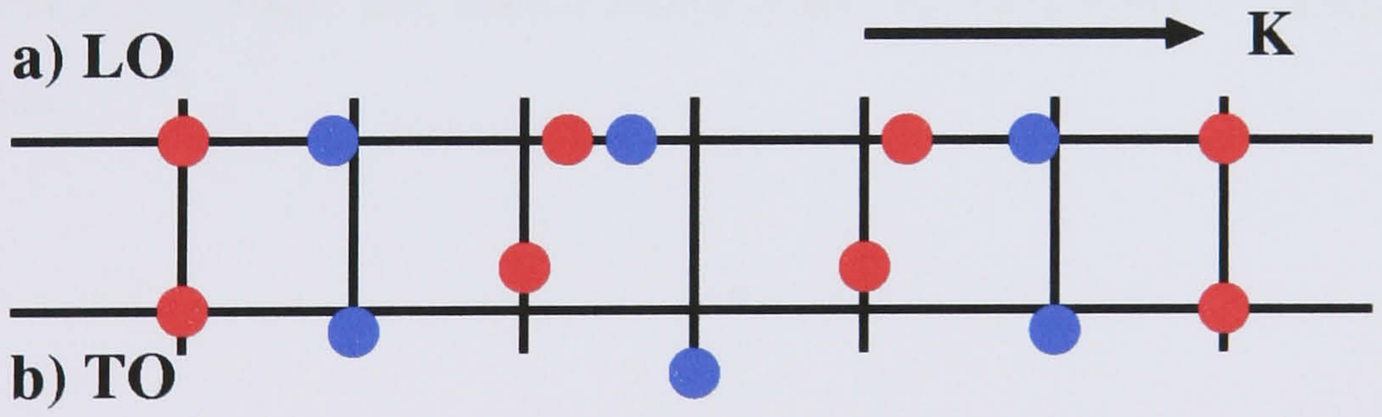

Figure 5.2: Schematic illustrations of the atomic displacements in **a)**longitudinal optic (LO) and **b)**transverse optic (TO) phonon modes.

The wave-like nature of the lattice vibrations allows them to be described by an angular frequency ω and a wave vector $\mathbf{q}$. Therefore the energy of a phonon is $\hbar\omega$ and the momentum of a phonon is said to be quantised and of value $\mathbf{q}$. Furthermore, phonons are diffracted by the crystal lattice just like electrons and holes, and thus a Brillouin zone type summary of the energy-momentum curves can be employed, as can be seen in Figure 5.3.

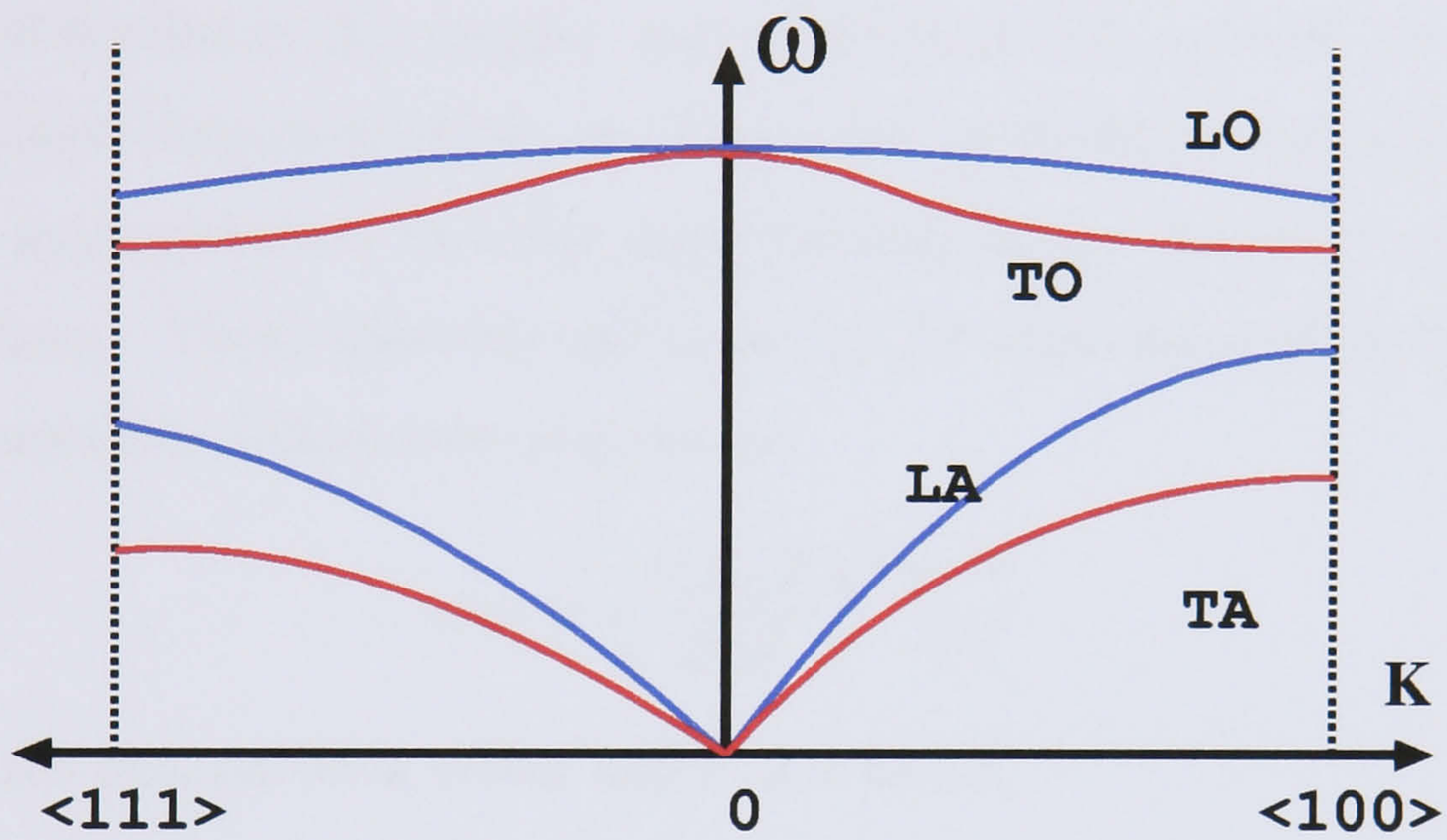

Figure 5.3: Phonon energy, $\hbar\omega$, versus momentum, $\mathbf{K}$, curves for a typical semiconductor.

As the phonons themselves represent the motion of atoms which are centres of electric charge, they also represent time-dependent perturbations $\tilde{\mathcal{H}}$ of the crystal potential and can therefore scatter charge carriers.

5.3.1 Carrier - LO-phonon coupling.

The models we study are heterostructures made from compound semiconductors. These materials are polar as the different electronegativites of the constituent atoms lead to a degree of ionicity in the chemical bonds. In such materials, the dominant electron-phonon interaction (scattering) is with the longitudinal optic phonon[1].

In the model studied in this chapter, only phonons in bulk material are considered. The LO-phonon dispersion curve, see Figure 5.3, is relatively flat, and hence it is possible to approximate it as being dispersionless, approximating the LO-phonon energy as $\hbar\omega_{\mathrm{LO}}$. Then, following reference [1], the normalised wave function of a single dispersionless LO-phonon is given by:

$$\psi_{\mathrm{LO}} = \left(\frac{\hbar\omega_{\mathrm{LO}}P}{2|\mathbf{q}|^2}\right)^{\frac{1}{2}} \frac{\mathrm{e}^{-\mathbf{iqr}}}{V^{\frac{1}{2}}} \tag{5.2}$$

where $\mathbf{q}$ is the phonon wave vector and P is a factor

$$P = \left(\frac{1}{\epsilon_\infty} - \frac{1}{\epsilon_0}\right) \tag{5.3}$$

where ϵ_∞ and ϵ_0 are the high- and low-frequency permittivities of the material.

The total phonon interaction is thus obtained by summing over all phonon wave vectors, i.e.

$$\tilde{\mathcal{H}} = e\sum_{\mathbf{q}} \psi_{\mathrm{LO}} \tag{5.4}$$

and therefore the phonon interaction term may be written as

$$\tilde{\mathcal{H}} = e\sum_{\mathbf{q}} \left[\frac{\hbar\omega_{\mathrm{LO}}P}{2q^2}\right]^{1/2} \frac{e^{-i\mathbf{qr}}}{V^{1/2}} \tag{5.5}$$

5.4 Two dimensional carrier capture into a SAD due to LO-phonon interaction

One of the key concerns regarding the speed and efficiency of QD lasers is the rate of carrier relaxation from the barrier states to the QD states. In this section we study the capture of carriers from the wetting layer which are scattered into the QD emitting or absorbing a LO-phonon. Only bulk phonons will be taken into account. The relative importance of these processes depends on temperature, carrier density within the wetting layer and the structural parameters of the QD's such as size, shape and electron and hole potential depths. At elevated temperatures, thermal escape of carriers from the QD's may also contribute to the dynamics.

Once in the dot, the carriers relax to their respective ground states. Due to the discrete nature of the carrier density of states in a quantum dot, the relaxation due to the interaction with a single LO-phonon is not allowed unless the energy difference between levels is exactly the energy necessary to emit/absorb a LO-phon, $\hbar\omega_{\mathrm{LO}}$, which is very improbable. What is possible is the carrier relaxation due to a multiphonon interaction[2], which could be considered as further work.

The carrier capture probability from any possible state in the WL emitting or absorbing a bulk LO-phonon can be calculated using Fermi's Golden Rule:

$$\frac{1}{\tau} = \frac{2\pi}{\hbar} \sum_{|i\rangle} \left| \langle f | \tilde{\mathcal{H}} | i \rangle \right|^2 \delta(E_f - E_i) \tag{5.6}$$

where $|i\rangle$ is the initial carrier state, $|f\rangle$ is the final carrier state. $\tilde{\mathcal{H}}$ is the interaction between an electron and a LO-phonon, also called the Frölich electron - LO-phonon coupling.

In a capture process, $|i\rangle$ is a two dimensional (2D) state which corresponds to a carrier confined to the wetting layer lowest subband energy and $|j\rangle$ is a zero

dimension (0D) state which corresponds to a carrier confined within the SAD.

Phonons are bosons, and therefore the occupancy number per unit volume is given by Bose-Einstein statistics:

$$N_0 = \frac{1}{e^{\hbar\omega/KT} - 1} \tag{5.7}$$

In the case of a LO-phonon emission or absorption, the capture probability of a carrier from any 2D state $|i\rangle$ to a 0D state $|j\rangle$ state is given by:

$$\frac{1}{\tau} = \frac{2\pi}{\hbar} \sum_{\mathbf{k}^{\mathrm{W}}} \frac{e^2 \hbar \omega_{\mathrm{LO}} P}{2V} \left| \int \left[\Psi^{\mathrm{D}}(\mathbf{r})\right]^* \Psi^{\mathrm{W}}(\mathbf{r}) \sum_{\mathbf{q}} \frac{e^{-i\mathbf{qr}}}{q} \mathrm{d}\mathbf{r} \right|^2 \delta(E_f - E_i) \tag{5.8}$$

where $\mathbf{k}^{\mathrm{W}}$ is the wave vector of a carrier initial state inside the wetting layer. For convenience we have introduced P as:

$$P = \left(\frac{1}{\epsilon_\infty} - \frac{1}{\epsilon_0}\right)(N_0 + 1/2 \mp 1/2) \tag{5.9}$$

$$|i\rangle = \Psi^{\mathrm{W}}(\mathbf{r}) \tag{5.10}$$

$$|j\rangle = \Psi^{\mathrm{D}}(\mathbf{r}) \tag{5.11}$$

where $(N_0 + 1/2 \mp 1/2)$ represents the phonon density within the crystal. The upper sign of the $\mp$ represents absorption while the lower sign represents emission of a phonon.

Now we need to consider the wavefunctions of the initial and final states. The initial state corresponds to a carrier confined to the lowest subband of the wetting layer quantum well and the final states is one of the SAD confined states.

5.4.1 SAD model

Self-assembled quantum dots have been studied in Section 2.5. The model is composed of a QD formed on a narrow wetting layer of thickness t_w, and modelled as

a semi-ellipsoid of height h and radius R at the base. Thus, carriers are confined in the narrow wetting-layer quantum well due to the step in the conduction-band edge at the interface, and they are further localised in the area of the dot due to the increase in thickness of the layer.

Therefore, a single carrier of effective mass m^* localised inside the SAD must satisfy the Schrödinger Equation described in Section 2.5:

$$[H_z^0 + H_\rho^0 + V(z,\rho)]\Psi^{\mathrm{D}} = E^{\mathrm{D}}\Psi^{\mathrm{D}} \tag{5.12}$$

Using the adiabatic approximation and taking into account that the carriers are strongly confined to the lowest sub-band in the narrow wetting-layer quantum well, the eigenstates of last expression are given by Equation 2.85

$$\Psi^{\mathrm{D}}_{ml}(\rho,\phi,z) = \frac{e^{im\phi}}{\sqrt{2\pi}} g_{0\rho}(z) f_m(\rho) \tag{5.13}$$

and eigenvalues, E_{ml}, may be estimated as described in Chapter 2.

5.4.2 Wave function and energy within the wetting layer

Carriers within the wetting layer are strongly confined in the z-direction, therefore their wave functions can be approximated as the product of an envelope along the growth axis and an in-plane travelling wave. The solutions of the Schrödinger equation along the confined direction produce discrete states of energy E_n^{W}, while within xy-plane there is a continuous range of allowed energies, $\epsilon_{xy}^{\mathrm{W}}$. These energy domains associated with confined levels are referred to as 'sub-bands'. Therefore the effect of z-direction confinement is to remove a degree of freedom, restricting the momentum of the charge carrier from three-dimensions to two. The energy, E^{W},

can be expressed as a summation of z and xy-plane components [1].

$$\Psi^{\mathrm{W}}(\mathbf{r}, \mathbf{k}^{\mathrm{W}}_{xy}) = \psi^{\mathrm{W}}_{n}(z)\frac{e^{-i\mathbf{k}^{\mathrm{W}}_{xy}\mathbf{r}_{xy}}}{A^{1/2}} \tag{5.14}$$

$$E^{\mathrm{W}} = E^{\mathrm{W}}_{n} + \epsilon^{\mathrm{W}}_{xy} \tag{5.15}$$

where

$$\epsilon^{\mathrm{W}}_{xy} = |\mathbf{k}^{\mathrm{W}}_{xy}|^2 \tag{5.16}$$

represents the continuous range of allowed energies associated with the xy-plane. The magnitude of the xy-plane wave vector is:

$$k^{\mathrm{W}}_{xy} = \sqrt{\epsilon^{\mathrm{W}}_{xy}} \tag{5.17}$$

The confined z-component wavefunctions, $\psi^{\mathrm{W}}_{n}(z)$, and the associated confined energy levels, E^{W}_{n}, may be obtained solving the finite potential quantum well problem [3].

The Schrödinger equation has finite number of eigenstates for energies $V_0 > E > 0$. Due to the symmetry of the potential, the solution of this system gives states with even and odd parity, where the even parity eigenstates are given by:

$$\psi^{\mathrm{W}}_{n}(z) = \begin{cases} A\cos(k_I a)\mathrm{e}^{k_{II}(z+a)} & \text{region II} \\ A\cos(k_I z) & \text{region I} \\ A\cos(k_I a)\mathrm{e}^{-k_{II}(z-a)} & \text{region III} \end{cases} \quad k_I \tan k_I a = k_{II} \tag{5.18}$$

and odd parity eigenstates are given by

$$\psi^{\mathrm{W}}_{n}(z) = \begin{cases} B\sin(k_I a)\mathrm{e}^{k_{II}(z+a)} & \text{region II} \\ B\sin(k_I z) & \text{region I} \\ -B\sin(k_I a)\mathrm{e}^{-k_{II}(z-a)} & \text{region III} \end{cases} \quad k_I \cot k_I a = -k_{II} \tag{5.19}$$

where the normalisation condition $\int_{-\infty}^{\infty} |\psi^{\mathrm{W}}_{n}(z)|^2 \mathrm{d}z = 1$ determines constants A, B and k_I, k_{II} are given by $k_I = \sqrt{E}$ and $k_{II} = \sqrt{E - V_0}$ in effective units.

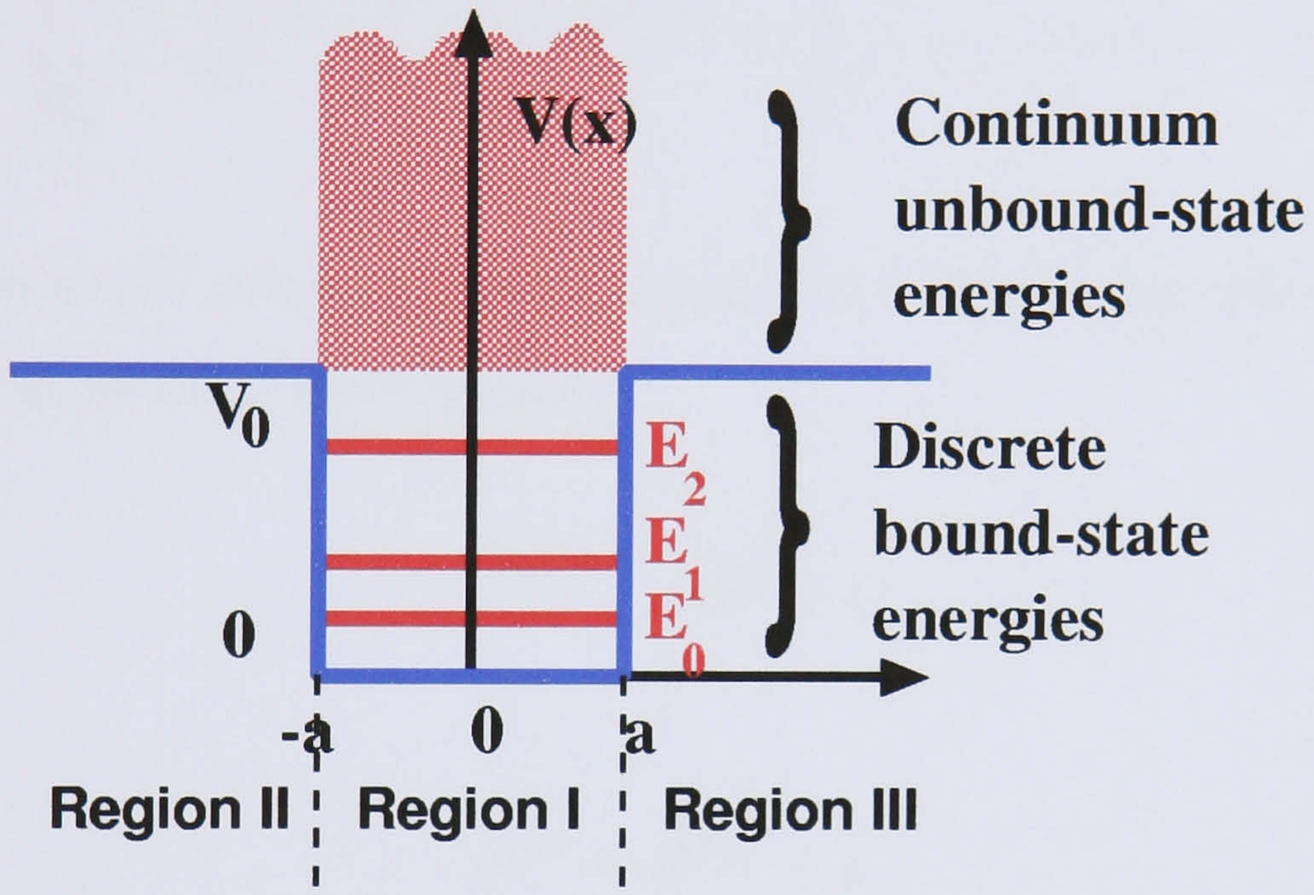

Figure 5.4: Finite potential quantum well. Discrete bound-state energies correspond to energies such $V_0 > E > 0$, whereas continuum unbound-state energies correspond to $E > V_0$.

5.5 Capture rate

The carrier capture rate will be calculated from the lowest QW sub-band into a confined QD state. Therefore the summation over the QW wave vector, $\mathbf{k}^{\mathrm{W}}$, is converted into a summation over k_x^{W} and k_y^{W} components. Suppressing the summation over k_z^{W} in Equation 5.8 gives:

$$\frac{1}{\tau} = \frac{2\pi}{\hbar} \sum_{\mathbf{k}_{xy}^{\mathrm{W}}} \frac{e^2 \hbar \omega_{LO} P}{2V} \left| \int \left[\Psi^{\mathrm{D}}(\mathbf{r})\right]^* \Psi^{\mathrm{W}}(\mathbf{r}) \sum_{\mathbf{q}} \frac{e^{-i\mathbf{q}\mathbf{r}}}{q} \mathrm{d}\mathbf{r} \right|^2 \delta(E_f - E_i) \tag{5.20}$$

Carriers within a QW sub-band are distributed as a 2D gas and hence, as Fermions, occupy a 2D Fermi-Dirac distribution.

$$f_D(\epsilon) = \frac{1}{e^{\frac{\epsilon-\mu}{KT}} + 1} \tag{5.21}$$

where

$$e^{\frac{\mu}{KT}} = e^{\frac{\pi\hbar^2 N}{mKT}} - 1 \tag{5.22}$$

and N is the carrier density within the wetting layer.

Assuming a thermal equilibrium, the Fermi-Dirac distribution function can be included in Equation 5.20 as:

$$\frac{1}{\tau} = \frac{2\pi}{\hbar} \sum_{\mathbf{k}_{xy}^{\mathrm{W}}} f_D(\epsilon_{xy}^{\mathrm{W}}) \frac{e^2 \hbar \omega_{LO} P}{2V} \left| \int \Psi^{\mathrm{D}}(\mathbf{r})^* \Psi^{\mathrm{W}}(\mathbf{r}) \sum_{\mathbf{q}} \frac{e^{-i\mathbf{q}\mathbf{r}}}{q} \mathrm{d}\mathbf{r} \right|^2 \delta(E_f - E_i) \tag{5.23}$$

Substituting $\Psi^{\mathrm{W}}(\mathbf{r})$ from Equation 5.14 into Equation 5.23 leads to:

$$\frac{1}{\tau} = \frac{2\pi}{\hbar} \sum_{\mathbf{k}_{xy}^{\mathrm{W}}} f_D(\epsilon_{xy}^{\mathrm{W}}) \frac{e^2 \hbar \omega_{LO} P}{2V} \left| \sum_{\mathbf{q}} \int \left[\Psi^{\mathrm{D}}(\mathbf{r})\right]^* \psi_n^{\mathrm{W}}(z) \frac{e^{-i(\mathbf{q}+\mathbf{k}_{xy}^{\mathrm{W}})\mathbf{r}}}{q} \mathrm{d}\mathbf{r} \right|^2 \delta(E_f - E_i) \tag{5.24}$$

Now, the integral over all space, specified by $\mathbf{dr}$, can be expressed as a *form factor*, $G(k_x, k_y, k_z)$;

$$\frac{1}{\tau} = \frac{2\pi}{\hbar}\frac{e^2\hbar\omega_{LO}P}{2VA}\sum_{\mathbf{k}_{xy}^{\mathrm{W}}} f_D(E_{xy}^{\mathrm{W}})\left|\sum_{\mathbf{q}}\frac{G(k_x^{\mathrm{W}}+q_x, k_y^{\mathrm{W}}+q_y, q_z)}{q}\right|^2 \delta(E_f - E_i) \tag{5.25}$$

where the form factor expression is:

$$G(k_x^{\mathrm{W}}+q_x, k_y^{\mathrm{W}}+q_y, q_z) = \int_{-\infty}^{\infty}\iiint \left[\Psi^{\mathrm{D}}(\mathbf{r})\right]^* \psi_n^{\mathrm{W}}(z)\frac{e^{-i(\mathbf{q}+\mathbf{k}_{xy}^{\mathrm{W}})\mathbf{r}}}{q}\mathrm{d}x\mathrm{d}y\mathrm{d}z \tag{5.26}$$

Converting the summation over the phonon wave vector to an integral introduces a factor of $L/2\pi$ per dimension from the density of states [1].

$$\begin{aligned}\frac{1}{\tau} &= \frac{2\pi}{\hbar}\frac{e^2\hbar\omega_{LO}P}{2VA}\sum_{\mathbf{k}_{xy}^{\mathrm{W}}} f_D(\epsilon_{xy}^{\mathrm{W}})\left|\frac{V}{(2\pi)^3}\int \mathrm{d}\mathbf{q}\frac{G(\mathbf{k}_{xy}^{\mathrm{W}}+\mathbf{q})}{q}\right|^2 \\ &\quad\times\delta(E_f - E_i)\end{aligned} \tag{5.27}$$

In a similar manner, the summation over $\mathbf{k}_{xy}^{\mathrm{W}}$ can also be converted into an integral introducing a factor of $A/(2\pi)^2$.

$$\begin{aligned}\frac{1}{\tau} &= \frac{e^2\hbar\omega_{LO}P}{2\hbar}\frac{V}{(2\pi)^7}\int \mathrm{d}\mathbf{k}_{xy}^{\mathrm{W}} f_D(\epsilon_{xy}^{\mathrm{W}})\left|\int \mathrm{d}\mathbf{q}\frac{G(\mathbf{k}_{xy}^{\mathrm{W}}+\mathbf{q})}{q}\right|^2 \\ &\quad\times\delta(E_f - E_i)\end{aligned} \tag{5.28}$$

Proceeding as Paul Harrison in [1], p.256, it will be supposed that the result depend on the 'integral of a square' rather than 'a square of an integral'. It can be achieved adding a δ-function which only gives a contribution when $\mathbf{q} = \mathbf{q}'$. Using this approach simplifies the capture rate expression and therefore requires less computational time. Rearranging the last equation leads to

$$\begin{aligned}\frac{1}{\tau} &= \Gamma''\int \mathrm{d}\mathbf{k}_{xy}^{\mathrm{W}} f_D(\epsilon_{xy}^{\mathrm{W}})\int \frac{G(\mathbf{k}_{xy}^{\mathrm{W}}+\mathbf{q})}{q} \\ &\quad\times\int \frac{G^*(\mathbf{k}_{xy}^{\mathrm{W}}+\mathbf{q}')}{q'}\mathrm{d}\mathbf{q}\mathrm{d}\mathbf{q}'\delta(E_f - E_i)\end{aligned} \tag{5.29}$$

where

$$\Gamma'' = \frac{e^2\hbar\omega_{LO}P}{2\hbar}\frac{V}{(2\pi)^7}$$

Now applying Harrison's approximation:

$$\begin{aligned}\frac{1}{\tau} &= \Gamma'' \int \mathrm{d}\mathbf{k}_{xy}^{\mathrm{W}} f_D(\epsilon_{xy}^{\mathrm{W}}) \int \frac{G(\mathbf{k}_{xy}^{\mathrm{W}}+\mathbf{q})}{q} \\ &\quad \times \left[\left(\frac{2\pi}{L}\right)^3 \int \frac{G^*(\mathbf{k}_{xy}^{\mathrm{W}}+\mathbf{q}')}{q'}\delta(\mathbf{q}-\mathbf{q}')\right] \mathrm{d}\mathbf{q}\mathrm{d}\mathbf{q}'\delta(E_f - E_i) \qquad (5.30)\end{aligned}$$

In order to satisfy dimensionality a factor $2\pi/L$ is introduced per dimension integral. Performing the integration over $\mathbf{q}'$ first and writing the constant prefactor Γ' as $\Gamma' = \Gamma''(2\pi)^3/V$ gives;

$$\frac{1}{\tau} = \Gamma' \int \mathrm{d}\mathbf{k}_{xy}^{\mathrm{W}} f_D(\epsilon_{xy}^{\mathrm{W}}) \int \frac{|G(\mathbf{k}_{xy}^{\mathrm{W}}+\mathbf{q})|^2}{q^2}\mathrm{d}\mathbf{q}\delta(E_f - E_i) \qquad (5.31)$$

5.5.1 Energy conservation

As studied in Section 2.5, a SAD is composed of a dot formed on a quantum well wetting layer of thickness $t_w = 0.55$ nm, and in this thesis is modelled as a semi-ellipsoid of a short axis of length $h = 2$ nm (height) and two long axis of length $R = 5 - 10$ nm (radius), as can be seen in Figure 2.13. The dot (InGaAs-QD) is grown on top of the wetting layer (InGaAs-QW), both embedded in bulk material (GaAs). The confinement potential of the carriers within the dot or the wetting layer results from the different bandgaps between them and the bulk material. The composition of the dot and the wetting layer is usually slightly different therefore with different bandgaps. For simplicity this difference is neglected.

Figure 5.5 shows a schematic of the confining potential. In order to differentiate the wetting layer from the dot a gap between them has been included in the figure (although it does not exist).

A carrier confined in the wetting-layer has freedom of movement in two-dimensions (2D state), whereas the motion of a carrier confined in the dot is restricted in all three dimensions (0D state). In this model only captures of carriers confined to the lowest subband of the wetting layer will be taken into account.

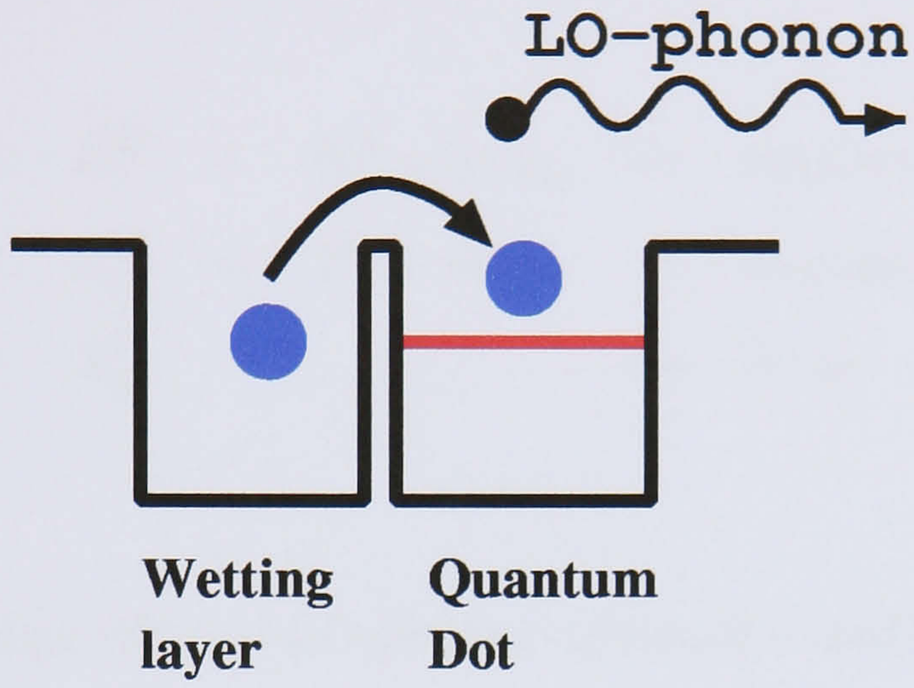

Figure 5.5: A carrier is captured from the wetting layer (QW) into a quantum dot confined state emitting a LO-phonon.

Carrier energies within the WL and QD are E^{W} and E^{D} respectively, where E^{W} may be written as

$$E^{\mathrm{W}} = E_n^{\mathrm{W}} + \frac{\hbar^2 k_{xy}^{\mathrm{W}}}{2m} \tag{5.32}$$

Assuming the initial state corresponds to a carrier within the wetting layer and the final state corresponds to a carrier within the QD emitting or absorbing an LO-phonon we may write the initial and final energies, E_i and E_f, as

$$E_i = E_n^{\mathrm{W}} + \frac{\hbar^2 k_{xy}^{\mathrm{W}}}{2m} \tag{5.33}$$

$$E_f = E^{\mathrm{D}} \pm \hbar\omega_{LO} \tag{5.34}$$

where the upper sign in the $\pm\hbar\omega_{LO}$ term accounts for scattering processes involving the emission of a phonon and the lower sign represents absorption.

Emission and absorption processes are only allowed within an energy range determined by the WL sub-band energy E_n^{W}. Taking into account that the carrier kinetic energy inside the WL ($\epsilon_{xy}^{\mathrm{W}}$) must be positive, the energy range which make possible a LO-phonon emission or absorption is described in Table 5.1 and represented in Figure 5.6.

0	$<$	E_n^{W}	$<$	$E^{\mathrm{D}} - \hbar\omega_{LO}$	$\rightarrow$ emission + absorption
$E^{\mathrm{D}} - \hbar\omega_{LO}$	$<$	E_n^{W}	$<$	$E^{\mathrm{D}} + \hbar\omega_{LO}$	$\rightarrow$ emission
$E^{\mathrm{D}} + \hbar\omega_{LO}$	$<$	E_n^{W}			$\rightarrow$ none

Table 5.1: Energy range where a LO-phonon absorption and/or emission is allowed.

Energy values may be substituted into Equation 5.31 obtaining:

$$\frac{1}{\tau} = \Gamma' \int \mathrm{d}\mathbf{k}_{xy}^{\mathrm{W}} f_D(\epsilon_{xy}^{\mathrm{W}}) \int \frac{\left|G(\mathbf{k}_{xy}^{\mathrm{W}} + \mathbf{q})\right|^2}{q^2} \mathrm{d}\mathbf{q}\delta\left(\Delta - \frac{\hbar^2 k_{xy}^{\mathrm{W}\,2}}{2m}\right) \tag{5.35}$$

where

$$\Delta = E^{\mathrm{D}} \pm \hbar\omega_{LO} - E_n^{\mathrm{W}} \tag{5.36}$$

Using $\delta(ax) = \delta(x)/a$, then:

$$\frac{1}{\tau} = \Gamma' \frac{2m}{\hbar^2} \int \mathrm{d}\mathbf{k}_{xy}^{\mathrm{W}} f_D(\epsilon_{xy}^{\mathrm{W}}) \int \frac{\left|G(q_z, \mathbf{k}_{xy}^{\mathrm{W}} + \mathbf{q}_{xy})\right|^2}{q^2} \mathrm{d}\mathbf{q}\delta\left(\frac{2m\Delta}{\hbar^2} - k_{xy}^{\mathrm{W}\,2}\right) \tag{5.37}$$

The term inside the δ-function can be factorised as:

$$\delta\left(\frac{2m\Delta}{\hbar^2} - k_{xy}^{\mathrm{W}\,2}\right) = \delta\big((\alpha - k_{xy}^{\mathrm{W}})(\alpha + k_{xy}^{\mathrm{W}})\big) \tag{5.38}$$

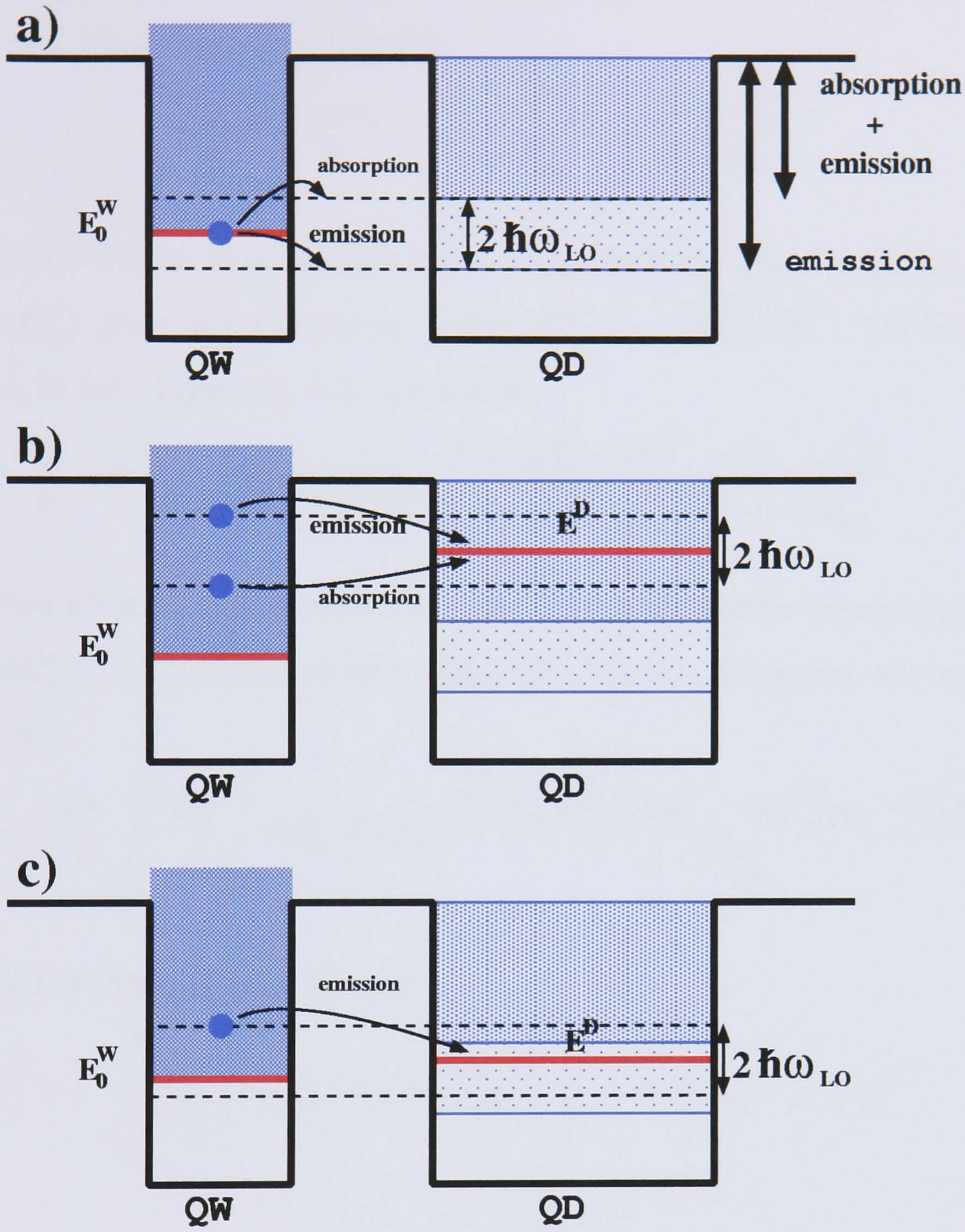

Figure 5.6: **a)**A carrier in the subband E_0^{W} with no kinetic energy $\epsilon_{xy} = 0$, can be scattered into the QD state of energy $E_{nm} = E_0^{\mathrm{W}} + \hbar\omega_{\mathrm{LO}}$ or $E_{nm} = E_0^{\mathrm{W}} - \hbar\omega_{\mathrm{LO}}$ absorbing or emitting a LO-phonon respectively. The scattering process into lower energies than $E_{nm} = E_0^{\mathrm{W}} - \hbar\omega_{\mathrm{LO}}$ is not allowed. **b)**Capture into the QD state of energy E^{D} is allowed emitting or absorbing a LO-phonon. **c)**Capture into the QD state of energy E^{D} is allowed only emitting a LO-phonon.

where $\alpha = \sqrt{2m\Delta/\hbar^2}$. Around the solution $k_{xy}^{\mathrm{W}} = \alpha$, the factor $(\alpha + k_{xy}^{\mathrm{W}})$ is a constant, and vice-versa, therefore [1]:

$$\delta(\alpha^2 - k_{xy}^{\mathrm{W}\,2}) = \frac{\delta(\alpha - k_{xy}^{\mathrm{W}})}{\alpha + k_{xy}^{\mathrm{W}}} + \frac{\delta(\alpha + k_{xy}^{\mathrm{W}})}{\alpha - k_{xy}^{\mathrm{W}}} \tag{5.39}$$

The magnitude of the wave number must be positive therefore only the term $\delta(\alpha - k_{xy}^{\mathrm{W}})/(\alpha + k_{xy}^{\mathrm{W}})$ gives a contribution, when $k_{xy}^{\mathrm{W}} = \sqrt{2m\Delta/\hbar^2}$. Then substituting Equation 5.39 into Equation 5.37 we obtain:

$$\frac{1}{\tau} = \Gamma' \frac{2m}{\hbar^2} \int \mathrm{d}\mathbf{k}_{xy}^{\mathrm{W}} f_D(\epsilon_{xy}^{\mathrm{W}}) \int \frac{|G(\mathbf{k}_{xy}^{\mathrm{W}} + \mathbf{q})|^2}{q^2} \mathrm{d}\mathbf{q} \frac{\delta(\alpha - k_{xy}^{\mathrm{W}})}{\alpha + k_{xy}^{\mathrm{W}}} \tag{5.40}$$

Now the two-dimensional integral over the Cartesian carrier wave number, as denoted by $\mathrm{d}\mathbf{k}_{xy}^{\mathrm{W}}$, can be changed into polar coordinates. Changing the order of integration gives:

$$\frac{1}{\tau} = \Gamma' \frac{2m}{\hbar^2} \int_{-\infty}^{\infty} \frac{\mathrm{d}\mathbf{q}}{q^2} \int_{-\pi}^{\pi} \mathrm{d}\theta_{xy}^{\mathrm{W}} \int_{0}^{\infty} \mathrm{d}k_{xy}^{\mathrm{W}} \frac{f_D(\epsilon_{xy}^{\mathrm{W}}) k_{xy}^{\mathrm{W}} |G(\mathbf{k}_{xy}^{\mathrm{W}} + \mathbf{q})|^2 \delta(\alpha - k_{xy}^{\mathrm{W}})}{\alpha + k_{xy}^{\mathrm{W}}} \tag{5.41}$$

Performing the integral over k_{xy}^{W} gives:

$$\frac{1}{\tau} = \Gamma \int_{-\infty}^{\infty} \frac{\mathrm{d}\mathbf{q}}{q^2} \int_{-\pi}^{\pi} \mathrm{d}\theta_{xy}^{\mathrm{W}} |G(\alpha\cos(\theta_{xy}^{\mathrm{W}}) + q_x, \alpha\sin(\theta_{xy}^{\mathrm{W}}) + q_y, qz)|^2 \tag{5.42}$$

where

$$\Gamma = \frac{me^2\omega_{LO}Pf_D}{2\hbar^2(2\pi)^4} \tag{5.43}$$

$$f_D = f_D\left(\frac{\hbar^2\alpha^2}{2m}\right) \tag{5.44}$$

5.5.2 An example of capture rate calculation. SAD.

Using the same parameters as in Section 2.5, the model consists of a InAs self-assembled ellipsoidal QD whose height is $h = 2$ nm, the radii varies between $R = 5 - 11$ nm and wetting layer thickness $t_w = 0.552$ nm surrounded by GaAs.

The capture rate of an electron of mass $m = 0.023m_0$ from the wetting layer into a SAD due to bulk LO-phonon interaction is calculated. The electron barrier potential is set to $V_0 = 1$ eV, the electron density within the wetting layer is $N_e = 10^{14}$ $1/\mathrm{m}^2$ and the temperature $T = 300$ K.

An LO-phonon is absorbed(emitted) if an electron within the wetting layer gains(loses) enough energy, $\hbar\omega_{\mathrm{LO}}$, to scatter into a confined QD energy level. This process is possible if the wetting layer subband energy is lower than the QD energy level plus(less) the LO-phonon energy: $E_0^{\mathrm{W}} < E^{\mathrm{D}} - \hbar\omega_{\mathrm{LO}}$($E_0^{\mathrm{W}} < E^{Q}D + \hbar\omega_{\mathrm{LO}}$). Figure 5.7a) shows the capture rate into the first four QD energy levels emitting a LO-phonon. It is found that over the range of dot radius where the capture into the first excited state (of energy E_{11}, also called 1P) is energetically possible, the capture rate varies from $1/\tau_{11} = 0.6 \times 10^9$ $1/s$ ($E_{11} = 850$ meV) to $\tau_{11} = 2 \times 10^9$ $1/s$ ($E_{11} = 815$ meV). Ferreira et al [4] calculate the electron capture rate using a slightly different SAD model and different electron mass and confined potential. For an orbital 1P (E_{11} in the model used in this section) when the setting layer is occupied by 10^{14} $1/\mathrm{m}^2$ electrons at temperature $T = 300$ K, he obtained $n_{1P} \sim 1/\tau 11 = 2.5 \times 10^{10} - 8.5 \times 10^{10}$ $1/\mathrm{s}$ within the capture allowed dot size radius. Those results are more than an order of magnitude higher, but it has to be taken into account that Ferrera's model uses different QD shape and parameters than in this thesis.

Due to the narrow wetting layer, the subband energy level in the quantum well wetting layer is higher than most of the confined energy levels within the QD, as can be seen in Figure 5.7b). Increasing the QD radius decreases the energy levels within the QD and new levels appear. Electron capture into a QD energy level, E_{nm}, emitting a LO-phonon is possible if $E_{nm} > E_0^W - \hbar\omega_{\mathrm{LO}}$. Therefore within some radius ranges the capture process is not allowed due to the energy conservation and when it is allowed, only it occurs in the highest levels. Within the radius range

considered, $R = 5 - 11$ nm, the ground state energy level E_{10} never reaches the energy of the subband, making the capture into this state impossible.

A capture process absorbing an LO-phonon is possible if $E_{nm} > E_0^W + \hbar\omega_{\text{LO}}$. As can be seen in Figure 5.7b), none of the QD energy levels, reaches this value and hence the absorption of a LO-phonon is not allowed.

In order to study how the capture rate changes with the wetting layer thickness, it is calculated the capture rates again for a wetting layer of thickness $t_w = 1.1$ nm. The capture rates can be seen in Figure 5.8b). It can be observed that there are no remarkable differences between Figure 5.7a) and 5.8a). The subband energies within the wetting layer are $E_0^W = 0.957$ eV and $E_0^W = 0.851$ eV for $t_w = 0.552$ nm and $t_w = 1.104$ nm, respectively. The energy decreases with the increase of the thickness, but this also affects the QD energy levels, which also decrease, as can be seen comparing Figures 5.7b) and 5.8b). Only the QD radius range where the capture into the state of energy E_{20} experiences an increase, but the capture rates remain constant with the wetting layer thickness.

Within the wetting layer, the carrier distributions are described by Fermi-Dirac statistics, defined by the temperature of the system. We calculate the capture rate into the QD states of energy E_{11}, E_{12} and E_{20}, varying the temperature and plot the results in Figure 5.9. The Fermi-Dirac distribution of this electron is also plotted, which is the only factor in the capture rate expression (Equation 5.42) which depends on the temperature.

The energy, ϵ_{xy}^{W}, which a carrier within the wetting layer requires to be captured into a QD confined state, increases with the separation between the energy level of the QD state, E_{nm}, and the wetting layer subband energy, E_0^{W}. The Fermi-Dirac distribution gives the probability of finding a carrier with energy ϵ_{xy}^{W}. In Figures 5.9d),e),f) this probability is plotted for capture into different QD states at different

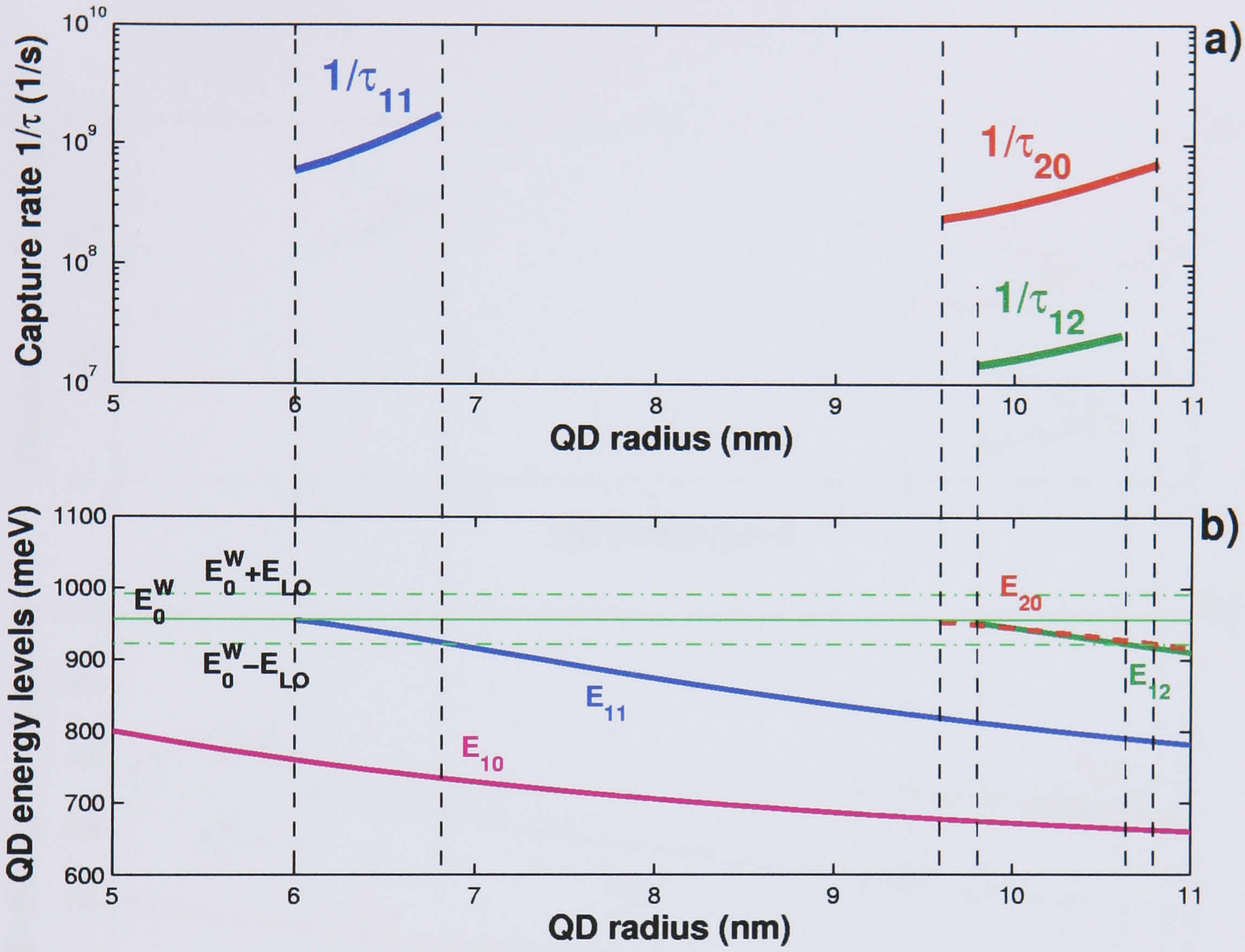

Figure 5.7: **a)**Capture rate of an electron from the wetting layer into the QD energy level E_{nm} due to LO-phonon scattering. The wetting layer thickness considered is $t_w = 0.552$ nm. **b)**QD energy levels versus radius. The capture into a QD energy level E_{nm} is allowed if $E_{nm} > E_0^W - \hbar\omega_{\rm LO}$ emiting a LO-phonon. Absorption of a LO-phonon is not allowed because the condition is $E_{nm} > E_0^W + \hbar\omega_{\rm LO}$ and none of the energy levels reach this level.

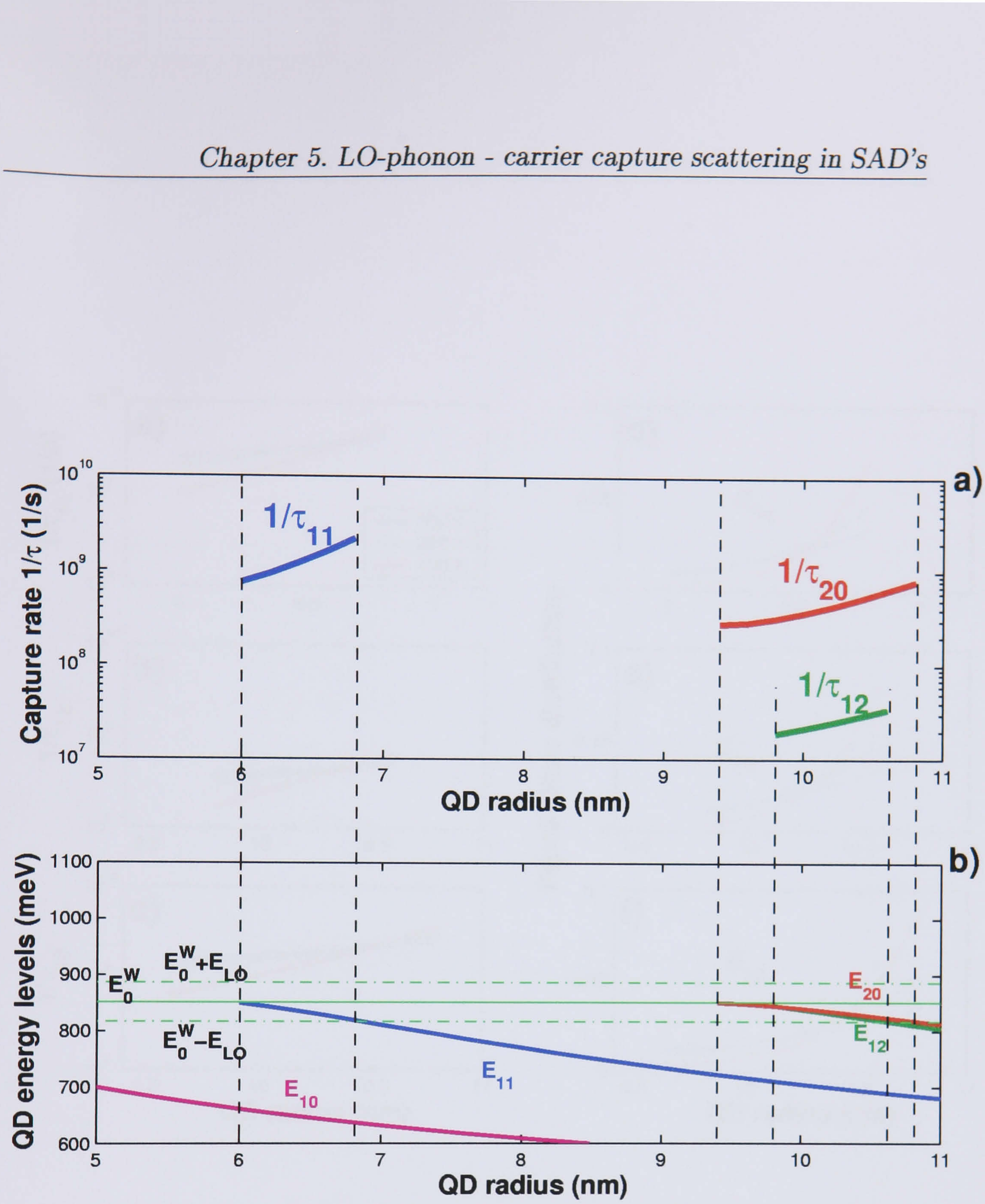

Figure 5.8: **a)**Capture rate of an electron from the wetting layer into the QD energy level E_{nm} due to LO-phonon scattering. The wetting layer thickness considered is $t_w = 1.104$ nm. **b)**QD energy levels versus radius.

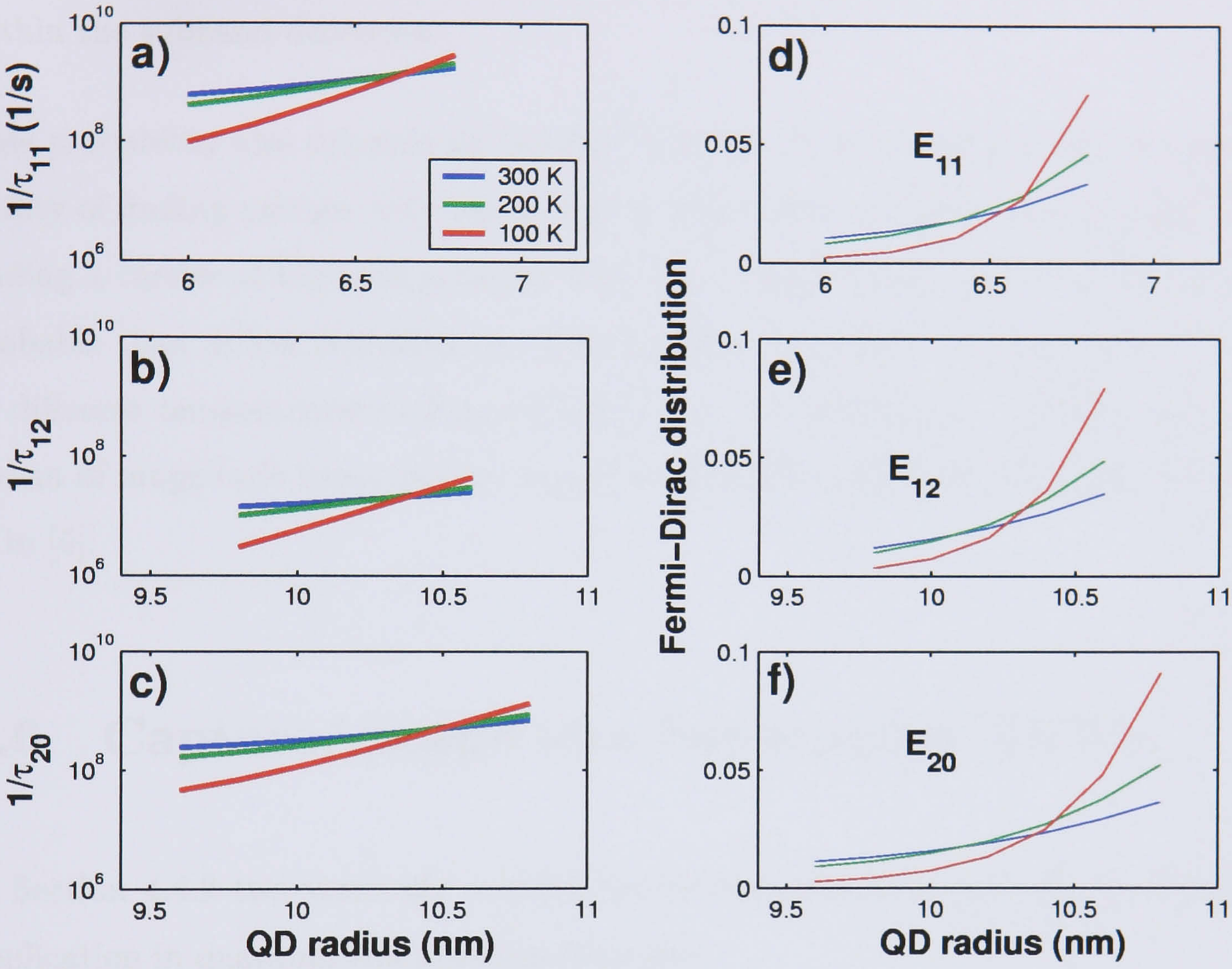

Figure 5.9: Capture rate of an electron from the wetting layer into the QD energy level **a)** E_{11}, **b)** E_{12}, **c)** E_{20} due to LO-phonon scattering changing the temperature $T = 300, 200, 100$ K. The wetting layer thickness considered is $t_w = 0.552$ nm. Fermi-Dirac distribution of an electron captured from the wetting layer into the QD energy level **d)** E_{11}, **e)** E_{12}, **f)** E_{20} due to LO-phonon scattering changing the temperature $T = 300, 200, 100$ K.

temperatures. The energy levels of these QD states decrease with the QD radius. This increases the energy ϵ_{xy}^{W} of the carrier to be captured in the quantum well wetting layer and therefore the probability of finding a carrier with this energy within the subband decreases.

This probability also depends on the temperature. At low temperatures, the probability of finding carriers with low energy is higher than at high temperatures, and finding a carrier at high temperature with high energy within the subband is more probable than at low temperature. This explains the crossing of the capture rates at different temperatures in Figures 5.9a),b),c). This behaviour, though with two orders of magnitude lower results, agrees with calculations obtained by Ferreira et al in [5].

5.6 Capture/escape into two coupled SAD's

In Section 4.4.2 two vertically coupled SAD's have been studied and the possible application in quantum computation discussed.

When two dots are coupled and an electron is inserted, the system behaves as a single dot, and the electron occupies one of the discrete energy states, which have been calculated in Section 4.4. When the coupling between two identical dots is weak, the energy levels are degenerate and an electron within the QD system is localised in one of the QD's. Once the coupling becomes strong the energy level degeneracy is removed producing new delocalised states.

Only the two lowest energy levels are considered, the ground and first excited states, $|+\rangle$ and $|-\rangle$, which possess even and odd parity, respectively, as can be seen in Figure 5.10.

temperatures. The energy levels of these QD states decrease with the QD radius. This increases the energy ϵ_{xy}^{W} of the carrier to be captured in the quantum well wetting layer and therefore the probability of finding a carrier with this energy within the subband decreases.

This probability also depends on the temperature. At low temperatures, the probability of finding carriers with low energy is higher than at high temperatures, and finding a carrier at high temperature with high energy within the subband is more probable than at low temperature. This explains the crossing of the capture rates at different temperatures in Figures 5.9a),b),c). This behaviour, though with two orders of magnitude lower results, agrees with calculations obtained by Ferreira et al in [5].

5.6 Capture/escape into two coupled SAD's

In Section 4.4.2 two vertically coupled SAD's have been studied and the possible application in quantum computation discussed.

When two dots are coupled and an electron is inserted, the system behaves as a single dot, and the electron occupies one of the discrete energy states, which have been calculated in Section 4.4. When the coupling between two identical dots is weak, the energy levels are degenerate and an electron within the QD system is localised in one of the QD's. Once the coupling becomes strong the energy level degeneracy is removed producing new delocalised states.

Only the two lowest energy levels are considered, the ground and first excited states, $|+\rangle$ and $|-\rangle$, which possess even and odd parity, respectively, as can be seen in Figure 5.10.

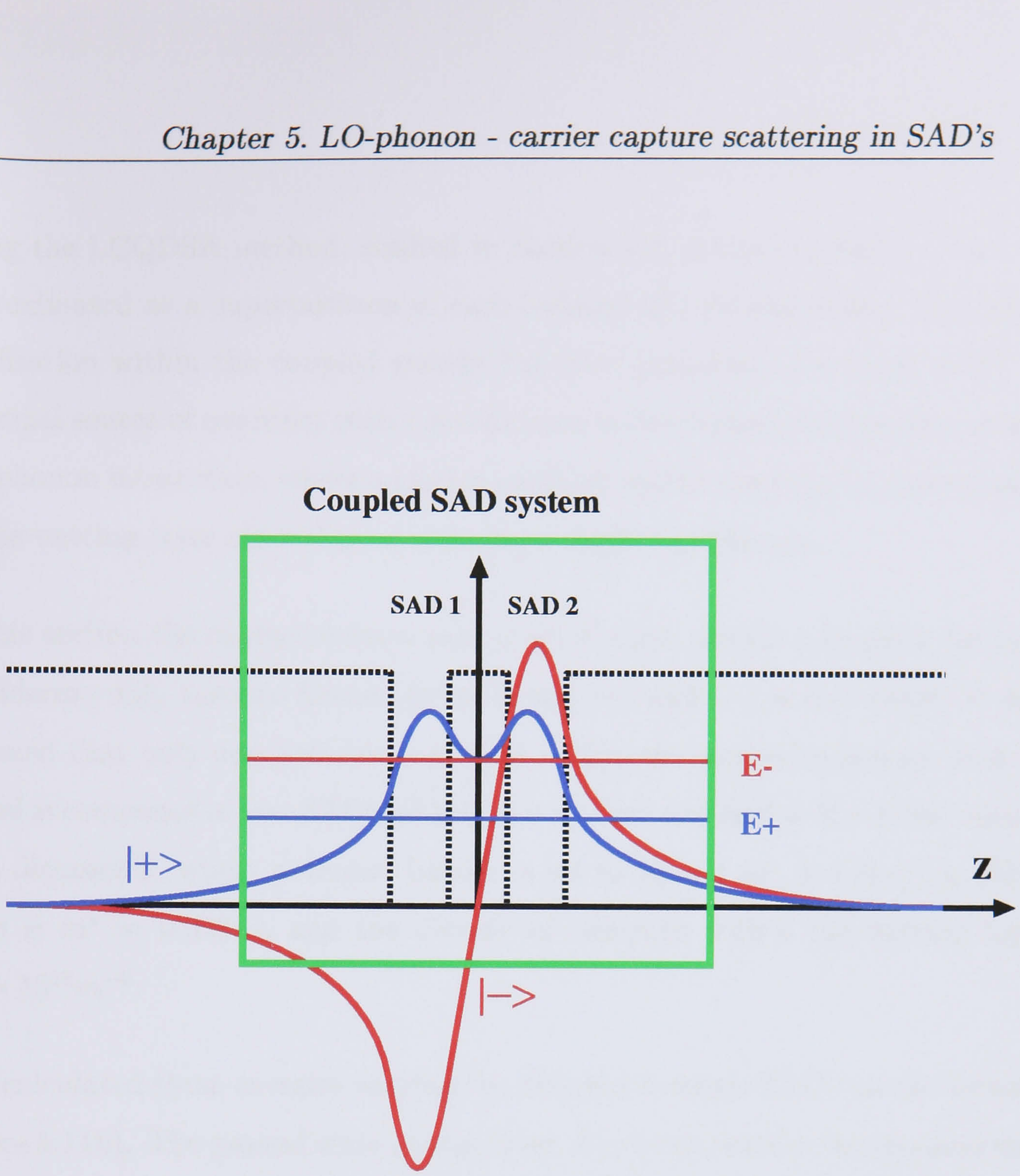

Figure 5.10: Schematic representation of the ground and first excited state wavefunctions, $|+\rangle$ and $|-\rangle$, of a carrier inserted within a two vertically coupled SAD system. The system behaves like a single dot, where the two lowest energy levels are E_+ and E_-.

Using the LCQDSA method, studied in Section 4.2, states $|+\rangle$ and $|-\rangle$ have been approximated as a superposition of each isolated QD ground states. The electron localisation within the coupled system has been proposed as a qubit in [6]. The principal source of quantum states decoherence is the capture/escape process due to LO-phonon interaction, where a carrier confined within the coupled system escapes to the wetting layer absorbing or emitting a single LO-phonon.

In this section the capture/escape rate of an electron within a coupled dot system considering only the two lowest energy states $|+\rangle$ and $|-\rangle$ is calculated. It is also assumed that only one electron is present within the coupled quantum dots. The model is composed of two SAD's of height $h = 2$ nm and radius $R = 6$ nm separated by a distance d, where potential barrier is set to $V_0 = 1$ eV, the electron effective mass is $m^* = 0.023m_0$ and the density of electrons within the wetting layer is $N_c = 10^{14}m^{-2}$.

It is calculated these energies varying the distance between SAD's as can be seen in Figure 5.11b). The ground state energy level, E_+, never reaches the required energy for the carrier to escape from the QD system to the wetting layer ($E_+ > E_0^{\mathrm{W}} - \hbar\omega_{\mathrm{LO}}$). Therefore an electron confined within the system cannot be scattered from the ground state to the wetting layer due to the interaction of a single LO-phonon. In the case of the first excited estate, $|-\rangle$, the escape is allowed within the inter-dot distance range $d = 1.6 - 2.2$ nm.

The capture rate is given by Equation 5.42

$$\frac{1}{\tau} = \Gamma \int_{-\infty}^{\infty} \frac{\mathrm{dq}}{q^2} \int_{-\pi}^{\pi} \mathrm{d}\theta_{xy}^{\mathrm{W}} |G(\alpha\cos(\theta_{xy}^{\mathrm{W}}) + q_x, \alpha\sin(\theta_{xy}^{\mathrm{W}}) + q_y, qz)|^2 \tag{5.45}$$

where

$$\Gamma = \frac{me^2\omega_{LO}Pf_D}{2\hbar^2(2\pi)^4} \tag{5.46}$$

$$f_D = f_D\left(\frac{\hbar^2\alpha^2}{2m}\right) \tag{5.47}$$

In the escape process, the Fermi-Dirac term gives the probability of finding an unfilled state within the wetting layer, which is $1 - f_D$. It has to be taken into account that the carrier escapes from the QD emitting an LO-phonon. In both processes the constant Γ is given by

$$\Gamma_{\text{capture}} = \frac{me^2\omega_{LO}P^+ f_D}{2\hbar^2(2\pi)^4} \tag{5.48}$$

$$\Gamma_{\text{escape}} = \frac{me^2\omega_{LO}P^-(1-f_D)}{2\hbar^2(2\pi)^4} \tag{5.49}$$

where

$$P^{\pm} = \left(\frac{1}{\epsilon_\infty} - \frac{1}{\epsilon_0}\right)(N_0 + 1/2 \pm 1/2) \tag{5.50}$$

Figure 5.11a) shows the electron escape rate from the SAD into the wetting layer due to the absorption of a LO-phonon, while Figure 5.11b) shows the electron capture rate from the wetting layer into the SAD state due to the emission of a LO-phonon. As can be observed, the escape rate from state $|-\rangle$ is higher than the capture rate to the same state. The difference between rates can be modified changing the Fermi-Dirac distribution, i.e. altering the number of carriers within the wetting layer, N_c, as illustrated in Figures 5.12a),b).

It can also be observed that capture/escapes processes are allowed within the inter-dot distance range $d = 1.6 - 2.2$ nm, thus those processes could be avoided choosing inter-dot distances of $d > 2.2$ nm and therefore, they would not cause any dephasing to a carrier within the system.

As can be seen in Figure 5.12b), the escape rate is higher for low electron densities, which is the order of $1/\tau \approx 10^9$ 1/s, which means that the state $|-\rangle$ decoherence time due to the interaction with a single LO-phonon is the order of the nanosecond. The capture process is a source of decoherence for the two-level model, but choosing low carrier densities it can be neglected.

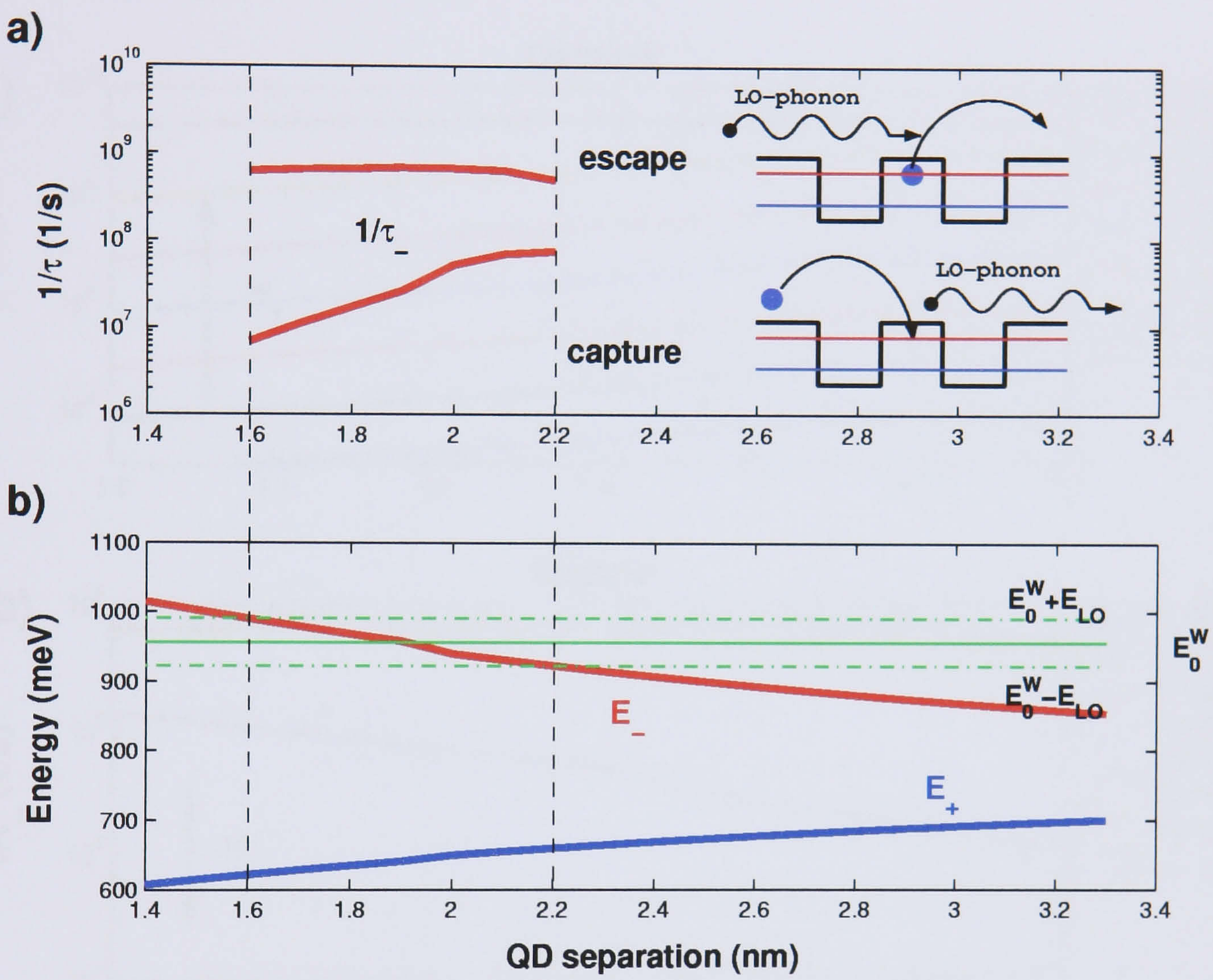

Figure 5.11: **a)**Electron escape(capture) rate from the SAD(wetting layer) into the wetting layer(SAD) absorbing(emitting) a single LO-phonon. **b)**Electronic two lowest energy levels of a double vertically coupled SAD's versus the inter-dot distance.

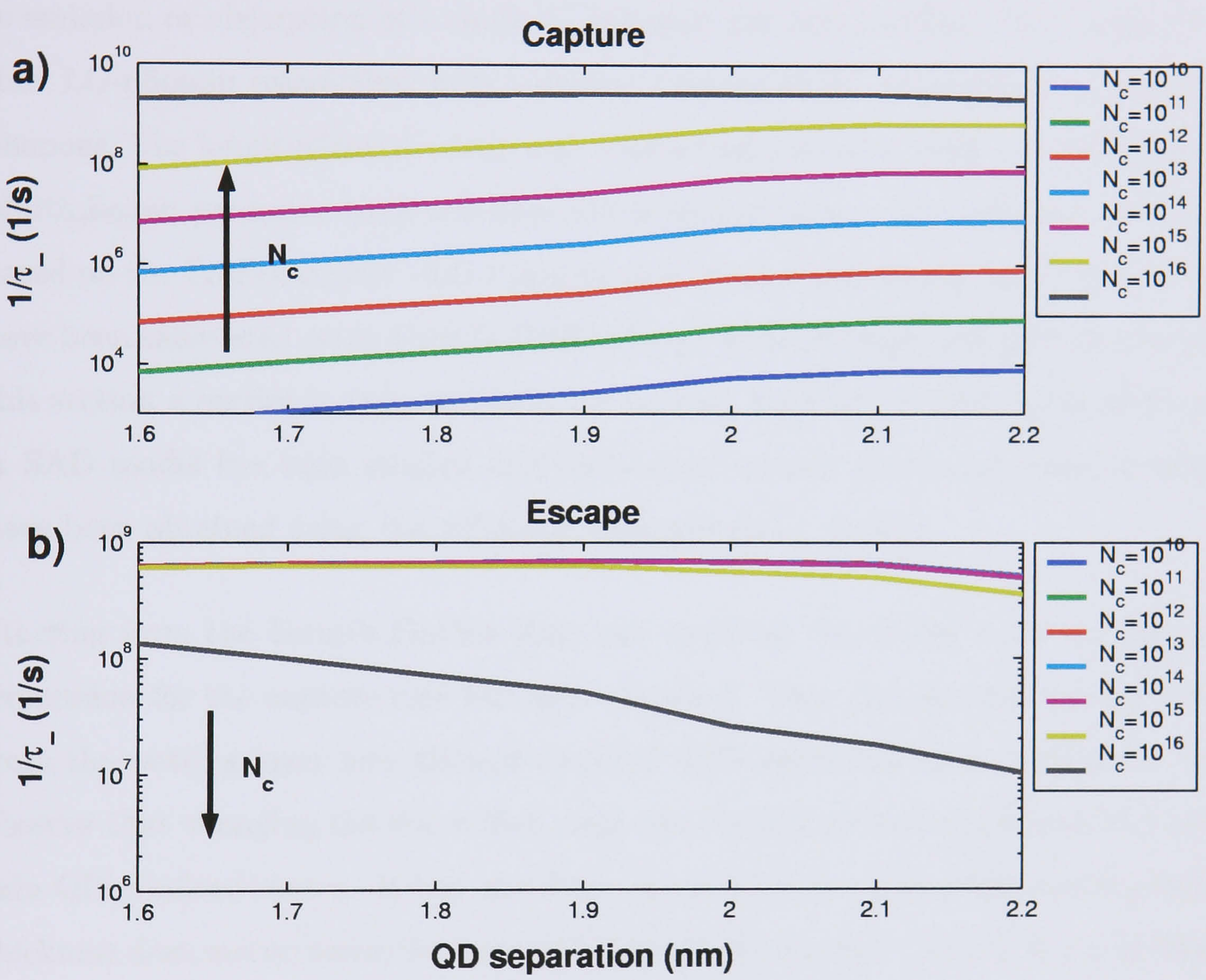

Figure 5.12: Electron **a**)capture and **b**)escape rates versus the inter-dot distance changing the density of carriers within the wetting layer, N_c.

5.7 Summary

The process of an electron capture(escape) from the wetting layer(QD) into the QD(wetting layer) for a single SAD and two vertically aligned coupled SAD's due to emission or absorption of a single LO-phonon has been studied. Due to the fact that LO-phonon interaction with carriers is dominant[1], interactions with other phonons, like longitudinal acoustic and transversal phonons, have been neglected. Multiphonon processes have not been taken into account. Calculations have been based on the Frölich carrier - LO-coupling and capture and escape rates probability have been calculated using Fermi's Golden Rule. In the capture processes studied in this section a carrier is captured from the wetting layer into a SAD confined state. A SAD model has been studied and its confined energy levels and wavefunctions have been obtained using the adiabatic approximation method.

Starting from the Fermi's Golden Rule and applying the energy conservation, an expression for the capture rate has been obtained. Then the electron capture rate from the wetting layer into allowed confined SAD states has been calculated. We observe that changing the dot radius, only the capture process is allowed into certain QD confined states. It has also been observed that varying the wetting layer thickness does not increase/decrease significantly the capture rates. It has also been compared capture rates changing the temperature. Due to the discrete nature of the carrier states in a quantum dot, the relaxation due to the interaction with a single LO-phonon is not allowed. However the carrier relaxation due to multiphonon interaction may be possible, which is considered as further work. Carrier escape/capture rates from/into two vertically aligned SAD system lowest energy levels have been calculated. Two vertically aligned SAD's have been proposed for use as a quantum gate in quantum computation. In this section those escape/capture processes are proposed as a possible source of decoherence when both dots are coupled.

We find that escape/capture processes are not allowed from/into the QD system ground state. We also observed that the escape and capture processes are permitted within a range of inter-dot distance, where the escape process is the fastest process for low electron densities (within the wetting layer) which is the order of the nanosecond. Therefore the decoherence time due to carrier - single LO-phonon scattering could be reduce to nanoseconds at low wetting layer carrier densities or it could be avoided choosing the right inter-dot distance.

Bibliography

[1] Paul Harrison. *Quantum Wells, Wires and Dots.* Wiley, 2000.

[2] Takeshi Inoshita and Hiroyuki Sakaki. Density of states and phonon-induced relaxation of electrons in semiconductor quantum dots. *Phys. Rev. B*, 56(8):4355, 1997.

[3] Richard L. Liboff. *Introductory Quantum Mechanics.* Addison Wesley, 1931.

[4] R. Ferreira and G. Bastard. Phonon-assisted capture and intradot auger relaxation in quantum dots. *Applied Phys. Letters*, 74(19):2818, 1999.

[5] R. Ferreira and G. Bastard. Carrier capture and intra-dot auger relaxation in quantum dots. *Physica E*, 7:342–345, 2000.

[6] M. Bayer, P. Hawrylak, K. Hinzer, S. Fafard, M. Korkusinski, Z. R. Wasilewski, O. Stern, and A. Forchel. Coupling and entangling of quantum states in quantum dot molecules. *Science*, 291:451, 2001.

Chapter 6

Conclusions and further work

6.1 Conclusions

In this thesis the electronic structure and wavefunctions of quantum dots of different shapes have been calculated: spherical geometry, for colloidal QD's and ellipsoidal/cylindrical geometry for SAD's and elongated colloidal QD's. These results are also the basis to investigate the coupling between QD's. The coupling of two SAD's and two colloidal QD's are studied and their possible application in quantum computation discussed. Carrier - LO-phonon interaction has been investigated as a source of decoherence in coupled SAD's systems.

In Chapter 2 the Schrödinger equation has been solved for an electron within different geometry potentials using the effective mass approximation. In order to obtain the solution for spherical and cylindrical QD's the free particle problem has been solved in spherical and cylindrical coordinates and then they have been used to obtain the solution for step-like potentials. Finite potential barriers has been considered for spheres and infinite potential barriers for spheres and cylinders. In

order to study the colloidal QD model, the solution of the Schrödinger equation for a capped spherical QD has been also obtained, where the QD is capped by a layer of higher bandgap material. Finally the Schrödinger equation is solved for a self-assembled quantum dot applying an adiabatic method.

In Chapter 3 a numerical method to solve QD structures with cylinder symmetric models is introduced, the Full Diagonalisation of the system Hamiltonian (FDH) method. In this chapter the Schrödinger equation is solved for an electron within a cylindrical symmetric quantum dot. For these structures the analytical solution is only available for certain cases like spheres or infinite potential cylinders. In other cases numerical methods must be applied. Firstly, the FDH method has been explained and applied for a spherical QD and a spherical capped colloidal QD. In both cases the results have been checked against the analytical solution calculated in Chapter 2. This example is also used to estimate the dimension of the basis set which is used to expand the Hamiltonian, where the analytical solution is not possible to obtain. Therefore, using the same basis as for the spherical QD, the solution is obtained for an ellipsoidal QD and an ellipsoidal capped QD. Another numerical method, the finite difference method, is also studied and applied to the case of a spherical QD. This method is checked against the solutions obtained analytically and using the FDH method. We find that the FDH method is much faster and accurate than the FD method making the former one a good candidate to determine the electronic structure of cylindric symmetry structures.

In Chapter 4 the coupling between two coupled dots has been studied and its application to quantum computation discussed. The linear combination of quantum dot states approximation has been outlined and used in order to obtain the electronic structure of an electron within the coupled system. This method has been verified by comparison with the FDH method for an electron within two identical coupled QD's. Due to the fact that the LQDSA method requires less computational time

than the FDH method, it is used to calculate the two lowest energy levels of an electron within two spherical QD, two vertically aligned SAD and two colloidal QD systems.

- **Two spherical QD's.** The LCQDSA method has been applied to two spherical QD's to illustrate the technique to the reader. The coupling between dots, described as the splitting energy between the first and ground state energy levels, has been calculated varying the inter-dot distance and the potential barrier showing that controlling one of these two parameters, thermal perturbations can be avoided.

- **Two vertically aligned SAD's.** The coupling between two ellipsoidal-shaped SAD's has been studied and the variation with the inter-dot distance, the confining potential and the dot dimensions investigated. Varying these parameters the coupling changes, which makes this model a good candidate to be used in quantum computation. For two identical SAD's it has been shown that changing the QD radius at the base does not alter the coupling significantly. In the case of two different SAD's the splitting energy dependence upon changes in the upper QD has been shown. Again the coupling remains nearly constant under changes on the radius, whereas it decreases when the upper dot height is increased.

- **Two colloidal QD's.** The coupling between two colloidal QD's has been studied in order to assess their suitability for use in quantum information applications. The model is composed of two spherical core-shell (CdSe-ZnS) QD's of radius around 15-20 Å and layer thickness 3 Å. The coupling has been calculated for two identical QD's varying the inter-dot distance obtaining similar results as with the FDH method. As CdSe nanocrystals are slightly elongated along the z axis, the case of two vertically aligned ellipsoidal capped QD's is investigated and compared with the two spherical QD's model. Only

changes in the QD z axis has been considered in order to preserve the cylindrical symmetry. It has been found that increasing the z axis in both QD's, while the separation is constant, decreases the coupling between them. For the case of two ellipsoidal QD's, we found that the coupling reaches a maximum with both QD's have the same dimensions.

The two-level electronic structure of the system is calculated within the effective mass approximation. The inter-dot distance affects the coupling between dots, therefore varying the separation of QD's may tune the coupling, giving a mechanism to switch it 'on' and 'off'. We observe that choosing the appropriate inter-dot distance, the model may avoid thermal perturbations. In the case of two coupled SAD's, the exchange energy between dots is insensitive to small variations in the shape of both dots within the xy-axis. Small variations are observed changing the upper QD radius at the base. In contrast, the exchange energy experiences large changes when the height of a single SAD is varied. We have also investigated the case of two aligned colloidals QD's (z-aligned in the case of ellipsoidal QD's) varying their shape. We find that without changing the separation between QD's, a maximum coupling is reached when both QD's have identical dimension and shape. Due the liquid nature of the surrounding material, the main source of decoherence, the charge-phonon scattering, can be neglected, making it a good candidate for use in quantum computation applications.

In order to study a source of the decoherence time, in Chapter 5 the electron capture(escape) process from the wetting layer(QD) into the QD(wetting layer) for a single SAD and two vertically aligned coupled SAD's due to emission or absorption of a single LO-phonons has been investigated. Calculations have been based on the Frölich carrier - LO-coupling and capture and escape rates probability have been calculated using Fermi's Golden Rule. Then the electron capture rate from the wetting layer into allowed SAD confined states have been calculated. Changing

the dot radius it has been observed that the capture process is only allowed into certain QD states. We observe that varying the wetting layer thickness does not increase/decrease significantly the capture rates. It has been also compared capture rates changing the temperature. Carrier escape/capture rates from/into two vertically aligned SAD system lowest energy levels have been calculated. Two vertically aligned SAD's have been proposed to be used as a quantum gate in quantum computation. In this thesis these escape/capture processes are studied as a possible source of decoherence when both dots are coupled. Using the model proposed it has been found that escape/capture processes are not allowed from/into the QD system ground state. It has been also observed that the escape and capture processes are permitted within a range of inter-dot distance, where escape process is faster than the capture for WL low electron densities which is the order of the nanosecond. Therefore the decoherence time due to carrier - single LO-phonon scattering could be reduce to nanoseconds at low wetting layer carrier densities or could be avoided choosing the right inter-dot distance.

6.2 Further work

- **The use of tight binding method for colloidal QD's.** In this thesis colloidal QD's of diameter $\sim 3-4$ nm have been studied. For such dimensions the effective mass approximation is not an accurate method to obtain the electronic structure and the use of other numerical methods is needed in order to be more precise. As the aim of this thesis is to provide a qualitative study of coupled colloidal QD's, the effective mass approximation has been applied. In order to obtain more accurate results, the use of tight-binding method for small colloidal QD's will be considered in further work.

- **Adding a second electron to the system**. All the calculations have been

made taking into account that only a single electron was confined within the model. Once another electron is added, the electronic structure change due to coulomb interaction. Including this effect in the model would lead to a more accurate study of the coupling between dots when each dot is populated by an electron.

- **Relaxation rates.** Due to the discreteness nature of the carrier density of states in a quantum dot, the relaxation due to the interaction with a single LO-phonon is not allowed unless the energy difference between levels is exactly the energy necessary to emit/absorb an LO-phonon, $\hbar\omega_{\mathrm{LO}}$, which is very improbable. What is allowed is the carrier relaxation to lower energy levels due to multiphonon interaction, which is left as further work. It is also left as further work the inclusion in the model carrier-carrier scattering processes which also causes the relaxation of a carrier within the QD.

- **Study DiVincenzo conditions for coupled colloidal QD's.** We have studied the coupling of colloidal QD's, but in order be a serious candidate for the implementation in quantum computing the model has to satisfy the DiVincenzo conditions (explained in Section 1.6.1). This would also make interesting future work.